Neuronal Logistics

Axonal Transport in Development and Disease

Neuronale Logistiek

Axonaal Transport in Ontwikkeling en Ziekte

Proefschrift

ter verkrijging van de graad van doctor aan de
Erasmus Universiteit Rotterdam
op gezag van de rector magnificus

Prof.dr. H.A.P. Pols

en volgens besluit van het College voor Promoties.

De openbare verdediging zal plaatsvinden op
dinsdag 29 november 2016 om 09:30 uur

door

Robert van den Berg
geboren te Sliedrecht

Erasmus University Rotterdam

Promotiecommissie:

Promotoren
Prof. dr. R.Q. Hintzen
Prof. dr. C.C. Hoogenraad

Overige leden kleine commissie
Prof. dr. J. Van Horssen
Prof. dr. P.A. Sillevis Smitt
Prof. dr. C.I. De Zeeuw

CONTENTS

LIST OF FIGURES

LIST OF TABLES

Scope of this thesis

Due to their highly asymmetrical shape and long projections, neurons are more than other cell types dependent on active transport. Motor proteins carry mitochondria and cargo vesicles along the microtubule cytoskeleton towards the cell periphery and back in a highly regulated fashion. Dysfunction of this transport system is linked to a large number of neurological disorders. Clarifying the exact mechanism in which transport deficits contribute to neurodegeneration using microscopy is a demanding endeavor, since all processes take place on a spatial scale below the diffraction limit and are therefore not resolvable using light microscopy. Superresolution microscopy using single molecule localization provides a method for studying molecular processes with nanometer resolution. This thesis aims to investigate the role of active transport along microtubules in brain development and neurodegenerative disease, as well as optimize superresolution microscopy as a research tool.

In Chapter 1 we provide a general introduction to the cytoskeleton, active transport in neurons and its role in neurological disorders.

In Chapter 2 we discuss how the function of molecular motors is essential for the function of individual neurons and the central nervous system as a whole.

In Chapter 3 we show how the dynein adaptor protein Bicaudal-D performs an essential role in the migration of granule cell neurons in the embryonic cerebellar cortex.

In Chapter 4 we investigate the mechanisms through which genetic variation affecting intracellular transport could play a role in the pathogenesis of multiple sclerosis.

In Chapter 5 we describe the outcome of a study in which experimental autoimmune encephalomyelitis (EAE) was induced in a *Kif1b* heterozygous knockout mouse.

In Chapter 6 we provide a workflow for the analysis of EAE, using a neuroscientific approach to improve the translatability to multiple sclerosis.

In Chapter 7 we discuss the limits encountered when using light microscopy and the mathematical solutions to circumvent these restrictions.

In Chapter 8 we show that stochastic optical reconstruction microscopy (STORM), using small antibody fragments for labelling, results in a significant increase of resolution.

In Chapter 9 we summarize and discuss the results obtained by the studies described in this thesis.

Chapter Headings

- Chapter 1: Simplified 3D model of the cerebrum, cerebellum, midbrain and myelum.

- Chapter 2: Model of a dynein motor protein transporting a mitochondrion along a microtubule.

- Chapter 3: The cerebellar cortex, with granule cells migrating from the external granule cell layer (top) to the internal granule cell layer (bottom) along the Bergmann glia.

- Chapter 4: Cross-section of an axon depicting the situation in health on the left, with a well-organized myelin sheath enveloping the axon. In the center, local inflammation leads to disruption of the myelin sheath. Finally, on the right the axon has lost its membrane integrity and is degrading.

- Chapter 5: Model of a kinesin motor protein transporting a mitochondrion.

- Chapter 6: *Mus musculus*, one of the most commonly used animal models in multiple sclerosis.

- Chapter 7: 3D reconstruction of a STORM dataset obtained by imaging a U2OS cell using anti-tubulin antibodies.

- Chapter 8: Fragment of a microtubule labeled with a combination of primary and secondary antibodies (back), primary antibodies only (center) and anti-Tubulin $\mathrm{VH_H}$ (front).

- Chapter 9: Möbius-tubule with kinesin and dynein motor proteins walking along it.

- Abstract: Artist impression of motor proteins as molecular machines, carrying the energy source of the cell to its destination.

- Bibliography: Wordcloud depicting the relative frequency of nouns in the titles of publications included in the references. A larger font size corresponds with a higher frequency.

- About the author: Wordcloud depicting skills, interests and hobbies of the author.

- Acknowledgements: Line drawing of the Kruyt Building in Utrecht (front) and the faculty tower of the Erasmus MC in the background.

All drawings were created by the author of this thesis.

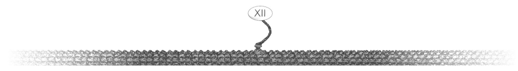

Introduction

1

GENERAL INTRODUCTION

> The chief function of the body is to carry the brain around.
>
> Thomas A. Eddison

The Brain

Inside our skull resides a miraculous organ. It processes input from our sensory organs and uses this information to plan, initiate and coordinate movement. Far beyond being limited to this menial labor, this structure is able to reflect on space and time, beauty and justice. It enables us to learn and to love, to regret and to rejoice. All that makes us human depends on the proper function of the just over a kilogram of matter that forms our brain. When a disease affects the brain, its consequences affect every aspect of our humanity. Diseases affecting other organs of the body can dramatically affect our lives, causing pain and suffering. However, as long as the brain is spared, our core identity remains intact. When an illness impairs the function of our nervous system, however, we face the frightening prospect of losing our self. Who we are, is defined by our brain.

Every organ in the body consists of cells, and the brain forms no exception. The main cell type of the nervous system is called a neuron. The unique property that sets the neuron apart from other cell types is its ability to generate and conduct electrical signals. Neurons communicate with each other through synapses, contact points between cells where the electrical signal is converted into a chemical signal, passed on to the next cell and transformed back into an electrical signal. A signal can be strengthened or weakened depending on the number of receptors present at each synapse. Neurons that work together on a certain task strengthen their connections, making it easier to perform this task in the future. This mechanism of synapse potentiation is thought to be the neurological basis of learning and memory. The receiving parts of the synapses are located on the dendrites, branched tree-like structures protruding from the cell body (figure 1.1 **A**). Every neuron has an excitation threshold, it will only fire and pass on a signal if the input through the synapses exceeds a certain limit. If this is the case, an action potential is generated in the axon hillock and an electrical signal travels along the axon to the terminals at the far end of the cell, where it will either contact the synapse of another neuron or an end-organ such as a muscle.

The Need for Speed

From a molecular biology perspective, neurons have another even more unique property: their size. Most cells, such as those located in the skin, are round or rectangular in shape and approximately 30 30 µm in diameter. The largest cell in the human body, the female ovum, is 130 µm in diameter. Although most human axons have a modest diameter of no more than 5 µm, their length can be up to 1.5 m and more. To put that to scale, imagine a common drinking straw with a diameter of 5 mm. Adjusting its length to the scale of an axon would result in a rather inconvenient 1.5 km long straw. This size presents the cell with unique challenges. To keep its axon alive and functional, it needs to provide it with membrane components, neurotransmitters and proteins. Mitochondria, the organelles producing the energy source ATP, should be available where they are needed most, at the sites where the energy consumption is highest (figure 1.1 **B**). Smaller cells and bacteria can partially rely on diffusion, the motion of molecules from regions with a high concentration to areas with a lower concentration. The speed of diffusion in three dimensions can be estimated using the following simplified formula $x^2 = 6Dt$, where x signifies mean-square displacement, D the diffusion coefficient and t time. Considering a small protein inside a cell has a diffusion coefficient of approximately $30\,\mu\mathrm{m\,s^{-2}}$ to $50\,\mu\mathrm{m\,s^{-2}}$ (Kühn et al., 2011), it can cross a 30 µm cell in three to five seconds. However, a one-and-a-half meter trip from the cell body to the axon terminal using diffusion only would take the same protein an incredible 396 *years*. Clearly, neurons need a much more efficient solution than diffusion for their logistic needs.

This solution consists of a transport system of remarkable complexity. Through every part of the neuron run microtubules, hollow tubes composed of tubulin-α and -β subunits. Motor proteins called kinesins and dynein can bind to these microtubules and use them to 'walk' through the cell, carrying cargo along with them (figure 1.1 **C**). Through this system, a continuous flow of mitochondria and cargo vesicles is transported to and from the cell body, taking approximately a week to complete the entire journey along the axon. The proteins attaching the cargo to the motor protein are able to detect environmental signals such as a high calcium concentration -indicating high energy consumption- and detach the cargo at these sites. Anchoring proteins are able to bind cargo vesicles and mitochondria to the microtubules, keeping them at these high-demand locations until the need for their cargo has passed. With every signal fired and every synapse strengthened, this transport system has to adapt and

rearrange its cargo delivery pattern (Van den Berg and Hoogenraad, 2012). Without it, there is no way a neuron can continue to function properly, or even survive.

Without Transport, Nothing Moves

This explains why a defective or less efficient transport system is associated with a large number of -mostly neurological- disorders (figure 1.2). In a few cases, mutations in genes encoding transport proteins may directly lead to a disease, for example in brain developmental disorders. However, it is likely that in most situations a suboptimal transport system will diminish the ability of a neuron to withstand stress caused by other factors, leading to increased neuronal cell death (neurodegeneration). This would explain the vast range of diseases to which transport is linked. The common issue in all these disorders is that they cause cellular stress to the neuron, either through accumulation of protein aggregates, a toxic micro-environment or decreased mitochondrial function. All these situations lead to an increased thirst for ATP, which has to be quenched by transporting additional mitochondria into the stress zone. The functioning of the axonal transport system essentially determines how long a neuron is able to hold its breath.

One of the disorders to which transport has been linked is multiple sclerosis (MS). MS is a disease that mainly affects young women, causing severe disability (Alastair and Alasdair, 2008). The immune system plays a key role in MS, as an autoimmune response is triggered against the myelin sheath surrounding the axon, causing immune cells to infiltrate the central nervous system and destroy the myelin. However, it is not understood what the primary cause of MS is, the event that triggers the immune response. As the disease progresses, patients with MS gradually experience more and more lasting symptoms. This is not caused by the immune reaction itself, but by the loss of axons it causes. Defects in axonal transport reduce the capability of the neuron to survive a period of demyelination and inflammation, increasing the risk of neurodegeneration and therefore accelerating the progression of clinical disability.

Transport reaching its Destination

In the previous two decades, neuroscience, the field of science dedicated to studying the function of the nervous system, has made tremendous progress. It's clinical counterpart, the discipline of neurology, is currently in the process of translating all these findings to the clinic. This thesis builds on the extensive body of basic research on axonal transport collected in the previous years and attempts to use it to better understand MS. Currently, no treatments exist that slow down neurodegeneration through modulation of the transport system. Such medication would be applicable in a large range of neurological disorders, slowing disease progression and greatly reducing suffering. However small its contribution might be, that is the final goal of this thesis.

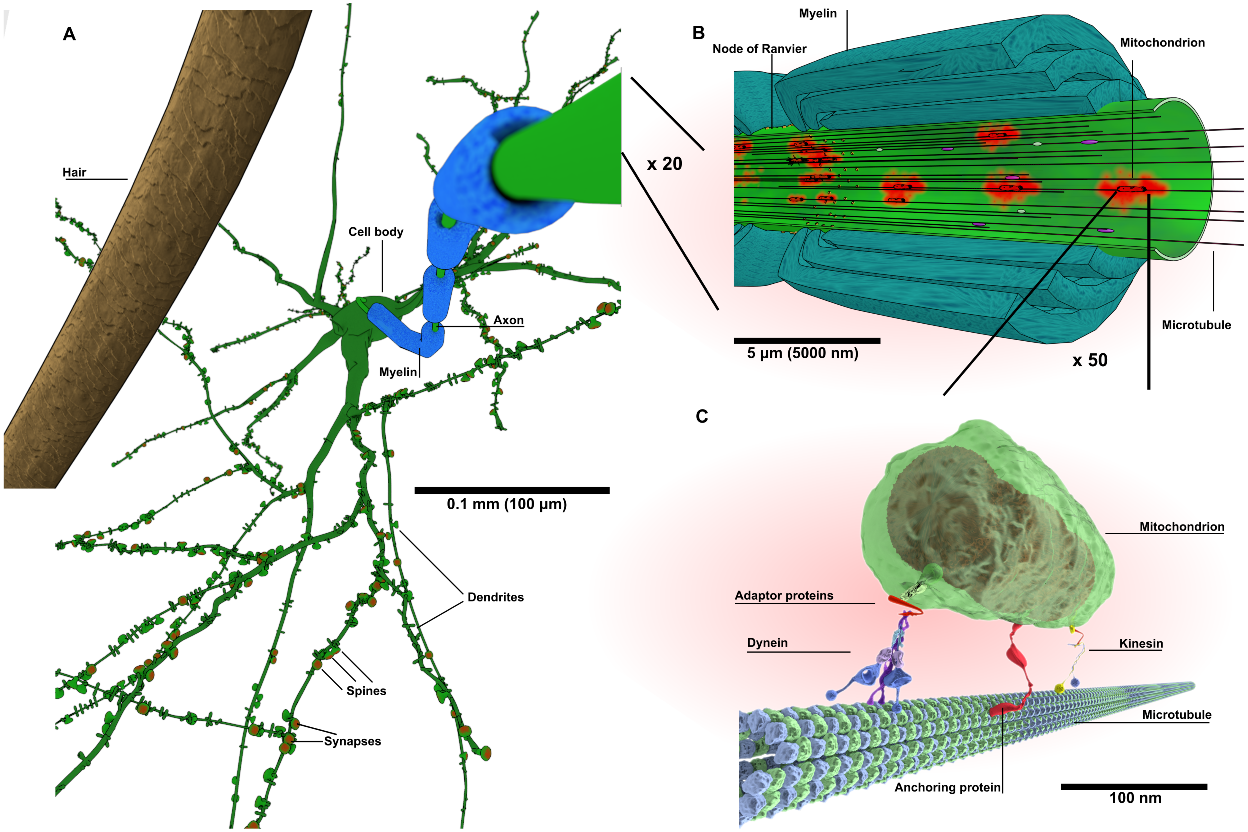

Figure 1.1: Neurons and transport. The neuron (**A**) is the functional cellular subunit of the nervous system. The dendrites are covered with mushroom-shaped spines, on top of which the synapses are located (red dots), through which the neuron receives its signals. The axon (upper right) is covered with myelin sheaths, interrupted by nodes of Ranvier. For reference, a high magnification image of a human hair is shown in the upper left corner. When we magnify our image another 20 times (**B**), the microtubules become visible running through the axon, along which mitochondria and other cargo organelles are transported. Mitochondria produce ATP (red clouds) primarily at cellular zones with high energy consumption, like the nodes of Ranvier. Another 50 times magnification (**C**) shows a single microtubule along which a pair of motor proteins walk, carrying a mitochondrion, while an anchoring protein attempts to keep the mitochondrion in position. Adaptor proteins form the connection between motor and cargo.

Figure 1.2: Transport and disease. Wordcloud showing neurological disorders associated in literature with components of the transport system. This figure was created using an R (R Core Team, 2014) script searching PubMed for all MeSH-terms hierarchically ordered under 'Neurological Disorders' and one of the terms 'axonal transport', 'kinesin', 'dynein', 'tubulin', 'microtubule-associated proteins' or 'secretory pathway'. Double entries were removed, but some publications were listed more than once under different hierarchical headers. Size of the term indicates number of publications. Only terms with more than 3 publications have been included.

Molecular motors in cargo trafficking and synapse assembly

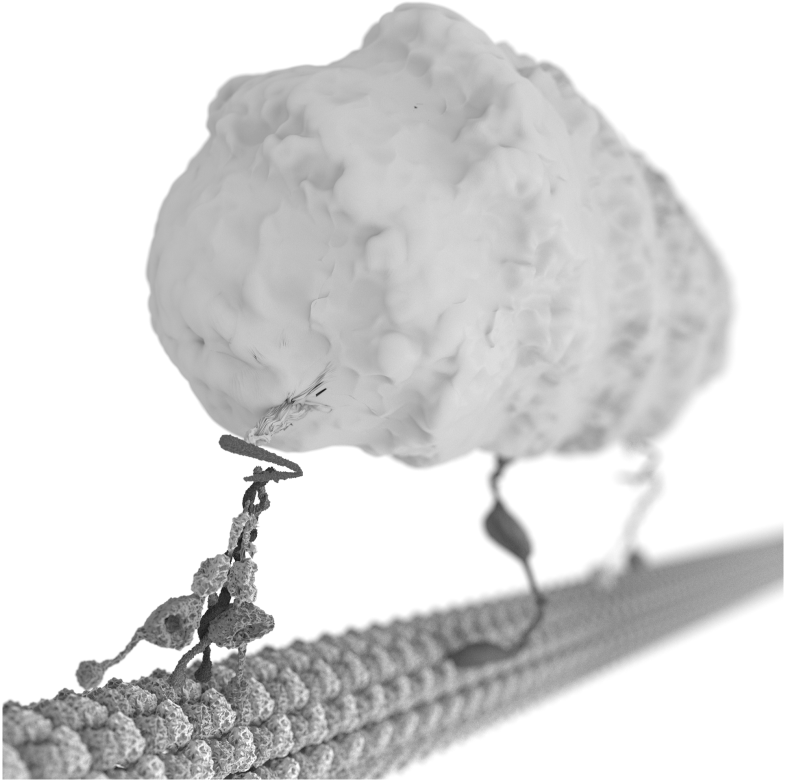

Published as:
Van den Berg, R and Hoogenraad, CC
Molecular motors in cargo trafficking and synapse assembly
Advances in Experimental Medicine and Biology 2012

2

MOLECULAR MOTORS IN CARGO TRAFFICKING AND SYNAPSE ASSEMBLY

Every production process, be it cellular or industrial, depends on a constant supply of energy and resources. Synapses, specialized junctions in the central nervous system through which neurons signal to each other, are no exception to this rule. In order to form new synapses and alter the strength of synaptic transmission, neurons need a regulatory mechanism to deliver and remove synaptic proteins at synaptic sites. Neurons make use of active transport driven by molecular motor proteins to move synaptic cargo over either microtubules (kinesin, dynein) or actin filaments (myosin) to their specific site of action. These mechanisms are crucial for the initial establishment of synaptic specializations during synaptogenesis and for activity-dependent changes in synaptic strength during plasticity. In this chapter, we address the organization of the neuronal cytoskeleton, focus on synaptic cargo transport activities that operate in axons and dendrites, and discuss the spatial and temporal regulation of motor protein-based transport.

Introduction

One apparent feature of neurons is that once the axon and dendrites have grown out, they establish synaptic contacts forming neuronal networks that propagate information in a unidirectional fashion. Excitatory synaptic signaling in the brain occurs by releasing glutamate from ‘sending’ neurons and activating glutamate receptors at ‘receiving’ neurons (Sheng and Hoogenraad, 2007; Sudhof, 2004). Structurally, synapses are divided into two specialized domains: the presynaptic bouton on the axon side of the ‘sending neuron’ and the postsynaptic compartment on the dendrite of the ‘receiving’ neuron. The directional nature of signal relay requires that synaptic contacts are morphologically asymmetric with distinct protein components. Recent studies have identified the molecular components of synapses, particularly by using genetic and proteomic strategies, and have revealed that the specification of synaptic function, for example, excitatory or inhibitory, at both pre- and postsynapses is achieved via the recruitment and assembly of very distinct synaptic complexes (Jin and Garner, 2008; Kim and Sheng, 2004; Margeta et al., 2008; Sheng and Hoogenraad, 2007). Proper arrangement of pre- and postsynaptic membranes and organization of pre- and postsynaptic compartments is essential for accurate synaptic signaling, neural network activity, and cognitive processes such as learning and memory formation (Kasai et al., 2010; Lisman et al., 2007; Yuste and Bonhoeffer, 2001).

Most of the synaptic cargos, such as neurotransmitter receptors, ion channels, integral membrane proteins, signaling complexes, mRNAs, synaptic vesicle precursors or mitochondria, are made and pre-assembled in the cell soma and need to be transported to the proper synaptic destinations. Studies on intracellular trafficking have demonstrated various mechanisms for compartment-specific localization (Goldstein and Yang, 2000; Hirokawa and Takemura, 2005; Hoogenraad and Bradke, 2009; Winckler and Mellman, 2010). For example, several synaptic cargos are non-specifically transported to both axons and dendrites and are then selectively retained at the required compartments (Bel et al., 2009; Garrido et al., 2001; Leterrier et al., 2006; Sampo et al., 2003; Wisco et al., 2003). Alternatively, many presynaptic cargos are correctly sorted into axons (Kaether et al., 2000; Pennuto et al., 2003), whereas postsynaptic components move specifically into dendritic branches and spines, which are specialized dendritic protrusions that mediate most of the excitatory synaptic transmission (Craig et al., 1993; Ruberti and Dotti, 2000; Stowell and Craig, 1999; Wang et al., 2008). In consequence, synaptic precursor vesicles need to be steered into axons in order to reach the presynaptic terminals, and glutamate receptors need to be transported into dendrites to be correctly inserted in the postsynaptic membrane. Importantly, several neurological diseases are linked to abnormalities in the machinery that controls synaptic cargo trafficking (Chevalier-Larsen and Holzbaur, 2006; Gunawardena and Goldstein, 2004; Lau and Zukin, 2007; Shepherd and Huganir, 2007; Van Spronsen and Hoogenraad, 2010).

Most intracellular cargo transport is driven by molecular motor proteins that move along two types of cytoskeletal elements: actin filaments and microtubules (Schliwa and Woehlke, 2003; Vale, 2003). Actin facilitates motility of motor proteins of the myosin superfamily, whereas microtubules serve as tracks for two families of motor proteins, kinesin and dynein. While many different motor proteins have been found to participate in neuronal cargo trafficking (Goldstein and Yang, 2000; Hirokawa and Takemura, 2005), for many of these their precise contribution to synaptic cargo transport has remained unclear. Most current models for neuronal trafficking rely heavily on microtubule plus-end-directed kinesin family members (Hirokawa and Takemura, 2005); however, recent work reported important roles for dynein and myosin in synaptic cargo transport (Kapitein et al., 2010a; Lewis et al., 2009; Zheng et al., 2008). Further evidence suggests that the docking of molecular motors to synaptic cargo vesicles via adaptor molecules is an important mechanism to achieve transport specificity (Akhmanova and Hammer, 2010; Schlager and Hoogenraad, 2009).

It has intrigued scientists for a long time how synaptic cargo can be sorted in neurons along the cytoskeleton network to ensure precise cargo delivery. How are motor-cargo complexes able to choose between transport routes to the axon or dendrites? Here, it is important to consider that the actin and microtubule filaments themselves are intrinsically polarized structures with two functionally distinct ends, a 'plus' and 'minus' end. The polarity of the cytoskeleton filaments exists not only at the two ends but also all along the length of its lattice, which is critical for the directional movement of molecular motor proteins. For example, dynein transports cargo toward the minus end of microtubules, while kinesins motor proteins move toward the plus end of microtubules. In this way, local polarity patterns of microtubules and actin filaments in axon and dendrites can direct motor-driven cargo trafficking within neurons. Recent evidence suggests that a well-organized cytoskeleton network exists in neurons that can facilitate directional motor-driven cargo trafficking and establish asymmetric distributions of specific synaptic proteins (Kapitein et al., 2010a). Moreover, variations in cytoskeleton density, binding proteins, and posttranslational modifications could also drive synaptic cargo transport in specific directions. Thus, knowing the polarity and modification pattern of microtubules and actin in axon and dendrites is an instrumental piece of information for understanding how molecular motors direct synaptic cargo traffic.

In this chapter, we aim to give an overview of the molecular trafficking mechanisms important for the delivery of synaptic proteins. We will review current knowledge about the organization of the neuronal cytoskeleton, focus on synaptic cargo sorting and trafficking into axons and dendrites, and discuss the spatial and temporal regulation of motor protein-based transport. Studying the basic cellular machinery for synaptic cargo trafficking will help us to understand fundamental principles of synapse formation, function, and plasticity.

Microtubule and Actin Cytoskeleton in Neurons

The cytoskeletal organization in neurons is specialized in several ways, involving intracellular variations in density, orientations, binding proteins, and posttranslational modifications. Recently, it has become increasingly clear that these specific cytoskeletal properties directly modulate the activity of specific molecular motor proteins. In this section, we will review current knowledge about the structure, organization, and modifications of the microtubule and actin cytoskeleton (Fig. 2.1).

Actin and Microtubule Structure and Dynamics

The main transport infrastructure in eukaryotic cells is formed by the microtubules and actin cytoskeleton. To serve this function, the cytoskeleton must be organized into a wide variety of configurations, ranging from the higher-order actin-based networks in dendritic spines to the dense anti-parallel microtubule array in dendritic shaft. Without the cytoskeleton, neurons would not be able to maintain their complex axonal and dendritic architectures and synaptic organization.

Microtubules are noncovalent polymers of α- and β-tubulin dimers that form a hollow

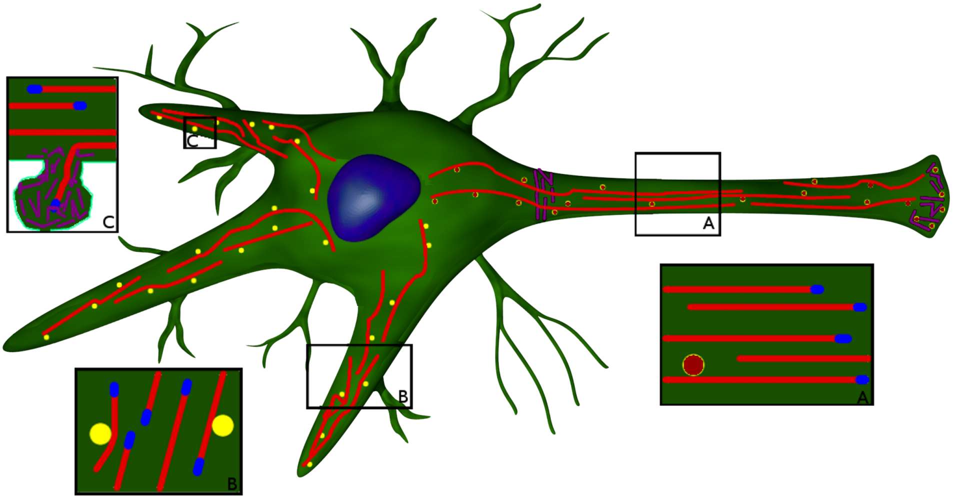

Figure 2.1: Cytoskeleton organization in neurons. Microtubules (red) are present in both axons and dendritic shaft, while actin (purple) is enriched in the axon initial segment and dendritic spines. From the cell soma, synaptic cargo vesicles are sorted into the dendrites (yellow vesicles) or the axon (red vesicles). (a) In the axon, all microtubules are oriented with their plus ends (blue comets) pointing outward. (b) In dendrites, microtubules have a mixed orientation. (c) Dynamic microtubules occasionally enter spines.

cylinder with a diameter of 25 nm and actin filaments consist of monomers of the protein actin that polymerizes to form 8-nm fibers (Howard and Hyman, 2009); (Pollard and Cooper, 2009). There are multiple actin and α- and β-tubulin genes that are highly conserved among and between species and might be utilized for distinct neuronal functions. With the recent discovery of several congenital neurological disorders that result from mutations in genes that encode different α- and β-tubulin isotypes, novel paradigms have emerged to assess how selective perturbations in microtubule subunits affect neuronal functioning (Baran et al., 2010; Keays et al., 2007). For example, a series of heterozygous missense mutations in TUBB3, encoding the neuron-specific β-tubulin isotype III, have been described that result in a spectrum of human nervous system disorders (Tischfield et al., 2010). A knock-in disease mouse model reveals axon guidance defects without evidence of cortical cell migration abnormalities. Importantly, it was demonstrated that the disease-associated mutations impair tubulin heterodimer formation and disrupt the interaction with kinesin motors.

Microtubules and actin filaments are intrinsically polar structures and contain two distinct ends, a ‘plus end’ favored for assembly/disassembly and a ‘minus end’ which is less favored for these dynamics. Minus ends of microtubules are often, but not always, attached to the centrosome from which the microtubule is nucleated. It was recently found that the centrosome loses its function as a microtubule-organising center during development of hippocampal neurons (Stiess et al., 2010). It is well possible that acentrosomal microtubule nucleation arranges the neuronal microtubule cytoskeleton in mature neurons and is responsible for the extended and complex morphology of neurons. In living cells, microtubules and actin filaments are highly dynamic, and their dominant kinetic behavior is known as dynamic instability, where the individual ends alternate between bouts of growth ('polymerization') and shrinkage ('depolymerization') (Mitchison and Kirschner, 1984). Microtubules and actin filaments may also undergo treadmilling, a phenomenon in which filament length remains approximately constant, while monomers add at the plus end and dissociate from the minus end (Kueh and Mitchison, 2009).

Regulation of microtubule and actin dynamics and turnover plays an important role in neuronal development and synaptic plasticity (Conde and Caceres, 2009; Dent and Gertler, 2003; Frost et al., 2010a; Hotulainen and Hoogenraad, 2010). It is not surprising that recently, a lot of attention has been given to the plus ends of the microtubule, the site where most dynamics takes place. The microtubule plus end can grow, then undergo a shrinking event ('catastrophe'), pause, and grow again ('rescue'), all in a matter of seconds. The fate of the microtubule is determined by a large number of plus-end tracking proteins, most of them only found on the microtubule tip, that can control microtubule dynamics (Akhmanova and Steinmetz, 2008; Gouveia and Akhmanova, 2010). Plus-end tracking proteins regulate different aspects of neuronal architecture by mediating the cross talk between microtubule ends, the actin cytoskeleton, and the cell cortex, and participate in transport and positioning of signaling factors and membrane organelles (Hoogenraad and Bradke, 2009; Jaworski et al., 2008). For example, it was recently found that the microtubule plus-end binding protein EB3 regulates actin dynamics in dendritic spines and is involved in spine morphology and synaptic plasticity (Jaworski et al., 2009).

Actin Organization in Neurons

Microtubules and actin filaments are present throughout the cell body and axonal and dendritic compartments (Cingolani and Goda, 2008; Conde and Caceres, 2009; Hotulainen and Hoogenraad, 2010). In mature neurons, actin is the most prominent cytoskeletal protein at synapses, being present at both the pre- and the postsynaptic terminals but highly enriched at dendritic spines (Landis et al., 1988; Landis and Reese, 1983). Neurons treated with latrunculin, an inhibitor of actin polymerization, showed that the actin cytoskeleton is necessary for synapse formation, stability, and normal synaptic activity (Krucker et al., 2000; Okamoto et al., 2004). At the presynaptic terminal, actin filaments are important in organising and recycling of synaptic vesicle (Cingolani and Goda, 2008), while at the postsynaptic site, actin is involved in receptor trafficking and spine plasticity (Frost et al., 2010a; Hotulainen and Hoogenraad, 2010). Spines exhibit a continuous network of both branched and long, linear actin filaments (Korobova and Svitkina, 2010). In the spine heads, actin filaments are oriented with their plus ends to the postsynaptic density and synaptic membrane and their minus ends toward the dendritic shaft. The most likely role of actin in mature spines is to stabilize postsynaptic proteins and modulate spine head structure in response to postsynaptic signaling (Frost et al., 2010a; Hotulainen and Hoogenraad, 2010). Several recent studies using advanced microscopy techniques present new insights in the organization and molecular composition of actin cytoskeleton in dendritic spines (Frost et al., 2010b; Honkura et al., 2008; Korobova and Svitkina, 2010). For example, electron microscopy revealed that actin filaments in the neck of dendritic spines exhibit mixed polarity, although the plus ends are predominantly oriented away from the dendritic shaft (Hotulainen et al., 2009; Korobova and Svitkina, 2010). Mutations in genes that code for actin regulatory proteins, like Rho GTPases, are commonly associated with mental retardation (Govek et al., 2004). Subtle variations in spine size and shape, mediated by the actin cytoskeleton, are associated with a variety of neurological and psychiatric disorders like schizophrenia and drug addiction (Blanpied and Ehlers, 2004; Van Spronsen and Hoogenraad, 2010).

Apart from its organization in synapses and spines, little is known about the arrangement of the actin cytoskeleton in the axonal and dendritic shafts in mature neurons (Kapitein et al., 2010a). Evidence suggests that actin is present as short, branched filaments in the axon oriented perpendicular to the plasma membrane and is sometimes aligned with microtubules (Bearer and Reese, 1999). Several papers showed that actin is enriched in the axon initial segment (Nakada et al., 2003; Winckler et al., 1999). Here, actin is an important regulator of Na^+- channel stability at the initial segment membrane and is actively involved in the maintenance of neuronal polarity (Rasband, 2010). The actin network in the initial segment could also function as a selective barrier for cargo transport to enter the axon. In fact, a recent paper presented evidence for an actin-based molecular sieve that prevents the diffusional entry of large macromolecules at the initial segment and isolates the axon from the cell body (Song et al., 2009). In contrast, other work proposed that the actin organization in axons promotes retrograde cargo transport by myosin Va motors (Lewis et al., 2009), which would require actin filaments of uniform polarity oriented parallel to the axon long axis. To better understand actin-based transport activity in neurons, detailed studies are required to reveal the actin cytoskeleton organization in axons, dendrites, and at the initial segment.

Microtubule Organization in Neurons

In mature neurons, most neuronal microtubules are not attached to the centrosome (Stiess et al., 2010) and form dense bundles running along the length of axons and dendrites (Fig. 2.1). Individual microtubules do not extend along the entire length of neuronal processes; instead, microtubule fragments stabilized at their minus ends form regularly spaced longitudinal arrays cross-linked by microtubule-associated proteins (MAPs) (Chen et al., 1992). Two abundant neuronal MAPs whose distributions are polarized between axons and dendrites are tau and MAP2 (Dehmelt and Halpain, 2005). Since tau and MAP2 induce the formation of longitudinal microtubule bundles with a distinct spacing, it is plausible that MAPs are directly involved in the organising of polarized cargo trafficking in axons and dendrites. So far, there is no evidence that this different spacing directly influences the transport machinery. In contrast, the presence of MAPs on the microtubule lattice seems to affect motor protein motility in vitro (Dixit et al., 2008). MAPs can cause decreased attachment and/or increased detachment of kinesin-1 motors and/ or vesicles (Verhey and Hammond, 2009). However, a direct role of MAPs in guiding polarized transport seems unlikely, as tau and MAP2 knockout mice show relatively mild phenotypes (Dehmelt and Halpain, 2005).

Microtubule arrays within axon and dendrites are highly organized with respect to their intrinsic polarity (Hoogenraad and Bradke, 2009; Kapitein et al., 2010a). In the late :1980s, an elegant hook-decoration technique was used to determine the orientation of microtubules in axons and dendrites by electron microscopy (Baas et al., 1988; Burton, 1988). Surprisingly, microtubules in the axon are generally long and uniformly oriented, with their plus ends facing outward, while the microtubules in the dendrites are oriented in both directions (Fig. 2.1). Thinner, more distal dendrites, however, contain unipolar microtubules oriented the same way as axonal ones (Baas et al., 1988, 1989). This specialized microtubule organization has also been captured in action by visualising EB3-GFP in living neuronal cells (Jaworski et al., 2009; Morrison et al., 2002; Stepanova et al., 2003). Stepanova et al. showed that in axons and distal dendrites, all dynamic microtubule plus ends point toward growth cones, while in proximal dendrites, significant EB3-GFP displacement was directed toward the cell body (Stepanova et al., 2003). Remarkably, the use of EB1-GFP tracking in Drosophila neurons provided strong evidence that axons and dendrites both have microtubule arrays of uniform polarity orientation. However, while axonal microtubules were uniformly plus-end distal, dendritic microtubules were of the opposite orientation, nearly all minus-end out (Rolls et al., 2007; Stone et al., 2008). These results show a striking difference in microtubule orientations in axons and dendrites and further prompt the idea that these distinct patterns might underlie polarized sorting of synaptic cargos (Fig. 2.2). Distinct patterns of microtubule orientation can directly generate asymmetries in the composition of each neuronal compartment by directing specific motor protein transport into axons or dendrites. Indeed, recent work in vertebrates, worms, and flies reported a specific role for plus- and minus-end-directed motor proteins in steering synaptic cargo transport into either axons or dendrites (Kapitein and Hoogenraad, 2011; Zheng et al., 2008) and found that the cyclin-dependent kinase pathway regulates polarized trafficking of presynaptic components (Ou et al., 2010).

Microtubule Modifications in Neurons

One other way to directly influence synaptic cargo transport is to generate functional diversity by modifying the cytoskeleton; motor proteins recognize the various spatial cues and establish specific synaptic cargo trafficking routes. It has also recently been demonstrated that posttranslational modification of microtubules can alter their stability and motor protein-binding characteristics (Verhey and Hammond, 2009). Stable microtubules in neurons typically accumulate a variety of posttranslational modifications, like acetylation, detyrosination, and (poly)glutamylation. Although both dendrites and axons have high levels of acetylated microtubules, acetylated microtubules are abundantly present in axons (Witte et al., 2008). The selective

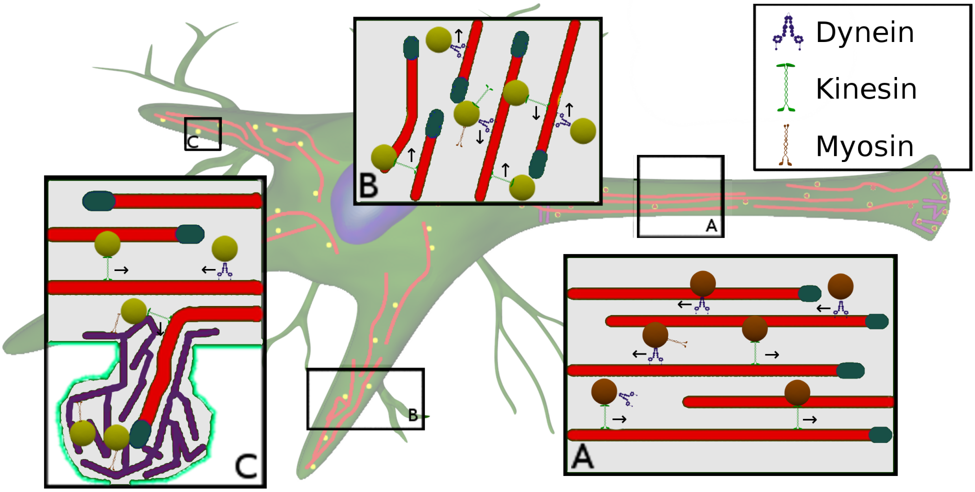

Figure 2.2: Essential components of the synaptic cargo transport machinery. Kinesin, dynein, and myosin are the three classes of motor proteins that form the workforce of the transport system. (a) In the axon, dynein typically moves its cargo retrograde, toward the cell body, while kinesins move outward toward the synapse. Multiple active and inactive motors can be simultaneously attached to one synaptic cargo vesicle. (b) The situation in the dendrite is more complex, as both kinesins and dynein can move in antero- and retrograde direction, depending on the orientation of the underlying microtubule. (c) Upon arrival at the base of the spine, cargo vesicles are transported along the actin network by myosin motors

enrichment of acetylated microtubules in axons can be abolished by inhibition of a known α-tubulin deacetylase, histone deacetylase 6 (HDAC6), suggesting that in normal situations, the activity of tubulin-modifying enzymes differs between axons and dendrites rather than that the acetylation reaction is restricted to the axon (Janke and Kneussel, 2010). Biochemical evidence revealed that kinesin-1 has an increased affinity for acetylated microtubules, consistent with the observation that in fibroblast cells, kinesin-1 motility occurs predominantly over modified microtubules (Cai and Sheng, 2009b). It was proposed that acetylation of microtubules was the major determinant for the selective motility of kinesin-1 motors into specific neurites. Kinesin-1 also preferentially binds detyrosinated microtubules (Liao and Gundersen, 1998), which are also enriched in the axon. Recent work identified a specific region in kinesin-1, termed b5-L8, to be responsible for this preference (Konishi and Setou, 2009). Interestingly, upon knockdown of tubulin tyrosine ligase (TTL), the fraction of dendrites that contained kinesin-1 increased. Recently, synaptic activity has been shown to modify microtubules posttranslational modifications (Maas et al., 2009). Treatment of neurons with strychnine, an inhibitor of the glycine receptor, increases neuronal activity, leads to increased polyglutamylation, and influences synaptic cargo transport. In this way, microtubule modifications are intimately related to synaptic changes and synaptic cargo transport.

Microtubule- and Actin-Based Motor Proteins

In general, cargos are transported over long distances along microtubules before transferring to the actin cytoskeleton for the final part of their journey. A common feature of both actin- and microtubule-based transport is that the force required for cargo transport is generated by molecular motor proteins through ATP hydrolysis (Kardon and Vale, 2009; Schliwa and Woehlke, 2003; Vale, 2003; Woolner and Bement, 2009). The motor proteins that use microtubules as tracks are the minus-end-directed dynein and plus-end-directed kinesins, whereas myosins move along actin filaments. Neuronal cargo trafficking is achieved by the concerted efforts of both microtubule-based and actin-based motors (Hirokawa and Takemura, 2005; Schlager and Hoogenraad, 2009). Several classes of myosin motors participate in synaptic cargo transport in axon and dendrites most commonly used are myosin V and myosin VI. Although the basic machinery for microtubule- and actin-dependent transport in neurons is well established, how synaptic cargos achieve specificity and directionality to their site of action is an emerging field of investigation. In this section, we will introduce the actin and microtubule transport system and its main components. We will also explain the role the actin network plays in selecting the destination of cargo and its role in synaptic function.

Myosin Motor Proteins in Neurons

Myosins were the first molecular motors to be discovered and comprise a large (∼25 classes) evolutionary conserved family of actin-based motor proteins (Conti and Adelstein, 2008). Early studies focused on the role of myosins as force generators in muscle tissue. The head region in the myosin heavy chain contains the motor domain; this is the site of ATP hydrolysis, which leads to a force generating conformational change (Conti and Adelstein, 2008). It was long thought that the sole function of myosin was to generate force in muscles; however, with the discovery of non-muscle (unconventional) myosin, new roles for myosin motors were uncovered. Several myosin motors can move directionally along actin filaments, such as myosin V toward the plus end and myosin VI toward the minus end (Sweeney and Houdusse, 2010; Woolner and Bement, 2009). Myosin motors have been implicated in short-range transport of synaptic cargos, especially in the areas of the neuron where there is hardly any microtubule network, like dendritic spines and presynaptic terminals. For example, myosin V and VI regulate the mobility of synaptic vesicles at the presynapse (Cingolani and Goda, 2008) and AMPA receptor-containing recycling endosomes in dendritic spines (Nash et al., 2010); (Osterweil et al., 2005; Rudolf et al., 2011; Wang et al., 2008). Moreover, myosin motors can also be involved in regulating microtubule-based cargo transport, either by making direct physical contact with kinesin motors and enhancing each others processivity (Ali et al., 2008; Huang et al., 1999) or by cooperative actions of actin- and microtubule-based motors on a single cargo (Gross et al., 2007). These motor-motor interactions may represent a mechanism by which the transition of vesicles from microtubules to actin filaments or vice versa is regulated. In contrast, recent data suggest that myosin V and VI can facilitate organelle docking by opposing, rather than complementing, microtubule-based movements (Pathak et al., 2010). Emerging data show that myosin motors are not only important for transport of cargo, they also regulate the secretion of exocytotic vesicles by docking them in actin-rich areas (Desnos et al., 2007). Moreover, myosin II can also regulate actin dynamics in spines in response to synaptic stimulation (Rex et al., 2010; Ryu et al., 2006). All these different actions of myosin motors, such as regulating synapse shape and stability, transporting and docking synaptic vesicles, and influencing actin dynamics, are important for synaptic function and plasticity (Hotulainen and Hoogenraad, 2010).

Kinesin Motor Proteins in Neurons

Kinesin-1 was the neuronal transport motor to be identified based on assays of vesicular motility along microtubules in extruded axoplasm (Vale et al., 1985). Similar to the myosin superfamily nowadays, many different kinesin motors have been found. It is thought that approximately 45 different mammalian kinesin genes exist which, by virtue of alternative splicing, code for as many as 90 different kinesin proteins (Hirokawa and Noda, 2008). The vast majority of kinesin proteins share a number of structural characteristics: a highly conserved kinesin motor domain,responsible for microtubule binding and force generation by ATP hydrolysis; one or more coiled-coil domains for protein dimerization; and a cargo-binding domain (Hirokawa and Noda, 2008; Lawrence et al., 2004; Schliwa and Woehlke, 2003; Vale, 2003). The motor domain is ATP bound and upon attachment to the microtubule, ATP is hydrolyzed to ADP, resulting in a conformational change of the kinesin protein. This conformational change effectively results in a step of 8 nm along the microtubule (Schnitzer and Block, 1997). Since most kinesin form a homodimer, the two heads of the kinesin molecule move in a hand-over-hand mechanism along the microtubule (Yildiz et al., 2004). Kinesin movement is highly processive, meaning that once bound to the microtubule, the motor will move prior to detaching, allowing it to transport cargo over long distances in axons and dendrites. The position of the kinesin motor domain determines the direction in which it moves: kinesin proteins with an N-terminal motor domain (the most common layout) move to the microtubule plus end, whereas kinesins with a C-terminal motor domain move toward the minus end. Kinesins with a motor domain in the middle are involved in regulating microtubule dynamics (Hirokawa and Noda, 2008; Verhey and Hammond, 2009). The non-motor regions of kinesin motor proteins are poorly conserved and have been shown to regulate both motor function (by intramolecular folding and inhibition of ATPase activity) (Verhey and Hammond, 2009) and cargo binding (by interacting with adaptor proteins) (Schlager and Hoogenraad, 2009). Most cargos bound to kinesin-1 motor proteins, such as amyloid precursor protein (APP) and Reelin receptor AporER2, interact indirectly via kinesin-1 light chains (Hirokawa et al., 2010). However, some cargos bind directly to the kinesin heavy chain, such as the AMPA receptor, which binds via adaptor protein GRIP1 (Setou et al., 2002), and mitochondria, which bind via adaptor protein Milton (Glater et al., 2006). A recent study showed that kinesin-1 binds synaptic precursor vesicles via syntabulin and syntaxin-1 (Cai et al., 2007). Knockdown of syntabulin impairs the anterograde transport of synaptic vesicle precursors. Members of the kinesin-3 family, including KIF1A and KIF1Bβ, also transport synaptic vesicle precursors in the axon. Both KIF1A and KIF1B knockout mice exhibit defects in sensory and motor neurons, including a loss of synaptic vesicles (Hirokawa et al., 2010). The delivery of GABA_A receptors to synapses is mediated by the kinesin-HAP-1 complex and is disrupted by mutant huntingtin (Twelvetrees et al., 2010). Several kinesin motors are now critically involved in neuronal disease pathogenesis (Goldstein, 2001; Hirokawa and Noda, 2008; Mandelkow and Mandelkow, 2002; Morfini et al., 2009). For example, mutations in kinesin-1/KIF5A are associated with spastic paraplegia (Ebbing et al., 2008), truncating mutations in KIF17 are associated with schizophrenia (Tarabeux et al., 2010), and heterozygous missense mutations in KIF21A have been found to cause congenital fibrosis of the extra-ocular muscles (CFEOM), a rare congenital eye movement disorder that results from the dysfunction of the oculomotor nerve (Yamada et al., 2003).

Dynein Motor Proteins in Neurons

Similar to kinesin motors, the motor proteins of the dynein family move along microtubule structures. However, while most kinesin motors move toward the microtubule plus end, dyneins move toward the minus end of the microtubule. In most species, more than 15 dynein encoding genes have been identified, where the majority of dynein motor proteins are involved in non-transport actions but drive flagellar beating (Kardon and Vale, 2009). In stark contrast to kinesin proteins where many different motor types perform many different tasks, only one dynein motor, cytoplasmic dynein 1, is responsible for the bulk of the minus-end-directed cargo transport. In other respects, dynein is very different from kinesin and myosin motor proteins. One of the most obvious differences is the sheer size of the dynein motor complex: with a mass of 1-2 MDa, it is several times larger than a typical myosin or kinesin motor. At the core of the motor complex is the dynein heavy chain (DHC1), a polypeptide of over 500 kDa, which is essential for the motor activity consisting of three different domains: the stalk, motor, and tail domains. While in kinesin and myosin motors, the polymer-binding site and catalytic site are integrated within a single globular motor domain; in dynein, the microtubule-binding domain is separated from the motor domain by a $\sim$15-nm stalk (Carter et al., 2008). The stalk is a coiled-coil structure that extends directly from the motor domain and is thought to function as a lever (Houdusse and Carter, 2009; Kardon and Vale, 2009). The circular motor domain consists of six ATPase domains, the tail domains mediate dimerization and form the interaction site for five additional dynein subunits. The intermediate chain (IC) and light intermediate chain (LIC) bind directly to the heavy chain tail, whereas light chain 8 (LC8), light chain 7 (LC7 or roadblock), and T-complex testis-specific protein 1 (Tctex1) bind to the intermediate chain (Kardon and Vale, 2009). The dynein subunits are essential in determining the binding of dynein to specific cargos, the cellular localization, and even intrinsic properties of dynein, like its processivity. Interestingly, missense point mutations in the tail domain of cytoplasmic dynein heavy chain have been shown to result in progressive motor neuron degeneration in mice (Hafezparast et al., 2003). Recent data show that the mutations in the non-motor part of the protein inhibit dynein motor run length and significantly alter motor domain coordination (Ori-McKenney et al., 2010). These results suggest a potential role for the dynein tail in motor function and provide direct evidence for a link between single-motor processivity and disease.

The efficient function of cytoplasmic dynein critically depends on the dynactin (dynein activator) accessory complex. Most dynein-dependent processes from yeast and filamentous fungi to invertebrates and mammals require dynactin (Schroer, 2004). Dynactin has been shown to regulate dynein transport in several ways; it is involved in targeting of dynein, functions as adaptor protein, and regulates processive dynein movement (Kardon and Vale, 2009; Schroer, 2004). Dynactin is a large complex that contains 11 different subunits, and since some subunits are present in multiple copies, the complete assembly can be comprised of as many as 20 proteins. Detailed EM studies have revealed that dynactin basically consists of two parts, a rod domain and arm domain projecting from the rod (Schroer, 2004). Mutations in the p150glued gene, coding for one of the large dynactin subunits, are found in a family with motor neuron disease (Puls et al., 2003). Affected patients develop adult-onset vocal fold paralysis, facial weakness, and distal limb muscle weakness, mainly caused by the selective loss of motor neurons. Mutant mice with impaired dynein/dynactin function showed disrupted retrograde axonal transport and develop motor neuron disease similar to amyotrophic lateral sclerosis (ALS) (LaMonte et al., 2002; Teuling et al., 2008). This

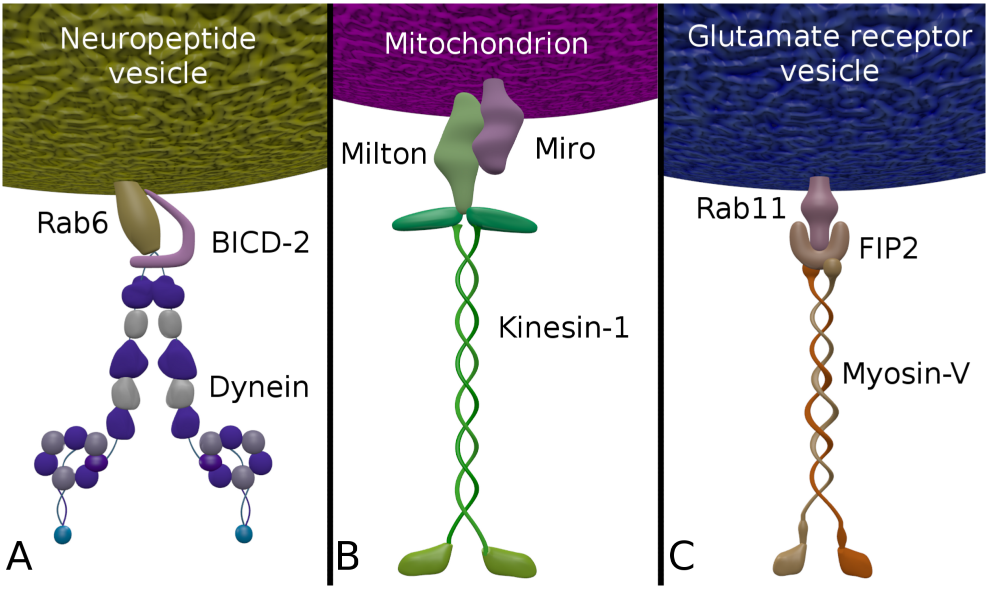

Figure 2.3: Motor-adaptor-cargo transport complexes. Three typical examples of motor-adaptor-cargo transport machineries. Each motor protein connects to its cargo via adaptor molecules. Although the motor proteins, adaptors, and cargos vary, the essential building blocks are the same in each case. (a) Dynein motor complex connected to neuropeptide containing Rab6-positive vesicles via adaptor BICD-2. (b) Kinesin-1 is connected to mitochondria via Miro and Milton. This complex is regulated by calcium. (c) Myosin V transports glutamate receptor-containing vesicles by connecting to Rab11-FIP2

illustrates both the importance of subunits in the dynactin complex as well as the crucial role of dynein-based transport in the nervous system.

Cytoplasmic dynein transports neurotrophic tyrosine kinase receptor family (Trk) (Ha et al., 2008), Rab6-positive neuropeptide-containing secretory vesicles (Colin et al., 2008; Schlager et al., 2010), the piccolo/bassoon complex (Fejtova et al., 2009) and mitochondria (Hollenbeck and Saxton, 2005) retrogradely in the axon, while in the dendrites, the cargos carried by cytoplasmic dynein include glycine receptor vesicles (Maas et al., 2006), messenger ribonucleoproteins (mRNPs) (Villacé et al., 2004), Rab5 endosomes (Satoh et al., 2008), and AMPA receptor vesicles (Kapitein et al., 2010a). In these cases, the cargos bind to the dynein complex either directly or through adaptor proteins such as gephyrin (glycine receptor) or Bicaudal-D and related proteins (Rab6, BDNF, NPY) (Fig. 2.3). Regulation of the binding is controlled via phosphorylation, GTP hydrolysis of the small Rab-GTPases, or Ca2+ signaling (Schlager and Hoogenraad, 2009).

Regulating Motor Protein Based Transport

Precise regulation of motor-based transport is essential to ensure precise cargo delivery to synapses. The list of molecules that are known to link specific transport motors to synaptic cargos is rapidly expanding (Hirokawa et al., 2010; Schlager and Hoogenraad, 2009). Biochemical and proteomics approaches and high-throughput yeast two-hybrid screens have identified more than 100 proteins that bind to kinesin-1 in mammals, flies, and worms (Gindhart, 2006). Most of these proteins act as cargo molecules themselves or function as motor-adaptor proteins (scaffolding proteins, Rab GTPases, signaling proteins); some are regulators of motor activity. Emerging data from several organisms and different experimental systems suggest that transport motors can be regulated at several points, including motor- cargo binding, motor activation, motor switching, microtubule track selection, cargo release at the destination, and the recycling of motors (Schlager and Hoogenraad, 2009; Verhey and Hammond, 2009). It is becoming increasingly clear that motor-adaptor-cargo interactions play a key role in identifying synaptic cargos and regulating synaptic cargo trafficking. In this section, we discuss recent work that has shed light on the regulation of the synaptic cargo-motor interactions. To illustrate the common layout and components of motor-adaptor-cargo complexes, we will focus here on two calcium-regulated motor adaptors, the endosomal myosin-V-FIP2 and mitochondrial kinesin-1-Milton-Miro complexes (Fig. 2.3).

Motor-Adaptor-Cargo Interactions

In the large majority of cases, motor proteins do not bind directly to vesicles or synaptic proteins, but they interact with cargo via so-called adaptor proteins. The main role of adaptor proteins is to provide an additional layer of regulation for transport specificity and selectivity. Adaptors can be single proteins, such as GRIP linking KIF5 to AMPA receptors (Hoogenraad et al., 2005; Setou et al., 2002), or protein complexes such as the Mint/CASK/MALS linking KIF17 to NR2B subunits of NMDA receptors (Setou et al., 2000). Interestingly, recent findings show that CaMKII activity is correlated with regulated cargo release near the postsynaptic membrane. Here, CaMKII has been shown to phosphorylate KIF17, which induces the dissociation of the Mint scaffolding protein complex and release of NMDA receptor-containing cargo near the postsynaptic membrane (Guillaud et al., 2008). In this way, regulated CaMKII activity provides an attractive mechanism for targeting NMDA receptor complexes to active synapses where an activity regulated kinase is switched ‘on’. The significance of KIF17 function to brain function is further illustrated by the observation that transgenic mice overexpressing KIF17 show enhanced spatial and working memory (Wong et al., 2002). Additional examples of regulated adaptor proteins are the DENN/MADD adaptor protein that binds KIF1A and KIF1Bβ and interacts with Rab3 vesicles (Niwa et al., 2008), liprin family proteins as adaptors that link KIF1A to synaptic vesicle precursors (Miller et al., 2005; Wagner et al., 2009), and Bicaudal-D family proteins connecting dynein motors to Rab6-positive neuropeptide secretory vesicles (Grigoriev et al., 2007; Matanis et al., 2002; Schlager et al., 2010).

Interestingly, these Rab6-positive secretory vesicles also contain semaphorin 3A and BDNF and are anterogradely transported in axons by kinesin-3 motors (Barkus et al., 2008; De Wit et al., 2006; Schlager et al., 2010). Thus, regulation of cargo binding can be controlled via phosphorylation or GTP hydrolysis of the small Rab-GTPases (Schlager and Hoogenraad, 2009).

A third way to control intracellular trafficking is to regulate motor-cargo interactions by responding to changes in local ion concentrations. It is well known that activation of NMDA receptors causes a rapid influx of Ca^{2+} in dendritic spines. A recent study shows that myosin Vb is a 'Ca^{2+} sensor' for actin-based postsynaptic AMPA receptor trafficking (Wang et al., 2008). Increased Ca^{2+} levels lead to unfolding of myosin Vb motors and allows for binding to Rab11-FIP2 adaptors on recycling endosomes (Schlager and Hoogenraad, 2009) (Fig. 2.3). The association of myosin Vb with Rab11-FIP2 transports AMPA receptor-containing recycling endosomes into the actin-rich spines. Thus, elevated Ca^{2+} levels in spines promote local postsynaptic trafficking. On the other hand, Ca^{2+} influx reduces mitochondrial motility (Boldogh and Pon, 2007). The Milton-Miro complex was identified as an adaptor between kinesin-1 and mitochondria and a candidate for Ca^{2+}-dependent regulation of mitochondrial transport. Indeed, recent studies suggest that the mitochondrial Miro-Milton adaptor complex is important for the Ca^{2+}-dependent regulation of mitochondria trafficking (Wang and Schwarz, 2009)(Fig. 2.3). Elevated Ca^{2+} levels permit Miro to interact directly with the motor domain of kinesin-1. The interesting aspect of this model is that kinesin-1 remains associated with mitochondria regardless of whether they are moving or stationary. In the 'moving' state, kinesin-1 is bound to mitochondria by binding to Milton, which in turn interacts with Miro on the mitochondrial surface. In the 'stationary' state, in the presence of high Ca^{2+} levels, the kinesin-1 motor domain interacts directly with Miro and prevents microtubule interactions. In contrast, another recent paper showed that the presence of Ca^{2+} inhibits the Miro1/kinesin-1 protein-protein interaction and that the motor is dissociated from mitochondria yielding arrested movement (Macaskill et al., 2009). Both findings imply the existence of 'Ca^{2+} sensors' that detect neuronal activity stimuli and convert Ca^{2+} influx into mechanisms regulating cargo trafficking.

Conclusions and Future Directions

A typical fully differentiated neuron within an active neuronal circuitry faces an enormous logistical challenge. Synaptic cargo needs to be sorted into dendrites and axons both during basal neuronal activity and changes in activity, such during firing of action potentials. Not all synapses are equally active, and their requirements can vary greatly; some may require a constant flow of receptors and neurotransmitters, while others undergo depression and mainly need transport out of the synapse into a reserve pool or back to the cell body. Moreover, the distance between the cell soma and the most distant synapse can be huge, for example, up to 1 m for a motor neuron. And all these transported proteins, mitochondria, neurotransmitters, and synaptic vesicle precursors flow through an axon of only 5 micrometer in diameter. Therefore, neurons are equipped with a well-balanced and meticulously regulated transport system in order to facilitate synapse formation, function, and plasticity. First of all, the actin and microtubule cytoskeleton play a pivotal role in synaptic plasticity together they determine synaptic architecture, organize subcellular compartments, and transport intracellular synaptic constituents. Second, the characteristic dynamics, polarity, and modifications patterns of cytoskeleton elements are instrumental for establishing and maintaining the structural and compositional polarity of synapses. Third, this highly specialized microtubule and actin cytoskeletal organization facilitates local, polarized transport by guiding specific motor proteins to specific directions. Fourth, synaptic activity may regulate the cytoskeleton organization and motor protein transport in neurons. All these mechanisms occur simultaneous and can influence each other, creating a highly dynamic infrastructure that is able to rebuild itself in order to adapt to changes in the cellular environment. Without this highly dynamic cytoskeleton system, synaptic plasticity and cognitive brain functions would be impossible.

The relationship between cytoskeleton, motor protein transport, and synaptic signaling is never more apparent than when the brain becomes dysfunctional. Molecular motor proteins, especially kinesin proteins, are prime candidates to be involved in several psychiatric and neurological disorders (Goldstein, 2001; Mandelkow and Mandelkow, 2002), ranging from schizophrenia (Tarabeux et al., 2010) to spastic paraplegia (Ebbing et al., 2008). Both KIF5 and dynein may be involved in the pathology of Huntington and other polyQ diseases (Colin et al., 2008; Twelvetrees et al., 2010). The role of dynein and dynactin in neurological diseases is best described in the motor neuron disease ALS (Chevalier-Larsen and Holzbaur, 2006), and mutations in tubulin isotypes have been observed in patients with severe neurodevelopmental disorders (Keays et al., 2007; Tischfield et al., 2010). There is also a strong link between the activity of tubulin modifying enzymes and neuronal abnormalities. Mutant mice that lack the gene for tubulin tyrosine ligase (TTL), the enzyme that catalyzes the addition of a C-terminal tyrosine residue to a-tubulin in the tubulin tyrosination cycle, die shortly after birth because of neuronal disorganization, including premature axon specialization (Erck et al., 2005). On the other hand, mice that lack functional cytosolic carboxypeptidase (CCP1), the enzymes catalysing deglutamylation, have increased microtubule hyperglutamylation and Purkinje cell degeneration (Rogowski et al., 2010). However, a number of key mechanistic questions remain to be answered. What are the downstream effects of transport deficits that lead to neurodegeneration? In some cases, it may be a failure to supply new material to the distal axons and dendrites, so that synapses degrade over time. Consistently, defects in both axon and dendritic transport in various organisms can lead to neuropathies (Hirokawa et al., 2010). In other cases, neuronal degeneration may result from the accumulation of toxic substances in the processes. The molecular motor machinery itself could be critically involved in removing toxic waste in neurons, but these protein accumulations may also lead to traffic jams and disrupt normal synaptic trafficking routes.

In this chapter, we have shown how the cellular infrastructure is essential for neuronal development and plasticity. This highly adaptive network of filaments, motor, adaptor, and cargo proteins is able to answer the ever-changing demands of neuronal networks in action. As a large number of neurological diseases illustrate, there is little room for error. If this fascinating intracellular transport system is not working at peak efficiency, neurons are not able to function properly and will eventually degenerate and die. Future studies on neuronal cytoskeletal dynamics and the synaptic transport machinery may lead to new insights and, hopefully, new treatments for neurological and psychiatric disorders.

Acknowledgments R.v.d.B. is supported by a grant from the 'Stichting MS Research'. C.C.H. is supported by the Netherlands Organization for Scientific Research (NWO-ALW and NWO-CW), the Netherlands Organization for Health Research and Development (ZonMW-VIDI and ZonMW-TOP), the European Science Foundation (EURYI), EMBO Young Investigators Program (YIP), and the Human Frontier Science Program (HFSP-CDA).

A role for Bicaudal-D2 in cerebellar granule cell migration

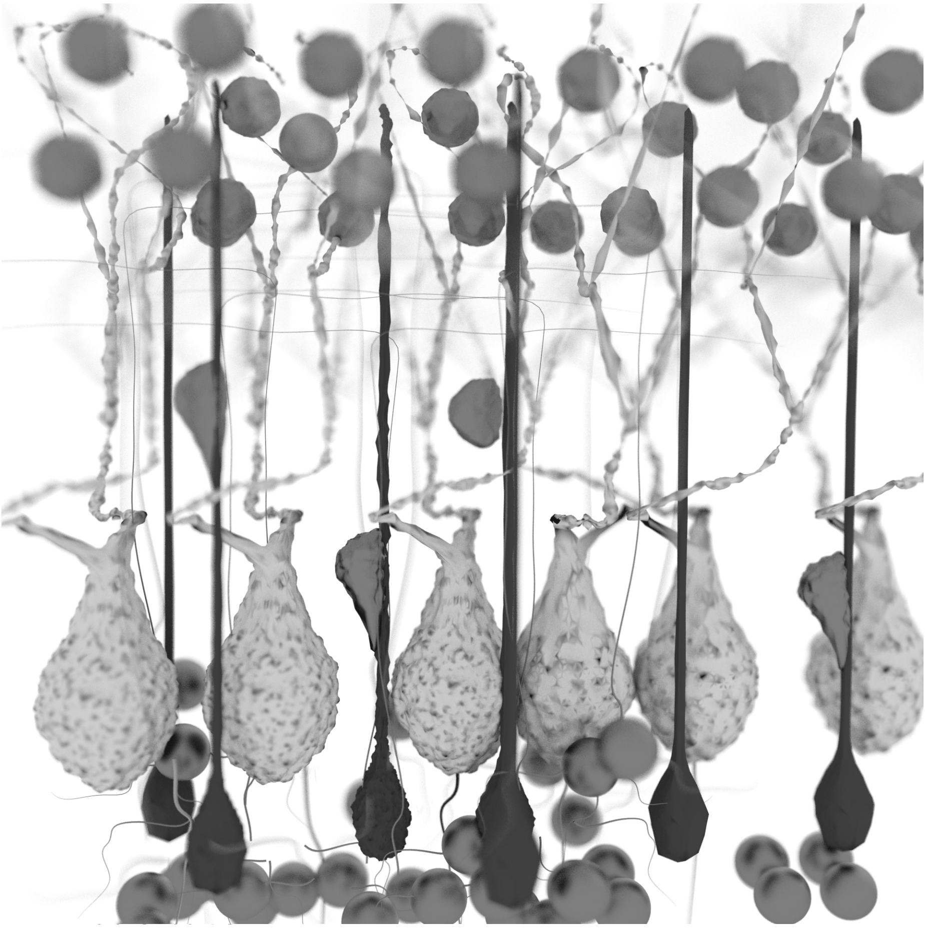

Jaarsma D*, van den Berg R*, Wulf PS*, van Erp S, Keijzer N, Schlager MA, de Graaff E, De Zeeuw CI, Pasterkamp RJ, Akhmanova A, Hoogenraad CC; A role for Bicaudal-D2 in cerebellar granule cell migration; Nature Communications 2014.
*authors contributed equally.

3

A ROLE FOR BICAUDAL-D2 IN RADIAL CEREBELLAR GRANULE CELL MIGRATION

Bicaudal-D (BICD) belongs to an evolutionary conserved family of dynein adaptor proteins. It was first described in *Drosophila* as an essential factor in fly oogenesis and embryogenesis. Missense mutations in a human BICD homologue, BICD2, have been linked to a dominant mild early onset form of spinal muscular atrophy. Here we further examine the *in vivo* function of BICD2 in *Bicd2* knockout mice. BICD2-deficient mice develop disrupted laminar organization of cerebral cortex and the cerebellum, pointing to impaired radial neuronal migration. Using astrocyte and granule cell specific inactivation of BICD2, we show that the cerebellar migration defect is entirely dependent upon BICD2 expression in Bergmann glia cells. Proteomics analysis revealed that *Bicd2* mutant mice have an altered composition of extracellular matrix proteins produced by glia cells. These findings demonstrate an essential non-cell-autonomous role of BICD2 in neuronal cell migration, which might be connected to cargo trafficking pathways in glia cells.

Introduction

The Bicaudal D (*BicD*) gene was initially identified in *Drosophila* based on dominant mutations that induce mirror-image pattern duplications along the anteroposterior axis, thereby giving rise to Bicaudal embryos (Wharton and Struhl, 1989) It was later established that the BICD protein facilitates dynein-mediated transport and is involved in the proper localization of posterior mRNA in *Drosophila* embryos (Bullock and Ish-Horowicz, 2001; Claussen and Suter, 2005). In mammals two homologues of Bicaudal D are present, named BICD1 and BICD2, which associate with microtubule minus-end directed motor dynein (Hoogenraad et al., 2001, 2003) and various cargos, such as the nuclear envelope (Splinter et al., 2010) and Rab6 secretory vesicles (Matanis et al., 2002). One currently favored hypothesis is that BICD family members are adaptor proteins involved in microtubule-based transport by docking the dynein motor proteins to appropriate cargos (Grigoriev et al., 2007; Coutelis and Ephrussi, 2007; Januschke et al., 2007). Recently, mutations in BICD2 have been linked to a spectrum of motor neuron disorders, in particular a dominant mild early onset form of spinal muscular atrophy (Neveling et al., 2013; Oates et al., 2013; Peeters et al., 2013), suggesting that BICD2 plays an important role in the nervous system.

To further examine the *in vivo* function of BICD2, we generated *Bicd2* knockout (KO) mice. Here we report that these mice develop defects in laminar organization of the cerebral cortex, hippocampus and cerebellar cortex, indicative of radial neuronal migration defects. Cell-specific inactivation of BICD2 in astrocytes and neuronal precursors revealed that radial cerebellar granule cell migration is non-cell-autonomous and intrinsic to cerebellar Bergmann glia cells. Mass spectrometry analysis revealed that *Bicd2* mutant mice have strongly reduced levels of the extracellular matrix protein Tenascin C. Our data demonstrate that Bergmann glia cells provide critical cues for granule neuron polarization and migration, and that BICD2 is a critical part of the Bergmann glia signaling mechanism responsible for granule cell migration. This study reveals an unexpected action of BICD2 in glia cell-guided granule cell migration that is of key importance for cerebellar development and function.

Results

BICD2 is required for cerebral cortex development

To generate an inducible *Bicd2* knockout allele, we introduced two resistance markers by sequential rounds of homologous recombination. In the first round, a neomycin cassette surrounded by loxP sequences was inserted into intron 1. In the second round, a puromycin selection marker, surrounded by loxP sequences and followed by a β-galactosidase (lacZ) reporter gene fused to a nuclear localization signal (NLS), was inserted downstream of the mouse *Bicd2* gene (Figure S3.1). ES cells with this floxed *Bicd2* allele (termed *Bicd2*^{f}), were transfected with a plasmid expressing Cre recombinase yielding a knock-out *Bicd2 (Bicd2*$^{-}$*)* allele, that generates a transcript consisting of exon 1 of *Bicd2* and the lacZ reporter gene (Figure S3.1). *Bicd2*^{f} ES cell clones were used to generate mice carrying the inducible and knockout *Bicd2* alleles (Figure S3.1A).

Matings between heterozygous *Bicd2*$^{+/-}$ mice yielded *Bicd2*$^{-/-}$ mice at near-Mendelian frequencies, but *Bicd2*$^{-/-}$ mice displayed increased mortality during early post-natal life resulting in a sub-Mendelian frequency of *Bicd2*$^{-/-}$ mice (13% of 208 mice) at P10. Late embryonic and newborn *Bicd2*$^{-/-}$ mice were indistinguishable in gross appearance and weight from heterozygous and wildtype littermates (Figure 3.1A), but after birth the *Bicd2*$^{-/-}$ mice developed an enlarged dome-shaped skull, indicative of hydrocephalus (Figure 3.1B). By P14 *Bicd2*$^{-/-}$ mice started to show reduced weight compared to their littermates (Figure 3.1C), and by P30 all *Bicd2*$^{-/-}$ mice died. Behaviorally, *Bicd2*$^{-/-}$ mice at P20 displayed motor abnormalities: the mice walked with an abnormal wide-based gait of both fore- and hind paws, and frequently made missteps when placed on a grid (Movie 3). Furthermore, at 3 weeks of age, the mice were unable to walk on a balance beam and showed clasping rather than extension of the hind limbs when lifted by their tail.

Examination of *Bicd2*$^{-/-}$ mice at P15-P25 revealed no gross alterations in internal organs, except for a smaller size, and confirmed that *Bicd2*$^{-/-}$ mice developed severe hydrocephalus, which was characterized by progressive expansion of lateral ventricles (ventriculomegaly), loss of white matter and ependymal cells surrounding the ventricles, severe thinning of the cortex and atrophy of other telencephalic areas, including striatum, hippocampus and septum (Figures 5.1D, S3.2A-D). Apart from cerebellar cortex (see below) other brain regions and spinal cord appeared normal (Figure S3.2F). Analysis of the aqueduct at P5 suggested a smaller diameter indicative of aqueductal stenosis (Figure S3.2E).

In addition to the *Bicd2*$^{-/-}$ mice which completely lack the gene in all tissues, we generated mice that were deficient in BICD2 in the entire nervous system but showed normal BICD2 expression in most internal organs by crossing floxed *Bicd2*$^{f/f}$ mice with Nestin-Cre mice (Dubois et al., 2006). Nestin-Cre *Bicd2*$^{f/f}$ mice reproduced the severe progressive hydrocephalus, neurological features and short life span of *Bicd2*$^{-/-}$ mice (Table 3.1). Crossing of *Bicd2*$^{f/f}$ mice with GFAP-Cre mice, which exhibit sustained Cre-recombinase expression in astrocytes and transient Cre activity in some neuronal precursor cells (Zhuo et al., 2001) resulted in less severe or no hydrocephalus (Table 3.1). GFAP-Cre *Bicd2*$^{f/f}$ mice without hydrocephalus revealed a second major nervous system abnormality of BICD2-deficient mice, i.e. a disordered laminar organization of the cerebral cortex (Figure 5.1E) and hippocampus (Figure S3.3). Consistent with impaired radial migration, Foxp2, a marker predominantly found in deep corticofugal layer V and VI neurons, was present in superficial layers in GFAP-Cre *Bicd2*$^{f/f}$ mice (Figure 3.1F). Corticofugal axonal trajectories (labeled with anti-neurofilament M antibody) arose in superficial instead of deep cortical layers. Importantly the same cortical and hippocampal phenotype was also observed in EMX1-Cre *Bicd2*$^{f/f}$ mice that are selectively deficient for BICD2 in radial glia, glutamatergic neurons and astrocytes in the cortex and hippocampus (Gorski et al., 2002) (Table 3.1; Figure 3.1G). Together, the data from GFAP-Cre and EMX1-Cre *Bicd2*$^{f/f}$ mice indicate that BICD2 is essential for the proper development of the cerebral cortex, and suggest that BICD2 plays a role in radial migration of excitatory neurons. These data are consistent with the neurogenesis and early neuronal migration defects observed after BICD2 knockdown in cortical brain slices by in utero electroporation (Hu et al., 2013).

BICD2 is required for cerebellar granule cell migration

In the cerebral cortex, radial glia progenitor cells give rise to neurons and glia cells and act as a scaffold for radial migration, making it difficult to differentiate between potential glia- and neuron-specific defects and to decipher to which extent disorganized laminar organization follows from neurogenesis abnormalities or impaired migration (Kriegstein and Alvarez-Buylla, 2009). In the cerebellar cortex, however, granule cells

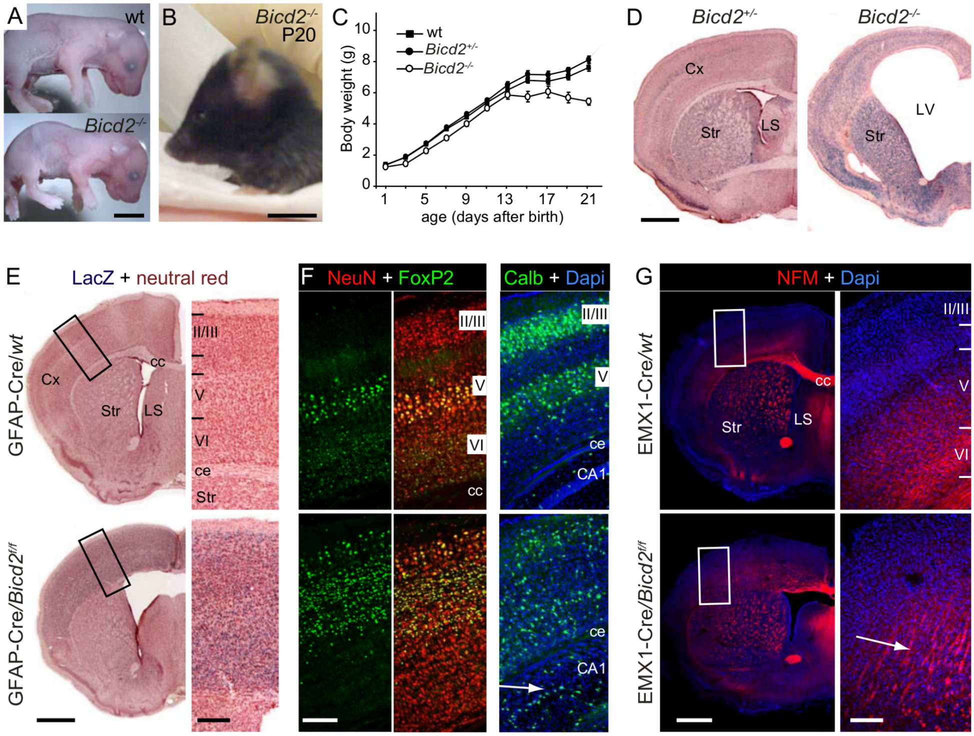

Figure 3.1: Hydrocephalus and disrupted laminar organization of the cortex in BICD2-deficient mice A, B) Photographs of BICD2 knockout (*Bicd2*$^{-/-}$) mice showing a normal gross appearance at embryonic day 19 (A), and a dome-shaped head indicative of hydrocephalus at post-natal day 20 (B). C) XY plot of body weight (mean ± SE, n ¿ 4 per group) showing near-normal weight of *Bicd2*$^{-/-}$ mice up to post-natal day 13, and weight loss during subsequent days. D) Coronal brain sections of P20 mice stained for LacZ and neutral red reveal enlarged lateral ventricles (LV), thinning of the cortex (Cx) and atrophy of several telencephalic areas including striatum (Str) and lateral septum (LS) in homozygote *Bicd2*$^{-/-}$ and no change in heterozygote *Bicd2*$^{+/-}$ mice. Note the moderate and high level of LacZ staining throughout the forebrain of *Bicd2*$^{+/-}$ and *Bicd2*$^{-/-}$ mice, respectively, indicative of widespread BICD2 expression. E) Coronal LacZ/neutral red-stained sections of the cortex of floxed *Bicd2*$^{f/f}$ crossed with a GFAP-Cre line; the high magnification of the primary somatosensory cortex illustrates disrupted cortical laminar organization. Also note the thin corpus callosum (cc) and capsula externa (ce) in *GFAP-Cre/Bicd2*$^{f/f}$ mice. F) Immunofluorescence of NeuN and FoxP2 or Calbindin showing altered laminar distribution of FoxP2 and calbindin in *GFAP-Cre/Bicd2*$^{f/f}$ cortex. FoxP2 that in control mice is present in lamina V and VI pyramidal neurons, in *GFAP-Cre/Bicd2*$^{f/f}$ cortex is distributed in superficial lamina. Note the absence of a laminar organization of NeuN+ cells in *GFAP-Cre/Bicd2*$^{f/f}$ cortex. Also note disorganized pyramidal cell layer in the CA1 of *GFAP-Cre/Bicd2*$^{f/f}$ hippocampus (arrow). G) Immunofluorescence of neurofilament-M (NFM) showing abnormally oriented axonal bundles coursing from the superficial lamina towards the capsula interna in neocortex of *EMX1-Cre/Bicd2*$^{f/f}$ mice (arrow). Scale bars: 5 mm (A, B), 1 mm (D, E, G), 200 μm (E, F, G).

originate in the external granule cell layer (EGL) and migrate inward to the internal granule cell layer (IGL) along radial processes of Bergmann glia. Granule and glial cells originate from different precursors (Buffo and Rossi, 2013; Xu et al., 2013a), which makes it easier to establish the origin of migration deficits. *Bicd2*$^{-/-}$ mice showed a disproportionately small cerebellum with grossly intact subdivision in vermis and hemispheres and foliation (Figure 3.2A; Figure S3.2), but an altered laminar organization, indicative of the absence of radial granule cell migration. Instead of laminar subdivision into molecular, Purkinje cell, and granular layer, in *Bicd2*$^{-/-}$ cerebellar cortex the cell bodies of Purkinje cells (Calbindin+, NeuN-) were positioned near the white matter, while other neurons (NeuN+) were spread over a single superficial layer (Figure 3.2B, C). This layer contained both molecular layer interneurons (NeuN+, Parvalbumin+, Calbindin-), as well as a high density of granule cells, identified by immunostaining for the $\alpha 6$ GABA$_A$ receptor subunit that is only expressed by adult, post-migratory granule cells (Figure 3.2D-G). Cerebellar Golgi cells (mGluR2+), which are localized in the granule cell layer of wild-type mouse cerebellar cortex, were concentrated between the white matter and the Purkinje cell layer, and did not occur in *Bicd2*$^{-/-}$ molecular/granule cell layer (Figure S3.4). Staining for the glutamate synaptic vesicle transporter VGluT1, which is present in parallel fiber and mossy fiber endings in the cerebellar molecular and granular layers, respectively, revealed prominent punctate staining in the *Bicd2*$^{-/-}$ molecular/granular layer, indicative of the presence of parallel fiber endings (Figure 3.2F,G). VGluT1-immunostaining near the Purkinje cell layer also revealed sporadic larger irregular structures resembling mossy fiber endings, which accordingly codistributed with $\alpha 6$ GABA$_A$ receptor-immunoreactivity, indicative of granule cell dendritic processes in the glomeruli (Figure 3.2G). Immunostaining for VGluT2, which is present in an additional and partially overlapping population of mossy fiber endings as well as in climbing fiber endings, confirmed the presence of a low number of mossy fiber endings and indicated impaired climbing fiber innervation of Purkinje cells in *Bicd2*$^{-/-}$ cerebellar cortex (Figure S3.4C,D). Immunostaining for zebrin II suggests preserved parasagittal compartmentalization of Purkinje cells (Figure S3.4E, F).

Analysis of early post-natal brain indicated that *Bicd2*$^{-/-}$ cerebellar cortex appeared normal at post-natal day 2, before the onset of radial migration. As in control the subsequent days was characterized by proliferation of granule cells and the gradual expansion of the area between the Purkinje cell layer and the pial surface. However, instead of migrating and forming the interior granule cell layer, granule cells accumulated throughout the molecular layer (Figure 3.3A,B). Consistent with impaired inward radial migration, no granule cells with a polarized radially-oriented elongated shape characteristic for migration (Komuro and Rakic, 1995) were present in the molecular layer of *Bicd2*$^{-/-}$ P5-P15 cerebellar cortex (Figure 3.3C,D). Thus, the absence of profiles of radially migrating cells, the accumulation of granule cells in the molecular layer and the absence of an internal granule cell layer show that inward radial granule cell migration is severely disrupted in *Bicd2*$^{-/-}$ mice (Movie 3).

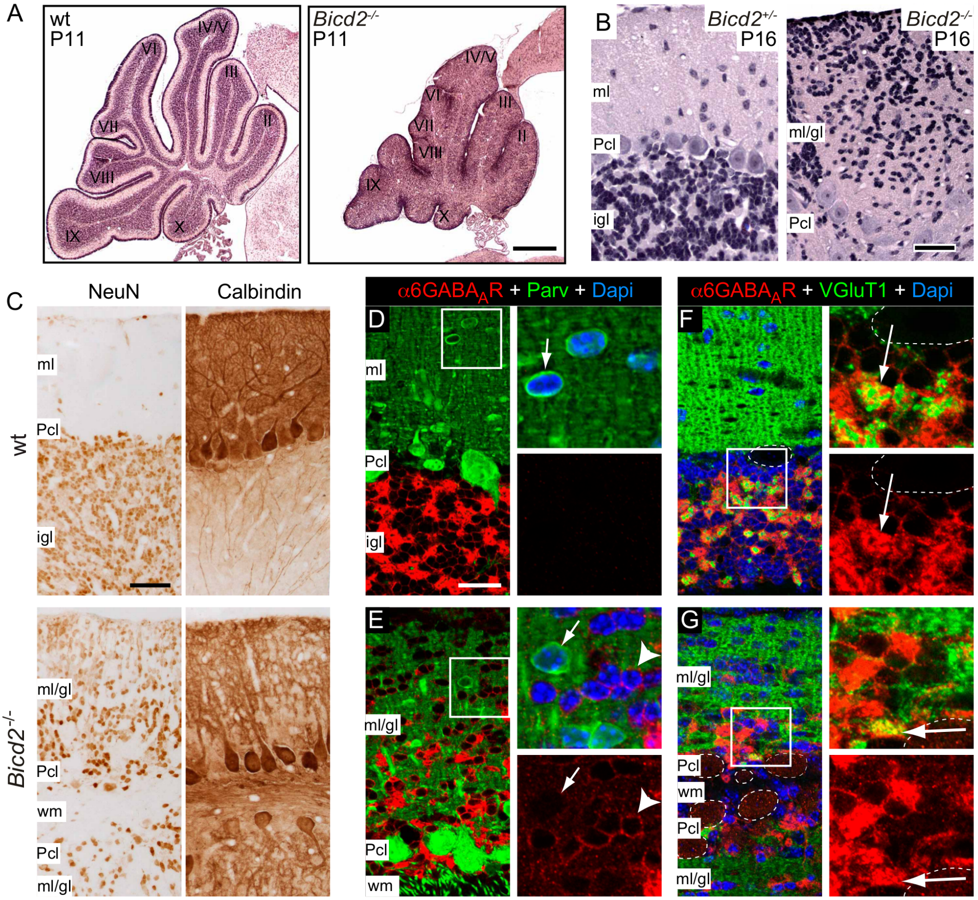

Figure 3.2: Granule cells populate the molecular layer in *Bicd2*$^{-/-}$ cerebellar cortex A, B) Sagittal sections of P11 and P16 cerebellum stained with H&E. The low magnification in A illustrates the intact folial organization of the vermis of *Bicd2*$^{-/-}$ cerebellar cortex. The high magnification in B shows the absence of the internal granule cell layer (igl) and a high density of cells in the molecular layer (ml) in *Bicd2*$^{-/-}$ cerebellum. C) Sagittal sections of P16 cerebellum immunostained with anti-NeuN and anti-calbindin. Note that in *Bicd2*$^{-/-}$ cerebellar cortex the Purkinje cell layer (Pcl, calbindin+ cells) is localized adjacent to the white matter (wm), and that Purkinje cell dendritic arbors extend up to the pial surface. D-G) Double-labelling confocal immunofluorescence of α6 GABA$_A$ receptor subunit (α6GABA$_A$R) with Parvalbumin (Parv) and VGluT1, respectively, in transverse sections of P20 cerebellum. Note the presence of many α6GABA$_A$R+ cells (arrow head in E), a moderate amount of Parv+ cells (arrow in E), and abundant VGluT1 labelling (G) in the ml/gl layer of *Bicd2*$^{-/-}$ cerebellar cortex. The arrow in F points to a glomerulus containing both α6GABA$_A$R+ granule cell dendritic processes and a VGluT1+ mossy fiber ending. Occasionally, double-labeled glomeruli-like structures occur near the Pcl of *Bicd2*$^{-/-}$ cerebellar cortex (arrow in G). Optical sections in D-G, 1 μm. Scale bars: 200 μm (A), 25 μm (B, D), 50 μm (C)

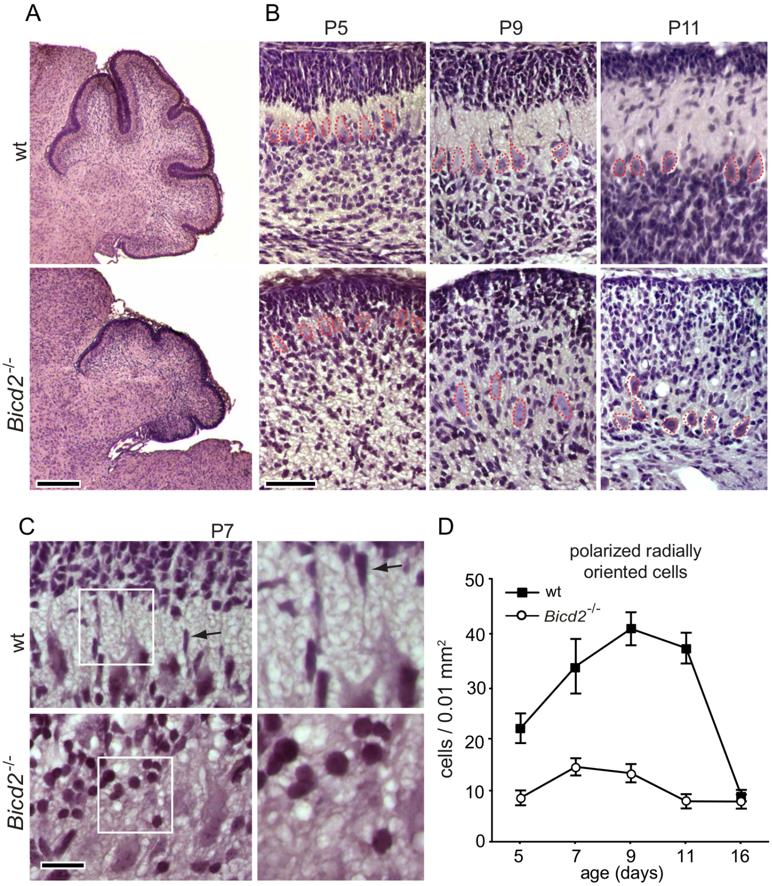

Figure 3.3: No radial granule cell migration in Bicd2-/- cerebellar cortex A-C) Sagittal paraffin sections of P5 (A, B), P7 (C), P9 and P11 section stained with H&E showing development of *Bicd2*$^{-/-}$ cerebellar cortex during the period of radial granule cell migration. Note the multiple flattened radially-oriented cells in the nascent molecular layer of wild-type (arrows in B and C) but not *Bicd2*$^{-/-}$ cerebellar cortex. D) Plot of density of flattened radially-oriented cells (mean ± SE, N = 10) in the molecular layer (wt mice) or the mixed molecular/granular layer (*Bicd2*$^{-/-}$) extending from the Purkinje cell layer up to 20 μm below the pial surface. Scale Bars: 200 μm (A), 50 μm (B), 20 μm (C)

BICD2 is expressed in Bergman glia but not in granule cells

Analysis of BICD2 expression by Western blotting showed the presence of BICD2 protein in multiple tissues including the brain. It also confirmed the absence of BICD2 in tissue homogenates from *Bicd2*$^{-/-}$ mice and reduced expression in heterozygous *Bicd2*$^{+/-}$ mice (Figures 3.4A, S3.5). BICD2 is expressed at relatively high levels in embryonic and early post-natal brain, while its expression decreases after P10, resulting in relatively low levels in adulthood (Figures 3.4B, S3.5). The absence of BICD2 in the knockout mice did not lead to a significant change in the expression level of its close homologue BICD1 (Figure 3.4C), indicating that there is no up- or down regulation of BICD1 in the absence of BICD2. Moreover, absence of BICD2 in the cerebellum and cortex did not change the expression levels of BICD2 binding partners, such as Rab6 and cytoplasmic dynein (DIC74) and its regulatory proteins dynactin (p150Glued) and Lis1 (Figures 3.4C, S3.5).

Immunohistology shows that BICD2 is diffusely distributed throughout the nervous system. Relatively high staining intensities occurred in non-neuronal cells (NeuN-) and some populations of neurons (NeuN+), including motor neurons in cranial nerve motor nuclei and large neurons throughout the reticular formation (Figure S3.6A-E). The specificity of the staining for BICD2 was confirmed by the absence of staining in sections from *Bicd2*$^{-/-}$ mice. In post-natal and adult cerebellar cortex, BICD2 immunoreactivity occurred in all layers, with the highest staining intensity in the molecular layer and the white matter (Figure 3.4D). In the molecular layer, BICD2 immunoreactivity colocalized with GFAP and the excitatory amino acid transporter EAAT2 (GLT1, SLCIA2) indicating that it is associated with Bergmann glial cells (Figure 3.4E, F). No staining above background was observed in Purkinje cells and pre- and post migratory granule cells in the external and internal granule cell layer, respectively. The preferential labelling of BICD2 in Bergmann glia is in agreement with in situ hybridization data from the Allen Mouse Brain Atlas (Lein et al., 2007), and with the preferential distribution of LacZ staining in Bergmann glial cells in cerebellar cortex of heterozygous *Bicd2*$^{+/-}$ mice (Figure 3.4G). Furthermore, also in neuron-astrocyte cerebellar co-cultures BICD2 staining was present in GFAP-positive astroglial cells but not in MAP2-positive cells (Figure S3.6F). Taken together, our data indicate that BICD2 is not expressed in pre-migratory or migrating granule cells, but rather in Bergmann glial cells, which are essential for successful radial migration of granule neurons in the cerebellum.

BICD2 has a non-cell-autonomous function in migration

The predominant expression of BICD2 in Bergman glia cells raises the possibility that defects in radial granule cell migration in *Bicd2*$^{-/-}$ mice result from the loss of BICD2 function in Bergmann glia. Accordingly, crossing of *Bicd2*$^{f/f}$ mice with GFAP-Cre mice, which show sustained Cre-recombinase expression in astrocytes including Bergmann glia, results in the same granule cell migration defects that are observed in global *Bicd2*$^{-/-}$ mice (Figure 3.5A). However, in view of Cre activity in some neuronal precursor cells including cerebellar granule cells (Zhuo et al., 2001), the data from GFAP-Cre/$Bicd2^{f/f}$ mice do not exclude a role of BICD2 in migrating granule cells. We therefore crossed $Bicd2^{f/f}$ mice with Math1-CreERT2 mice, which express tamoxifen-inducible Cre-recombinase in granule precursor cells (Machold and Fishell, 2005), and injected pregnant mothers with tamoxifen. *Math1-CreERT2/*$Bicd2^{f/f}$ offspring showed a normal cerebellar cortex, and systematic analysis of sections stained for the post-migratory granule cell marker α6 GABA$_A$ receptor showed that all granule cells were in the internal granule cell layer at P20 (Figure 3.5B). This indicated that elimination of BICD2 in pre-migratory cells does not affect radial granule cell migration. To further exclude that BICD2 has a cell intrinsic role in migrating granule cells, we performed shRNA mediated knockdown of BICD2 in pre-migratory granule cells using ex vivo electroporation of P10 rat cerebella. Consistent with the data from *Math1-CreERT2/*$Bicd2^{f/f}$ mice, radial granule cell migration was unaltered in BICD2 shRNA treated granule cells (Figure 3.5C). These data indicate that cerebellar granule cell migration defects in $Bicd2^{-/-}$ mice are non-cell-autonomous and intrinsic to astrocytes.

BICD2 does not influence Bergmann glial cell morphology

All the results indicate that the radial granule cell migration deficit in $Bicd2^{-/-}$ mice results from a loss of function of BICD2 in Bergmann glia, which has a scaffolding function in radial granule cell migration. It is thus conceivable that the disruption of Bergmann fiber scaffold causes the $Bicd2^{-/-}$ cerebellar phenotype. GFAP-immunohistochemistry showed that $Bicd2^{-/-}$ mice show abundant radial glial fiber labelling (Figure 3.6A,B). $Bicd2^{-/-}$ radial glia showed an ordered radial organization of in the external granule cell layer with orthogonal orientation relative (Figure 3.6A-C). In view of a small proportion of GFAP-positive fibers with abnormal non-radial orientation (Figure 3.6B), we further analyzed Bergmann glial cells in $Bicd2^{-/-}$ mice crossed with GFAP-GFP transgenic mice that express GFP in a subset

Figure 3.4 *(on the next page)*: Preferential BICD2 expression in Bergman glia in cerebellar cortex A) Western blot with BICD2 antibody (#:2294) showing reduced and no expression of BICD2 in tissue homogenates of P20 heterozygote $Bicd2^{+/-}$ (+/-) and homozygote $Bicd2^{-/-}$ (-/-) mice, respectively. B) Western blot showing relatively high BICD2 expression in developing nervous system. C) Comparative Western blot analysis showing unaltered BICD1 (antibody #:2295 for BICD1, and upper band in strip stained with antibody #:2293 for BICD1/2), dynein components and interacting proteins (dynactin p150, dynein intermediate chain 74, Lis1) and Rab6 expression in $Bicd2^{-/-}$ cortex and cerebellum. Full size Western blots can be found in Figure S3.5. D) Immunohistochemistry with anti-BICD2 antibody showing the absence of staining in P10 $Bicd2^{-/-}$ cerebellar cortex and prominent staining in the molecular layer (ml) and the white matter (wm) of wild-type cerebellar cortex. E, F) Double-labelling confocal immunofluorescence (optical sections 1m) showing codistribution of BICD2 with GFAP and the excitatory amino acid transporter EAAT2 in the ml and the external granule cell layer (egl). Note in right panel in F that EAAT2 labelling appears the same as in wildtype in $Bicd2^{-/-}$ cerebellar cortex. G) LacZ staining in sagittal cerebellar section of P10 heterozygote $Bicd2^{+/-}$ mice is predominantly present in the Purkinje cell layer. Scale Bars: 50 μm (D), 20 μm (F, G), 10 μm (E)

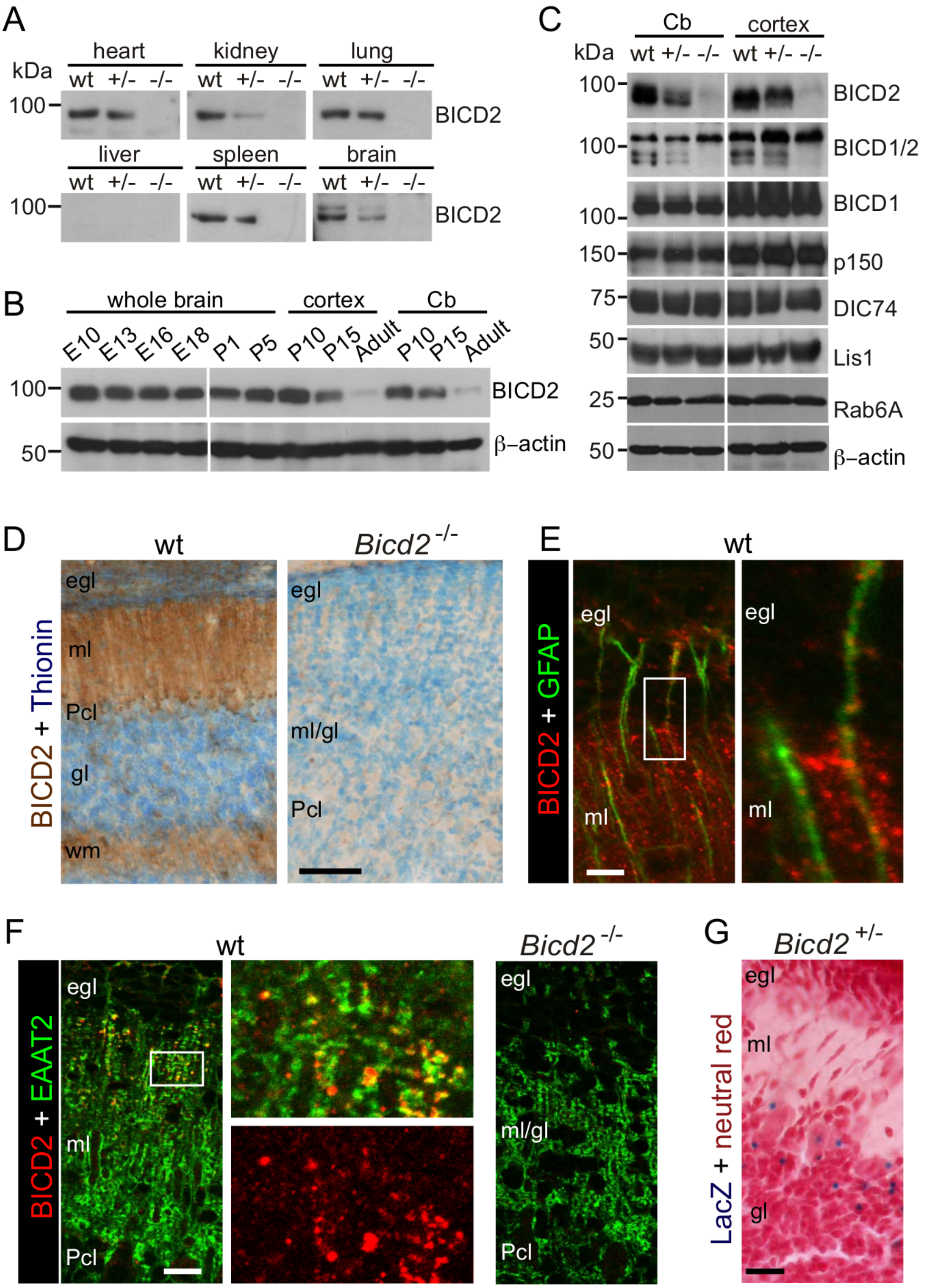
A
kDa
heart
kidney
lung
wt +/- -/-
100
BICD2
liver
spleen
brain
wt +/- -/-
100
BICD2
B
whole brain
cortex
Cb
E10 E13 E16 E18 P1 P5 P10 P15 Adult P10 P15 Adult
100
BICD2
50
β–actin
C
Cb
cortex
kDa
wt +/- -/-
100
BICD2
100
BICD1/2
100
BICD1
150
p150
75
DIC74
50
Lis1
25
Rab6A
50
β–actin
D
wt
Bicd2 -/-
BICD2 + Thionin
egl
ml
Pcl
gl
wm
ml/gl
E
wt
BICD2 + GFAP
egl
ml
F
wt
Bicd2 -/-
BICD2 + EAAT2
egl
ml
Pcl
ml/gl
G
Bicd2 +/-
LacZ + neutral red
egl
ml
gl

of Bergmann glial cells. Consistent with a grossly normal organization of Bergmann glia, the far majority of GFP-labeled Bergmann glia cells had the cell body near the Purkinje cells and radial processes extending up to the pial surface as in wild-type mice (Figure 3.6D-G). These results indicate that morphology and structure of Bergmann glial cells are largely unaffected in *Bicd2*$^{-/-}$ mice.

BICD2$^{-/-}$ mice have altered extracellular matrix composition

Having shown that migration defects in *Bicd2*$^{-/-}$ mice are intrinsic to the Bergmann glial cells, we wanted to gain a better understanding of how BICD2 regulates cerebellar granule cell migration. We first focused on the subcellular distribution of known BICD2 binding partners, such as Rab6, dynein/dynactin and RanBP2. Immunofluorescence with antibodies against these proteins revealed no major changes in *Bicd2*$^{-/-}$ Bergmann glia (Figure 3.6E,G). Moreover, no change in centrosome position or Golgi apparatus morphology was observed in these cells.

Next, we searched for molecular changes in *Bicd2*$^{-/-}$ mice using mass spectrometry. Proteomics analysis was performed with biological duplicates on cerebellar extracts from control and homozygote *Bicd2*$^{-/-}$ mice at P15. Mass-spectrometry analysis of whole lanes revealed several up- and down regulated proteins, and we decided to focus on the factors that were previously found to influence neuronal migration, including signaling factors, extracellular matrix and adhesion molecules (Solecki, 2012; Hatten, 1999; Chizhikov and Millen, 2003; Govek et al., 2011; Chédotal, 2010). Some of these proteins were only mildly affected in the *Bicd2*$^{-/-}$ cerebellum, while others like N-cadherin and integrin β1 showed a strongly reduced expression (Tables 3.2 and 3). Only two proteins were absent from the *Bicd2*$^{-/-}$ cerebellum in two separate experiments, Doublecortin (DCX) and Tenascin-C. Since microtubule-associated protein DCX is restricted to migrating neurons and absent from Bergmann glia cells (Bai et al., 2003; Huynh et al., 2011), we further analyzed the extracellular matrix protein Tenascin C. Tenascin C is produced by Bergmann glia cells (Bartsch et al., 1992), has been implicated in neuron-glia cell recognition (Chiquet-Ehrismann and Tucker, 2011; Jones and Jones, 2000) and is known to be important for granule cell migration in the cerebellum (Kruse et al., 1985; Grumet et al., 1985; Chuong et al., 1987; Husmann et al., 1992). We determined the Tenascin C distribution by immunofluorescence experiments using antibody

Figure 3.5 ***(on the next page)*****: BICD2 depletion in pre-migratory cerebellar granule cells does not influence radial migration** A) Coronal thionin-stained sections showing that *GFAP-Cre/Bicd2*$^{f/f}$ do not develop an internal granule cell layer. B) Unaltered distribution of α6GABA$_A$R-labeled granule cells in P25 *Math1-CreERT2/Bicd2*$^{f/f}$ cerebellar cortex. C) P10 rat cerebella were ex vivo electroporated with *Bicd2* or scrambled control shRNAs and GFP expression vector. The fraction of GFP+ granule cells was quantified for each layer per picture (three separate experiments were performed, total number of pictures analyzed for shScr = 40, shBicd2 = 33). The average distribution of GFP+ granule cells is shown in the graph (error bars are SEM, n = 3). Scale Bars: 1 mm (top A, B), 100 μm (B), 50 μm (A, C)

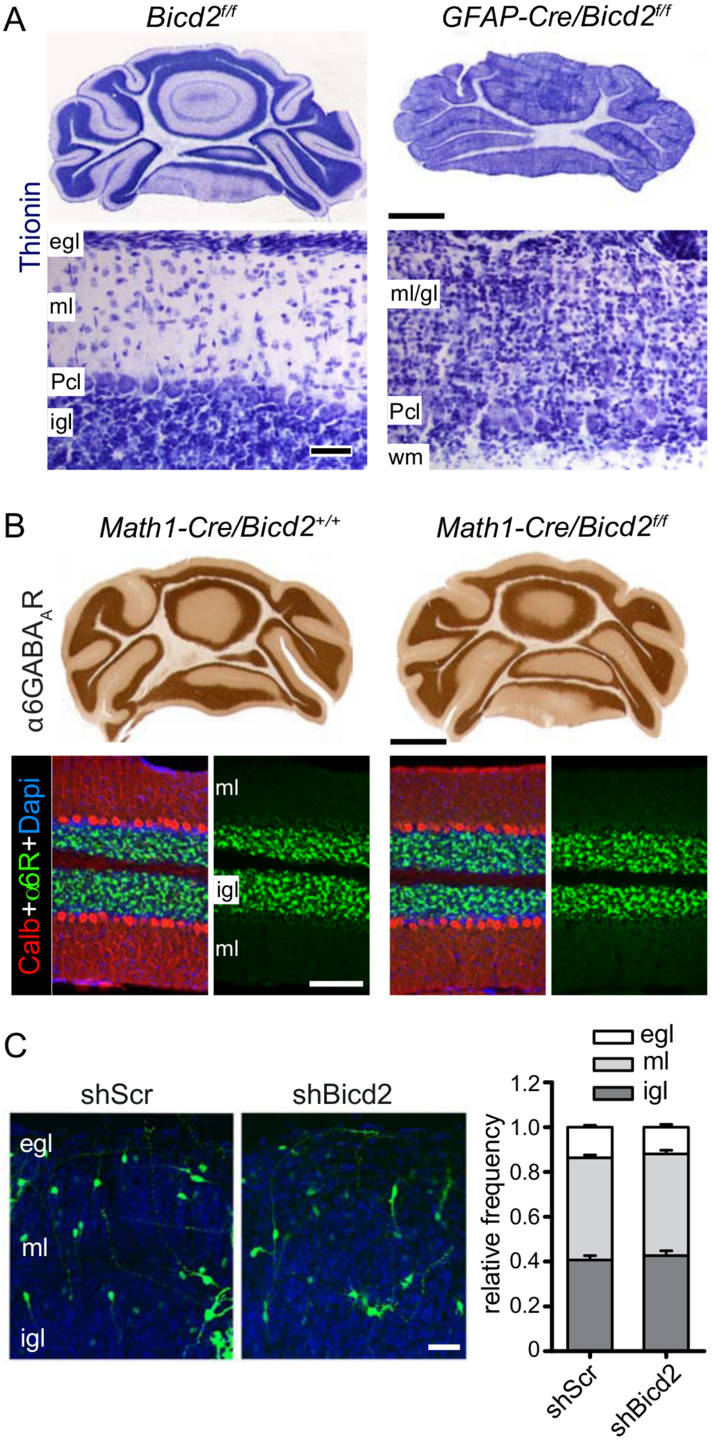
A
Bicd2f/f
GFAP-Cre/Bicd2f/f
Thionin
egl
ml
Pcl
igl
ml/gl
Pcl
wm
B
Math1-Cre/Bicd2+/+
Math1-Cre/Bicd2f/f
α6GABAAR
Calb+α6R+Dapi
ml
igl
ml
C
shScr
shBicd2
egl
ml
igl
egl
ml
igl
1.2
1.0
0.8
0.6
0.4
0.2
0
relative frequency
shScr
shBicd2

staining and confirmed that the levels of Tenascin C in the *Bicd2*$^{-/-}$ cerebellum were low (Figure 3.6H-J). Thus while Tenascin C was abundantly present in the molecular layer of P7-P15 wild type cerebellum the levels of Tenascin C were low throughout the cerebellar cortex in *Bicd2*$^{-/-}$ mice at this age (Figure 3.6I-M). Together these data show that *Bicd2*$^{-/-}$ mice have an altered extracellular matrix composition in the molecular layer, which could be responsible for the defects in granule cell migration.

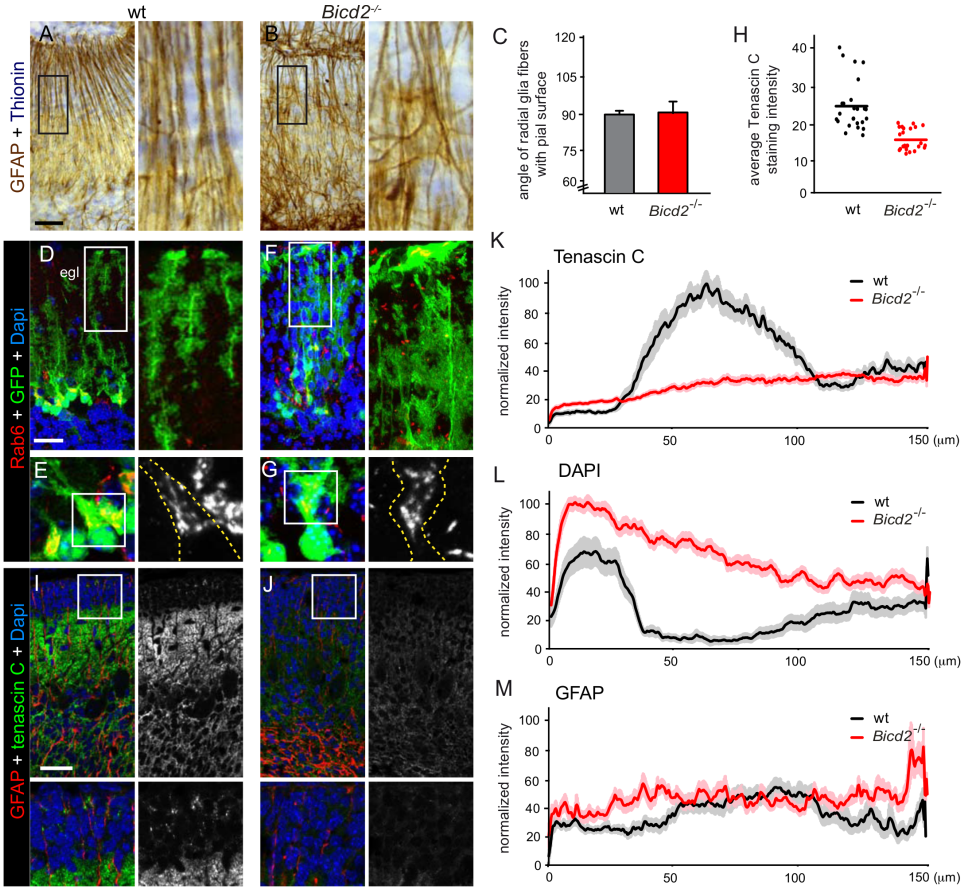

Figure 3.6: Altered extracellular matrix composition in BICD2-deficient cerebellar cortex A, B) GFAP immunoperoxidase-histochemistry in P10 coronal sections showing ordered radially-oriented Bergmann glia processes in wt and more disorganized processes *Bicd2*$^{-/-}$cerebellum. C) Quantification of the angle of the Bergmann glia cell radial processes with the pial surface (mean ± SE, N=250) from *wt* and *Bicd2*$^{-/-}$ mice. D-G) Maximal projection of confocal stack (11 sections, total thickness of optical section, 5 μm) of Rab6 immunofluorescence in coronal P20 cerebellar sections from *wt* and *Bicd2*$^{-/-}$ mice that also are transgenic for a GFAP-EGFP construct resulting in the expression of EGFP in subsets of astrocytes, including Bergmann glia cells. Note EGFP-positive Bergman glia cells that extend radial processes to the pial surface cerebellum in both *wt* (D) and *Bicd2*$^{-/-}$ (F) cerebellum. Also note that Rab6 immunoreactivity which is mainly distributed in the trans-Golgi apparatus shows the same distribution in *wt* and *Bicd2*$^{-/-}$ Bergman glia cell body (E, G). H-J) Double-labelling confocal immunofluorescence (optical sections 1.5 μm) of tenascin and GFAP immunoreactivity showing reduced labelling in *Bicd2*$^{-/-}$ cerebellum. K-M) Fluorescent intensity of the indicated marker in the molecular layer (*wt* mice) or the mixed molecular/granular layer (*Bicd2*$^{-/-}$ mice) from the pial surface up to the Purkinje cell layer. Scale Bars: 25 μm (A, D, I).

Discussion

In this study, we have shown that the conserved dynein adaptor protein BICD2 is essential for proper development of the brain, where it plays an important role in the establishment of the laminar organization of the cerebral and cerebellar cortices. In particular, by comparing different mouse lines missing BICD2 in specific cell populations, we demonstrated that BICD2 has a non-cell-autonomous function in driving inward radial migration of cerebellar granule cells. In addition, by using a proteomic approach we provide evidence that the extracellular matrix protein Tenascin C produced by the Bergmann glia cells may account for the non-cell-autonomous role of BICD2 in migration.

Multiple factors have been identified that control granule cell migration in a cell-autonomous manner (Solecki, 2012; Hatten, 1999; Chizhikov and Millen, 2003; Govek et al., 2011; Chédotal, 2010), such as proteins that control centrosome positioning and nucleokinesis (Tanaka et al., 2004; Ohshima et al., 1999; Yamasaki et al., 2001; Hippenmeyer et al., 2010) and neuronal adhesion molecules that mediate granule cell-Bergmann glia interaction (Renaud et al., 2008; Rio et al., 1997; Adams et al., 2002). Moreover, several abnormalities in Bergmann glia cell structure and function have been shown to cause granule cell migration alterations (Buffo and Rossi, 2013; Xu et al., 2013a). For instance, mutant mice that disrupt the radial scaffold structure of Bergmann glia fibers develop migration deficits (Yue et al., 2005; Wang et al., 2011; Lin et al., 2009). Also mutant mice with Bergmann glia fibers with abnormal end feet at the pial surface show impaired migration and develop clusters of ectopic granule cells (Belvindrah et al., 2006; Ma et al., 2012).

An important feature of the *Bicd2*$^{-/-}$ mice is the complete absence of an internal granule cell layer, indicating a severe disruption of granule cell migration (Movie 3). This phenotype is more severe than the migration deficits found in any other granule cell migration deficient mouse model. In addition, the laminar distribution of other cerebellar cortical neurons including Purkinje cells and molecular layer interneurons appears intact, indicating that the migration deficit is specific for granule cells. Furthermore, only subtle abnormalities in the overall Bergmann glia cell organization are observed, suggesting that the granule cell migration deficit in *Bicd2*$^{-/-}$ mice cannot be explained by structural changes in Bergmann glia morphology. Nevertheless, our data strongly indicate that the granule cell migration deficits result from a loss of function of BICD2 in Bergmann glia, as BICD2 is expressed in Bergmann glia cells, but not in pre-migratory or migrating granule cells. In addition, selective deletion of BICD2 in pre-migratory granule cells does not influence radial migration, while the depletion of BICD2 in astrocytes including Bergmann glia cells leads to the same granule cell migration defects as observed in global *Bicd2*$^{-/-}$ mice. The data indicate that BICD2 has a non-cell-autonomous role in granule cell migration in the cerebellar cortex.

How can BICD2 exert non-cell-autonomous effects? We envision two scenarios that are not mutually exclusive. First BICD2 could regulate dynein-mediated trafficking in Bergmann glia cells. BICD2 is a regulator of dynein function and plays a role in dynein-mediated cellular processes, such as microtubule minus-end directed trafficking (Claussen and Suter, 2005). BICD2 binds to the dynein motor complex (Hoogenraad et al., 2001), promotes a stable interaction between dynein and its accessory factor dynactin (Splinter et al., 2012) and induces microtubule dependent minus-end directed transport (Hoogenraad et al., 2003). Similar to the Drosophila BICD mutant embryos (Bullock and Ish-Horowicz, 2001), Bergmann glia cells lacking BICD2 could have defects in dynein-mediated transport pathways. However, we did not observe cellular phenotypes related to globally impaired dynein/dynactin function in Bergmann glia cells, such as Golgi fragmentation and other signs of impaired retrograde trafficking. Other dynein regulators, such as lissencephaly 1 (Lis-1) and nuclear distribution protein E (NDE1) have previously been found to control neuronal migration (Tanaka et al., 2004; Hippenmeyer et al., 2010).

Second, it is possible that BICD2 is involved in a specific cargo trafficking pathway in Bergmann glia cells. For instance, BICD2 also interacts with the small GTPase Rab6, which controls the targeting and fusion of secretory vesicles to the plasma membrane (Grigoriev et al., 2007; Coutelis and Ephrussi, 2007; Januschke et al., 2007). However, very little is known about the trafficking and secretion mechanisms in Bergmann glia cells. Based on the involvement of BICD2 in secretory transport in other systems, we speculate that the trafficking or secretion of neuron-glial cell recognition factors might be altered in *Bicd2*$^{-/-}$ mice. Indeed, the extracellular matrix protein Tenascin C produced by Bergmann glia cells is found at relative low levels in *Bicd2*$^{-/-}$ mice. Tenascin C is known to mediate the attachment of neurons to astrocyte surfaces in in vitro cell binding assays and stimulates granule cell migration in the cerebellum (Bartsch et al., 1992; Kruse et al., 1985; Grumet et al., 1985; Chuong et al., 1987; Husmann et al., 1992). It is interesting to note that the early neuronal migration and differentiation marker Doublecortin (DCX) is not detected in *Bicd2*$^{-/-}$ cerebellum extracts, suggesting a potential link between extracellular matrix components and granule cell migration (Dityatev et al., 2010). Our findings demonstrate an essential non-cell-autonomous role of BICD2 in neuronal cell migration, which might be connected to cargo trafficking pathways in Bergmann glia cells.

BICD2-deficient mice also displayed a disordered laminar organization of the cerebral cortex and hippocampus, which is compatible with a deficit in radial outward migration of newly born neurons to the cortical plate. These data imply that BICD2 may also have a similar non-cell-autonomous function in cortical radial glia cells. However, in the cortex radial glial cells also act as neuronal progenitor cells, making it difficult to differentiate between potential glia and neuron specific defects. At least part of the laminar abnormalities can be explained by a recently identified role of BICD2 in cell-cycle dependent nuclear oscillation in radial glial progenitors (Hu et al., 2013). BICD2 recruits dynein to the nucleopore complex in G2 to mediate apical nuclear migration and BICD2 knockdown causes cell cycle arrest and neurogenesis deficits (Splinter et al., 2010; Hu et al., 2013). The extent to which different potential functions of BICD2 contribute to cortical and hippocampal migration deficits remains to be determined.

Recently, mutations in BICD2 have been linked to a dominant mild early onset form of spinal muscular atrophy (Neveling et al., 2013; Oates et al., 2013; Peeters et al., 2013). The motor symptoms show congenital or early post-natal onset, are nonprogressive and are associated with chronic muscle denervation and reinnervation, suggesting problems with maintaining the axon or the neuromuscular synapse. Spinal cord and motor neurons appeared normal in the *Bicd2*$^{-/-}$ mice, and we did not observe any motor neuron abnormalities or signs of impaired retrograde transport defects. The differences in phenotypes between *Bicd2*$^{-/-}$ mice and the SMA patients with mutations in BICD2 gene indicate that the motor neuron defects cannot be explained by the loss of BICD2 function. Indeed, a transgenic mouse expressing the N-terminal part of BICD2, which has a strong dynein-recruiting activity and chronically impaired dynein-dynactin function, develops several cellular phenotypes in motor neurons including Golgi fragmentation and neurofilament accumulation in the proximal axon (Teuling et al., 2008). These phenotypes are compatible with the pathology developed by patients. The missense BICD2 mutations found in SMA patients could thus exert a gain of function effect, consistent with the dominant character of the disease. Future studies are needed to further unravel the multiple essential roles of BICD2 in nervous system development.

Acknowledgements We thank Dr Frank Kirchhoff for providing the GFAP-GFP transgenic mice, Dr. Frank Grosveld for providing the CAG-Cre transgenic mice, Dr Jeroen Demmers for help with mass spectrometry analyses and Elize Haasdijk for excellent technical assistance. This work is supported by the Netherlands Organization for Scientific Research (NWO-ALW-VICI, AA, CCH), the Netherlands Organization for Health Research and Development (ZonMW-TOP, CIDZ, AA, CCH; ZonMW-VIDI, RJP), the European Science Foundation (EURYI, CCH), EMBO Young Investigators Program (YIP, CCH) and Het Prinses Beatrix Spierfonds grants (DJ, CCH and CIDZ).

Contributions DJ, EG, RJP, AA, CCH conceived and designed the experiments; DJ, RB, PSW, SE, NK, MAS performed the experiments. DJ, RB, PSW, SE, NK analyzed the data. CIDZ contributed reagents/materials/analysis tools. DJ and CCH coordinated the study and wrote the paper.

Competing financial interests The authors declare no competing financial interests.

Methods

Animals

All animal experiments were performed in compliance with the guidelines for the welfare of experimental animals issued by the Federal Government of The Netherlands.

All animal experiments were approved by the Animal Ethical Review Committee (DEC) of the Erasmus Medical Center and Utrecht University. The BICD2 targeted and knockout alleles are crossed into the C57BL/6 inbred strain. For determination of the growth curve groups, we analyzed BICD2 mice (both males and females) of different genotypes every two days from birth to 21 days of age at fixed time points during the day. In addition to the home made BICD2 deficient mice, we used in this study transgenic mice expressing Nestin-Cre (Dubois et al., 2006) (Jackson Laboratory), EMX1-Cre (Gorski et al., 2002) (Jackson Laboratory), Math1-CreERT2 (Machold and Fishell, 2005) (Jackson Laboratory), GFAP-Cre (Zhuo et al., 2001) (Jackson Laboratory) and GFAP-GFP transgenic mice (kindly provided by Frank Kirchhoff). Information about the mouse lines can be found in the Jackson Laboratory mouse database (`http://jaxmice.jax.org`).

Generation of BICD2-deficient mice

Targeting techniques and the procedures for selection of ES cells and generation of KO mice have been described (Hoogenraad et al., 2002). We introduced the resistance markers in embryonic stem (ES) cells by two sequential rounds of homologous recombination (first round, neomycine cassette, 4.2% (9 out of 213) of picked clones targeted; second round, puromycine cassette, 0.3% (1 out 350) of the picked clones targeted. To test if Cre-mediated excision occurs within the BICD2 locus, we electroporated ES cells with a construct containing the Cre recombinase gene, driven by a thymidine kinase promoter, in a vector backbone with a Pgk hygromycin-resistance gene. After selection with hygromycin B, we detected the deletion of the BICD2 region between the outermost loxP sites by PCR analysis using primer a/d. The positive ES cell clone that was able to excise the BICD2 locus and contains a correct karyotype, was injected into blastocysts. The chimeras that gave germline transmission were mated into the C57BL/6 background to generate inbred *Bicd2f* (targeted) mice. Heterozygous BICD2 knockout (*Bicd2-*) mice were obtained by crossing F1 heterozygous *Bicd2f* mice with CAG-Cre transgenic mice that express Cre recombinase in the germ-cell lineage (kindly provided by Frank Grosveld). We determined the genotypes of the heterozygous and homozygous *Bicd2f* and *Bicd2-* mice by PCR analysis using the primer sets indicated in Figure S3.1A. PCR primers used are primer-a (5'-GTGTAGCACTTCAGGAAC-ATCCATGC), primer-b (5'-AATGGAGAAGATCTCATCTTGGCAGG), primer-c (5'-CGGCGGCATCAGAGCAGCCGATTG), primer-d (5'-TGTCAGCAAACTCCA-TCTCTAGCCTC). Western blot analysis using homemade anti-rabbit BICD2 antibodies (Hoogenraad et al., 2001) confirmed the lack of BICD2 protein in brain lysates of P20 $Bicd2^{-/-}$ mice.

To obtain nervous-system specific knockout of BICD2, $Bicd2^{f/f}$ mice were crossed with transgenic mice expressing Cre recombinase under control of the Nestin promotor (Dubois et al., 2006) (Jackson Laboratory). To examine the role of BICD2 in excitatory neurons in the cortex/hippocampus and pre-migratory granule cells in the cerebellum, $Bicd2^{f/f}$ mice were crossed with EMX1-Cre (Gorski et al., 2002) (Jackson Laboratory) and Math1-CreERT2 transgenic mice (Machold and Fishell, 2005)(Jackson Laboratory), respectively. To obtain sustained expression of Cre-recombinase in astrocytes, including Bergmann glia cells, *Bicd2*$^{f/f}$ mice were crossed with GFAP-Cre transgenic mice (Zhuo et al., 2001) (Jackson Laboratory). Wildtype and *Bicd2* knockout mice were also crossed with GFAP-GFP transgenic mice, to visualize the morphology of GFP-labeled Bergmann glia cells (Nolte et al., 2001) (kindly provided by Frank Kirchhoff). The primer sets for PCR genotyping of the various transgenic mouse lines used in this study are described in the Jackson Laboratory mouse database (`http://jaxmice.jax.org`).

Histological procedures

Mice were anesthetized with pentobarbital and perfused transcardially with 4% paraformaldehyde, and brains were either embedded in paraffin and sectioned at 4-6 μm, or incubated with increasing concentrations of sucrose (15 and 30%) and rapidly frozen and sectioned at 40 μm (freesing microtome) and collected in PBS. Sections were stained with haematoxylin/eosin (paraffin sections), thionin (frozen sections), processed for LacZ staining, or processed for immunohistology. For LacZ staining sections were washed with PBS and incubated overnight at 37 °in PBS buffer containing 1 mg/ml X-gal, 5 mM K3Fe(CN)6, 5 mM K4Fe(CN)6, 2 mM MgCl2, 0.01% SDS and 0.02% NP-40, washed, mounted on glass slides, and counter stained with Neutral Red. For double and triple-labelling immunofluorescence we used a two-step procedure with FITC-, cyanine 3 (Cy3)-, Cy5-, Alexa Fluor488-, Alexa Fluor468-, and Alexa Fluor633- conjugated secondary antibodies (Jackson ImmunoResearch, West Grove, PA; Invitrogen) diluted at 1:400 (see also the supplementary methods table 3.3). For immunohistochemistry we used an avidin-biotinimmunoperoxidase complex method (ABC; Vector Laboratories) with diaminobenzidine (0.05%) as the chromogen, and biotinylated secondary antibodies (Jackson ImmunoResearch).

Primary antibodies used in this study are as follows (see also *Supplementary Methods*): rabbit anti-BICD2 (Ab 2293 and 2294) (Hoogenraad et al., 2001); mouse anti-calbindin (Sigma, clone CB-955, 1:10000); rabbit anti-calbindin (Swant, 1:10000); guinea pig anti EAAT2 (Millipore, 1:5000); goat anti-FoxP2 (AbCam, 1:1000); rabbit anti-α6GABA$_A$ receptor (Sigma, 1:1000); rabbit anti-GFAP (DAKO, 1:5000); mouse anti-GFAP (Sigma, clone G-A-5, 1:10000); mouse anti-mGluR2 (AbCam 1:1000); mouse anti-NeuN (Millipore MAB377, 1:2000); mouse anti-neurofilament-M (Sigma, 1:10000); mouse anti-Parvalbumin (Sigma, 1:10000); mouse anti-Rab6 (Matanis et al., 2002), rabbit anti-Tenascin-C (GeneTex, 1:400), guinea pig anti-VGluT1 (Millipore, 1:2000), guinea pig anti-VGluT2 (Millipore, 1:1000) and mouse-anti-MAP2 (Sigma, 1:2000,). Sections stained for immunofluorescence were analyzed with Zeiss (Oberkochen, Germany) LSM 510 or LSM700 confocal laser scanning microscopes using 40x/1.3 and 63x/1.4 oil-immersion objectives. Immunoperoxidase-stained sections were analyzed and photographed using a Leica DM-RB microscope and a Leica DC300 digital camera.

Electroporation-mediated transfection of egl cells

Rat pups were decapitated at P10, the brain was isolated and placed in ice-cold Leibovitz 15 (L15; Invitrogen) medium. The cerebellum was dissected and meninges removed. The most superficial layer (EGL) of the cerebellum was injected at multiple locations to infuse the cerebellar surface with DNA solution (PBS with 0.02% Fast Green, 400ng/μl pSuper vector, $200\,\mathrm{ng\,\mu L^{-1}}$ eGFP vector). The cerebellum was placed between Genepaddles (5x7mm) of a BTX ECM 830 Electroporator and 5 pulses of 87 V for 50 ms with 1.0 s intervals were applied. After electroporation, sagittal slices of 350 µm were cut using a Tissue Chopper (McIlwain). Slices were cultured on inserts (Millipore, 0.4 mm) incubated in culture medium (50% Earls Basal Medium, 25% HBSS, 25% Normal Horse Serum, 5 mM L-glutamine and Penicillin/Streptomycin) for four days at 35°with 5% CO2. Slices were fixed at DIV4 in 4% paraformaldehyde in PBS overnight at 4°. Then slices were blocked for 6h in blocking buffer (5% Normal Goat Serum, 1% BSA, 1% glycine, and 0.4% Triton-X100 in PBS) and incubated with primary rabbit anti-GFP antibody (Abcam; 1:2000) in blocking buffer overnight at 4 °. Following 3 washes in PBS, slices were incubated in secondary goat anti-rabbit antibody (Invitrogen; Alexa 488, 1:750) in blocking buffer overnight at 4°. To visualize tissue structure, nuclei were stained with DAPI. GFP-positive cells were imaged using an Olympus Fluoview FV:1000MPE confocal microscope (20x objective). The number of GFP positive granule cells in each cerebellar layer was quantified with ImageJ (external granule layer, molecular/migratory layer, internal granule layer). The fraction of GFP positive granule cells was calculated for each layer per picture. Three separate experiments were performed (total number of pictures analyzed for shScrambled = 40, shBicd2 = 33).

Preparation of tissue extracts and mass spectrometry analysis

For tissue Western blots, total brain, cortex, cerebellum, kidney, lung, spleen, liver and heart were dissected from P20 wildtype, *Bicd2*$^{+/-}$ and *Bicd2*$^{-/-}$ mice and placed in ice-cold PBS, pH7.4. For developmental Western blots, wildtype E10.5 (whole embryo), E13.5, E16, E18, P1, P5 (head only), P10, P15 and adult (cortex and cerebellum) mice were placed in ice-cold PBS, pH 7.4. Samples were homogenized in homogenization buffer (150 mM NaCl, 50 mM Tris, 0.1% v/v SDS, 0.5% v/v NP-40, pH8, 1x complete protease inhibitors; Roche), briefly sonicated, 10 min centrifuged at 900 rcf, resuspended in SDS sample buffer and boiled for 5 minutes. Protein concentrations were measured using a BCA protein assay kit (Pierce) and 20 μg of protein was loaded in each lane for a subsequent Western blot analysis using standard protocols.

For mass spectrometry analysis, the cerebellum was dissected from P15 wildtype and homozygote *Bicd2*$^{-/-}$ mice, homogenized, centrifuged and proteins were separated on a 4-12% NuPAGE Bis-Tris gel and stained with the Colloidal Blue staining kit (Invitrogen). Gel lanes were cut into 2-mm slices using an automatic gel slicer and subjected to in-gel reduction with dithiothreitol, alkylation with iodoacetamide and digestion with trypsin as described previously (Grigoriev et al., 2007) . The Mascot score cut-off value for a positive protein hit was set to 100. Individual peptide tandem mass spectrometry spectra with Mascot scores below 100 were checked manually and either interpreted as valid identifications or discarded. Proteins present in the negative controls (pull-down assays with bio-GFP alone) were regarded as background. For the proteome analysis of the wildtype and homozygote *Bicd2*$^{-/-}$, we focused on proteins that where previously found to influence neuronal migration, including signaling factors, extracellular matrix and adhesion molecules (Solecki, 2012; Hatten, 1999; Chizhikov and Millen, 2003). We searched 4 mass spectrometry datasets (2 from wildtype and 2 from *Bicd2*$^{-/-}$ animals) for the corresponding Mascot score to determine probability of a positive hit and calculated the ratio of wildtype vs knockout (Table 3).

Mutant Mouse	BICD2-deficiency	Life span (weeks)	Hydrocephalus	Disrupted laminar organization		
				Cortex	Hippocampus	Cerebellar Cortex
Bicd$^{+/-}$	Whole body	>52	-	-	-	-
Bicd2$^{-/-}$	Whole body	3-4	+	+	+	+
Bicd2$^{f/f}$						
Nestin-Cre	Entire nervous system	3-4	+	+	+	+
GFAP-Cre	Astrocytes, some populations of neuron	8$^{\$}$	+ or -	+	+	+
EMX1-Cre	Excitatory neurons in cortex, hippocampus	>8*	-	+	+	-
Math1-Cre	Premigratory granule cells	>8*	-	-	-	-

*, animals were killed at 8 weeks; $, death at 3-4 weeks in case of hydrocephalus

Table 3.1: Principal features of ubiquitous and region-specific BICD2-deficient mice used in this study.

Identified protein	Protein acc./id	Mascot Score				Ratio
		WT-06	WT-08	KO-00	KO-02	WT/KO
Cdc42	IPI00016786	205	261	267	200	1.13
Rac1	IPI00010271	457	452	464	461	0.98
RalA	IPI00217519	247	172	290	227	0.81
Rap1A	IPI00019345	319	452	409	407	0.94
DCX	IPI00216744	107	163	ND	ND	ND
DCLK	IPI00004560	89	492	312	410	1.36
N-cadherin	IPI00290085	249	213	336	246	0.80
Integrin, beta1	IPI00217561	57	103	223	106	0.49
Contactin-1	IPI00029751	973	1107	987	1131	0.98
Contactin-2	IPI00024966	271	289	185	71	2.18
Tenascin C	IPI00220216	209	104	ND	ND	ND

Table 3.2: Proteomics analysis from biological duplicates of cerebellar extracts from control and homozygote *Bicd2*$^{-/-}$ mice at P15. Only the factors identified in the mass spectrometry analysis that where previously found to influence neuronal migration are indicated. The full mass spectrometry list can be found in Supplementary Table 1.

Supplementary Information

Suppementary Methods

Supplementary Movies

Movie 1. Walking behavior of *Bicd2*$^{-/-}$ mice on a grid. Compared to wiltype mice, *Bicd2*$^{-/-}$ mice at P20 display frequent missteps when placed on a grid.

Online available at `http://www.nature.com/ncomms/:2014/:140311/ncomms:4411/extref/ncomms:4411-s3.avi`.

Movie 2. Simulation of the granule cell migration phenotype in*Bicd2*$^{-/-}$ mice. Probability of initiating migration, speed of movement and borders of the simulation are identical between BICD2 wildtype and knockdown models, the only parameter that is altered is the probability of following the guidance of the radial glia. In the wildtype model, the probability of moving downwards, guided by the radial glia, is set to P=0.95. In the knockout model, the movement is completely random, with equal probabilities of moving up or downwards (P=0.50). Changing this single parameter is sufficient to reproduce the cortex organization seen in the cerebellum of *Bicd2*$^{-/-}$ mice.

Online available at `http://www.nature.com/ncomms/:2014/\discretionary{-}{}{}:140311/ncomms:4411\discretionary{-}{}{}/extref/ncomms:4411-s4.avi`.

Supplementary Tables

Supplementary Table 1. Proteins identified by mass spectrometry of BICD2 wildtype and homozygous knockout mice Proteomics analysis from biological duplicates of cerebellar extracts from control (WT-06, WT-08) and homozygote *Bicd2*$^{-/-}$ (KO-00, KO-02) mice at P15. All data is listed in supplementary excel file (Jaarsma et al., Supplementary Table 1). The file contains two sheets - comparison of BICD2 KO-00 vs BICD2 WT-06 and BICD2 WT-08 vs BICD2 KO-02. The Mascot score for each protein, accession number and short description of the protein are indicated. The factors identified in the mass spectrometry analysis that were previously found to influence neuronal migration are indicated in red. The summarising mass spectrometry list can be found in Table 3.2.

The full file is available online at: `http://www.nature.com/ncomms/:2014/:140311/\discretionary{-}{}{}ncomms:4411\discretionary{-}{}{}/extref/ncomms:4411-s2.xlsx`.

Supplementary Figures

Figure S3.1 ***(on the next page)*****: Generation of inducible BICD2 knock-out mice.** **A** The mouse BICD2 locus and gene targeting constructs. To generate an inducible Bicd2 knockout allele, we introduced a neomycin-resistance gene surrounded by loxP sequences into intron 1, and a puromycin selection marker, surrounded by loxP sequences and followed by β-galactosidase (lacZ) reporter gene fused to a nuclear localization signal (NLS), downstream of the mouse *Bicd2* gene. The top line represents *Bicd2*, with exons indicated by solid boxes (white boxes, 5' and 3' UTRs; black boxes, coding regions). Exon 1 contains the start codon (ATG) and exon 9 contains the stop codon (asterisk). The positions of Southern-blot probes 1 and 2 (horizontal lines) and PCR primers a, b, c and d (arrows) are indicated. Selected restriction enzyme sites are shown (BamHI and XbaI). The targeting constructs are shown below *Bicd2*. Homology with the *Bicd2* gene is indicated, as are the lengths of the homologous regions. The loxP sites are represented by arrows. NEO, neomycinresistance cassette; PURO, puromycin-resistance cassette; TK, thymidine kinase gene; HA-NLS-lacZ, HA- and NLS-tagged lacZ cassette, containing an engineered splice acceptor site (3' splice) and polyadenylation signal (not indicated). The doubly targeted BICD2 allele, $Bicd2^{f}$ (targeted), is shown below the targeting constructs. Cre-mediated recombination at the outermost loxP sites of the $Bicd2^{f}$ allele removes most of the *Bicd2* sequences and generates the $Bicd2^{-}$ allele, which is represented by the bottom line. The splice acceptor site at the 5' end of the reporter lacZ cassette can be spliced onto *Bicd2* exon 2 sequences, generating a hybrid *Bicd2lacZ* transcript. **B** Southern-blot analysis of gene targeting and Cre-mediated recombination events. Left, Southern blot of DNA derived from wildtype (wt) and 5' NEO-targeted ES cells and digested with BamHI. The blot was hybridized with (external) probe 1, which detects fragments of 8 kb (wildtype allele) and 4.2 kb (NEO-targeted allele). One NEO-targeted clone with the correct karyotype was electroporated with the PURO targeting construct. Middle, blot with XbaI-digested DNA from a doubly targeted line ($Bicd2^{f}$) probed with external probe 2, which detects fragments of 11.7 kb (NEO allele) and 5.8 kb (NEO/PURO allele). This $Bicd2^{f}$ ES cell line was electroporated with a Cre-recombinase construct to knocked-out the *Bicd2* locus ($Bicd2^{-}$). Cre-mediated recombination was identified (right) using PCR analysis using primers a/d.

Antibody	**Company**	**Name**	**Concentration**
Rabbit anti-BICD-2	Homemade	#2294	1:500
Mouse anti-calbindin	Sigma	Clone CB-955	1:10000
Rabbit anti-calbindin	Swant	CB-38a	1:10000
Guinea pig anti-EAAT2	Millipore	AB1738	1:5000
Goat anti-FoxP2	Abcam	Ab1307	1:1000
Rabbit anti-α6GABAa-r	Sigma	G5544	1:1000
Rabbit anti-GFAP	DAKO	Z0334	1:5000
Mouse anti-GFAP	Sigma	Clone G-A-5	1:10000
Mouse anti-mGluR2	Abcam	AB 15672	1:1000
Mouse anti-NeuN	Millipore	MAB377	1:1000
Mouse anti-neurofilament-M	Sigma	Clone RM044	1:10000
Mouse anti-parvalbumin	Swant	Mab 235	1:10000
Mouse anti-Rab6	Homemade	mRab6	1:400
Rabbit anti-Tenascin-C	Gene Tex	GTX62552	1:400
Guinea pig anti-VGluT1	Millipore	AB5905	1:2000
Guinea pig anti-VGlut2	Millipore	AB2251	1:2000
Mouse anti-MAP2	Sigma	Clone HM-2	1:2000
Cy5-donkey anti-guinea pig IgG		706-175-148	1:400
Alexa Fluor488-donkey anti-goat IgG		705-545-147	
Cy3-donkey anti-goat IgG		705-165-147	
Cy3-donkey anti-mouse IgG		715-165-151	
FITC-donkey anti-mouse IgG		715-095-151	
Alexa Fluor488-donkey anti-mouse IgG		715-545-150	
FITC-donkey anti-rabbit IgG		711-095-152	
Alexa Fluor488-donkey anti-rabbit IgG		711-545-152	
Cy3-donkey anti-rabbit IgG		711-165-152	
Cy5-donkey anti-rabbit IgG		711-175-152	

Table 3.3: Antibodies used in this study. All secondary antibodies were produced by Jackson Immunoresearch.

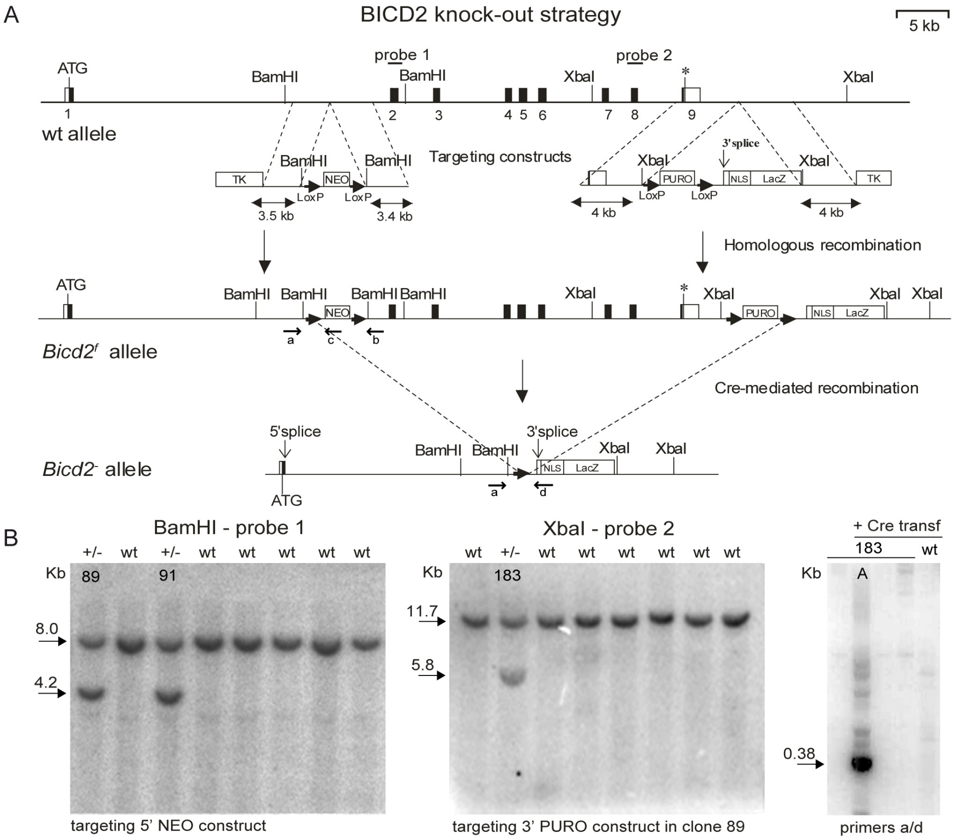
A
BICD2 knock-out strategy
5 kb
ATG
BamHI
probe 1
BamHI
XbaI
probe 2
*
XbaI
1
2
3
4 5 6
7
8
9
wt allele
BamHI
BamHI
Targeting constructs
3'splice
XbaI
XbaI
TK
NEO
LoxP
LoxP
PURO
LoxP
LoxP
NLS
LacZ
TK
3.5 kb
3.4 kb
4 kb
4 kb
Homologous recombination
ATG
BamHI BamHI
BamHI BamHI
XbaI
*
XbaI
XbaI XbaI
NEO
PURO
NLS
LacZ
a
c
b
Bicd2^f allele
Cre-mediated recombination
5'splice
3'splice
BamHI BamHI
XbaI
XbaI
Bicd2^- allele
NLS
LacZ
a
d
ATG
B
BamHI - probe 1
+/- wt +/- wt wt wt wt wt
Kb
89
91
8.0
4.2
targeting 5' NEO construct
XbaI - probe 2
wt +/- wt wt wt wt wt wt
Kb
183
11.7
5.8
targeting 3' PURO construct in clone 89
+ Cre transf
183
wt
Kb
A
0.38
primers a/d

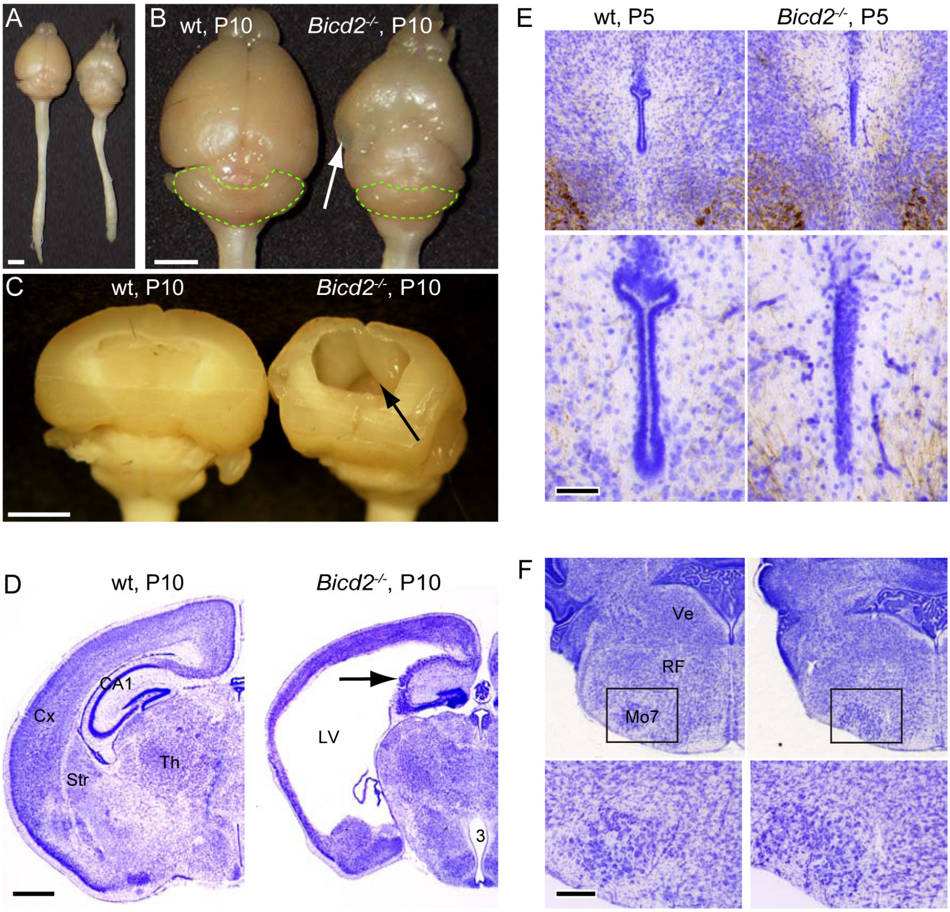

Figure S3.2: Hydrocephalus and disrupted laminar organization of the cortex in BICD2-deficient mice A-D) Macroscopic images (A-C) and coronal thionin-stained section of P10 nervous system showing enormous expansion of caudal lateral ventricles (LV, arrow in C) and thinning of the cortex (arrows in A B) in *Bicd2*$^{-/-}$ brain. Also note disorganized pyramidal layer in the hippocampus (arrow in D) and smaller cerebellum (green contour) in *Bicd2*$^{-/-}$ brain. E) Coronal sections at the level of the mesencephalon showing the aqueduct. Sections are processed for neurofilament-M immunohistochemistry and counterstained with thionin. Note the absence of a clear lumen in *Bicd2*$^{-/-}$ aqueduct indicative of aqueductal stenosis. F) Coronal thionin-stained sections at the level of the rostral myelencephalon. The facial motor nucleus (Mo7) has a normal appearance in *Bicd2*$^{-/-}$ mice; RF, reticular formation; Ve, vestibular nuclei. Scale bars: 2 mm (A-C), 1 mm (D), 200 μm (E,F)

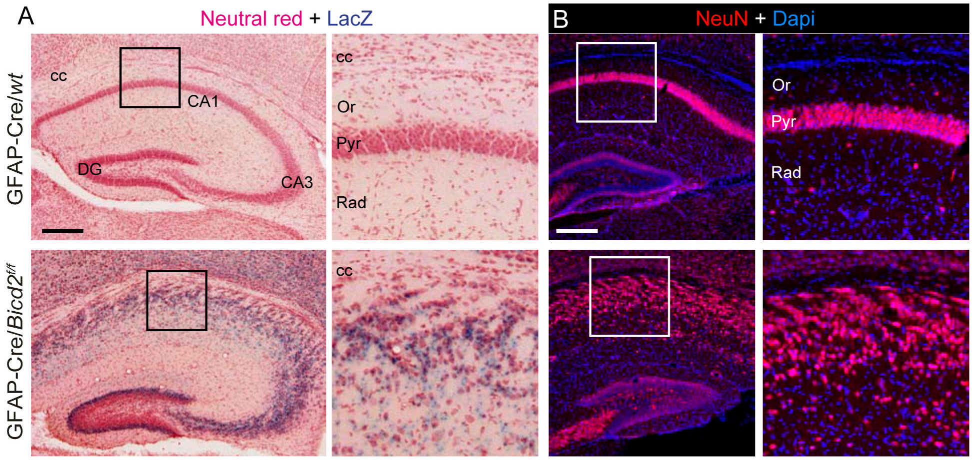

Figure S3.3: Hippocampal abnormalities in BICD2-deficient mice Coronal brain sections of P20 mice stained for LacZ and neutral red (A) or processed for NeuN immunofluorescence and Dapi counterstaining (B), showing disorganized pyramidal layer in CA1 and ubiquitous lacZ expression in hippocampus of GFAP-Cre *Bicd2*$^{f/f}$ mice. Scale bars: 200 μm.

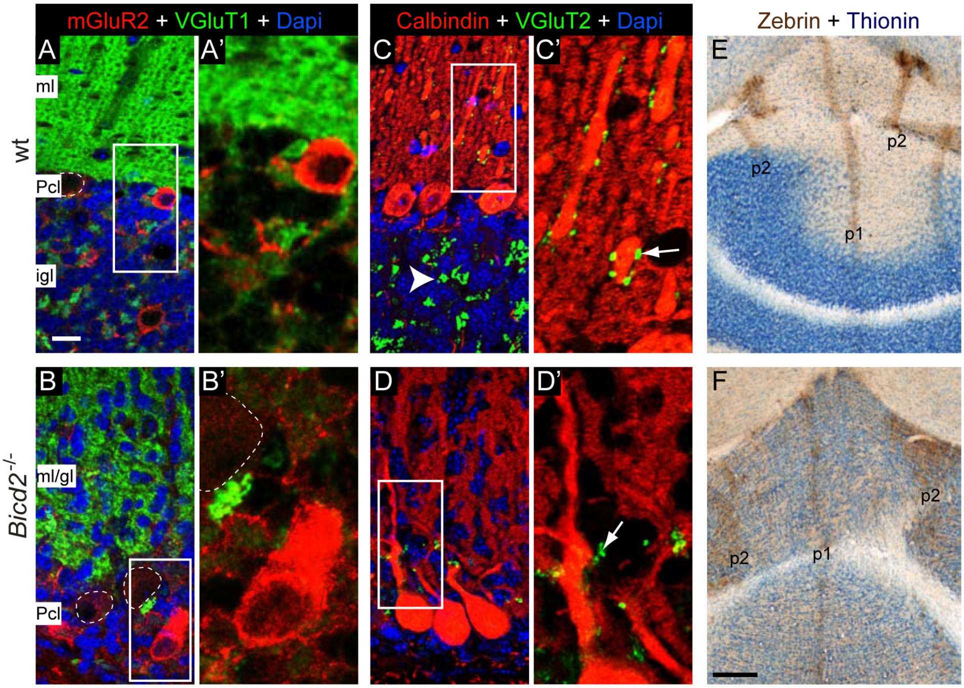

Figure S3.4: Unaltered laminar distribution of Golgi cells and mossy fibers in BICD2-deficient mice A, B) Maximal projections of confocal stacks (optical section, 5 μm) of anti-metabotropic mGluR2 receptor and anti-VGluT1 immunofluorescence in transverse sections of P20 cerebellum showing that cerebellar Golgi cells (mGluR2+, arrow in) are distributed in or below the Purkinje cells (mGluR2-, outlined by dashed lines) in *Bicd2*$^{-/-}$ cerebellum. C, D) Maximal projections (optical section, 5 μm) of VGluT2 and calbindin immunofluorescence showing VGluT2-labeled climbing fibers (arrow in C) and mossy fibers (arrow head in C) in wild-type cerebellum, and a few synaptic terminal-like structures on proximal Purkinje cell dendrites (Calb+) in *Bicd2*$^{-/-}$ cerebellum. F) Anti-zebrin immunohistochemistry and thionin counterstaining in transverse sections of the anterior vermis (lobule III, IV) showing parasagittal zones with zebrin-positive (p1, p2) and zebrin-negative Purkinje cells. *Bicd2*$^{-/-}$ cerebellum retains the zonal organization of Purkinje cells. Scale bars: 25 μm (A), 50 μm (B)

A - related to Figure 4A

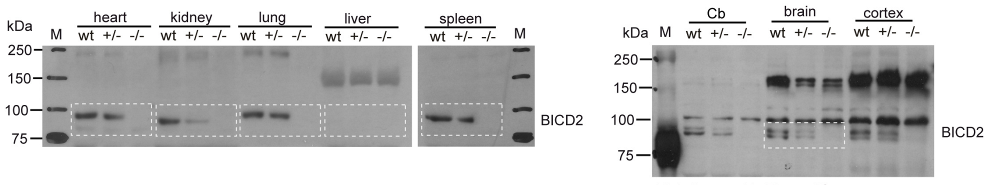

B - related to Figure 4B

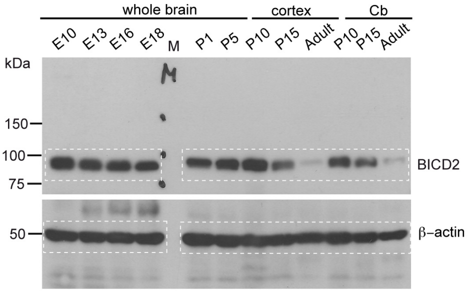

C- related to Figure 4C

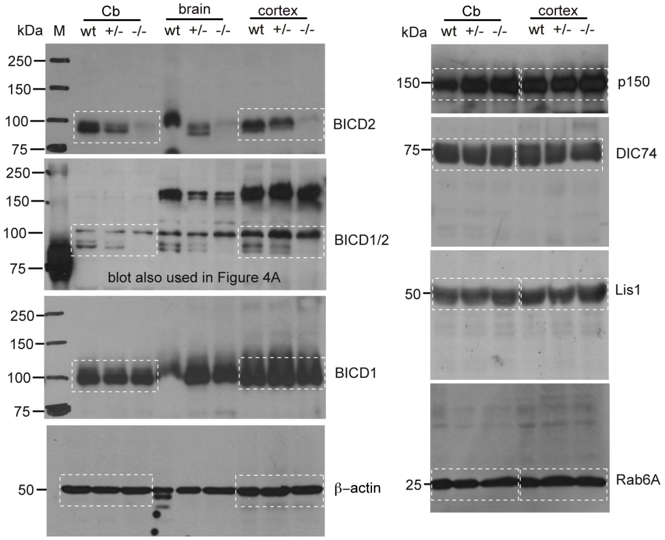

Figure S3.5: Full size Western blots related to Figure 3.4A-C A) Western blot with BICD2 antibody (#:2294) showing reduced and no expression of BICD2 in tissue homogenates of P20 heterozygote *Bicd2*$^{+/-}$ (+/-) and homozygote *Bicd2*$^{-/-}$ (-/-) mice, respectively. B) Western blot showing relatively high BICD2 expression in developing nervous system. C) Comparative Western blot analysis using BICD1 (antibody #2295 for BICD1 and antibody #2293 for BICD1/2), dynein components and interacting proteins (dynactin p150, dynein intermediate chain 74, Lis1) and Rab6 expression in *Bicd2*$^{-/-}$ cortex and cerebellum. M = marker. Selected parts of the Western blots (indicated in white boxes) can be found in Figure 3.4.

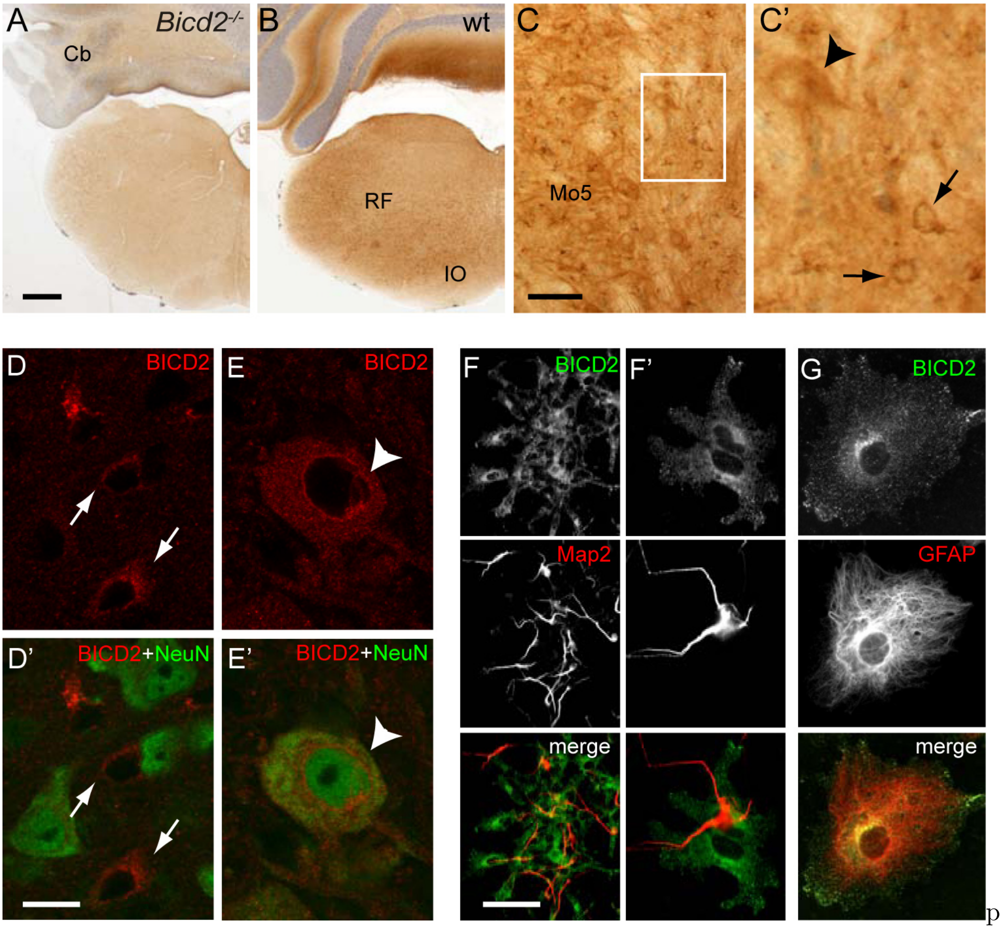

p

Figure S3.6: BICD2-immunoreactivity in glia and large neurons A, B) Immunohistochemistry with anti-BICD2 antibody in coronal sections of the caudal brain stem of P20 mice showing the absence of staining in *Bicd2*$^{-/-}$ mice and ubiquitous staining in wild-type brain stem and cerebellum. RF, reticular formation; IO, inferior olive. C) Anti-BICD2 staining in the trigeminal motor nucleus (Mo5) and adjacent reticular formation, showing increased staining levels in motor neurons (arrow head) and glial cells (arrows). D, E) Double-labelling confocal immunofluorescence (optical sections 1 μm) of BICD2 and NeuN showing the lower BICD2 staining intensities in neurons (NeuN+ in D) as compared to surrounding glia (NeuN- in D). Some neurons such as large neurons in the reticular formation (arrow head in E), however showed higher BICD2 staining levels. F, G) Double-labelling of BICD2 with MAP2 (F) or GFAP (G), respectively in primary neuron-astrocyte cerebellar co-cultures, indicates the absence of BICD2 in Map2+ cells and a fine punctate distribution of BICD2 in GFAP+ cells. Scale bars: 500 μm (A), 200 μm (C), 20 μm (D-F).

Axonal transport deficits in multiple sclerosis

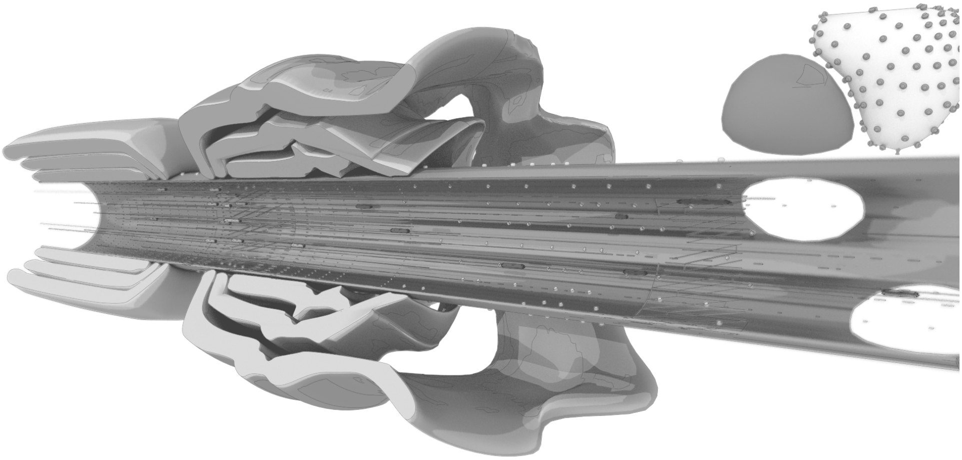

Van den Berg R, Hoogenraad CC and Hintzen RQ. Axonal Tranport Deficits in Multiple Sclerosis; Spiralling into the Abyss. Manuscript to be submitted.

4

AXONAL TRANSPORT DEFICITS IN MULTIPLE SCLEROSIS; SPIRALLING INTO THE ABYSS

Abstract

Multiple sclerosis (MS) is a relatively common neurological disorder of which the exact pathogenesis remains unclear. Evidence exists for contribution of both autoimmune and neurodegenerative mechanisms. Intracellular transport along the axonal cytoskeleton provides a bridge between these two components. The environment associated with neuroinflammation damages the cytoskeleton, leading to reduced efficiency of transport. As a result, the neuron is no longer able to redistribute mitochondria to balance demand and supply of ATP. Loss of integrity of the actin mesh disrupts the organization of the membrane, causing the nodes of Ranvier to fall apart, allowing ion channels to diffuse into the entire axonal membrane. The combination of reduced ATP production and increased consumption leads to a cascade of events finally resulting in axonal loss.

Introduction

In order to develop new therapeutic approaches towards curing any given disease, it is necessary to gain an understanding of the mechanisms that cause the illness, contribute to its progression and prevent its treatment. For multiple sclerosis (MS), an incurable neurological disorder mainly affecting young adults, medical science is still struggling to grasp the underlying pathological processes. The inflammatory component of the disease is obvious, and this is further supported by the recently identified risk genes that play a role in both adaptive and innate immunity (Lill et al., 2015; Moutsianas et al., 2015). Though the neurodegenerative component of the disease had already been described in the 19th century -even in the original descriptions by Charcot (Charcot, 1868)- there is a recent revival of research interest in the CNS tissue component of the disease. It maybe that in MS the CNS is more vulnerable to inflammation than average. Several observations have led to the idea that at least in a subset of patients there may be a prime role for CNS degeneration in the neuropathology of the disease. It has been observed that that myelin degeneration starts at the inner myelin sheaths, instead of on the outside as would be expected if caused by an external immune response (Rodriguez and Scheithauer, 1994). Next, there are strong indications that disturbed axoglial support can feed neurodegenerative processes (Trapp and Nave, 2008). In this respect it is of interest that already at the time of first attack in children, axoglial proteins appear abundant in CSF (Singh et al., 2015). In a response to damage model) any type of unknown tissue damage can elicit further auto-immune responses ('t Hart et al., 2009).

Furthermore, there are indications that the CNS tissue once damaged facilitates further neurodegenerative damage in an autonomous mode, irrespective of adaptive immune reactions (Frischer et al., 2009). This may account for the observation that immune modulating drugs, though quite active in suppressing inflammatory attacks, fail to halt progression, especially when started in later phases when demyelinating damage has already occurred (Hawker, 2011). A better understanding of the mechanisms involved in the neurodegenerative component of MS could potentially lead to new treatments, aimed at slowing down or preventing the disability caused by neuronal loss.

The cellular processes enabling neurons to generate and transmit signals demand a lot of energy, while at the same time the central nervous system contains very little energy reserves (Ames, 2000). This combination makes neurons highly vulnerable to energy deficits, which are considered to play a crucial role in neurodegeneration. As in other cell types, the main energy source of the neuron is ATP production by the mitochondria, with defects in mitochondrial function being highly associated with neurodegeneration (reviewed in (Lin and Beal, 2006). During the course of MS, neurons become even more vulnerable to energy deficits when they lose their myelin sheaths, increasing the energy needed to propagate a signal along the axon and to maintain the action potential (Trapp and Stys, 2009; Campbell and Mahad, 2012). Recent years have seen an increasing interest in the role of mitochondria in MS (Mahad et al., 2008; Campbell et al., 2014b).

Not only do neurons have a high energy demand, this demand is also distributed unevenly throughout the cell and shifts over time, depending on the activity of the cell and its neighbors. To facilitate the need for ATP, mitochondria are transported by motor proteins along the cytoskeleton to areas with high cellular activity, where they are anchored to the microtubule (Boldogh and Pon, 2007; Cai and Sheng, 2009b; Van Spronsen et al., 2013; Sheng, 2014). Defects in this transport system are found in a large variety of neurodegenerative disorders including Alzheimer's disease (Riemer and Kins, 2013), amyotrophic lateral sclerosis (ALS, (Bilsland et al., 2010) and Huntington's disease (Li and Conforti, 2013), and are now recognized to be one of the main underlying mechanisms of neurodegeneration (De Vos et al., 2008; Morfini et al., 2009; Millecamps, 2013).

For the transport system to function with the high efficiency required to maintain neuronal integrity, at least three conditions should be met. First of all, the infrastructure along which transport takes place, consisting of microtubules (Wade, 2007) actin networks (Cheever and Ervasti, 2013), must be intact in order for a cargo to reach its destination. However, infrastructure is useless without transporters to use it. Therefore, the motor proteins and their adapter proteins must be present in sufficient numbers and fully functional (Schlager and Hoogenraad, 2009; Hirokawa et al., 2010). Finally, for any complex transport system to work efficiently, control and guidance mechanisms should be in place (Verhey and Hammond, 2009; Maday et al., 2014). For axonal transport, regulation takes place through various mechanisms including chemical modification of the microtubules (Hammond et al., 2008; Janke and Kneussel, 2010), calcium sensor proteins (Cai and Sheng, 2009b; Macaskill et al., 2009) and anchoring proteins docking cargo at the desired destination (Kang et al., 2008; Cai and Sheng, 2009a). Defects in any part of this system can reduce its effectivity and put the neuron at risk for degeneration.

Taken together, there is now abundant evidence for the contribution of neurodegenerative processes to the pathology seen in MS. Also, more and more studies point at a role for axonal transport in this disease. In this review, we explore the current evidence pointing at axonal transport deficits in MS and discuss several mechanisms that can explain its role. Based on the increased understanding of these mechanisms, we will propose several scientific and therapeutic approaches which might be of interest to the MS research field in the coming decade.

Axonal transport in multiple sclerosis

Experimental autoimmune encephalomyelitis (EAE) is a commonly used model for MS (Baker and Amor, 2015). Through injection of a myelin component combined with an immunogenic adjuvant, an immune response is triggered against the myelin sheaths of the nervous system (Ralf et al., 2006). Interestingly, deficits in axonal transport are one of the earliest pathological findings in EAE, preceding structural abnormalities and other signs of axonal degeneration. Even before demyelination took place, both anterograde and retrograde transport of mitochondria were drastically reduced and remained down-regulated for weeks in a chronic EAE model (Sorbara et al., 2014). This is in line with earlier findings in the optical nerve of animals in which EAE was induced, showing a reduced transport of radioactive markers (Guy et al., 1989) and manganese ions (Lin et al., 2014). These EAE findings suggest that alterations in axonal transport form one of the first steps towards loss of the axon, both in EAE but also in MS itself (Dendrou and Fugger, 2014).

Many different factors contribute to MS susceptibility, including gender, environment and exposure of the immune system to pathogens (reviewed in (Alastair and Alasdair, 2008; Belbasis et al., 2015). In addition, there is a clear genetic component. For decades the only genetic risk factors known for MS were variations in the genes encoding human leukocyte antigens (HLAs, (Jersild et al., 1973). However, in recent years more than 110 genetic variants outside of the histocompatibility complexes have been found that each contribute to susceptibility to MS (reviewed in (Sawcer et al., 2014). The vast majority of the proteins encode by these genes either has a function in the immune system, primarily as part of a signaling pathway. Interestingly, several of the genes that do not fall in this category are involved in axonal transport. This includes three kinesin family member proteins (KIFs), the molecular motors responsible for anterograde transport along microtubules.

One of the KIFs that has been studied in the context of MS is Kif1b, a motor protein with at least two isoforms transporting mitochondria and synaptic vesicles (L et al., 1999; Mok et al., 2002). An effect of a SNP in Kif1b on MS susceptibility was first identified in a genetically isolated Dutch population. It was replicated in the same study in a second Dutch, a Swedish and a Canadian cohort (Aulchenko et al., 2008). Previous studies had already implicated this specific kinesin in the pathogenesis of Charcot-Marie-Tooth disease type 2A (CMT2A, (Zhao et al., 2001), a disorder of the peripheral nervous system showing myelin degeneration and associated with axonal transport impairments (Gentil and Cooper, 2012), suggesting that this mechanism was shared by both disorders. A more recent study showed that in zebrafish, Kif1b is essential for development of myelinated axons (Lyons et al., 2009). However, several attempts to replicate the genetic association, including a large multicenter study (R et al., 2010), failed to show a similar effect. Although this difference could be a consequence of the specific characteristics of this Dutch population, in which the control allele frequency of the gene was significantly lower than in the general population (Hintzen et al., 2010), it does appear that this gene does not contribute to MS susceptibility worldwide (Pierre-Antoine, 2011).

A second KIF was implicated when a large international consortium found an association between Kif21b and MS susceptibility (International Multiple Sclerosis Genetics Consortium (IMSGC), 2010), later replicated in an independent Belgian cohort (Goris et al., 2010). In neurons, Kif21b is enriched in the dendrites and involved in the transport of vesicles containing GABA receptor subunits (Labonte et al., 2013) . It is similar in structure to Kif21a, a kinesin associated with congenital fibrosis of the extra-ocular muscles type 1 (CFEOM1, (Yamada et al., 2003). Interestingly, rather than performing a transport function, Kif21a acts as a regulator of the cytoskeleton, inhibiting microtubule growth at the cell cortex (Van der Vaart et al., 2013).

A third association was found in a Spanish study, which identified a SNP in Kif5a as a risk factor for MS (Alcina et al., 2010). Kif5a is involved in the transport of neurofilament and mitochondria along microtubules (Xia et al., 2003) and forms a dimer with either Kif5b or Kif5c to transport mitochondria in axons (Schwarz, 2013). In zebrafish, cooperation between Kif5a and Kif1b is essential for maintaining axon integrity, with Kif5a taking over part of the tasks of Kif1b when this protein is lost and vice versa (Campbell et al., 2014a). Kif5a has been implicated in several axonopathies, including CMT2 (Liu et al., 2014). These findings strongly suggest that variations in Kif5a can contribute to neurodegeneration in MS, especially in combination with similar variations in Kif1b and/or Kif21b.

Transport deficits in MS neuropathology

A defective axonal transport system will lead to accumulation of organelles and proteins in places where they would not accumulate under normal conditions. A commonly used marker for disrupted axonal transport is the amyloid precursor protein (APP). In healthy neurons, this protein is transported through the axon to its final location in the synapse (Priller et al., 2006). If the transport system works at suboptimal efficiency, APP will accumulate in the axon. Several studies have reported that such accumulations can indeed be observed in post-mortem investigations of the brains of MS patients (Ferguson et al., 1997), in some case independent of demyelination (Bitsch et al., 2000). APP accumulation occurs already during the early phases of the disease, while the number of APP-positive axons showing a positive correlation with disease duration (Kuhlmann et al., 2002). A detailed study using both APP and the synaptic vesicle protein SPY as markers for axonal transport, found that accumulation of these proteins occurs not only in active demyelinating lesions, but also in normal appearing white matter. Also, the motor protein KIF5A as well as its associated cargo is found reduced in MS white matter (Hares et al., 2016), suggesting a reduced activity of the axonal transport system. Since the intracellular transport system is essential in developing and maintaining dendritic spines (Van den Berg and Hoogenraad, 2012), a reduced efficiency of this system might also explain the recent observation that the number of spines is significantly reduced in the cortex of MS patients (Jurgens et al., 2016).

A special challenge for intracellular transport is to match the distribution of mitochondria to the local ATP consumption. Although mitochondria are essential for ATP production, aging mitochondria become a source of radial oxygen species (ROS) contributing to neurodegeneration (Federico et al., 2012). The axonal transport system is able to distinguish decaying mitochondria based on their membrane potential, moving active mitochondria with a high membrane potential to the sites where ATP is required. In contrast organelles with a low membrane potential will be transported back to the cell body for autophagy (Federico et al., 2012). This means that both a reduced number of mitochondria as well as a persistence of aging mitochondria at the cell periphery pose a threat to axonal integrity. A number of post-mortem studies have shown that both situations can exist in the brains of MS patients. Several components of the mitochondrial respiratory chain were found reduced in activity, including complex I (Lu et al., 2000), III (Dutta and Trapp, 2007) and IV (Mahad et al., 2009). Demyelinated axons in the brains of MS patients were found to have a greater mitochondrial mass compared to myelinated axons and a higher expression of the docking protein syntaphilin (Mahad et al., 2009). This might initially be a protective mechanism. A larger number of mitochondria is transported to meet the higher ATP requirements and anchored to the mitochondria, prolonging the period the neuron can survive without myelin (Ohno et al., 2014). The mitochondrial density slightly decreases when axons are remyelinated, but remains high compared to myelinated axons. This higher density is entirely due to a larger number of stationary mitochondria, with the number of mobile mitochondria actually decreasing upon demyelination (Zambonin et al., 2011). Taken together, these studies suggest that transport of mitochondria plays an important role in the neuronal response to the energy deficit faced in MS lesions.

Transport deficits aggravate neurodegeneration

There is clear evidence suggesting transport deficits in MS. It is not so clear, however, how these deficits lead to axonal loss. One straightforward explanation would be that a reduced transport of active mitochondria leads to reduced ATP production in the axon. In demyelinated axons of MS patients, sodium channels normally restricted to the nodes of Ranvier are now expressed along large regions of the axon (Craner et al., 2004). A similar ectopic distribution is reported for calcium channels (Kornek et al., 2001). This will put additional strain on the neuron, since to maintain its membrane potential and prevent calcium toxicity both sodium and calcium have to be transported out of the cell using ATP-consuming transporters. Once ATP supplies are depleted, calcium levels in the axoplasm will rise to toxic levels, initiating a cascade resulting in axonal loss (reviewed in (Trapp and Stys, 2009; Stirling and Stys, 2010). Initially, the neuron will respond to the increased energy need by stimulating the transport of mitochondria, as observed in vitro (Kiryu-Seo et al., 2010) and in MS tissue (Ohno et al., 2014), leading to an increased density of mitochondria in dysmyelinated axons of MS patients (Mahad et al., 2008; Campbell and Mahad, 2012; Witte et al., 2014). Although the cell is able to maintain its axon for a short period in this ‘overload mode’, if the situation persists for too long, local ATP supplies will fall and axon integrity will be lost. This hypothesis is supported by the observation that reduced mitochondrial mobility alone, without accompanying stress to the neuron, is sufficient to cause neurodegeneration (Nguyen et al., 2014).

As mentioned before, demyelinated axons show an increased expression of syntaphilin, a protein thought to anchor mitochondria to the microtubules, prohibiting their transport and providing a stable local source of ATP (Mahad et al., 2009). The *shiverer* mouse, which shows severe dysmyelination of the CNS, is considered a model for progressive MS due to the metabolic challenges its axons face because of chronic myelin loss. As in MS patients, a highly significant upregulation of syntaphilin was observed in axons of this mouse, associated with an increase in nonmotile mitochondria. Interestingly, reducing the expression of syntaphilin by crossing the *shiverer* mouse with a syntaphilin knock-out line enhanced the transport of mitochondria from the axon back to the soma. Moreover, syntaphilin deletion also proved protective against both gray and white matter damage in the mouse, although it did not influence the outcome of EAE (Joshi et al., 2015). This indicates that a drug interfering with the binding between syntaphilin and either mitochondria or microtubule might theoretically reduce neurodegeneration in progressive multiple sclerosis, by improving mitochondria mobility.

Mitochondria are just one of the cargoes transported along microtubules. Vesicles containing a large variety of proteins, mRNA and membrane lipids are ferried through the cell. In the oligodendrocyte, the transport of mRNA by kinesins along microtubules is essential for the proper production of myelin (Carson et al., 1997; Lyons et al., 2009; Baron and Hoekstra, 2010). However, production alone is not enough to myelinate an axon. A complex interplay is required between oligodendrocyte and axon, communicating through cell-cell adhesion molecules (reviewed in (Sherman and Brophy, 2005; Simons and Trajkovic, 2006). These adhesion molecules are organized in sharply demarcated membrane domains through interaction of the adapter protein 4.1B with the underlying actin cytoskeleton (Horresh et al., 2010; Einheber et al., 2013). Formation of these domains, so-called paranodal junctions, is highly dependent on contactin-associated protein (Caspr (Einheber et al., 1997). Interestingly, the *shm* mouse in which the axonal transport of Caspr has been disrupted shows a distortion of myelin sheaths in the central nervous system, resulting in a reduced conduction velocity and a neurological disorder characterized by ataxia and hind limb paresis (Sun et al., 2009). Downregulation of Caspr has also been observed in MS lesions, where it is considered an early sign of impending myelin loss (Wolswijk and Balesar, 2003). This suggests a different route through which disruption of axonal transport can contribute to neurodegeneration, if the supply of adhesion molecules required to maintain the neuron-oligodendrocyte junctions is cut off.

Even though an axon denuded of its myelin is at high risk of degeneration, its situation is not hopeless. If it is able to survive, remyelination might occur (Franklin and Ffrench-Constant, 2008). As is the case in the initial myelination of the axon, remyelination depends on a number of signaling pathways activated through axon-glia cellular adhesion molecules (reviewed in (Taveggia et al., 2010). At least one of these adhesion molecules, Neuregulin 1, has been shown to depend on vesicle trafficking for its expression in the proper location on the membrane (Muthusamy et al., 2015). One pathway promoting oligodendrocyte proliferation and (re-)myelination is by activation of the Notch-pathway by F3/Contactin (Hu et al., 2003). Upregulation of F3/Contactin in denuded axons as observed in MS lesions (Nakahara et al., 2009) is considered essential for successful remyelination (Podbielska et al., 2013). F3/Contactin travels to the plasma membrane via a route that bypasses the Golgi apparatus (Bonnon et al., 2003, 2007). Although this means that delivery of the protein to the membrane can be facilitated in a microtubule-independent manner, the polarized trafficking of membranes to specific compartments still requires delivery through endosomes via the cytoskeleton (Lasiecka and Winckler, 2011; Kapitein and Hoogenraad, 2011). A less efficient transport would lead to a slower initiation of remyelination, prolonging the period of demyelination stress thereby increasing the risk of axonal loss.

Neurodegeneration aggravates transport deficits

As described in the previous paragraphs, there are various ways in which axonal transport deficits influence neurodegeneration. However, the opposite is also true, with the biochemical environment existing during neurodegeneration affecting the transport system. This holds true for mechanisms seen in a variety of neurodegenerative disorders, such as glutamate toxicity and mitochondrial decay, as well as for events more specific to MS, such as inflammation and demyelination.

Demyelination leads to dysregulation of axonal transport

Although axonal transport can function in individual neurons in culture, several studies have shown that myelination plays an important role in its regulation. In cocultures of neurons and oligodendrocytes, myelination is often incomplete, with only parts of the axon covered with a myelin sheath. These myelinated sections show a local slowing of axonal transport, resulting in a locally increased axon diameter (Monsma et al., 2014). Oligodendrocyte-axon interactions lead to specialization of segments of the axons around the nodes of Ranvier. These paranodal regions show a significantly larger mitochondrial content and increased speed of mitochondrial transport. In a myelin deficient mouse, mitochondria are localized throughout the axon and transported with a uniform speed (Ohno et al., 2011). Furthermore, in mice with a null mutation of the myelin *Plp* gene, a model system for hereditary spastic paraplegia type 2, an impairment of both anterograde and retrograde transport in axons was observed (Edgar et al., 2004). One could argue that this impairment is due to the energy deficit and calcium influx associated with demyelination. However, a similar phenotype is observed in the CNP knockout mouse, where myelin assembly is normal but only the signaling between oligodendrocyte and axon is disrupted (Lappe-Siefke et al., 2003). One possible explanation for the disruption of transport could be a local drop in ATP, since the mitochondria in the axon partially depend on lactate supplied by oligodendrocytes (Lee et al., 2012; Saab et al., 2013).

Inflammation leads to cytoskeleton destabilization

In active MS inflammatory lesions, the activated T-cells that have infiltrated the CNS induce microglia to produce tumor necrosis factor alpha (TNF-α, (Chabot et al., 1997). Apart from its function in regulating the immune response, exposing cells to high concentrations of this cytokine also leads to destabilization of microtubules and loss of cell integrity (Petrache et al., 2003; Shivanna and Srinivas, 2009). As of yet, the exact mechanism through which TNF-α leads to microtubule destabilization remains unknown. It is possible this effect is mediated through glutamate toxicity, as TNF-α induces secretion of glutamate while at the same time decreasing the glutamate uptake by glia cells (Olmos and Llad, 2014). However, the destabilising effect is also observed in non-neuronal cells, suggesting the involvement of a different pathway which does not depend on glutamate toxicity.

Activated microglia not only produce TNF-α and other cytokines, but also express the enzyme inducible nitric oxide synthase (iNOS, (Dasgupta et al., 2002). Nitric oxide (NO) acts as an almost universal signaling molecule, affecting a large variety of molecular pathways. This makes it hard to isolate its effect on the cytoskeleton. An extensive body of research exists on the action of NO on the plant cytoskeleton. In plants, stimulation of cells with NO leads to depolymerization of cortical microtubules (Shi et al., 2009), leading to an overall disorganization of both the actin (Kasprowicz et al., 2009) and the microtubule network (Lipka and Mller, 2014). Although less thoroughly studied, the same mechanism is also present in mammalian neurons. In these cells, stimulation with NO leads to reconfiguration of the microtubule network through nitrosylation of MAP1B, resulting in growth cone collapse and axon retraction

(Stroissnigg et al., 2007). The chemical environment associated with neuroinflammation is in itself already capable of disrupting microtubule-associated axonal transport.

Mitochondrial decay inhibits axonal transport

As mentioned previously, changes in mitochondria density, mobility and activity are a common finding in MS neuropathology (Mahad et al., 2009; Witte et al., 2010). Although these changes initially are aimed at protection of the axon by providing a steady supply of ATP, if these mitochondria are not turned over they become a prime contributor to neurodegeneration (Karbowski and Neutzner, 2012). One of the mechanisms through which decaying mitochondria lead to axonal loss is by disturbing the Ca^{2+} homeostasis (Rasola and Bernardi, 2011). As with glutamate excitotoxicity, the resulting increase in intracellular Ca^{2+} will lead to a cascade of events, including transport disruption, finally resulting in apoptosis or necrosis. Defects in the respiratory complexes can lead to excess production of radial oxygen species (ROS). The oxidative stress caused by the reaction of these free radicals with proteins in the neuron contributes to neurodegeneration (Lin and Beal, 2006; Trushina and McMurray, 2007). One of the first effects of artificially induced oxidative stress is inhibition of axonal transport, occurring hours before any effect is seen on other cellular structures (Fang et al., 2012). The same study showed that depletion of ATP, another consequence of mitochondrial degradation, will also inhibit axonal transport of mitochondria and Golgi-derived vesicles. As mitochondria fail, axonal transport will become dysfunctional as well.

Effects of glutamate toxicity on the cytoskeleton

Glutamate excitotoxicity has long been recognized as a contributor to neurodegeneration in a variety of neurological disorders (Kalia et al., 2008), including MS (Pitt et al., 2000; Geurts and Barkhof, 2008; Kostic et al., 2013). Under normal circumstances, glutamate can bind to channels in the plasma membrane, generating a small and strictly controlled flow of ions. When a neuron is overstimulated with glutamate, the size of this ion flux is increased, resulting in an rising Ca^{2+} concentration in the cytoplasm. This accumulation in turn triggers several signaling cascades, finally resulting in apoptosis (reviewed in (Trapp and Stys, 2009). Before the levels initiating apoptosis are reached, this increase in intracellular Ca^{2+} already has a detrimental effect on the cytoskeleton. The infrastructure for transport is degraded, as both microtubules (Mattson et al., 1991) and intermediate filaments (Chung et al., 2005) are destabilized and lost. Since the organization of the microtubule skeleton is essential for axon structure and integrity (Kevenaar and Hoogenraad, 2015), such degradation will lead to a breakdown of axonal transport and eventually neurodegeneration. In cultured neurons, the influx of Ca^{2+} caused by glutamate is indeed sufficient to slow down or inhibit fast axonal transport (Ackerley et al., 2000; Hiruma et al., 2003). This could explain why an estimated 50% of demyelinated axons in the brain of MS patients show fragmentation of the neurofilament network and a reduced organelle content (Dutta et al., 2006).

Apart from the direct effect of glutamate toxicity on microtubule stability, there is also an indirect effect on transport through alteration of post-translational modifications (PMTs). These modifications influence microtubule dynamics, but also function as traffic rules regulating binding affinity of molecules including motor proteins (Ikegami and Setou, 2010; Janke and Bulinski, 2011; Sirajuddin et al., 2014). A combination of at least two of these modifications, acetylation and detyrosination, enhances both the binding of Kinesin-1 (Kif5) to microtubules and its motor activity as well as its preferential localization to the axon (Reed et al., 2006; Hammond et al., 2010; Kaul et al., 2014). A decrease in the level of acetylated α-tubulin in a mouse model induced severe axonal transport deficits. Clinically this resulted in neurological deficits resembling either Charcot-Marie-Tooth disease or distal hereditary motor neuropathy, depending on the exact mutation in the deacetylase enzyme HDAC6 generated. Treating the animals with an inhibitor of HDAC6 rescued the transport deficits and led to disappearance of the clinical phenotype (d'Ydewalle et al., 2011). Microtubule modifications are not static, but can vary over time. For example, neuronal activity leads to a local increase of microtubule polyglutamylation causing a reduction of Kif5 mobility and cargo delivering (Maas et al., 2009) as well as an increase in in acetylation of *alpha*-tubulin (Pandey and Sharma, 2011). In contrast, loss of polyglutamylation leads to abnormal targeting of Kif1A and a decrease in density of synaptic vesicles (Ikegami et al., 2007). Decreases in acetylation have also been suggested to play a role in several human neurodegenerative disorders, most notably Alzheimer's disease (Hempen and Brion, 1996; Zhang et al., 2015). If activation of glutamate receptors leads to changes in tubulin acetylation (Pandey and Sharma, 2011), it is very likely that glutamate excitotoxity will also affect the balance between the different PMTs and therefore disrupt the proper regulation of axonal transport. Further research is required to determine if such a mechanism plays a role in neurodegeneration in MS.

The downward spiral

From the studies reviewed in this article, a picture emerges of axonal transport deficits as both cause and consequence of neuronal degeneration. In the healthy axon, fast intracellular transport is supported by a dense network of microtubules. Molecular motors transport a variety of cargoes using this infrastructure, including mitochondria and vesicles containing cellular adhesion molecules, amongst many others. This continuous stream of supplies is essential in meeting the energy demand of the axon through local ATP production, as well as maintaining contact with oligodendrocytes through cell-cell adhesions. The membrane is divided into several compartments, maintained by interaction of membrane proteins with the (actin) cytoskeleton. These domains prohibit diffusion of glutamate receptors outside of the nodes of Ranvier, concentrating the peak demand for ATP to these areas of the axon. Through post-translational modifications of microtubules and local concentration of anchoring proteins, a large number of mitochondria is retained these nodes, producing ATP where it is most needed (figure 4.1 **A**).

Failure of axonal transport has severe consequences for the axon. Local peaks in energy demand can no longer be answered by increased transport of mitochondria. Although mitochondria are able to divide and fuse in the axon (Amiri and Hollenbeck, 2008), defective mitochondria are usually transported back to the perinuclear region for mitophagy (Vives-Bauza et al., 2010). As transport fails, these mitochondria will remain in the axon and become a source of radical oxygen species (ROS) and Ca^{2+}. Since both anterograde and retrograde transport is affected, proteins will start to accumulate in the axon. When the organization of the cytoskeleton further deteriorates and transport of adhesion molecules to the membrane slows down, the boundaries between the nodes of Ranvier, the perinodal regions and the remainder of the membrane will become less clearly demarcated. This weakens the connections between the axon and its myelin sheath and allows for ion channels to diffuse outside of the nodes of Ranvier. The demand for ATP rises and becomes more uniformly spread throughout the axon, in stead of being concentrated in the nodes of Ranvier.

Figure 4.1 ***(on the next page)*****: Transport defects and axonal degeneration.** In the healthy axon (**A**), the membrane is organized in different compartments through interaction of adhesion molecules and other membrane proteins with the underlying actin mesh. In the nodes of Ranvier, this interaction confines the ion channels from diffusing out of the nodes. The ion flow through these channels has to be compensated in order by a similar magnitude outflow in order to maintain membrane potential. The main protein complex involved in this outflow is Na^+/K^+-ATPase, an enzyme that exchanges intracellular sodium for extracellular potassium, hydrolysing an ATP molecule in the process. This mechanism results in a peak in ATP demand at the nodes of Ranvier compared to the rest of the axon. The axonal transport system matches this demand by guiding a constant flow of mitochondria into the nodes and anchoring them to the microtubules where demand is highest, resulting in a careful balance between supply and demand (**A'**). In the micro-environment created by neuroinflammation, such as seen in MS, this balance is disturbed (**B**). Microglia, activated by T-lymphocytes infiltrating the CNS, produce a mixture of different compounds such as glutamate, TNF-α and nitric oxide, causing degradation of the actin network and fragmentation of the microtubule cytoskeleton. As a result, the membrane compartments fall apart and ion channels start to diffuse along the membrane. In addition, the reduced efficiency of mitochondrial transport along the fragmented microtubules results in aging mitochondria being stuck in the axon, leading to decreased mitochondrial efficiency. The diffusion of sodium channels and their activation through increased glutamate levels will lead to a peak in ATP consumption through Na^+/K^+-ATPase, which is no longer restricted to the nodes. As mitochondria can no longer be freely redistributed, the transport system is not able anymore to match ATP supply to demand (**B'**). When the ATP levels drop significantly, a backup mechanism enables the neuron to maintain its membrane potential a while longer by exchanging intracellular sodium for extracellular calcium. At this point, the damage to the axon is still reversible. If the inflammatory environment disappears and the transport defects are corrected, the situation in (**A**) can be restored. If intracellular calcium levels keep rising, damage to the transport system accumulates and becomes irreversible (**C**). The continued exposure to high levels of glutamate completely disintegrates the actin mesh. Transport along microtubules ceases as microtubules are depolymerized and motor proteins are unable to function because of low ATP levels, as the supply of ATP fails because of mitochondrial dysfunction (**C'**). The increase in intracellular Ca^{2+} activates a variety of enzymes, leading to loss of membrane integrity and finally loss of the axon.

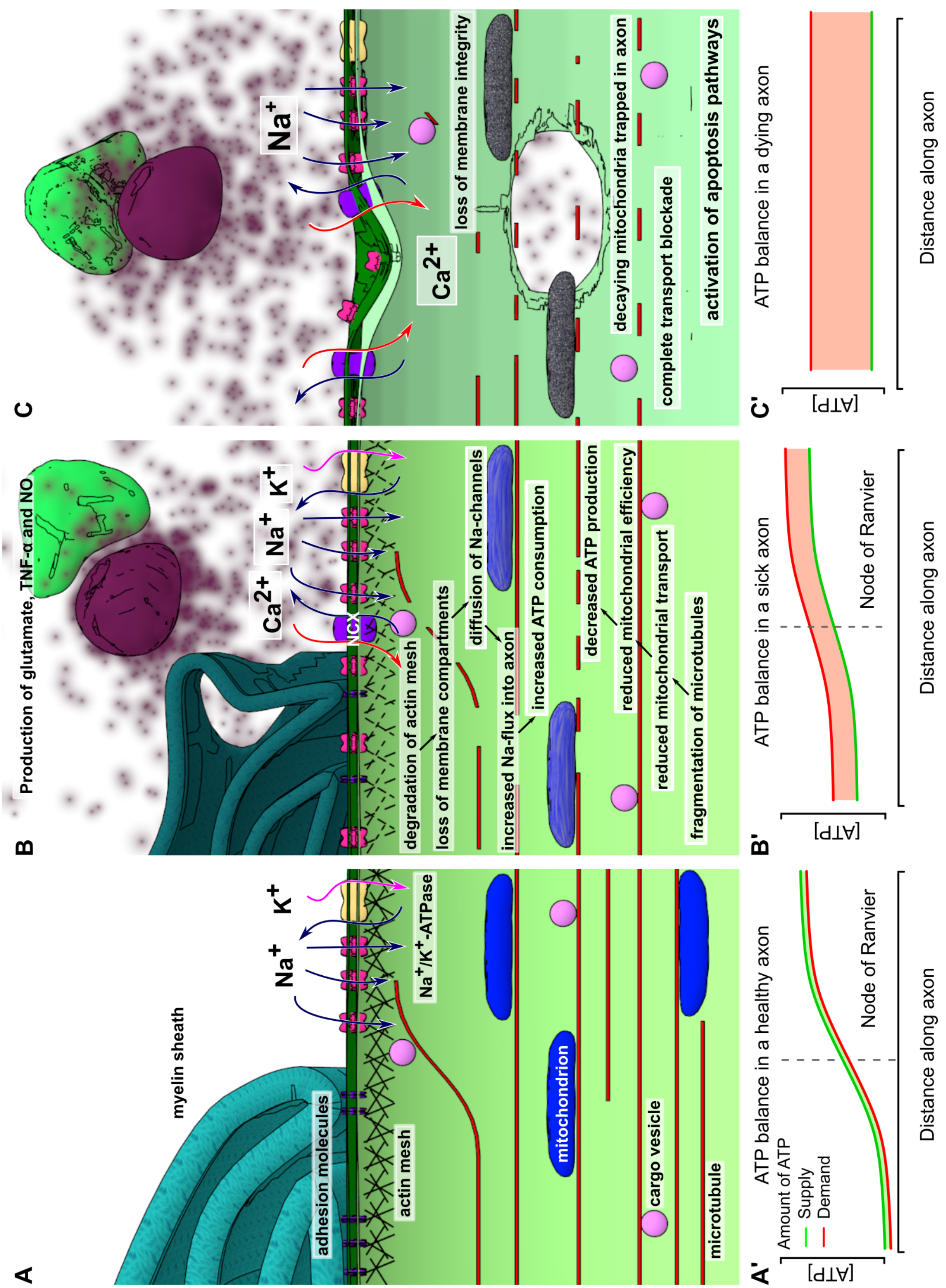
A
myelin sheath
adhesion molecules
actin mesh
Na^+
K^+
Na^+/K^+-ATPase
mitochondrion
cargo vesicle
microtubule
A'
ATP balance in a healthy axon
Amount of ATP
Supply
Demand
[ATP]
Node of Ranvier
Distance along axon
B
Production of glutamate, TNF-α and NO
Ca^{2+}
Na^+
K^+
NCX
degradation of actin mesh
loss of membrane compartments
diffusion of Na-channels
increased Na-flux into axon
increased ATP consumption
decreased ATP production
reduced mitochondrial efficiency
reduced mitochondrial transport
fragmentation of microtubules
B'
ATP balance in a sick axon
[ATP]
Node of Ranvier
Distance along axon
C
Na^+
Ca^{2+}
loss of membrane integrity
decaying mitochondria trapped in axon
complete transport blockade
activation of apoptosis pathways
C'
ATP balance in a dying axon
[ATP]
Distance along axon

At the same time, the ROS released by mitochondria, as well as the dropping levels of ATP further decrease the efficiency of the axonal transport system (figure 4.1 **B**).

In the context of MS, the molecular environment caused by neuroinflammation is an additional detrimental factor to axonal transport. T-cells infiltrating the central nervous system induce the activation of microglia. Microglia in turn become a source of a cocktail of chemicals, including TNF-α and NO. TNF-α disrupts glutamate homeostasis, simultaneously stimulating its release and inhibiting re-uptake. The axon is now exposed to high levels of glutamate, which are even more harmful due to the increased and more diffuse concentration of sodium channels in the axon membrane. The resulting influx of Na_+ has to be compensated through action of the Na_+/K_+-ATPase, one of the most energy-consuming processes in the cell (Howarth et al., 2012). High concentrations of NO lead to depolymerization of the microtubule network, further hampering transport.

At this point, the neuron is basically holding its breath. If the toxic effects of neuroinflammation disappear in time and the damage to the transport system is limited, the cycle leading to neurodegeneration could be reversed. Microtubules will grow back into the axon, transport will resume and the damage will be restored. As membrane domains are reformed, even remyelination becomes possible. However, for this to happen, all conditions must be exactly right. If for example genetic variations in one of the motor proteins leads to a less efficient transport capacity, the balance might tip towards continuing down the road towards neurodegeneration. If the remaining ATP supplies are depleted, the intracellular Na^+ concentration raises to critical levels. This leads to a reversal of the calcium current along the Na^+/Ca^{2+} exchanger, allowing calcium to flow into the neuron while pumping sodium out, buying the neuron a little more time (Zhao et al., 2014). If this situation persists for too long, the intracellular Ca^{2+} concentration will be high enough to activate a number of enzyme systems, finally resulting in loss of membrane integrity and apoptosis(figure 4.1 **C**).

Ever since the first MS cases were described in the nineteenth century, the precise origin of neuropathological damage in this disease has to be elucidated. Two extreme views can be discerned. According to one, MS is an autoimmune, inflammatory disease while the other considers it a primary degenerative disorder with a secondary immune response (Alastair and Alasdair, 2008; Stys et al., 2012). The model in figure 4.2 attempts to reconcile these quite distinct hypotheses. We suggest that these two possible etiological pathways eventually may lead to the same vicious circle towards neurodegeneration. They may be happening at the same time in one patient, but in some cases perhaps also on their own. Both the neuroinflammation ignited via blood components as well as intracellular contributors such as axonal transport deficits or mitochondrial malfunction can trigger the same chain of events. This could at least partially explain the clinical variability observed in MS patients. If a patient has an efficient transport system, neurodegeneration will be mild, even after multiple inflammatory episodes. In contrast, if an underlying defect in transport or mitochondrial function is already present, even a mild neuroinflammatory event can lead to neurodegeneration. Although the outcome is identical demyelination and eventually neurodegeneration the exact combination of transport efficiency, mitochondrial function and constitution of the immune system, amongst others, will determine the clinical course for each individual MS patient.

In the pathogenesis of multiple sclerosis, axonal transport is as much a victim as it is an accessory, assisting others in committing the crime. Deficits in axonal transport can contribute to the neuropathology observed in MS, but the reverse is also true. The effects of demyelination and inflammation on the microtubule cytoskeleton initiate and amplify a chain of events resulting in axonal loss (summarized in figure 4.2. Interrupting the spiral of neurodegeneration is the only way to prevent the clinical progression seen in MS patients. We propose that a variety of therapeutic approaches could prove equally effective. Microtubule stabilising drugs could prevent the loss of axonal infrastructure, while medication targeting mitochondria preserves the local production of ATP and prevents the leakage of calcium and ROS. Anti-inflammatory drugs diminish the neuronal stress caused by exposure to TNF-α, NO and glutamate, while NMDA-receptor blockers and calcium chelators reduce the toxic effects of glutamate excitotoxicity. As of yet, there are no drugs present that can increase the efficiency of the axonal transport system, although substances such as tubastatin that modify post-translational modification are an interesting candidate (d'Ydewalle et al., 2011). The damage that has already occured can not be undone, but these approaches can increase the probability that an axon will survive the toxic environment of an active MS lesion.

Concluding Remarks

The association between axonal transport and neurodegeneration is complex and bidirectional. Deficiencies in intracellular transport can lead to a positive feedback loop, a loop in which reduced transport of mitochondria and other components leads to local ATP shortages, which further hamper transport (figure 4.2). If the circumstances interfering with transport persist for a certain amount of time, this loop will inevitably lead to axonal loss. There is substantial evidence that such a loop could play a role in a large variety of neurodegenerative disorders (reviewed in Hirokawa et al. (2010); Millecamps (2013)). In MS, this cycle becomes even more vicious because of the contribution of inflammation and demyelination, further increasing both transport defects and ATP demand. This feedback loop would explain a number of puzzling findings in MS, since it suggests that a number of different initial events will lead to the same outcome. A combination of deficiencies in mitochondrial activity, a hampered axonal transport system or a specific immune makeup will all lead to the same outcome, but in each patient the emphasis will be different. Some MS patients with a severe mitochondrial or transport phenotype will show a large amount of neurodegeneration with little inflammation, while other patients will be more on the inflammatory end of this spectrum. Such a spectrum of disease could explain the large variability in disease progression and therapy response observed in MS patients. This neurodegenerative loop also offers new hypothetical approaches towards MS treatment, since it suggests that weakening any part of the loop could reduce neurodegeneration and therefore disease progression. Therapy focused on restoring the ATP balance or increasing transport efficiency would weaken the loop and slow down neurodegeneration. Developing such neuroprotective strategies and combining it with the immunomodulatory drugs already available to MS patients will, hopefully in the near future, greatly reduce the suffering caused by this debilitating disease.

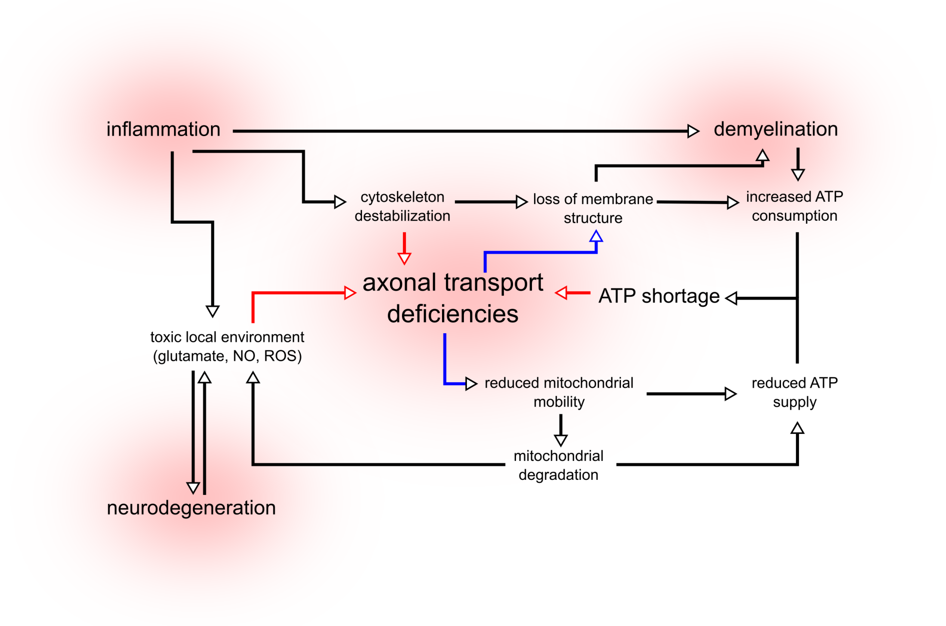

Figure 4.2: The cycle of neurodegeneration. In MS, both inflammation and neurodegeneration lead to a toxic local environment composed of high concentrations of glutamate, nitric oxide (NO) and reactive oxygen species (ROS). These chemicals destabilize the cytoskeleton and affect the function of the axonal transport system. Inflammation also leads to demyelination, exposing large sections of the axon to the hostile micro-environment and increasing the demand for ATP. As transport efficiency is decreased, transport of mitochondria is impaired, leading to a reduced supply of ATP and accumulation of degrading mitochondria in the axon. These mitochondria become an additional source of ROS, contributing to toxicity. Due to transport failure, the constant flow of membrane lipids and proteins diminishes, leading to the loss of membrane structure and integrity. This further contributes to demyelination and prevents remyelination. The increased demand for ATP combined with the reduced supply leads to ATP shortages, preventing motor protein function. Through this loop, axonal transport deficiencies, mitochondrial defects and inflammation amplify each other, creating a positive feedback system that leads to neurodegeneration.

Heterozygous KIF1B deletion in a model of multiple sclerosis

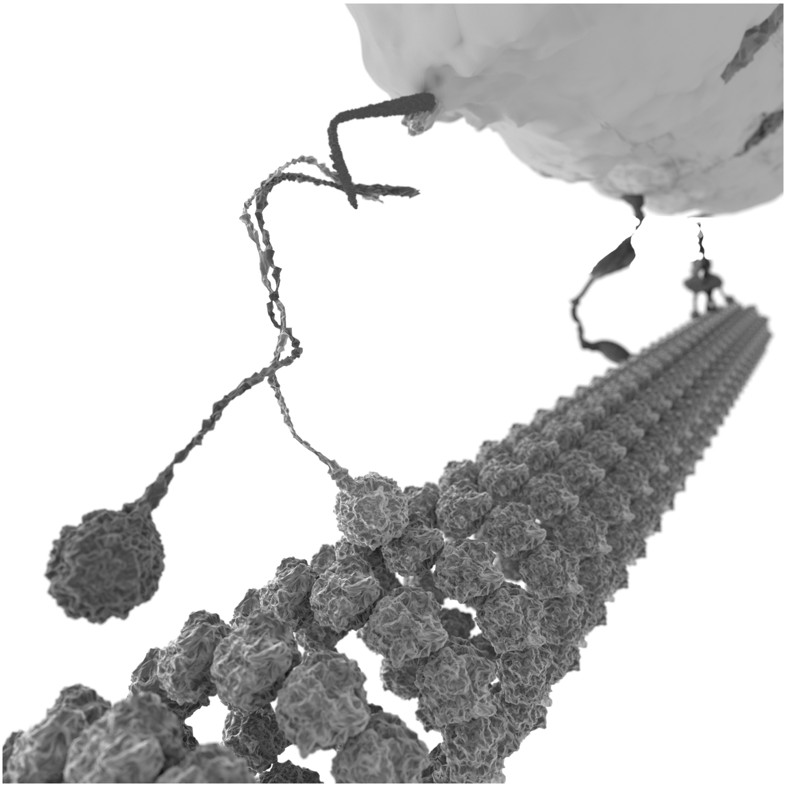

Van den Berg R, Van Meurs M, Will L, Laman JD, Hintzen RQ and Hoogenraad CC. Heterozygous Kif1b deletion does not affect clinical disease or neuropathology in a demyelinating EAE model of multiple sclerosis. Manuscript to be submitted.

5

HETEROZYGOUS KIF1B DELETION DOES NOT AFFECT CLINICAL DISEASE OR NEUROPATHOLOGY IN A DEMYELINATING EAE MODEL OF MULTIPLE SCLEROSIS

Multiple sclerosis (MS) is a neuroinflammatory disease in which the myelin sheath around the nerve fibers of the brain and spinal cord is affected, leading to demyelination and axonal damage. Recent genome-wide association studies found that genes encoding for kinesin motor proteins, such as kinesin-3 family protein *Kif1b* are susceptibility loci for MS. Gene mutations in *Kif1b* were previously reported in a family with Charcot-Marie-Tooth disease type 2A (CMT2A) and *Kif1b* mutant mice develop progressive muscle weakness. However, mechanistic links between *Kif1b* function and MS risk have not been explored. Here, we tested the relevance of *Kif1b*-driven mechanisms to the neurological and pathological signs in an experimental autoimmune encephalomyelitis (EAE) animal model of MS. Since homozygous *Kif1b* knockout mice are not viable, we used heterozygous *Kif1b* deficient mice for the induction of EAE. We found that $Kif1b^{+/-}$ mice do not show any significant differences in disease characteristics, including rotarod performance, clinical score and surface area of white matter lesions. These data show that significantly reduced *Kif1b* expression does not contribute to clinical and pathological expression in at least one mouse model for autoimmune demyelinating disease.

Introduction

Multiple sclerosis (MS) is an inflammatory demyelinating disease of the central nervous system, characterized by alternating periods of inflammation and recovery. Over time the disease slowly advances, leading to progressive neurological disability for which no treatment is currently available (Alastair and Alasdair, 2008). Advances in the technology for large-scale genotyping of single nucleotide polymorphisms (SNPs) have facilitated unbiased, genome-wide association studies (GWAS). The most prominent genetic risk factor for MS is HLA-DR (Lincoln et al., 2005), but in addition more than 100 non-HLA susceptibility loci have been identified, as risk factors for MS (Hafler et al., 2007; International Multiple Sclerosis Genetics Consortium (IMSGC), 2013). The majority of these genes are thought to play an important role in the immune system, supporting the notion that neuroinflammation is a key driving component of MS.

Recent GWAS found that genes encoding for kinesin motor proteins are susceptibility loci for MS. Kinesin-1 family protein KIF5A, kinesin-3 family protein *Kif1b* and kinesin-4 family proteins *Kif21b* are all associated with MS risk (Aulchenko et al., 2008; International Multiple Sclerosis Genetics Consortium (IMSGC), 2010; Alcina et al., 2013). Proteins from the kinesin family are the main players in anterograde axonal cargo transport of many different subcellular components, such as mitochondria and synaptic vesicles, as well as basic building blocks, such as proteins (Vale, 2003; Hirokawa et al., 2009; Van den Berg and Hoogenraad, 2012). A large number of different kinesin molecules has been identified, many of which are linked to human diseases, especially neurodegenerative disorders (De Vos et al., 2008; Morfini et al., 2009; Millecamps, 2013; Neefjes and Van der Kant, 2014). For example, *Kif1b* has been indicated in the pathogenesis of Charcot-Marie-Tooth, a hereditary neuropathy of the peripheral nervous system. Gene mutations in *Kif1b* were previously reported in a Charcot-Marie-Tooth disease type 2A (CMT2A) family and global *Kif1b* knockout mice develop progressive muscle weakness at high age due to a defect in the transport of synaptic vesicle precursors (Zhao et al., 2001). Moreover, *Kif1b* is required for the transport of MBP (myelin basic protein) mRNA in oligodendrocytes, a process essential for the development of myelinated axons in zebra fish (Lyons et al., 2009).

Follow-up studies supported the correlation between KIF5A and *Kif21b* and MS susceptibility (Goris et al., 2010; Alcina et al., 2013) but the reported associations with the rs:1049:2972(C) allelic variant of *Kif1b* gene variants in the *Kif1b* gene have proven difficult to replicate. Sequence analysis in an Italian primary progressive MS dataset (Martinelli-Boneschi et al., 2010) and in a large multicenter study by the International Multiple Sclerosis Genetics Consortium (IMSGC) (International Multiple Sclerosis Genetics Consortium (IMSGC), 2010) provided no evidence for association with MS. Contrary to the findings of the original study, findings in a Russian cohort showed a small protective effect of the rs10492972(C) allele (Kudryavtseva et al., 2011). Finally, a meta-analysis using equivalence-based statistics suggested that the proposed association between the SNP variant in *Kif1b* and MS is not present in the worldwide patient population (Pierre-Antoine, 2011). On the other hand, a recent independent study showed a significant reduction in mRNA and protein levels of *Kif1b* in the grey matter of MS cases (Hares et al., 2013). Thus, although it is widely recognized that axonal dysfunction plays an important role in MS disease progression (Stys et al., 2012), the relevance of axonal transport mechanisms to disease pathology and mechanistic links between *Kif1b* function and MS is not clear.

Here, we directly tested the hypothesis that reduced *Kif1b* expression affects the neurological and pathological signs and symptoms in an animal model of MS. We created a heterozygous *Kif1b* deficient knockout mouse and subjected it to experimental autoimmune encephalomyelitis (EAE), a model in which injections of components of the myelin sheath trigger an autoimmune reaction against the native myelin. Much of our current understanding of MS is derived from studies on EAE, most commonly induced in C57Bl/6 mice using MOG$_{35-55}$ emulsified in complete Freund adjuvant (CFA) (McGavern et al., 2000; Baxter, 2007; Pachner, 2011). Although it does not fully mimic human MS, EAE in mice is characterized by demyelination and inflammation of the CNS, with corresponding tail and limb weakness and paralysis. C57Bl/6 mice are a well-studied line for creating transgenic animals, an additional advantage that turns this protocol for EAE into one of the most commonly used MS models (Pachner, 2011). The use of the rotarod, a slowly accelerating rotating rod, is common in neuroscience field but much less in MS research. Previously it has been shown that rotarod performance is highly correlated to demyelination and especially to axonal loss (McGavern et al., 2000). Here we show that heterozygous *Kif1b* deficient mice do not show any significant differences in disease progression according to rotarod performance, clinical disease and pathology. These data demonstrate that strongly reduced *Kif1b* expression does not contribute to disease severity in at least one mouse model for inflammatory demyelinating disease.

Results

Generation of heterozygous *Kif1b* knockout mice

To generate an inducible *Kif1b* knockout allele, a resistance marker was introduced in the *Kif1b* locus by homologous recombination in mouse embryonic stem (ES) cells. The mouse *Kif1b* gene is located on chromosome 4 and 47 exons have been identified, with the ATG start code in exon 2 and TGA stop codon in exon 47. Exons 3 and 4 were selected as conditional knockout regions since deletion will lead to a frame shift, and a premature translation stop of the *Kif1b* transcript. The first loxP sequence was inserted into intron 2, and a neomycin selection cassette surrounded by frt sites and followed by a loxP sequence was inserted into intron 4 of the *Kif1b* gene (Figure 5.1A). Their integration was confirmed by Southern-blot and PCR analysis (Figure 5.1B-D). The positive ES cell clones with the floxed *Kif1b* allele (termed *Kif1b*f) were injected into blastocysts. The chimeras that gave germ line transmission were mated into the C57BL/6 background to generate inbred *Kif1b*f (targeted) mice. Heterozygous *Kif1b* knockout (*Kif1b*$^{+/-}$) mice were obtained by crossing F1 heterozygous *Kif1b*f mice with CAG-Cre transgenic mice that express Cre recombinase in the germ-cell lineage. Genotyping of the mutant lines was performed by PCR analysis (Figure 5.1E). By Western-blot analysis, we demonstrated that as predicted, *Kif1b* was produced at 2-fold lower level in heterozygous mice (*Kif1b*$^{+/-}$) compared to wildtype mice (Figure 5.1F). Reduction in the amount of *Kif1b* mice did not lead to a significant upregulation of other members of the kinesin-3 family (Figure 5.1F), indicating that there was no compensation by closely related kinesin-3 family members at the expression level.

Matings between *Kif1b*$^{+/-}$ mice yielded transgenic animals that were born in a non-Mendelian ratio, with complete absence of homozygous *Kif1b* knockout mice. This is consistent with a previous report, which found that *Kif1b* knockout mice die at birth most likely due to nervous system defects (Zhao et al., 2001). Heterozygous animals were born in slightly lower numbers than expected, but this difference was not statistically significant (Figure 5.1G). At 3 months of age, adult *Kif1b*$^{+/-}$ mice were indistinguishable in gross appearance and weight from heterozygous and wildtype littermates (Figure 5.1H). Behaviorally, *Kif1b*$^{+/-}$ mice displayed no motor abnormalities: the motor activity measured by rotarod performance of 3 months old heterozygous *Kif1b* mice was comparable to wildtype littermates (Figure 5.1H).

Figure 5.1 *(on the next page)*: Characteristics of *Kif1b* heterozygous knockout mice A) The mouse *Kif1b* locus and gene targeting constructs. To generate an inducible *Kif1b* knockout allele, a loxP sequence was inserted into intron 2, and a neomycin selection cassette surrounded by frt sites and followed by a loxP sequence was inserted into intron 4 of the *Kif1b* gene. The top line represents *Kif1b*, with exons indicated by black solid boxes. The positions of Southern-blot probes 1 and 2 (horizontal lines) and PCR primers a, b, c and d (arrows) are indicated. Selected restriction enzyme sites are shown (BamHI, EcoRI and HdIII). The targeting constructs are shown below *Kif1b*. Homology with the *Kif1b* gene is indicated, as are the lengths of the homologous regions. The loxP sites are represented by arrows. NEO, neomycin resistance cassette; gray boxes are frt sites; DTA, diphtheria toxin A gene. The targeted *Kif1b* allele, *Kif1b*^{f}, is shown below the targeting constructs. Cre-mediated recombination at the outermost loxP sites of the *Kif1b*^{f} allele removes exon 3 and 4 the *Kif1b* sequences and generates the *Kif1b*$^{-}$ allele, which is represented by the bottom line. Deletion of exon 3 and 4 of the *Kif1b* gene leads to a frame shift and a premature stop of translation of the transcript. B-D) Southern-blot analysis of the *Kif1b* gene targeting event. Southern blot of DNA derived from wildtype (wt) and targeted ES cells (+/-) were digested with BamHI (B), EcoRI (C) and HdIII (D). The blot was hybridized with external probe 1 (B), which detects fragments of 14.2 kb (wildtype allele) and 13.2 kb (NEO-targeted allele), external probe 2 (C), which detects fragments of 6.0 kb (wildtype allele) and 5.0 kb (NEO-targeted allele) and internal probe 3 (NEO probe), which only detects the 14.0 kb fragment of the NEO-targeted allele. E) PCR analysis of a typical litter, showing the bands obtained after amplification of wildtype (250 bp) and knockout (500 bp) alleles. F) *Kif1b* heterozygous animals display an approximately 50% reduction of *Kif1b* expression, as determined using Western blot. There is no decrease in expression of KIF5C or the dynein complex component IC74. G) *Kif1b* litters were born according to a non-Mendelian ratio, with complete absence of *Kif1b* homozygous knockouts. *Kif1b* heterozygous animals were born in numbers slightly but not significantly lower than expected (P = 0.16, Fishers exact test) H) Before the onset of EAE, there was no significant difference in weight or rotarod performance between *Kif1b* heterozygotes and wildtype littermates

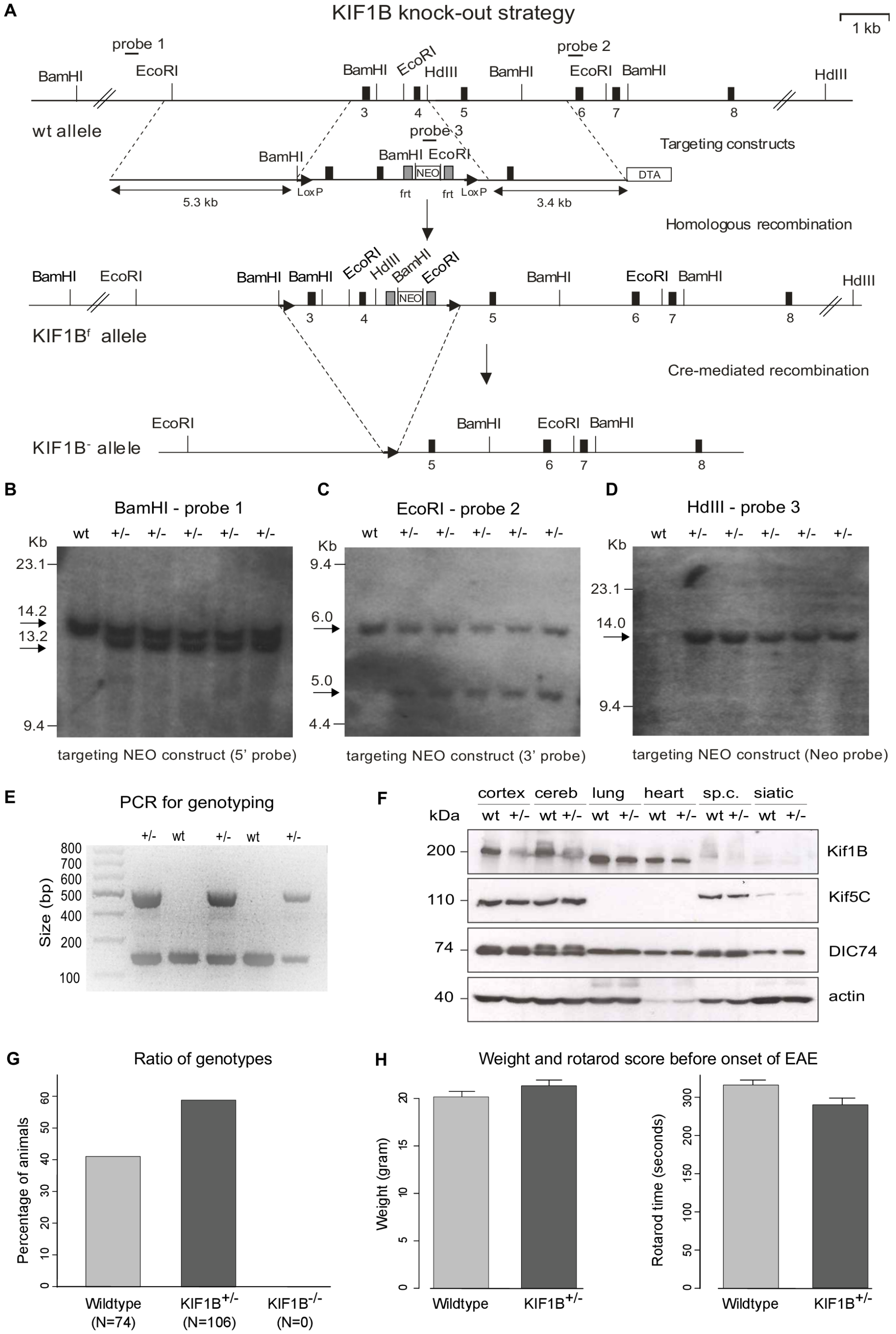
A
KIF1B knock-out strategy
1 kb
probe 1
probe 2
BamHI
EcoRI
BamHI
EcoRI
HdIII
BamHI
EcoRI
BamHI
HdIII
3
4
5
6
7
8
wt allele
probe 3
Targeting constructs
BamHI
BamHI EcoRI
NEO
DTA
5.3 kb
LoxP
frt
frt
LoxP
3.4 kb
Homologous recombination
BamHI
EcoRI
BamHI
BamHI
EcoRI
HdIII
BamHI
EcoRI
BamHI
EcoRI
BamHI
HdIII
NEO
3
4
5
6
7
8
KIF1B^f allele
Cre-mediated recombination
EcoRI
BamHI
EcoRI
BamHI
5
6
7
8
KIF1B$^-$ allele
B
BamHI - probe 1
Kb
wt +/- +/- +/- +/- +/-
23.1
14.2
13.2
9.4
targeting NEO construct (5' probe)
C
EcoRI - probe 2
Kb
wt +/- +/- +/- +/- +/-
9.4
6.0
5.0
4.4
targeting NEO construct (3' probe)
D
HdIII - probe 3
Kb
wt +/- +/- +/- +/- +/-
23.1
14.0
9.4
targeting NEO construct (Neo probe)
E
PCR for genotyping
+/- wt +/- wt +/-
Size (bp)
800
700
600
500
400
200
100
F
cortex cereb lung heart sp.c. siatic
kDa
wt +/- wt +/- wt +/- wt +/- wt +/- wt +/-
200
110
74
40
Kif1B
Kif5C
DIC74
actin
G
Ratio of genotypes
Percentage of animals
0
10
20
30
40
50
60
Wildtype (N=74)
KIF1B$^{+/-}$ (N=106)
KIF1B$^{-/-}$ (N=0)
H
Weight and rotarod score before onset of EAE
Weight (gram)
0
5
10
15
20
Wildtype
KIF1B$^{+/-}$
Rotarod time (seconds)
0
50
100
150
200
300
Wildtype
KIF1B$^{+/-}$

Experimental setup and baseline measurements for studying EAE in the mouse

EAE was induced in 46 twelve-week-old animals, 30 *Kif1b* heterozygous knock-outs (17 females, 13 males) and 16 wildtype littermates (11 females, 5 males) (Figure 5.2B). To induce EAE, mice were injected with synthetic MOG$_{35-55}$ peptide emulsified in complete Freund's adjuvant (CFA), a strong water-in-oil adjuvant emulsion containing heat-inactivated *M. tuberculosis* required to break immune tolerance of T and B lymphocytes to MOG as a self-antigen. A classic arbitrary clinical score was used to determine the severity of symptoms, ranging from 0 (no disease) to 5 (moribund), as described previously (Huizinga et al., 2012). Animals were given a tail code and wildtype and heterozygous animals were placed together in cages for observers blinded to animal identity. To more accurately and objectively estimate neuronal damage in these animals, we subjected them daily to the rotarod test (Jones and Roberts, 1968), a motor performance test in which the animals walk on a slowly accelerating rotating rod. The time the animals are able to maintain their balance is recorded as outcome parameter. During the first week of the experiment, before the onset of symptoms, animals were trained daily on the rotarod, both to avoid the superimposition of a learning curve on EAE symptoms, and to compare wildtype and heterozygous baseline performance.

Clinical parameters of EAE in heterozygous ***Kif1b*** deficient mice

Eight days after induction of EAE the first animals developed symptoms according to clinical score, followed by a decrease in rotarod performance from day 10 onward. The day of onset of symptoms did not differ significantly between $\mathit{Kif1b}^{+/-}$ animals and wildtype littermates (Figure 5.2C-D). Two weeks after induction, most animals reached their maximum clinical score and were no longer able to maintain their balance on the rotarod for longer than 30 seconds. After three weeks, the majority of the animals started to recover (Figure 5.2C-D). During the entire experiment, all animals kept gaining weight apart from some small decreases shortly after disease induction. A notable exception was a single heterozygous animal that reached clinical score 4.5 and kept losing weight. This animal was euthanized on day 19 according to the ethical guidelines of our institute (Figure 5.2E).

Based on the maximum clinical score reached during EAE, we could distinguish two separate populations, each comprising exactly half our population. One group of 23 animals developed no or only mild symptoms (score below 1.5 or lower), while the other group also containing 23 animals developed more severe symptoms and reached scores up to 4 (Figure 5.2F-G). The maximum clinical score achieved during EAE did not differ significantly between wildtype animals and $\mathit{Kif1b}^{+/-}$ littermates (Figure 5.2F-G). The course of EAE, as summarized by mean clinical score and mean rotarod performance per day, did not differ significantly between wildtype and knockout animals (Figure 5.2H, K). Since analysing the mean of a clinical score with non-equal intervals can lead to artefacts (Fleming et al., 2005), we also converted the clinical score and rotarod performance into a categorical variable. Animals with a clinical score of 0 or a rotarod performance of >280 seconds were labeled as 'asymptomatic', while animals with a clinical score over 2.5 or a rotarod performance <100 seconds were classified as 'severe EAE'. Analysing the fraction of the population with either classification did not identify significant differences between wildtype and *Kif1b*$^{+/-}$ animals (Figure 5.2I-J, L-M).

Pathological parameters EAE in heterozygous *Kif1b* deficient mice

After 28 days, animals were euthanized and their spinal cord removed. After embedding in paraffin, 5 µm thick slices were cut and stained according to Klüver and Barrera (Klüver and Barrera, 1953). Using this staining, lesions can be identified by loss of myelin and leukocyte infiltration of the white matter (Figure 5.3E-F). The spinal cords of animals with a high clinical score and a reduced rotarod performance showed a high number of pathological lesions, covering large areas of the white matter (Figure 5.3A-D). To more precisely determine the location and size of the lesions in the spinal cord of wildtype and *Kif1b*$^{+/-}$ mice, we systematically analyzed all microscopy pictures, using segmentation to separate the images into white and grey matter and registering the contours against an anatomical atlas to determine the approximate position within the spinal cord.

In this quantitative procedure, the position of each slice within the spinal cord was determined by observing its position within the block and matching each image to a labeled series of the spinal cord from (Watson et al., 2009). Images were manually converted to a set of coordinates of the circumference of the white matter, grey matter and lesions. Using these coordinates and the position of each slice within the spinal cord, a table was created containing for each lesion the corresponding segment, area in absolute units and as percentage of the white matter, and the anatomical systems involved (Figure 5.3G). We observed that the amount of damage to the spinal cord was highly variable within each individual animal, depending on the position in the spinal cord. In extreme cases, animals showed no damage at all over several segments of the spinal cord, with up to 45% of the white matter affected at a different level (data not shown). The percentage of white matter surface area containing lesions did not differ significantly between *Kif1b*$^{+/-}$ and wildtype mice (Figure 5.3H).

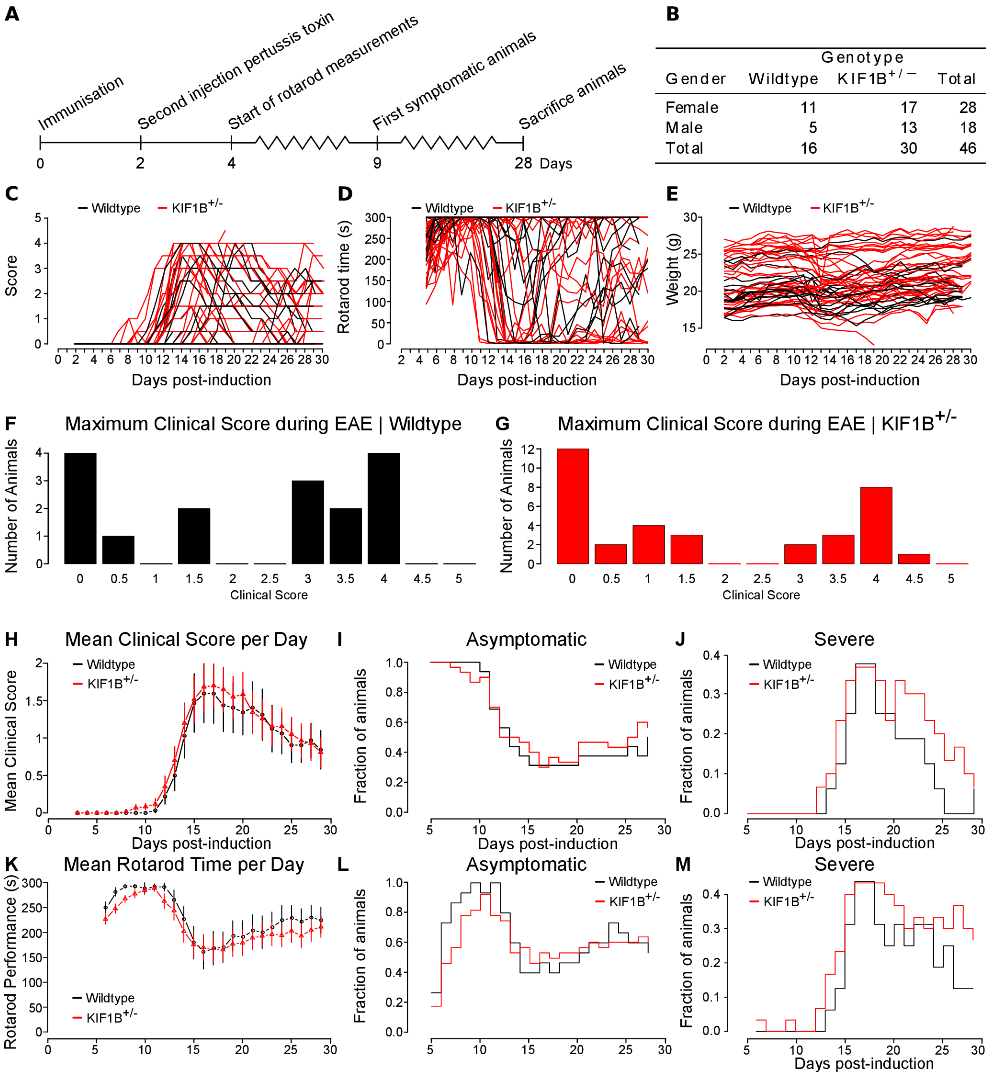

	Genotype		
Gender	Wildtype	KIF1B$^{+/-}$	Total
Female	11	17	28
Male	5	13	18
Total	16	30	46

Figure 5.2: Course of EAE according to clinical score and rotarod A) Time course experiment. B) Number of animals used in EAE experiment by and genotype. C-E) Observed clinical score (C) rotarod performance (D) and weight (E) for *Kif1b*$^{+/-}$ and wildtype animals over time. F-G Maximum clinical score recorded during EAE for each individual animal in wildtype (F) and *Kif1b*$^{+/-}$ cohort (G). H) Mean clinical score over time. I-J) Animals were considered asymptomatic if their clinical score was 0 and classified as severe EAE if their clinical score exceeded 2.5. At every time point, the fraction of animals falling into either of these categories was determined for both wildtype and *Kif1b*$^{+/-}$ animals. K) The same approach was used with regard to the rotarod performance, where the mean performance per day was calculated, but also again animals were classified as asymptomatic (rotarod time >280 seconds, L) or severe EAE (rotarod time <100 seconds, M) Error bars in panels H and K indicate standard error of the mean.

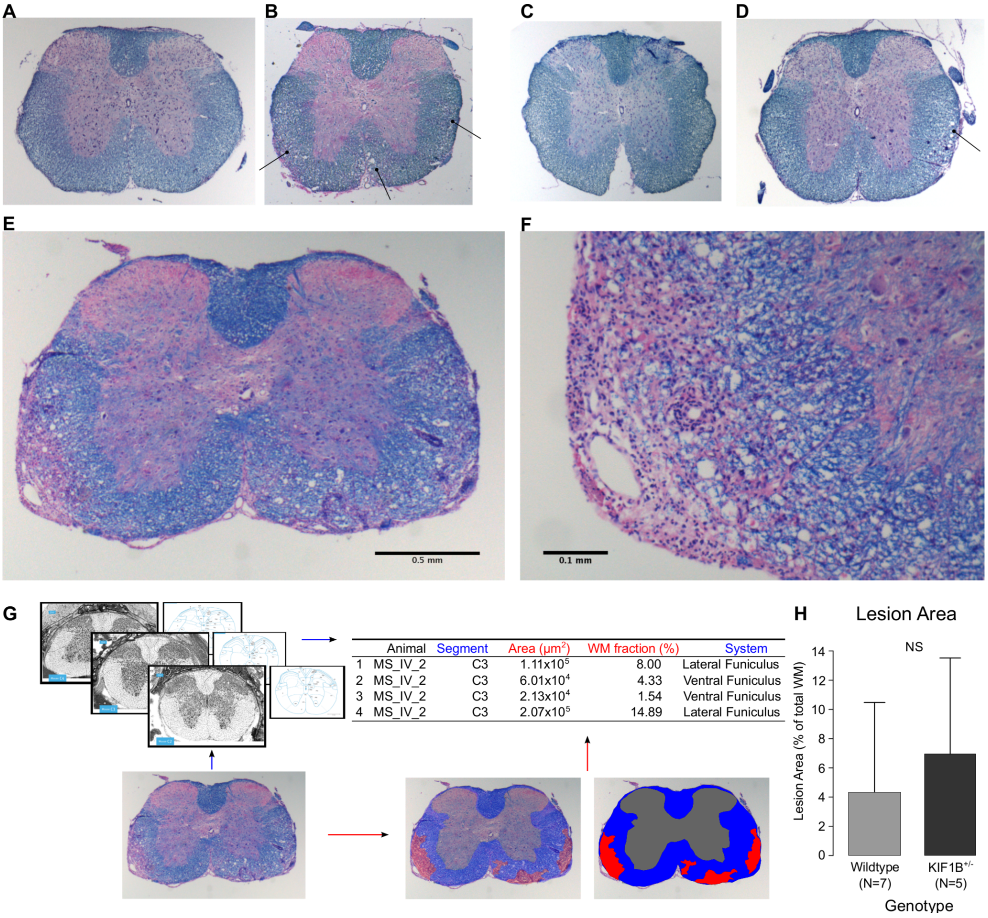

	Animal	Segment	Area (μm²)	WM fraction (%)	System
1	MS_IV_2	C3	1.11×10^5	8.00	Lateral Funiculus
2	MS_IV_2	C3	6.01×10^4	4.33	Ventral Funiculus
3	MS_IV_2	C3	2.13×10^4	1.54	Ventral Funiculus
4	MS_IV_2	C3	2.07×10^5	14.89	Lateral Funiculus

Figure 5.3: Spinal cord pathology in wildtype and *Kif1b*$^{+/-}$ animals. A-D) Animals were sacrificed 28 days after immunization, after which the spinal cord was extracted, embedded in paraffin and cut in 5 μm thick slices. Spinal cord damage was assessed by Klüver-Barrera staining, in which lesions could be identified by loss of myelin staining and increased cell numbers. Examples are shown of the thoracic spinal cords of wildtype (A-B) and *Kif1b*$^{+/-}$ animals (C-D) with either very mild symptoms (A, C) or severe symptoms (B, D) as determined by clinical score. EAE lesions are denoted by the arrows. E) Fragment of the cervical spinal cord of a *Kif1b*$^{+/-}$ animal showing multiple demyelinated lesions. F) Detail of panel E showing the demyelination and cellular infiltrates in more detail. G) Workflow of analysis. All slices were matched to a mouse spinal cord atlas (from (Watson et al., 2009)) to confirm the corresponding spinal cord segment as estimated by their position in the paraffin block. The outline of the white matter, grey matter and any lesions present in the slice were traced, after which for each segment the area affected by lesions as a percentage of the total white matter could be calculated. H) The percentage of white matter surface area affected by lesions did not differ significantly between wildtype and KIF1B heterozygotes.

Discussion

This study assessed the relevance of *Kif1b*-based mechanisms to the neurological and pathological signs in an MS animal model. We demonstrate that heterozygous *Kif1b* deficient mice do not show significant differences in disease according to rotarod performance, clinical score and neuropathology upon EAE induction. These data indicate that twofold reduced *Kif1b* expression does not contribute to disease in at least one very frequently used mouse model for autoimmune inflammatory demyelinating disease.

The role of *Kif1b* in MS

Identification of *Kif1b* as a protein involved in disease comes from studies of neural crest-derived tumors such as neuroblastomas and medulloblastomas (Nagai et al., 2000; Ohira et al., 2000), where it acts as an apoptosis inducer and potential tumor suppressor (Munirajan et al., 2008; Schlisio et al., 2008; Yeh et al., 2008). Interest in *Kif1b* as a disease protein intensified with its identification as a potentially causative gene in one family with Charcot-Marie-Tooth disease type 2A (CMT2A), a progressive peripheral neuropathy. A heterozygous *Kif1b* knockout mouse was generated which at the age of twelve months developed progressive muscle weakness similar to the peripheral neuropathy seen in humans (Zhao et al., 2001). However, follow-up studies were not able to confirm the *Kif1b* gene association with CMT2A, and instead found mutations in the mitofusin 2 gene, involved in mitochondrial fusion and just like *Kif1b* located on chromosome 1, only 1.6 Mb apart (Bissar-Tadmouri et al., 2004; Zuchner et al., 2004; Kijima et al., 2005). A large number of genes have been linked to CMT2A, many of which are related to intracellular transport pathways, suggesting a potential role for impaired transport in its pathogenesis (Gentil and Cooper, 2012). This interpretation is further supported by the finding that a pharmacological increase of microtubule acetylation rescues the transport defect in a mouse model of CMT and even increases motor performance (d'Ydewalle et al., 2011).

Kif1b was first linked to MS susceptibility when a GWA study in a genetically isolated Dutch population with multiplex MS families reported an increased susceptibility associated with an intronic SNP in the *Kif1b* gene, named rs10492972*C (Aulchenko et al., 2008). This finding pointed to a possible role for intracellular transport in MS, supporting the hypothesis that MS is not a purely autoimmune disease as previously thought, but rather a neurodegenerative disorder with a secondary immune component (Stys et al., 2012). However, this SNP association could not be reproduced in other populations (International Multiple Sclerosis Genetics Consortium (IMSGC), 2010; Martinelli-Boneschi et al., 2010; Koutsis et al., 2011), leading to the conclusion that rs10492972*C in *Kif1b* does not lead to an increased susceptibility to MS as a general rule (Pierre-Antoine, 2011). It has been proposed that these discrepant findings could at least partially be explained by a founder effect in the inbred Dutch cohort, leading to differences in allele frequency (Hintzen et al., 2010). Although the contribution of *Kif1b* to MS is as of yet uncertain, there is substantial evidence for a role of intracellular transport in MS pathogenesis. SNPs in other kinesin motors such as *Kif21b* (Goris et al., 2010; International Multiple Sclerosis Genetics Consortium (IMSGC), 2010) and KIF5A (Alcina et al., 2013) are associated with MS and the expression of motor proteins in non-lesional grey matter of MS patients is reduced (Hares et al., 2013). Furthermore, analysis of autopsy tissue from MS patients shows an increase in mitochondrial mass in chronic MS lesions (Mahad et al., 2009), consistent with a reduction in intracellular transport and sequential accumulation of mitochondria.

Functional redundancy within the kinesin family

Defects in axonal transport have been linked to a large variety of neurodegenerative disorders (De Vos et al., 2008; Millecamps, 2013). Alterations in the transport machinery can leave the axon more vulnerable to additional damage, for example mediated by cytokines (De Vos et al., 2000) or through glutamate toxicity (Ackerley et al., 2000), a process considered to play an important role in axonal loss in MS (Trapp and Stys, 2009). In this study we demonstrate that a twofold reduced *Kif1b* expression does not contribute to disease progression in a demyelinating animal model of MS. This result could be explained by the complexity of the transport system and the redundancy of its components.

Kif1b was first described as a motor protein involved in axonal transport of mitochondria (Nangaku et al., 1994). Subsequent studies found that the *Kif1b* gene generates two major isoforms (Gong et al., 1999), which can interact with several different cargos, including postsynaptic proteins such as PSD-95 (Mok et al., 2002) and Rab3 labeled synaptic vesicle precursors (Norihiro et al., 2002), lysosomes (Masafumi et al., 2009) and RNA transport granules (Lyons et al., 2009). Currently, 45 kinesin superfamily genes have been identified, classified into 15 families. Since most genes generate more than one isoform, approximately 90 kinesin motor proteins are estimated to exist, many of which are capable of transporting the same cargo (Hirokawa et al., 2009). For instance, both *Kif1b* (kinesin 3 family) and *Kif5b* (kinesin 1 family) transport mitochondria (Tanaka et al., 1998) and both *Kif1b* and *Kif1a* transport synaptic vesicle precursors (Niwa et al., 2008). It is very likely that in the heterozygous *Kif1b* mice other kinesin family members can compensate for the reduction in *Kif1b* transport. Cell-specific homozygous deletion of *Kif1b* will lead to a better understanding of the role of *Kif1b* mediated cargo transport. Future studies should systematically subject cell type-specific, both neuronal and oligodendroglial homozygous *Kif1b* knockouts to acute and chronic forms of EAE, using classic induced and novel spontaneous models (Wekerle et al., 2012), which will provide additional information on the role of *Kif1b* in MS.

Materials and Methods

Ethics Statement

All animal experiments were performed in compliance with the guidelines for the welfare of experimental animals issued by the Government of The Netherlands. All animal experiments were approved by the Animal Ethical Review Committee (DEC) and were performed in the animal facilities of the Erasmus Medical Centre.

Generation of *Kif1b* knock-out mice

Taconic Biosciences (Hudson, NY, USA) created the *Kif1b* knockout mouse by targeted gene disruption of *Kif1b* gene in embryonic stem (ES) cells. Targeting techniques and the procedures for selection of ES cells and generation of KO mice have been described (Hoogenraad et al., 2002). Exons 3 and 4 of the *Kif1b* gene, which encode part of the motor domain of the *Kif1b* protein, were selected as conditional knockout regions since their deletion leads to a frame shift, and a premature translation stop of the *Kif1b* transcript. The first loxP sequence was inserted into intron 2, and a neomycin selection cassette surrounded by frt sites and followed by a loxP sequence was inserted into intron 4 of the *Kif1b* gene. The neomycin targeting construct was introduced in ES cells by homologous recombination. Two plates of G418 resistant ES clones (∼192) were selected for screening and five potential targeted clones were identified (2.6% targeting efficiency). The homologous recombination strategy was validated by Southern analysis. Two positive ES cell clone were injected into blastocysts and the chimeras that gave germ line transmission were mated into the C57BL/6 background to generate inbred $\mathit{Kif1b}^{+/f}$ (targeted) mice. Heterozygous *Kif1b* knockout ($\mathit{Kif1b}^{+/-}$) mice were obtained by crossing F1 heterozygous $\mathit{Kif1b}^{+/f}$ mice with CAG-Cre transgenic mice that express Cre recombinase in the germ-cell lineage (kindly provided by Frank Grosveld, Erasmus MC, university Medical Centre Rotterdam). Two PCR assays were designed for genotyping: the targeted allele assay amplifies the wildtype and targeted allele from WT and heterozygous $\mathit{Kif1b}^{+/f}$ mice (using primers *Kif1b*LoxP-forward and *Kif1b*LoxP-reverse); and the knockout allele assay amplifies the wildtype, targeted and knocked out allele from WT and heterozygous $\mathit{Kif1b}^{+/-}$ mice (using the same primers as the previous assay with the addition of primer *Kif1b*ko). The following PCR primers were used (as indicated in Figure 5.1A).

*Kif1b*LoxP-forward	5'-GGATTTTAGAAACCCAAACTTGGCTATG-3'
*Kif1b*LoxP-reverse	5'-CTCATCTGGGTGTTACCAGTATTCAGC-3'
*Kif1b*ko	5'-GAATATAAGGTGTGGAGCTCAGTTGGTAAA-3'

PCR protocol - The PCR was performed in a 20 µL volume, using 0.5 µL of genomic DNA in 10× PCR buffer, 50 mM $MgCl_2$, 10 mM dNTP, 2% formamide, 50% glycerol, GoTaq polymerase and dH_2O. A complex temperature profile was adopted to ensure maximum specificity in the early rounds of amplification. An initial DNA denaturation for 2 minutes at 94 °C was followed by 10 cycles at 98 °C for 10 seconds, 72 °C for 15 seconds, with temperature for this step decreasing by 1 °C every cycle, followed by 72 °C for 1 minute and another 25 cycles at 98 °C for 10 seconds, 62 °C for 15 seconds and 1 minute at 72 °C, finally a 10 minutes extension at 72 °C.

For tissue Western blots, cortex, cerebellum, spinal cord, sciatic nerve, heart and lung were dissected from a wildtype or heterozygous female adult mouse from the same litter. Tissue from lung and heart was copped in ice cold modified Ripa buffer supplemented with protease inhibitor, followed by sonification. Neuronal tissue was homogenized in ice cold modified Ripa buffer supplemented with protease inhibitor using a micro pestle and incubated on a rotator for one hour. All samples were snap-frozen and spinned down for 30 minutes. From the supernatant protein-lysate 10 µg was loaded on an 8% SDS-page gel and afterwards transferred to a nitrocellulose membrane. Membranes were blocked in 4% BSA/0.5% fat-free milk for one hour and incubated overnight with the indicated antibodies in the blocking solution. Antibodies: KIF1B (Bethyl Laboratories, Montgomery, TX, USA; 1:400), KIF5C (Abcam, Cambridge, UK; 1:1000), IC74 (Millipore, Billerica, MA, USA; 1:1000) and Actin (Millipore, Billerica, MA, USA; 1:10.000).

EAE induction and assessment

Animals were housed in specified pathogen-free conditions. The mice were 12 weeks old at the start of the experiment. EAE was induced by subcutaneous immunization at 4 sites in the flanks with 200 µg $\text{MOG}_{35\text{-}55}$ peptide in total, emulsified in CFA (Difco/Voigt, Lawrence, KS, USA) on day 0 as described previously (Stromnes and Goverman, 2006). 500 µg heat-killed *Mycobacterium tuberculosis* H37RA (Difco/Voigt, Lawrence, KS, USA) was added per 100 µL CFA to evoke a better immune response and more extensive neuropathology. At day 0 and 2 mice were injected i.p. with 150 ng pertussis toxin (PTX). After EAE induction, mice were monitored daily, and weight and clinical status were recorded. Clinical signs of EAE were graded daily on a scale of 0 to 5: 0, no signs; 0.5, tail paresis; 1, tail paralysis; 1.5, paraparesis without tail paralysis; 2, paraparesis; 2.5, partial paralysis; 3 complete paralysis; 3.5, paraplegia; 4, quadriplegia; 5, death. If an animal experienced a score higher than 2, gel packs and soft food pellets were provided. In addition, from day 6 onwards motor performance was tested daily using a rotarod device. On day 28, animals were humanely euthanized and perfused with 4% paraformaldehyde.

Rotarod test

Animals were trained to walk on the accelerating rotarod (Ugo Basile 47600, Milan, Italy). The rotarod consists of a cylinder with a diameter of 3 cm on which 5 animals can run simultaneously, separated by panels of sufficient size to prevent the animals from detecting each other visually. The speed of the rod was linearly increased from 4 rpm to 40 rpm during 300 seconds, after which the animals were returned to their cages. When the animal was not capable of maintaining its balance and fell of the device, it triggered a sensor and the time was recorded. The first week of the experiment, before the onset of symptoms, was used to train the animals in the use of the device and to obtain baseline values. Animals were subjected to the rotarod on a daily basis, unless they were unable to move due to paralysis of the limbs (EAE score higher than 3), in which case their latency time was recorded as 1 second.

Histology

After perfusion with 4% paraformaldehyde, the brain and spinal cord were extracted and embedded in paraffin using an automated Microm HMP110 paraffin tissue processor. Paraffin material was cut into 5 µm thick coronal (brain) or transverse (spinal cord) sections. Prior to staining, sections were deparaffinised in xylene and rehydrated in ethanol of decreasing percentage (from 100% to 70%) followed by rinsing with distilled water. Histochemical staining was performed according to Klüver-Barrera (Klüver and Barrera, 1953). In short, sections were stained overnight with Luxol Fast Blue solution (Sigma-Aldrich) at 60 °C and rinsed in 95% ethanol and distilled water. To wash away non-specific labelling, sections were rinsed with a 0.05% lithium carbonate solution (Sigma-Aldrich) and washed with 70% ethanol. Sections were then stained with a 0.5% Eosin-Y solution (Sigma-Aldrich), washed with distilled water and stained with a 0.25% Chresyl Echt Violet solution (Chresyl violet acetate, Sigma-Aldrich). After these stainings, slides are rinsed with distilled water, dehydrated using an ethanol series with increasing percentage (80% - 100%), followed by two washes with xylene.

Computational analysis of spinal cord sections

Slices were imaged on a Zeiss Axioskop upright microscope with 2.5x and 10x objectives. Processing was performed using the tools available in the open source image analysis package FIJI (Schindelin et al., 2012). All images were aligned to a line from the gracile fasciculus through the central canal to the ventral fasciculus with the dorsal side facing up. The contours of the white matter, the grey matter and any lesions present in the slice were manually tracked using the multi-point selection tool, resulting in a table of coordinates. These coordinates were loaded by a custom script written in R (R Core Team, 2014) and converted into areas of which both the absolute surface and for each lesion its area relative to the white matter was calculated. All images from a single animal were aligned according to their position in the paraffin block and matched by eye with the corresponding element from the reference series to determine the spinal cord segment.

Competing Interests The authors have declared that no competing interests exist.

Author Contributions Conceived and designed the experiments: RvdB, MvM, JDL, RQH and CCH. Performed the experiments: RvdB, MvM and LW. Analysed the data: RvdB. Contributed reagents/materials/analysis tools: MvM and JDL. Wrote the paper: RvdB and CCH, contributed to revisions: RQH and JDL.

Funding This work was supported by the Netherlands Organization for Health Research and Development (ZonMW-TOP, C.C.H.) and the Dutch MS Research Foundation (research grant to C.C.H and R.Q.H., and program grant to R.Q.H. and J.D.L.). The funders had no role in study design, data collection and analysis, decision to publish, or preparation of the manuscript.

Translational Impact

Clinical Issue Multiple sclerosis is a chronic demyelinating disease of the central nervous system. It is estimated that more than 2 million people worldwide are affected by MS, with the disease onset typically at a relatively young age of around 30 years. Although MS can be progressive from the start, in most patients the first phase of the disease is characterised by periods of disability, followed by (partial) recovery. Over a time period of two to three decades after diagnosis, almost all patients develop severe persistent disability. Although immune modulating drugs are able to decrease the frequency of attacks, there are no treatments available to slow progression or cure this disease. In recent years, more and more research has focused on the neurodegenerative components of MS, raising the hope that insight into the loss of axons and neurons during the disease could lead to new therapeutic approaches.

Results Several genes related to transport of cellular components in neurons have been linked to MS using gene-wide association studies. One of these genes is *Kif1b*, a member of the kinesin family of motor proteins. A knockout mouse for this gene was generated and subjected to experimental autoimmune encephalomyelitis (EAE), a model system for MS. These animals did not show any differences in disease course or amount of damage received compared to wildtype littermates.

Implications These findings illustrate the difficulties encountered when translating findings in genomics to molecular mechanisms. The heterozygous loss of one specific motor protein is not sufficient to influence disease severity in this model for MS.

Assessment of neurodegeneration in EAE

Published as:
Van den Berg R, Laman JD, Van Meurs M, Hintzen RQ, Hoogenraad CC;
Rotarod motor performance and advanced spinal cord lesion image
analysis refine assessment of neurodegeneration in experimental
autoimmune encephalomyelitis; J Neuroscience Methods 2016

6

ROTAROD MOTOR PERFORMANCE AND ADVANCED SPINAL CORD LESION IMAGE ANALYSIS REFINE ASSESSMENT OF NEURODEGENERATION IN EXPERIMENTAL AUTOIMMUNE ENCEPHALOMYELITIS

Background. Experimental autoimmune encephalomyelitis (EAE) is a commonly used experimental model for multiple sclerosis (MS). Experience with this model mainly comes from the field of immunology, while data on its use in studying the neurodegenerative aspects of MS is scarce. *New Method.* The aim of this study is to improve and refine methods to assess neurodegeneration and function in EAE. Using the rotarod, a tool used in neuroscience to monitor motor performance, we evaluated the correlation between motor performance, disease severity as measured using a clinical scale and area covered by inflammatory lesions. *Results.* The included parameters are highly correlated in a non-linear manner, with motor performance rapidly decreasing in the intermediate values of the clinical scale. The relation between motor performance and histopathological damage is exclusively determined by lesions in the ventral and lateral columns, based on a new method of analysis of the entire spinal cord. Using a set of definitions for distinct disease milestones, we quantified disease duration as well as severity. *Comparison with Existing Methods.* The rotarod measures motor performance in a more objective and quantitative manner compared to using a clinical score. The outcome shows a strong correlation to the surface area of inflammatory lesions in the motor systems of the spinal cord. *Conclusions.* These results provide an improved workflow for interpreting the outcome of EAE from a neurological point of view, with the eventual goal of dissecting neurodegeneration and evaluating neuroprotective drugs in EAE for application in MS.

Introduction

Multiple sclerosis (MS) is the most common cause of neurological disability in young people. It affects 0.1-0.2% of the population with onset of disease at a mean age of 28 years Goodin (2014). As of yet, no curative treatment has been developed, despite very good progress in reduction of the inflammatory component, mostly by biological anti-inflammatory drugs (Ransohoff et al., 2015). MS is a complex disease entity, with characteristics of both an immunological and a neurodegenerative disorder (Stys et al., 2012). Research into the causes of MS is difficult, partially because a large discrepancy exists between biological and clinical onset with patients developing symptoms after years of subclinical disease. As more time passes, epidemiological or histological traces of any causative factor will be harder to detect. Also, the processes leading to disability in MS occur in the brain and spinal cord, areas of the central nervous system (CNS) that are hard to probe or study at the microscopic level from the outside. The majority of MS patients are initially diagnosed with relapsing-remitting MS, a form of the disease in which short periods of attacks are followed by timeframes in which disease activity is nearly absent. Although almost all individuals eventually show progression to a continuously active form of the disease as damage accumulates (Ebers, 2001; Tremlett et al., 2008). The variation seen in MS patients supports the growing conviction that MS should be considered a collection of several disorders with different causes and pathways involved, but with a relatively similar set of symptoms as result (Lassmann, 2005).

All these challenges stress the importance of an accurate experimental model for MS. Ever since it was first described in the 1920s, as a chance finding during vaccination trials (Koritschoner and Schweinburg, 1925), Experimental Autoimmune Encephalomyelitis (EAE) has been the most widely used model system for MS (Mix et al., 2010; Baker and Amor, 2015). In EAE animals are inoculated with myelin components, triggering an immune response against the injected compound which also targets the native myelin sheath. The resulting disease depends on the species and strain of animals selected, as well as the molecule or cell used to evoke an immune response and any adjuvants used to stimulate cell-mediated immunity (Ralf et al., 2006). Although EAE has greatly contributed to our understanding of MS (Baxter, 2007; Steinman and Zamvil, 2006), several disadvantages limit its use (Steinman and Zamvil, 2005; Ransohoff, 2012). The first and foremost of these is that in many protocols, EAE is an inflammatory disease of the CNS, only partially mimicking the neurodegenerative process seen in MS (Sriram and Steiner, 2005). Another concern involves the type of immune response, which in rodent EAE is mainly CD4$^+$ T-cell mediated, while active MS lesions in human patients tend to show a higher involvement of CD8$^+$ cells (Friese and Fugger, 2009; 't Hart et al., 2011).

EAE is not a trivial experimental procedure, and the consistency of measurements can vary depending on the experience of the person who implements the complex protocol(Stromnes and Goverman, 2006). Even seemingly minor decisions -such as the adjuvant used for immunization (Smith et al., 2011)and the dose and timing of pertussis toxin- will influence the disease course. Similar attention should be paid to the acquisition and analysis of results (Baker et al., 2011). It is common for EAE experiments to measure disease severity using a clinical score running from 0 to 5, with 0 indicating no symptoms and 5 death (e.g. (Kassiotis et al., 1999). This scale is observer-dependent, non-linear and produces a categorical variable, implying that any statistical analysis involving a mean score has to be interpreted with caution (Baker et al., 2014). Two animals with a mean score of 2.5 can both be moderately sick or one animal is dead while the other shows no symptoms. Representing the results of an EAE experiment accurately requires a thorough statistical analysis(Fleming et al., 2005). Failure to take the proper precautions may contribute to publication bias (Tsilidis et al., 2013).

In the field of neuroscience, it has been common for several decades to measure motor performance of rodents using a rotarod, a bar rotating at a slowly increasing speed. The animal is forced to increase its walking speed to keep up with the bar, until it can no longer maintain its balance and drops on a switch, connected to a clock. The latency time to fall can then be used as an objective and non-invasive measurement of motor performance(Jones and Roberts, 1968). As common as this method is in neuroscience, relatively few studies have explored its application in EAE ((Jones et al., 2008; Al-Izki et al., 2012; Moore et al., 2014)). In this paper, we demonstrate the use of a rotarod to evaluate the results of EAE induction in mice. We compare the rotarod measurements to a clinical score as well as to the number of inflammatory lesions found in the spinal cord of these animals. Using a set of definitions for crucial disease events based on clinical score and rotarod, we also provide a quantification of EAE disease course over time. The clinical impact of any CNS lesion is determined by its location as well as its size, where a minor lesion in a critical system can lead to severe clinical disability. Furthermore, we develop a novel image analysis approach in which for each spinal cord lesion the information on anatomical context is preserved, allowing for a better understanding of the three-dimensional distribution of inflammatory lesions and their relation to clinically observed disease severity.

Materials and Methods

Ethics Statement

All animal experiments were performed in compliance with the guidelines for the welfare of experimental animals issued by the Government of The Netherlands. All animal experiments were approved by the Animal Ethical Review Committee (DEC) of the Erasmus Medical Centre under protocol number 128-12-01. All experiments were performed in the animal facilities of the Erasmus Medical Centre.

EAE induction and assessment

C57BL/6Tac animals were originally obtained from Xenogen Biosciences (currently: Taconic Farms, Inc. NJ, USA). At the start of experiments, the strain had been in our facility for four generations. Animals were housed in specified pathogen-free conditions.

Both male and female animals were used for the experiments. The mice were 12 weeks old at the start of the experiment, all animals were born within 3 days of each other. EAE was induced by subcutaneous immunisation at 4 sites in the flanks with 200 μg MOG$_{35-55}$ peptide in total, emulsified in CFA (Difco/Voigt, Lawrence, KS, USA) on day 0 as described previously (Stromnes and Goverman, 2006). 500 μg heat-killed *Mycobacterium tuberculosis* H37RA (Difco/Voigt, Lawrence, KS, USA) was added per 100 μl CFA to evoke a better immune response and more extensive neuropathology. At day 0 and 2 mice were injected i.p. with 150 ng pertussis toxin (PTX, Sigma-Aldrich, MO, USA). After EAE induction, mice were monitored daily, and weight and clinical status were recorded. A clinical score was used as defined in table 6.1. If an animal was scored higher than 2, gel packs and soft food pellets were provided. In addition, from day 6 onward motor performance was tested daily using a rotarod device. On day 28, animals were humanely euthanized and perfused with 4% paraformaldehyde.

Score	Symptoms
0.0	None
0.5	Weakness of the tail.
1.0	Paralysis of the tail without weakness of the limbs.
1.5	Weakness of the limbs without paralysis of the tail.
2.0	Weakness of the limbs with weakness or paralysis of the tail.
2.5	Complete paralysis of one of the hind limbs, or weakness of three or four limbs while retaining the ability to walk.
3.0	Complete paralysis of front or hind limbs, or weakness of three or four limbs with the loss of walking ability.
3.5	Complete paralysis of the hind body, animal cannot turn its body.
4.0	Complete paralysis of front and hind body.
4.5	Complete paralysis with inability to eat and drink.
5.0	Death due to experiment.

Table 6.1: Scale for Clinical Score. During this experiment, all animals with a score higher than 2.0 were provided with gel packs and soft food pellets. If an animal reached a score of 4.5, it was euthanized. Scores of 4 and above are rare, only animal reached 4.5 and was euthanized.

Rotarod test

Animals were trained to walk on the accelerating rotarod (Ugo Basile 47600, Milan, Italy). The rotarod consists of a cylinder with a diameter of 3 cm on which 5 animals can run simultaneously, separated by panels of sufficient size to prevent the animals from detecting each other visually. The speed of the rod was linearly increased from 4 rpm to 40 rpm during 300 seconds, after which the animals were returned to their cages. When the animal was not capable of maintaining its balance and fell of the device, it triggered a sensor and the time was recorded. The first week of the experiment, before the onset of symptoms, was used to train the animals in the use of the device and to obtain baseline values. Animals were subjected to the rotarod on a daily basis, unless they were unable to move due to paralysis of the limbs (EAE score higher than 3), in which case their latency time was recorded as 1 second.

Histology

After perfusion with 4% paraformaldehyde, the brain and spinal cord were extracted and embedded in paraffin using an automated Microm HMP110 paraffin tissue processor. Paraffin material was cut into 5 μm thick coronal (brain) or transverse (spinal cord) sections. Prior to staining, sections were deparaffinised in xylene and rehydrated in ethanol of decreasing percentage (from 100% to 70%) followed by rinsing with distilled water. Histochemical staining was performed according to Klüver-Barrera (Klüver and Barrera, 1953). In short, sections were stained overnight with Luxol Fast Blue solution (Sigma-Aldrich) at 60°and rinsed in 95% ethanol and distilled water. To wash away non-specific labelling, sections were rinsed with a 0.05% lithium carbonate solution (Sigma-Aldrich) and washed with 70% ethanol. Sections were then stained with a 0.5% Eosin-Y solution (Sigma-Aldrich), washed with distilled water and stained with a 0.25% Chresyl Echt Violet solution (Chresyl violet acetate, Sigma-Aldrich). After these stainings, slides are rinsed with distilled water, dehydrated using an ethanol series with increasing percentage (80% - 100%), followed by two washes with xylene.

Computational analysis of spinal cord sections

Slices were imaged on a Zeiss Axioskop upright microscope with 2.5x and 10x objectives. Processing was performed using the tools available in the open source image analysis package FIJI (Schindelin et al., 2012). All images were aligned to a line from the gracile fasciculus through the central canal to the ventral fasciculus with the dorsal side facing up. The contours of the white matter, the grey matter and any lesions present in the slice were manually tracked in FIJI using the multipoint selection tool, resulting in a table of coordinates. These coordinates were loaded by a custom script written in R (R Core Team, 2014) and converted into areas for which both the absolute surface and for each lesion its area relative to the white matter was calculated. All images from a single animal were aligned according to their position in the paraffin block and matched by eye with the corresponding element from the reference series to determine the spinal cord segment.

Statistical Analysis

All statistical analysis was performed in R (R Core Team, 2014). Variables following a normal distribution were compared using Welch two sample t-test. Count or proportional data, such as the disease categories and time points were compared using Fisher's exact test for count data. Linear correlations were tested using Pearson's product-moment correlation, except for the relation between initial weight and clinical score / rotarod performance (figure 6.4**D-E**), where a linear model was fit to the data predicting either maximal clinical score or minimal rotarod performance based on gender and weight. An analysis of variance (ANOVA) was then performed to determine the significance of the gender and weight terms. To determine the best description for the relation between clinical score and rotarod performance (figure 6.1**G**), a two-step approach was used. By eye, the shape of the curve suggested a logistic decay function. In the first round, a brute force algorithm (Grothendieck, 2013) was used to get an initial estimate of the fit parameters. In the second round, these estimated values were used as starting points for a nonlinear least-squares estimate of the optimal parameters. The optimal fit was achieved when assuming a limit of 286 seconds rotarod performance, an EC_{50} midway point at a clinical score of 1.79, and slope coefficients of -0.08 and -5.21.

Results

Clinical score and rotarod performance show excellent correlation in a non-linear fashion.

For the methodological purposes of this study and guided by the IACUC, a single large EAE experiment was designed using both male and female mice, with a modified induction protocol to enhance neurological damage. The same experiment was co-opted to assess whether knocking out the molecular motor protein Kif1b affected EAE (Van den Berg et al, manuscript in preparation). During the course of EAE, all animals were scored daily by the same individual. To avoid an observer-expectancy effect, a coding system was used to keep the observer unaware of animal identity and score of the previous day. A classic and validated clinical EAE scale from 0 to 5 was used, as described in table 6.1. At the same time each day, all animals were placed on the rotarod and latency time to fall was measured. Approximately 7 days after induction, the first animals started to develop symptoms (figure 6.1**A**). During the first few days, animals need to get used to the rotarod, leading to a predicted initial increase in performance. All animals reached maximum performance before onset of symptoms. Ten days after induction, an increase in clinical score is mirrored in a decrease in rotarod latency time. (figure 6.1**B**).

It should be noted that a significant fraction of the animals in which EAE had been induced did not develop symptoms. The choice of whether or not to include these animals in the analysis significantly influences the outcome of the experiment, as illustrated by the two curves in figures 6.1**A-B**. To circumvent this issue, the score and rotarod results for each day where converted to a categorical variable according to the criteria shown in table 6.2. The number of animals assigned to each category as a fraction of the total population can then be used as a more informative readout of disease severity compared to only mean values. Although the patterns for the categories 'asymptomatic' (figure 6.1**C**) and 'severe' (figure 6.1**E**) are quite similar when defined according to clinical score or rotarod performance, only a few animals are considered moderately sick according to rotarod performance (figure 6.1**D**). This becomes even more apparent when calculating the predictive value of clinical score for rotarod performance. When an animal is categorised as 'asymptomatic' according to the clinical score, there is a 0.95 probability it will be similarly categorised according to the rotarod performance. In contrast, if the clinical score of an animal results in a classification of moderately sick, the probability that its rotarod performance falls in the same category is only 0.19 (figure 6.1**F**). This discrepancy can be explained by the distinctively non-linear correlation between clinical score and rotarod performance, which can best be described using a logistic decay function (figure 6.1**G**). Over the clinical score interval of 1.5-2.5 there is a rapid decrease in motor performance as measured by rotarod. While animals with a clinical score lower than 1.5 usually retain maximum rotarod performance and animals with clinical score over 2.5 are barely able to walk the rod, all loss of motor function takes place in the small interval between score 1.5 and 2.5.

Category	Clinical Score	Rotarod Performance
Asymptomatic	0.0	>250 seconds
Moderate	0.5 - 2.5	150 - 250 seconds
Severe	>2.5	<150 seconds

Table 6.2: Disease severity criteria. Definitions used to divide clinical score and rotarod performance into categories.

Analysing the natural history of EAE

The use of categories provides a more accurate representation of disease severity when compared to solely presenting a mean value. A similar approach can be used to analyse the chronological progression of disease. We defined four pivotal events in the natural history of EAE, according to both clinical score and rotarod (table 6.3). These definitions were applied to the disease course of the animals included in the experiment, resulting in the corresponding dates for each event (applied to an individual animal in figure 6.2**A-B**, to the entire population in figure 6.2**C-D**). Clinical score and rotarod are in agreement on the time point of most of the events, with the largest discrepancy in the median observed for recovery (figure 6.2**E**, table 6.4). When comparing the date for each individual event according to rotarod performance and clinical score, a strong linear correlation is observed (figure 6.2**F**, $\rho = 0.87$, $P < 0.001$, Pearson's product-moment correlation). Of all events ($N = 79$), 51.9% is assigned to the same date according to rotarod performance and clinical score, with an additional 25.3% showing a difference of a single day. In 9.2% of the cases, a disease milestone -mainly recovery- is reached according to rotarod performance, but not according to clinical score. The opposite is true in another 9.2%, where clinical score predicts an event -onset of disease- that does not take place according to rotarod performance. In these cases, an animal experiences a temporary weakness or paralysis of the tail, without a drop in motor performance.

EAE is more severe in males, but follows the same time pattern.

The susceptibility to MS as well as the disease course differ substantially between men and women(Schwendimann and Alekseeva, 2007; Bove and Chitnis, 2014). A simi-

Event	Clinical Score	Rotarod Performance
Onset	Day 1 in a period of at least 3 days with clinical score > 0.	Day 1 in a period of at least 3 days with rotarod performance lower than the maximum score during the first week of testing.
Maximum	Day on which the maximum clinical score is recorded.	Day at which the minimal rotarod performance is observed.
Remission	A period of at least 3 consecutive days after the disease maximum in which the animal shows a decreasing or equal score, with at least two of the days showing improvement.	A period of at least 3 consecutive days after the disease maximum in which the animals shows an increasing or equal rotarod performance, with at least two of the days showing improvement.
Recovery	A period of at least 3 consecutive days after the disease maximum in which the animals scores 0.	A period of at least 3 consecutive days after the disease maximum in which the animal achieves a rotarod score of at least 90% of the maximal performance before disease onset.

Table 6.3: Criteria used to define disease events.

lar disparity has been observed for male and female animals subjected to EAE(Massella et al., 2012). In humans, although women have an approximately two- to threefold higher risk of developing MS, the disease tends to be more rapidly progressive in men(Bove and Chitnis, 2013). In our animals, we observed a similar pattern, with a more severe disease course in males compared to females according to both clinical score (figure 6.3**A**) and rotarod performance (figure 6.3**B**). A significantly larger fraction of the male animals reached a maximum clinical score of 4.0 compared to the female animals (figure 6.3**C**, $P = 0.03$), and only 9 out of 28 (32.1%) female animals reached a minimum rotarod latency time of less than 25 seconds, compared to 14 out of 18 (77.8%) male animals (figure 6.3**D**, $P = 0.04$). This gender disparity is limited to the severity of disease, there is no difference in time to reach any of the disease

Event	*According to Score*		*According to Rotarod*		P-value
	Median	Range	Median	Range	
Onset	13	(9-19)	14	(8-19)	0.21
Maximum	16	(14-28)	15	(13-27)	0.63
Remission	17	(15-24)	17	(15-24)	0.99
Recovery	26	(21-27)	23	(17-27)	0.89

Table 6.4: Days post-induction to disease events. Date values indicate median and range in days post-induction. P-values indicate the probability assigned by Fishers' exact test for count data to the hypothesis that the date of the event is independent of the measurement method chosen, i.e. clinical score or rotarod.

milestones (figure 6.3**E**). No difference in susceptibility to EAE was observed. In both gender groups some animals did not develop EAE, with no significant differences between the groups.

Weight at disease onset does not influence EAE outcome.

Another commonly used indicator of disease is weight(Fleming et al., 2005), which has the advantage that it can be measured objectively with minimal stress to the animal. A disadvantage can be that weight at the start of the experiment varies greatly between individual animals and can differ between experimental groups. Also, since weight loss depends on the metabolic response of the animal to the stress associated with EAE, the magnitude of the weight loss is only indirectly related to disease intensity. We observed a highly significant linear correlation between weight and clinical score (figure 6.4**A**, ρ=-0.11, P = 1.33×10^{-7}) and rotarod performance (figure 6.4**B**, ρ=0.12, P = 2.3×10^{-4}), independent of gender. As expected, male animals are significantly heavier at the start of the experiment with a mean weight of 25.1 gram versus 19.4 gram for the female animals (figure 6.4**C**, P = 2.8×10^{-12}). This might raise the question if this weight difference plays a role in the gender disparity in disease intensity. However, no correlation exists between weight before the start of the experiment and the maximum disease intensity, both according to clinical score (figure 6.4**D**, P = 0.82) and rotarod performance (figure 6.4**E**, P = 0.90). Although limited by its high variance, weight can be used as a marker for disease progression. The weight of an animal at the start of an EAE experiment does not predict disease severity.

Both rotarod performance and clinical score correlate with the area of inflammatory lesions

Although non-invasive measurements can teach us a great deal about the severity and time course of EAE, the gold standard remains histological analysis. However, little research has been performed correlating clinical score to histological evidence of CNS damage. The available evidence suggests that the correlation with atrophy in the spinal cord might only be weak(Källen and Nilsson, 1986), although a stronger correlation exists with brain atrophy (Paz Soldán et al., 2015). Interestingly, a similar disparity between clinical signs and damage visible on MRI exists in MS patients (clinic-radiological paradox), possibly related to the inability of MRI to reliably and quantitatively visualise axonal damage(Rocca et al., 2013). To determine the correlation between our clinical measurements and the damage to the nervous system, the spinal cords from a representative subset of animals (N = 12) were embedded in paraffin and used to generate a series of microscopy slides covering the entire extent of the spinal cord. These slides were stained using the protocol provided by Klüver and Barrera(Klüver and Barrera, 1953), a method deploying luxol fast blue and eosin Y to chemically stain myelin, neuropil and neurons. Loss of luxol fast blue staining does not represent pure demyelination, but is more often the result of the combination of demyelination, axonal loss and immune cell infiltration ((Baker et al., 2011)). The correlation between loss of luxol fast blue and axonal degeneration has been confirmed using in vivo imaging studies ((Kim et al., 2006; Budde et al., 2009)).

The resulting stained slides were imaged in a systematic manner and manually traced, resulting in a list of coordinates for the outline of the white matter, the border between white and grey matter and the boundary of inflammatory lesions, if present. These resulting outlines were matched to an anatomical atlas of the spinal cord(Watson et al., 2009) to determine the exact segment of the spinal cord the slide was located in, as well as the anatomical structure which each of the inflammatory lesions occupied (figure 6.5$\mathbf{A}_{1-3}$). Using a custom written script in the programming language Python, the coordinate list was loaded into the open source animation suite Blender(Blender Online Community, 2015) to create a data-driven visualisation of the three-dimensional organisation of the lesions (figure 6.5**B-C**).

In agreement with previous reports, we find a large variation in the amount of histological damage, both between animals but also along the spinal cord of individual animals. Within the same animal, parts of the spinal cord can be covered with lesions (figure 6.5**B**), while a different section located only a few segments away in caudal direction can show virtually no lesions at all (figure 6.5**C**). Still, a significant correlation can be found between the mean percentage of white matter containing lesions and both the clinical score (figure 6.6**A**, ρ=0.70, P=0.01) and the rotarod performance (figure 6.6**B**, ρ=-0.61, P=0.04). However, it should be observed that these numbers are based on the assumption of a linear correlation, an assumption that is hard to confirm given the high variability. Although the amount of damage within one individual can vary from 0 to 50% of the white matter containing inflammatory lesions in the span of a few spinal cord segments, it appears there are some 'hot spots' in the spinal cord with a somewhat higher probability of containing inflammatory lesions. The most easily visible of these is located from approximately L3 to S2, the region of the spinal cord innervating the hind limbs (figure 6.6**C**).

Inflammatory lesions are located in every section of the white matter, close to the pia mater.

A total of 444 lesions were detected in 12 animals. For each lesion, the anatomical structure it occupied and the spinal cord segment in which it was located was determined. If the lesion crossed the border between two anatomical structures, it was excluded from further analysis (N = 43 / 9.7%, all of these lesions crossed the boundary between anterior and lateral funiculus). Since many anatomical structures only contained one or two lesions, the counts were aggregated into three funiculi. The posterior funiculus contained counts from the gracile fasciculus, the dorsal corticospinal tract and the cuneate fasciculus. The lateral funiculus included the counts from the rubrospinal tract, the lateral corticospinal tract, the lateral spinal nucleus and the lateral cervical nucleus, while the anterior funiculus contained the anterior spinothalamic, olivospinal and vestibulospinal tracts. The absolute number of lesions detected was approximately equal for the lateral and anterior funiculus and nearly halve this amount for the posterior funiculus (figure 6.6**D**). To get an estimate of the relative surface area of each of the anatomical subdivisions, the anatomical atlas used as a reference(Watson et al., 2009) was traced in a similar manner as the microscopy slides. When correcting the lesion counts for the relative area of each of the funiculi, a minor preferential localisation in the posterior funiculus appears, which is significant compared to the anterior funiculus ($P = 0.006$), but not compared to the lateral funiculus ($P = 0.07$). Interestingly, the tracts located in the posterior funiculus are involved in the transmission of information on fine touch, pressure and vibration, properties that are not tested in the clinical score and only mildly relevant for rotarod performance. It is therefore not surprising that when only the lesions in the motor systems are considered, the correlation with both clinical score and rotarod remains the same, while the quality of the fit improves (figure 6.6**H-I**). No significant correlation exists between the amount of damage in the posterior funiculus and clinical score ($\rho = 0.35$, $P = 0.26$) or rotarod performance ($\rho = -0.23$, $P = 0.46$, plots not shown).

To determine the relation between the position of the inflammatory lesions and the distance to the outer border of the spinal cord formed by the pia mater, a number of random points were generated within the area of the lesions and the minimal distance to the pia mater was calculated for each point. A similar sampling was performed on the white matter (figure 6.5$\mathbf{A}_2$). This method was chosen to take the irregular shape of the lesions into account, which would make a distance calculation based on centroid highly inaccurate. The average point within the inflammatory lesions is located 0.18 mm away from the pia mater, 2 times closer than the white matter as a whole (figure 6.6**F**, $P < 0.001$). This proximity to the pia mater is reflected by an increased distance to the boundary between white and grey matter, increased from 0.34 mm for the white matter as a whole to 0.57 mm for the lesions (figure 6.6**G**, $P < 0.001$). This subpial preferential localisation of lesions could suggest that meningeal inflammation plays a role in the pathogenesis of EAE, as has been suggested previously based on findings in the cerebral cortex(Errede et al., 2012; Kramann et al., 2014).

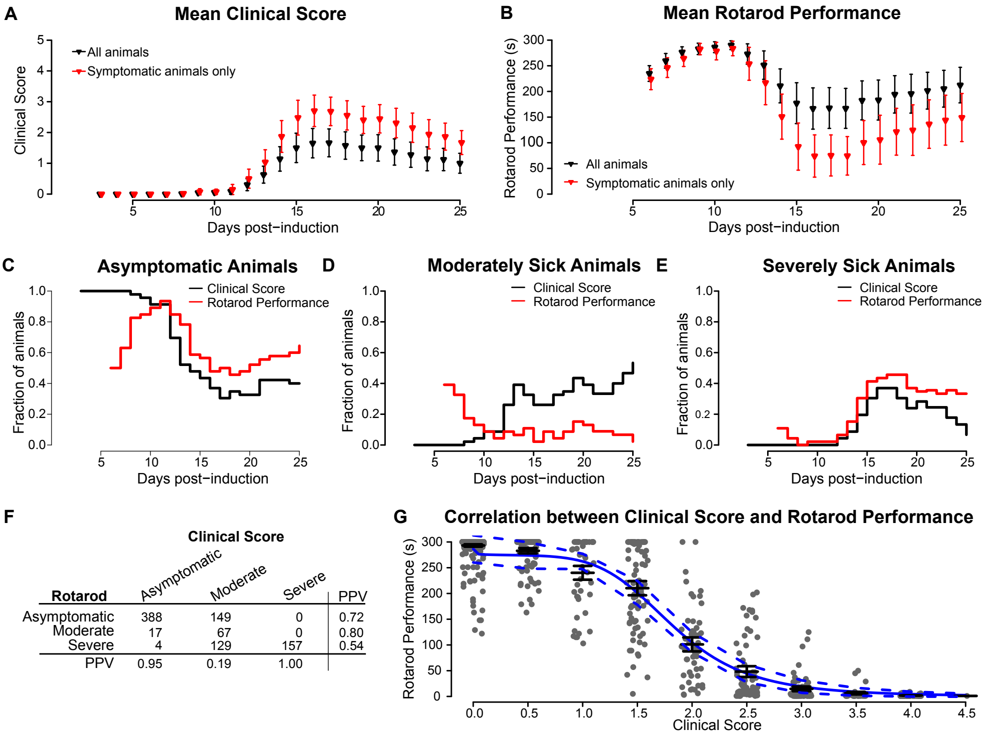

Rotarod	Clinical Score: Asymptomatic	Moderate	Severe	PPV
Asymptomatic	388	149	0	0.72
Moderate	17	67	0	0.80
Severe	4	129	157	0.54
PPV	0.95	0.19	1.00	

Figure 6.1: Rotarod motor performance is highly correlated to clinical score. **(A)** Average clinical score per day for all animals (black) and only the animals that develop symptoms (red). **(B)** Average rotarod performance in seconds for all animals (black) and only the animals that develop symptoms (red). The increase in clinical score around day 12 corresponds to a decrease in rotarod performance. **(C-E)** To get a more meaningful estimate of the variation in disease intensity over time, animals were classified into three categories. The plots show the fraction of the total population which shows no symptoms at all **(C)**, moderate **(D)** or severe symptoms **(E)** according to either the clinical score (black) or the rotarod performance (red). Rotarod performance and clinical score show a similar pattern for asymptomatic and severely sick animals, but differ in their classification of moderately sick animals. As predicted, the fraction of asymptomatic animals according to rotarod performance is not 1 at the start of the experiment, due to the learning curve the animals are experiencing while first using the device. **(F)** Table of concordance between clinical score and rotarod. On each day the animals were observed and classified as 'asymptomatic', 'moderately sick' or 'severely sick' according to the definitions described in the text. There is a high level of agreement between clinical score and rotarod performance, with the notable exception of the clinical score category 'moderately sick'. PPV indicates positive predictive value, the number of true positives divided by the total number of observations, in this situation using the other test (clinical score or rotarod) as gold standard. **(G)** There is a non-linear correlation between clinical score and rotarod performance, best fitted using a logistic decay function. Rotarod performance is not affected in the lower clinical scores, but rapidly decreases at scores higher than 1. Solid blue line indicates optimal nonlinear least squares fit, dashed lines indicate 95% confidence interval. Error bars in **A-B** and **G** indicate 95% confidence interval.

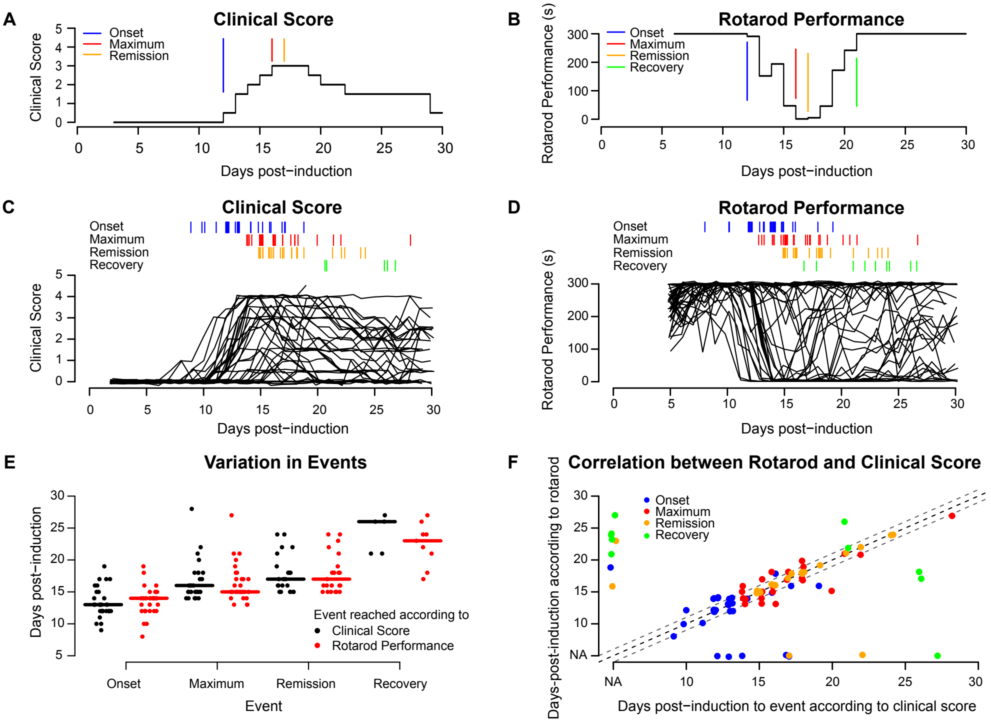

Figure 6.2: Major disease events according to rotarod and clinical score. (A-B) Disease course for one typical animal illustrating the different disease events as defined in the text, according to clinical score **(A)** and rotarod performance **(B)**. Although this animal shows clear signs of recovery, it never fulfils the criteria for complete remission according to clinical score. **(C-D)** Disease course for all animals with time points for disease events shown on top. Although the patterns for clinical score **(C)** and rotarod performance **(C)** are highly similar, complete remission is much more rare according to clinical score. **(E)** Median time to disease event according to clinical score (black) and rotarod performance (red), horizontal bars indicating the median. All event definitions are reached either on the same day or with one day difference, with the exception of recovery. **(F)** Correlation between date according to clinical score and rotarod performance for each individual event. If positioned on the middle grey line, a disease event takes place on the exact same day according to both clinical score and rotarod performance, with both parallel lines indicating plus or minus one day. All events show an excellent correlation, with the notable exception of recovery. The NA mark on the axes indicates that the criteria for this event was fulfilled according to one but not both measurements.

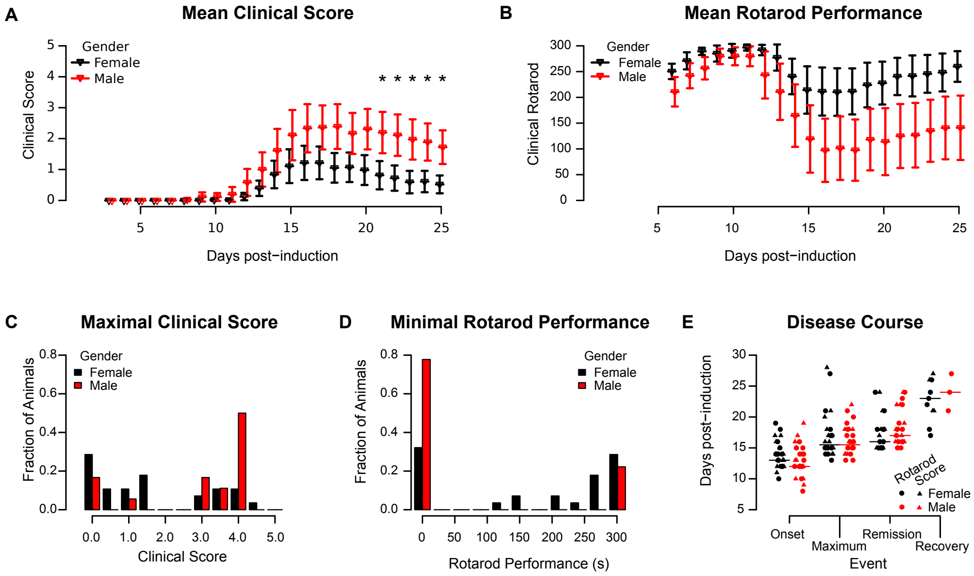

Figure 6.3: Gender strongly influences severity of EAE. Male animals experience a more severe form of EAE compared to females, both according to clinical score **(A)** and as measured by rotarod performance **(B)**. A significantly larger fraction of male animals reaches a clinical score of 4.0 compared to female animals **(C)** and are no longer able to walk the rotarod **(D)**. This difference is only present when considering disease severity, not when analysing duration or speed of onset. All disease events are reached on the same day or within one day of each other by both male and female animals **(E)**. Error bars in **(A-B)** indicate 95% confidence interval, asterisks indicate significance after correcting for multiple comparison using Bonferroni's method: * = p¡0.05. Horizontal lines in **(E)** indicate the median.

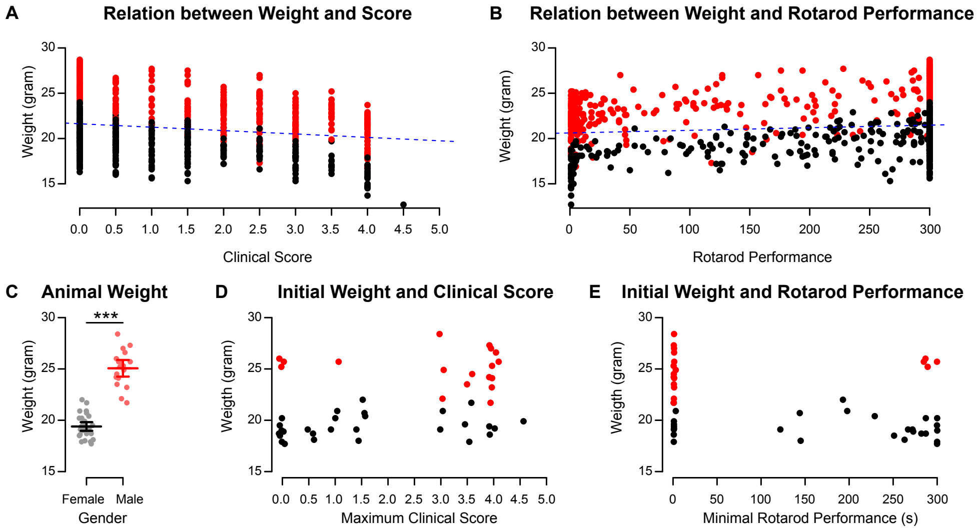

Figure 6.4: Weight difference between genders does not explain disease severity. When measuring the animals weight over time, there is a small but significant negative correlation with clinical score **(A)** and a similar sized and significant positive correlation with rotarod performance **(B)**. This effect is caused by the weight loss associated with severe disease. Although males are significantly heavier at the start of the experiment **(C)**, the initial weight shows no significant correlation with either the maximum clinical score achieved by the animal **(D)** or the minimal rotarod performance **(E)**. In all panels, data points from male animals are indicated in red, and females in black. A total of 966 weight measurements were included in **A** and **B**, a subset of 46 measurements (one for each animal on the first day) were used for panels **C-E**. Error bars in **C** indicate 95% confidence interval.

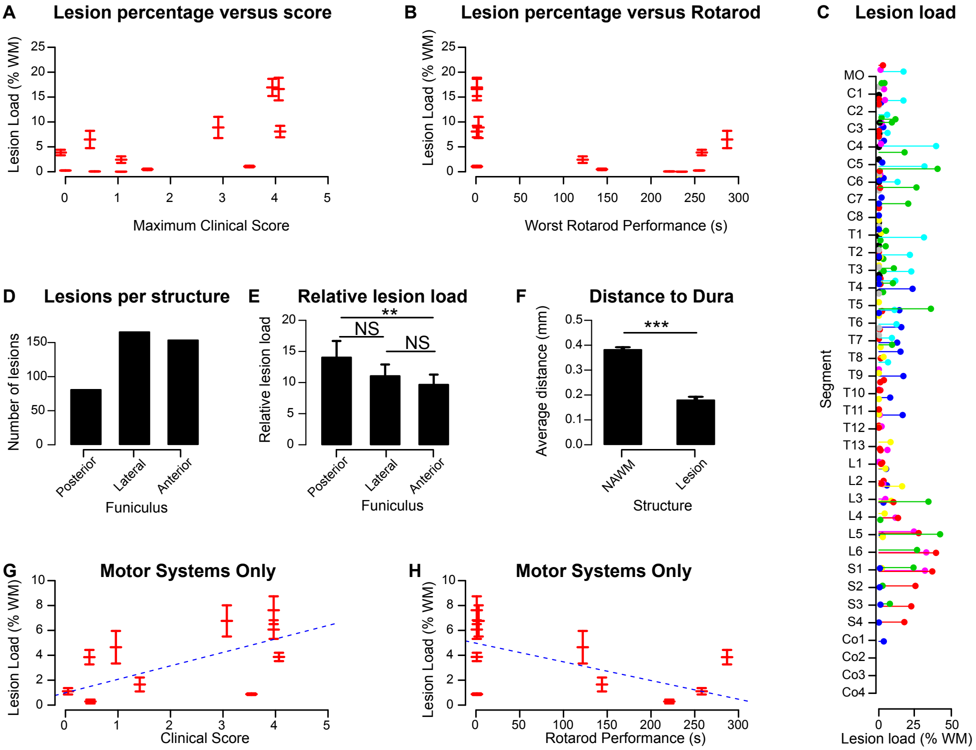

Figure 6.5: Computational methods for calculating lesion load and distance to pia mater. A standard series of Klüver-Barrera stained paraffin sections was prepared for each animal, covering the entire available spinal cord at regular intervals **(A_1)**. The outline of the spinal cord, the border between grey and white matter and all inflammatory lesions were traced. Within the area bounded by the traces, 250 points were sampled at random to function as starting points for distance calculation, as indicated with 'x' marks in **(A_2)**. For area calculations, the point clouds obtained by tracing were converted to polygons **(A_3)**. These point clouds also form the basis of the 3D reconstructions shown in **(B-C)**, which show two spinal cord segments from the same animal. In the low lumbar and high sacral region, inflammatory lesions cover most of the lateral and anterior funiculus, while at low thoracic level, only a few lesions are visible.

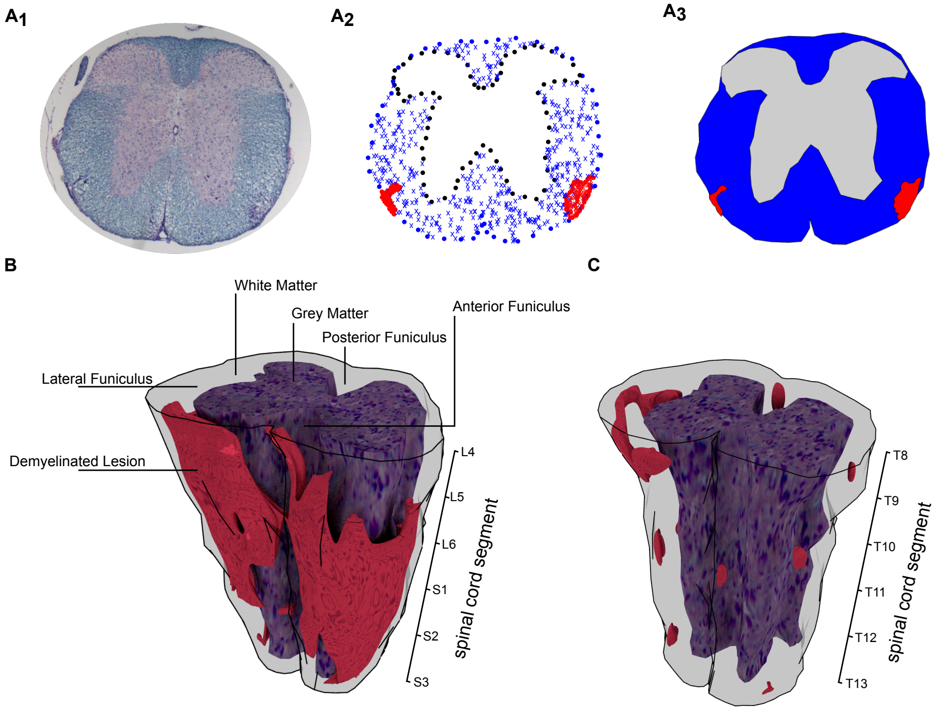

Figure 6.6: Lesion load shows a high inter- and intraindividual variability. Animals with a higher percentage of the white matter covered with inflammatory lesions tend to have reached higher clinical scores **(A)** and showed a shorter rotarod latency time **(B)**. However, there is a large variability in the relative percentage of lesions between animals as well as within the spinal cord of the same animal. **(C)** Distribution of relative lesion load along the spinal cord, each colour indicating one individual animal. MO = medulla oblongata. **(D)** Although every part of the white matter can be affected by inflammatory lesions, most lesions are present in the anterior and lateral funiculus, with a smaller number located in the posterior funiculus. **(E)** When corrected for the relative size of these anatomical structures, there appears to be a significantly higher lesion load in the posterior funiculus . Inflammatory lesions are preferentially located in the periphery of the white matter, in close proximity to the pia mater **(F)**. **G-H** Recalculating the correlation between lesion load and clinical score or rotarod performance based solely on the damage in the ventral and lateral columns, containing the motor tracts, provides a similar correlation as shown in panels **A-B** with a better quality of fit . NAWM = normal appearing white matter. Error bars in **A-B** and **E-H** indicate standard error of the mean, asterisks in **E-F** indicate significance, ** = $p<0.01$, *** = $p<0.001$.

Discussion

Driven by the need for developing and evaluating neuroprotective therapies to ameliorate disease progression in MS, multiple attempts have been made to improve the assessment of neurological impairment seen in EAE (e.g.(Buddeberg et al., 2004; Jones et al., 2008). The rotarod performance test provides an objective measurement of motor skills with a high level of inter-rater reliability. While the clinical score results in an ordinal variable, the rotarod provides a discrete numerical outcome (length of time till fall). In this study, we validated the usefulness of the rotarod to evaluate the course of EAE by comparing it to a commonly used clinical score and comparing both to the amount of damage observed in the spinal cord of the mice. Although there is an excellent negative correlation between neurological disability as determined using a clinical scale and the ability of the animal to maintain its balance on the rotarod, this relationship is decisively non-linear. It closely resembles a Gompertz curve, a commonly used mathematical model for a time series with slow growth at start and end of an interval, but fast growth in the middle (Gompertz, 1825; Winsor, 1932), used for example in (Chatterjee et al., 2015). When provided with a negative exponent, this curve can be used to model a logistic decay process. Using this model, we find that motor performance barely decreases when neurological disability is scored below 1.5, reflecting the fact that the criteria for these scores are mainly aimed at tail dysfunction. In contrast, the score interval from 1.5 to 2.5 shows a rapid decay of motor skills as measured using the rotarod. This part of the clinical disability scale seems to reflect a transitional state, since only a very small number of animals reach a maximum score in this interval (figure 6.3**C**). Animals either progress to a higher disability score or improve. If they progress and reach a clinical score of 3, the paralysis of the front or hind limbs will minimise their ability to use the rotarod. Therefore, while the rotarod provides an objective and quantitative measure of disability, a well-chosen clinical scale still has an added value in the intervals where the ability of the animal to walk the rotarod is either unaffected or, on the high end of the scale, very limited. However, we have also found that the relation between clinical score and the motor skills as measured using rotarod is not linear. A one-unit increase in clinical score is not reflected by a similar sized decrease in rotarod performance, strongly suggesting that the clinical score is an unequally spaced ordinal variable. Comparing mean clinical score between groups, as is commonly used in the EAE field, is based on the assumption that the measured categories reflect an underlying continuous variable. Since this is assumption is apparently not valid, analysis of clinical score using statistical tools developed for numerical variables can lead to artefacts (Bollen and Barb, 1981).

The majority of studies published on EAE focuses on disease intensity only. Clearly defined disease milestones (see table 6.3) allow quantifying the time course of EAE as well as its severity. Both a clinical scale and the rotarod performance are useful to this end. The clinical score is more sensitive to mild cases of EAE not affecting motor performance, where the animal's ability to walk the rotarod is not affected. The rotarod on the other hand is better suitable to monitor the slow recovery experienced by most animals. This method of analysing disease course is not unlike the common practice of measuring MS progression over time using Kurtzke's Expanded Disability Status

Scale (EDSS, (Kurtzke, 1983). Interestingly, several recent studies have suggested that a clinical test with a high similarity to the rotarod, gait analysis, could provide a prognosis of disability progression in MS (Hamilton et al., 2009; Flegel et al., 2012; Socie et al., 2013).

As in MS patients, we observed a large gender disparity in EAE severity in our mice. This gap only affects the magnitude of disability, not its progression over time. A similar effect was recently reported in a rat EAE model (Nacka-Aleksić et al., 2015). Although gender might be an unwanted confounder in most EAE experiments, the fact that a gender gap exists in EAE could be used to study the still unexplained female predominance seen in MS. It could also help to study the phenomenon that the reported female to male ratio in MS patients has been constantly increasing over time(Dunn and Steinman, 2013). The available research suggest that at least part of the difference is caused by hormonal influences, with female animals being more severely affected depending on the phase of their cycle (Rahn et al., 2014). Other studies have pointed at the role of genes on the sex chromosomes, both in the central nervous system and in the immune system (Du et al., 2014). Although including both genders in EAE experiments has the disadvantage of increased variability within groups, it is a necessary step to enhance our knowledge on sex differences in MS. Furthermore, in some countries regulatory bodies object against using only a single gender, necessitating sacrifice without experiment of the second gender.

The second major finding of this study provides a method for quantifying the amount of CNS damage in EAE. To this end, inflammatory lesions are measured while taking their three-dimensional surroundings into account, preserving information on all spinal cord segments and the and anatomical structures these lesions occupy. In most EAE studies, the number or relative area of inflammatory lesions is used as a measure for CNS pathology. However, a small lesion located in a critical system like the corticospinal tract will contribute disproportionately to disability. On the other hand a large lesion in a system with more redundancy such as the spinocerebellar tracts might not result in any clinical signs.

We now demonstrate a correlation between the magnitude of disease as measured using a clinical scale or rotarod performance and damage in the spinal cord. Importantly, this correlation is entirely based on damage to the lateral and ventral spinal cord. These parts contain amongst others the fibres forming the pyramidal and extrapyramidal tracts, responsible for controlling motor functions. Lesions in the posterior system, mainly involved in conveying sensory information, did not contribute to the correlation between neurological disability and histological damage. We suggest that adding a measure for sensory disability to the clinical test battery will provide a better estimate of CNS pathology. Several studies have been performed on neuropathic pain in EAE (Tian et al., 2013) and various sensory deficits have been reported to occur (Thibault et al., 2011). However, such measurements cause considerable stress to the animals. There is no method currently available for measuring vibration sense in rodents, although a recently published quantitative measurement using paw retraction in response to cold (Duraku et al., 2014) could be used. However, such a measurement would presumably be subjected to the same limitation as the rotarod. Animals which are too sick to walk the rod will also be unable to retract their paws in response to stimuli, prohibiting use in severely affected animals.

As previously suggested by other authors (Jones et al., 2008), the dorsal column of the spinal cord sustains a relatively large amount of damage compared to its size. Various explanations can be brought forward and should be explored, such as proximity to blood vessels, organisation of the meninges, and a possible preferential localisation in ascending versus descending fibre tracts. However, this relatively small preference might also be related to a higher axon density in the dorsal column compared to the ventral and lateral columns, as observed using quantitative MRI (Cohen-Adad and Wheeler-Kingshott, 2014). Inflammatory lesions are preferentially located near the edge of the white matter, close to the pia mater, supporting the hypothesis that the meninges can function as an entrance point for immune cell infiltration into the central nervous system (Polfliet et al., 2002; Walker-Caulfield et al., 2015). The peripheral accumulation of damage might also explain the frequent observation that disability starts in the hind limbs of animals. Several key systems in the spinal cord, including the pyramidal tract, share a somatotopical organisation in which the fibres from the sacral spinal cord segments are located on the outside and fibres from the cervical cord on the inside. The subpial localisation of lesions suggests that the function of the axons associated with the sacral and lumbar spinal cord segments is impaired first, while the thoracic and cervical fibres are preserved.

Overall, the workflow outlined in this paper provides a systematic method of quantifying neurological disability in EAE, both in magnitude and in terms of disease course. The severity of disease can be correlated to the area of inflammatory lesions found in the motor systems of the spinal cord. Our findings also emphasise the importance of gender as an influential factor, determining disease severity in EAE as it does in MS. Finally, we have shown that when studying damage to the CNS, lesion size and location is vital in order to link clinical signs to histopathology. In this manner, the vast immunological experience acquired using EAE can be combined with knowledge and techniques from the fields of neuroscience and experimental neurology, further upgrading EAE into a more accurate model for studying the neurodegenerative aspects of MS.

Acknowledgements

This work was supported by the Stichting MS Research (Project 09-691 MS to R.Q.H. and C.C.H.) and the Netherlands Organisation for Scientific Research (VICI grant 865.10.021 to C.C.H.).

Analysing and optimising STORM imaging results

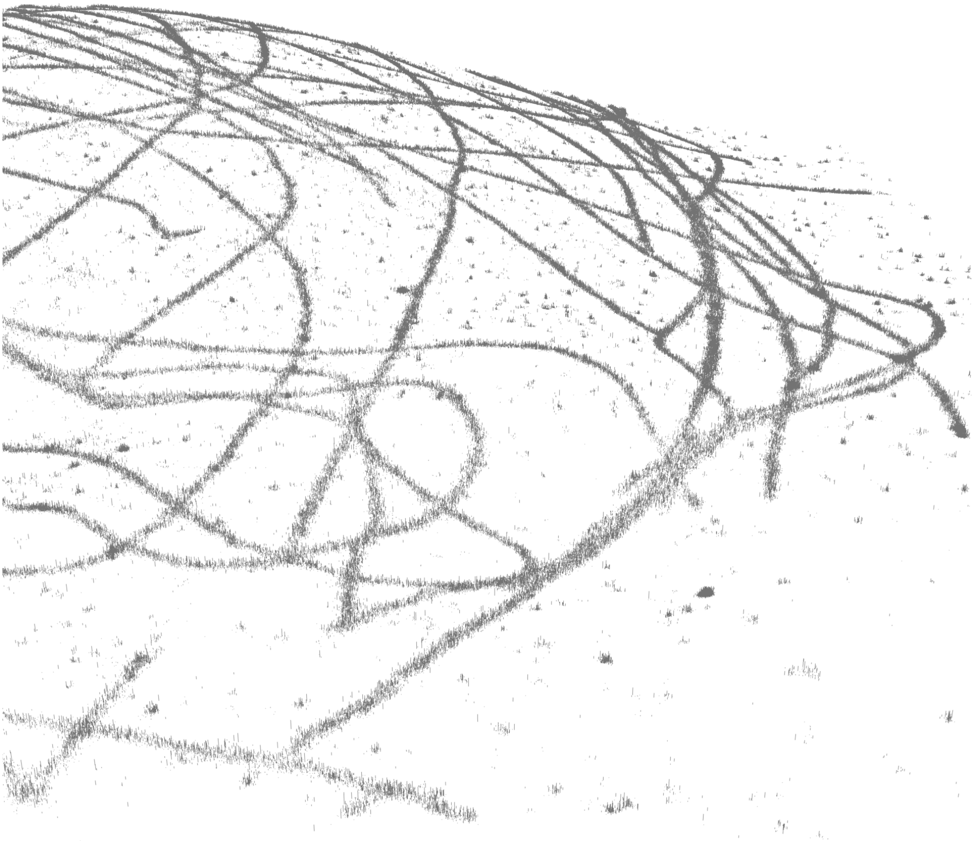

7

AS SHARP AS IT GETS: ANALYSING AND OPTIMISING STORM IMAGING RESULTS

Introduction

Light and Its Rules From the very dawn of mankind, light in all its different manifestations has fascinated and puzzled us. Our life is controlled by cycles of increased and diminished light, influencing our thinking in such a way that even in ethics, light and darkness became synonymous with good and evil. Over the ages, we managed to describe the behaviour of light in various circumstances and use this knowledge to create optical devices that ease our life, from the use of glasses to correct vision to the light-emitting diodes found in modern computer monitors.

But despite all this knowledge, the nature of light itself has continued to mystify us. Only the last two centuries have seen the beginning of an explanation, but much remains unknown. Descartes considered light to be a motion or a wave, transmitted through an elastic medium, the aether. A competing theory describing light as a stream of particles was strongly supported by Newton almost a century later, while his Dutch colleague Christiaan Huygens at the same time described light as travelling as a wave. These two theories kept the scientific field divided for three centuries. At the start of the nineteenth century, Thomas Young expanded on the wave theory of light by adding the concept of interference: when two or more light waves meet, their joint effect is equal to their sum. If two wave crests meet, the interference is constructive, leading to an increased amplitude of the resulting wave. In contrast, if a crest meets a through, the resulting destructive interference leads to near-total extinguishing of the light. Half a century later, James Maxwell added an extra dimension to our thinking about light by describing it as an electromagnetic phenomenon, with visible light being part of a spectrum ranging from radio waves to gamma rays, depending on the wavelength of the radiation.

The twentieth century saw the unification of these two theories through the work of Albert Einstein, Max Planck and many others. According to their ideas, referred to as quantum mechanics, light is *both* a wave and a stream of particles at the same time. Although almost impossible to visualise, light consists of individual bodies -photons- that manifest themselves simultaneously as wave and as particle, with the wavelength depending on the momentum of the particle. This is the current state of optical science. Though few would claim to understand light, we are able to describe it in ways that accurately explain the phenomena observed in nature.

The Rules and Their Limits This dual nature of light is not just a theoretical concept, but something experienced with every modern microscopy experiment. We detect emitted light using a sensor called a charge-coupled device (CCD), which is capable of detecting single photons as they hit a photosensitive layer, releasing an electron. On the other hand, the interaction of light with the various components of a microscope setup, such as mirrors and lenses is best described when we consider light as a wave. The wave properties of light also restrict how far a microscope is able to zoom in on a sample. As light leaves a light source, for example a fluorescent tag used in live cell imaging, it spreads in every direction. A lens is then used to collect and focus part of this light wavefront on the CCD. As light passes through a circular aperture like a microscope objective, the different wavefronts start to interact with each other, leading to destructive and constructive interference. The signal detected by the CCD chip is created by the sum of the interference of these wavefronts, leading to a pattern of brighter and darker bands (Hecht, 2002). For a perfect point light source, this resulting interference figure is called an Airy disk (Figure 7.1 **A**), first described in the 19th century by George Airy (Airy, 1835).

Even if we imagine the light source to be almost infinitely small and our microscope tuned to technical perfection, this still means that our resolution has a limit. Resolution is defined as the minimal distance between two objects at which they can still be distinguished as two individual objects. Since the Airy disk has a certain width, if two light sources are close together, there will be an overlap of their disks and we will observe them as one object instead of two (Figure 7.1 **B**). The minimal distance between two point sources at which their Airy disks overlap can be approximated by $\frac{0.61\lambda}{NA}$, where λ is the wavelength of light emitted by the object and NA stands for Numerical Aperture. The numerical aperture of an optical system describes the range of angles over which light is collected. This is determined by the refractive index of the medium touching the lens and the cone of light collected by the lens as described by the formula $NA = n_i sin\theta_{max}$, where n_i indicates the refractive index and θ the half-angle of the light cone. Since normal microscopy employs visible light, with λ between 405 and 650 nm, and the numerical aperture of a lens rarely exceeds 1.4, this puts the theoretical resolution of any microscope using visible light at approximately 200 nm.

This limit has major practical implications in the fields of cellular and molecular biology. Directly resolving proteins and cellular components is impossible, since these objects are much smaller than 200 nm. Neuronal microtubule networks, for

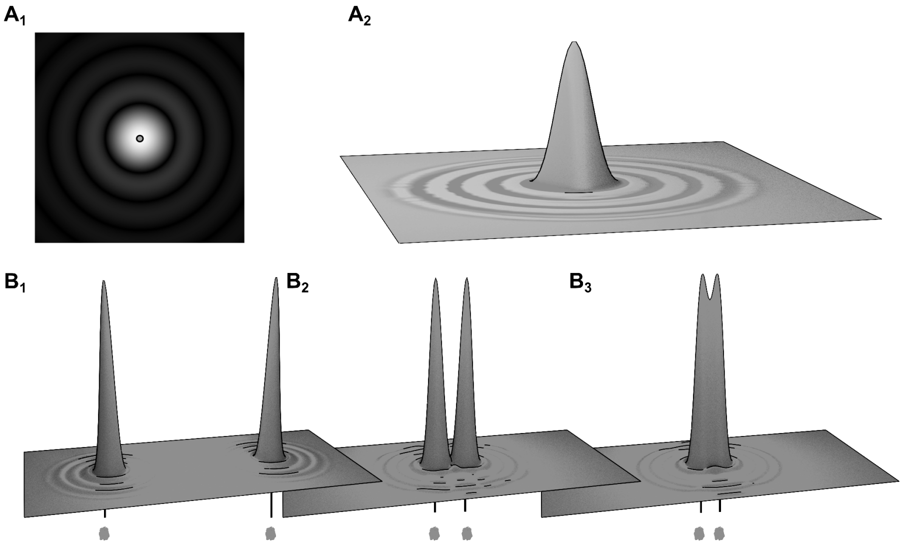

Figure 7.1: Basic principles of diffraction. A When light emitted by a point-sized light source passes through a circular aperture, such as the opening of a microscope objective, diffraction occurs. Due to constructive and destructive interference it is not projected on the camera as a point-sized image, but as a pattern with a bright central dot surrounded by darker and brighter rings. The size of this pattern, the Airy disk (shown in 2D in $\mathbf{A_1}$ and in 3D in $\mathbf{A_2}$), depends on the wavelength of light used and the optical properties of the system. $\mathbf{B_{1\text{-}3}}$ Interaction of Airy disks limits resolution. Two light-emitting molecules both generate their own Airy disks when imaged. If the molecules are far apart, both disks can be separated ($\mathbf{B_1}$). When the molecules are closer together, the disks start to overlap ($\mathbf{B_2}$), until they can no longer be distinguished as two separate objects ($\mathbf{B_3}$) even though there is still considerable space between the molecules.

example, consist of tube-shaped tubulin polymers with a diameter of 25 nm and a centre-to-centre distance of approximately 70 nm (Chen et al., 1992). The stability of the network, binding of motors and processivity of transport along these microtubules is determined in part by the chemical modifications to the tubulin subunits (Verhey and Hammond, 2009), as discussed in chapter **2** of this thesis. However, due to the close proximity of individual microtubules, the exact role of microtubule modifications and their influence on transport in health and disease can not be studied using light microscopy. Our knowledge of these processes is therefore mostly based on *in vitro* work or more global analyses, which limits the possibility of translating our findings into clinical research.

Bending the Rules In the previous paragraphs we have discussed the limits of light microscopy and our need to surpass them. We have described how the resolution is limited by the wavelength of the light used for imaging and the numerical aperture of the objective. This already suggests two opportunities for increasing our resolution, being a decrease of the wavelength used or an increase of the numerical aperture. Unfortunately, even in theory the numerical aperture can not increase much beyond 1.5, a value corresponding to collecting light over a range of 90 degrees. This is close to that of the best objectives currently in use, leaving little room for improvement.

Using shorter wavelengths does indeed lead to dramatic increases in resolution. This is the solution used by electron microscopy (EM), utilising the fact that electrons have an approximately 100.000 times shorter wavelength compared to visible light photons. Although the resolution of this technique is unmatched, it is not without its disadvantages. First of those is the problem of visualising specific cellular compartments or proteins. With light microscopy, one can use a large and expanding range of fluorescent dyes which can be bound to the protein of interest, but these are not available for EM. To be able to see anything at all under an electron microscope, a sample needs to be treated with potent fixatives and cut into extremely thin sections. As can be imagined, this excludes the application of EM for imaging living cells or observing changing processes over time. For our research interests, another approach is needed.

From the late 1960's, ideas have been put forward to circumvent the limitations of light microscopy (McCutchen, 1967; Betzig et al., 1986; Carrington et al., 1995), but only for the past ten years these ideas have resulted in new microscopy approaches. Spearheaded by highly influential papers from scientists like Eric Betzig (Betzig et al., 2006; Shroff et al., 2007, 2008), Jennifer Lippincott-Schwartz (Lippincott-Schwartz and Manley, 2009; Manley et al., 2010), Xiaowei Zhuang (Dani et al., 2010; Xu et al., 2012) and many others, these techniques are slowly expanding the range of scientific questions light microscopy is able to answer. Over the years, a variety of different methods has been developed, leading to a sometimes confusing collection of abbreviations. Stimulated emission depletion microscopy (STED) uses a combination of an excitation spot and a surrounding donut-shaped de-excitation beam to deplete surrounding fluorophores while activating fluorophores in a small area of interest(Klar

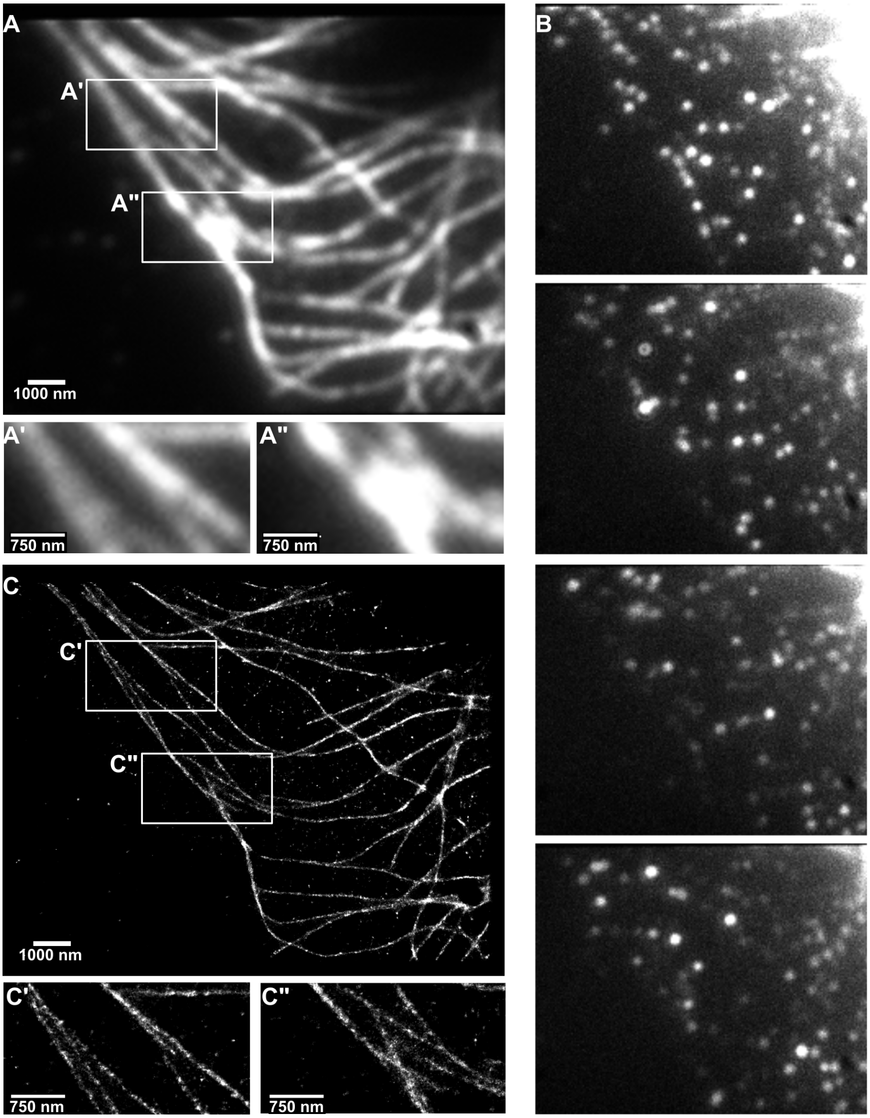

Figure 7.2: STORM Microscopy. U2OS cells were stained with primary antibodies targeting Tubulin and secondary antibodies labelled with Alexa-647. An image taken before the start of STORM image acquisition shows the microtubule network inside the cell (**A**). At the start of STORM acquisition, all fluorophores are bleached using high power laser illumination. Over time, individual fluorophores become excitable again, are imaged and subsequently bleached. Panel **B** shows four representative individual frames from a 50.000 frames acquisition. All individual fluorophores are localised and plotted with a radius corresponding to their localisation error (**C**). The increased resolution offered by this technique allows for tracing of individual microtubules inside dense microtubule bundles (details **A'-C'**,**A"-C"**).

et al., 2000; Chereau et al., 2015). In structured illumination microscopy (SIM), a grid pattern is superimposed on the specimen which during imaging slowly rotates. Using Fourier transformation, additional frequency information on the specimen in 3-5 different orientations can be extracted from these images and used to create a high-resolution reconstruction with a (maximally) two-fold increase in resolution (Gustafsson, 2000). Two other techniques which are closely related, photoactivated localisation microscopy (PALM, (Betzig et al., 2006)) and stochastic optical reconstruction microscopy (STORM, (Rust et al., 2006)) both use localisation of single molecules. In PALM, a few photo-activatable proteins such as PA-GFP are activated in each image, while in STORM, chemical fluorophores are induced to blink. Especially STORM has seen a rapid development, enabling multi-colour (Bates et al., 2007), three dimensional (Huang et al., 2008) and live-cell imaging (Jones et al., 2011).

Single molecule light microscopy techniques, such as STORM and PALM, make use of the fact that as explained previously, a point-shaped light source is observed as an Airy disk, a regular object that can be approximated with a mathematical function. This means that if we observe a single Airy disk, we can calculate the position of the peak with high precision, which corresponds to the position of the light source (see figure 7.1). With the development of digital image recording and enhancement, it became possible to measure the intensity profile of individual particles and calculate their position with nanometer precision (Yildiz et al., 2003). However, this method requires that the intensity profiles of particles do not overlap, limiting its application to highly artificial settings. This changed when techniques were developed to selectively activate and deactivate a subset of fluorophores, allowing for sequential detection and localisation of small subsets of fluorophores present in the sample. Through a combination of buffers and laser settings, suitable fluorescent molecules (probes) are induced either to blink or to be activated or deactivated. With the exact right settings, only a small subset of probes is active, reducing the chance of their Airy disks overlapping. By fitting the intensity profile with a Gaussian curve, the position of each probe can be determined with extremely high accuracy. By collecting a large number of images, up to 100.000 and beyond, the position of almost every probe in a sample can be mapped, allowing a reconstruction of structures of interest with nanometer precision (figure 7.2). A study deploying this technique to study the microtubule cytoskeleton is discussed in great detail in chapter **8** of this thesis. In this introductory chapter we will provide some background to this study and elaborate on the challenges encountered, which could not be discussed in detail in that publication.

Technical challenges in STORM microscopy

Drift Correction Although these superresolution techniques vary in the method applied to achieve selective activation of fluorophores, they share several analysis steps and difficulties. Prior among these difficulties is microscope drift, movement of the projection of the image on the detector. The lightpath of a typical microscope used for superresolution imaging consists of a large number of components made from a wide range of materials like various metals and glass, each with a different thermal expansion coefficient. Even minor temperature fluctuations, in the order of magnitude of 0.1 °C, can give rise to micrometer size drift as expansion and contraction of materials changes the projection of the image on the CCD chip. As superresolution imaging requires a large number of images, acquired over the course of several minutes, these changes can lead to a noticeable blurring of the reconstructed image. In many cases, the number of particles detected during imaging is not constant over time. At the start of image acquisition, a large number of fluorophores are activated, detected and subsequently bleached. As the number of localisations decreases, laser power will often be increased, leading to a second peak in activated fluorophores. Depending on the amount of drift in the interval between these two timepoints, the reconstruction might erroneously show these localisations as two separate microtubules (Mlodzianoski et al., 2011; Wang et al., 2014).

When the image acquisition is finished, the positions of all fluorophores are determined and registered in a particle table. This table contains information on the position of each fluorophore, but also on the image frames in which it was detected. Identifying and correcting drift can be done either on this table with particle localisations or on the superresolution reconstructions. Some methods require special sample preparation, while others rely only on post-processing computations. A fairly easy approach is to include non-blinking fluorescent particles to the sample, such as quantumdots, gold particles or tetraspect beads. These particles will remain active during the entire image acquisition, appearing as smears in a maximum projection of the dataset (shown in brown in figure 7.3**A**). The position of the particle can be determined in each frame, resulting in a record for the drift during the imaged time interval (shown for the X-coordinate in figure 7.3**B**, lower traces). This drift trace can then be used to correct the particle table. Though straight-forward, this approach has several disadvantages. First of all, the particles must be strongly attached to the surface of the glass slide. If the binding is not sufficiently strong, the particles will show individual residual movement independent of the rest of the sample. It is possible to filter out this residual noise by measuring the correlation between traces of several beads and removing uncorrelated movement, but this requires the presence of multiple particles in the same imaging window. Second, since the particles are bound to the surface of the glass slide, this limits the imaging range to the bottom of the sample, or the particles will be out of focus. Finally, particles that are fluorescent without blinking are in general almost an order of magnitude brighter than the fluorescent probes used for STORM imaging, oversaturating the CCD chip.

A variant to this approach does not require the addition of beads. If the fluorescent probes used for STORM imaging remain active for several frames in a row or can be picked up again after blinking, it is possible to reconstruct drift by averaging all the individual incomplete traces (figure 7.3**B**). In this manner, most of the disadvantages of bead tracing can be dealt with. However, this method requires that the labelling density is rather low. If probes are located close together, it becomes impossible to determine if the observed spot belongs to a reactivated linking probe or to a new appearance. Errors in linking lead to a noise on the trace that can not be filtered out.

Another method for drift correction involves cross-correlation of partial reconstructions. As mentioned before, all probe positions are stored in a particle table which also contains the frame in which a spot was imaged. This table can therefore be split in a number of subtables, each containing the detected fluorophores for a given range of frames. To correct drift, a reconstruction is generated for each subtable, which will have a lower resolution compared to the final result due to the reduced number of localisations included, but also a reduced drift effect since the images were acquired during a shorter time window. To extract information on the magnitude and direction of the drift from these images, a correlation coefficient is determined between two subsequent reconstructions while shifting one of the images along the x- and y-axis. This will result in a correlation matrix with a clear maximum at the coordinates corresponding to the drift over the interval between the two images. For further accuracy, this peak is fitted with a 2D-Gaussian (figure 7.3**C**). Repeating this procedure for every partial reconstruction results in an estimate of the drift throughout the dataset with a temporal resolution depending on the number of subtables (figure 7.3**D**). The subtables can be selected either based on number of frames or number of particle localisations. In most cases both options will result in the same quality of drift correction, as long as the number of localisations is approximately equal throughout the imaging session. Increasing the number of subtables will result in a higher temporal resolution at the cost of reduced spatial resolution, since the resulting reconstructions will be more sparse, reducing the accuracy and reliability of image to image cross-correlation.

Using the acquired drift trace to correct the position of localised fluorophores results in a markedly improved image. Estimating resolution using the full-width at half-maximum (FWHM) of microtubule intensity profiles for the dataset shown in this example shows the dramatic increase in resolution for STORM imaging compared to conventional microscopy. For this specific dataset, correcting for drift using cross-correlation leads to a further 50% improvement in resolution (7.3**E**).

Labelling A second challenge is inherent to the use of labelled probes for structure visualisation. A large collection of fluorescent labels is available for STORM imaging ((Dempsey et al., 2011)), chemically attached to probes with a high affinity for the target molecule. These probes, usually antibodies or antibody fragments (so-called $\mathrm{V_H}$H), range in size from several nanometer ($\mathrm{V_H}$H) to up to 15 nm for an IgG antibody. If a labelled secondary antibody is used to amplify the signal, the dimensions of the complex will further increase (7.4). This is not an issue in conventional light microscopy, since their size is far below the diffraction limit. When using superresolution techniques, however, this means that not the structure of interest itself is imaged, but a fluorescent probe that can be up to 30 nm away from the labelled surface.

Microtubules play an essential role in a large variety of cellular processes. Over the last few decades microtubule function, organisation and dynamics have been studied extensively, and the structure of individual tubulin subunits and the microtubule as a whole has been mapped with a resolution as high as 5 Å, revealing a hollow tube with an external diameter of 24 nm (Li et al., 2002; Alushin et al., 2014). A wide repertoire of methods has been developed to visualise microtubules, ranging from kits to assemble labelled microtubules *in vitro* to antibodies with a highly specific affinity for either tubulin-α or -β. These are mostly IgG immunoglobulins with a length of approximately 15 nm (Iijima et al., 2012). A relatively recent addition is the nanobody or $\mathrm{V_HH}$, the variable part of the heavy-chain of gamma-immunoglobulin that has a far smaller size (4.5 nm in length) compared to conventional antibodies (Arbabi Ghahroudi et al., 1997; Rothbauer et al., 2006). The decreased distance between target and fluorophore makes these nanobodies highly interesting tools for superresolution imaging, either by targeting them to the protein of interest directly or through a genetically encoded GFP-tag (Ries et al., 2012). Chapter **8** is entirely dedicated to the application of anti-tubulin nanobodies for the study of the (neuronal) microtubule cytoskeleton.

Figure 7.3 ***(on the next page)*****: Influence of setup drift and correction methods on STORM reconstruction.** **A** Cartoon showing a maximum projection of STORM imaging dataset. Microtubules are visible in red, but appear blurred. Outside the cell, gold particles are visibly smeared out, indicating significant drift during the imaging period. **B** Tracking the movement of the gold particles can be used to reconstruct the drift. Since individual particles can show residual movements, multiple tracks are averaged (black line) to filter these out. The calculated displacement per frame is then subtracted from the coordinates of localised particles and a drift-corrected reconstruction is generated. Similar as with beads, the displacement of fluorescent probes visible in multiple frames (bright dots in **A**, thin red lines in **B**) can be averaged (thick red line) and used to correct drift. **C** Principle of drift correction using intermediate reconstructions. After all particles have been localised, the resulting particle table is split based on the frame number. Each set of frames is reconstructed separately, resulting in partial reconstructions which are more fragmented and sparser compared to the full reconstruction. When calculating the correlation between two images, while shifting the images with respect to each other along the X- and Y-axis, a correlation matrix can be obtained (contour map in **C**, with displacement over X- and Y-axis on the corresponding axes and Pearson correlation coefficient on the Z-axis). This peak can be fitted with a Gaussian curve, with the X- and the Y-coordinate of the curve indicating the displacement over the X- and Y-axis during the interval between the two reconstructions. **D** Repeating this procedure over the whole imaging interval results in an estimate of the drift during the imaging period, which can be used to correct the original particle table. **E** The full width at half maximum (FWHM) of the microtubules in a representative dataset was measured in a maximum projection of the image series, a reconstruction of the particle table with the measured point spread function (PSF), a reconstruction without drift correction and with drift correction using correlation of partial reconstructions. FWHM is plotted on a logarithmic scale. Although not as profound as the difference between conventional microscopy and STORM, drift correction significantly increases resolution (250 profiles per reconstruction method, error bars indicate mean±SD, Max = maximum projection, PSF = reconstruction with point spread function, DoM = Detection of Molecules, an algorithm for superresolution localisation of single fluorophores, DoM drift = as DoM, but with drift correction using intermediate reconstructions).

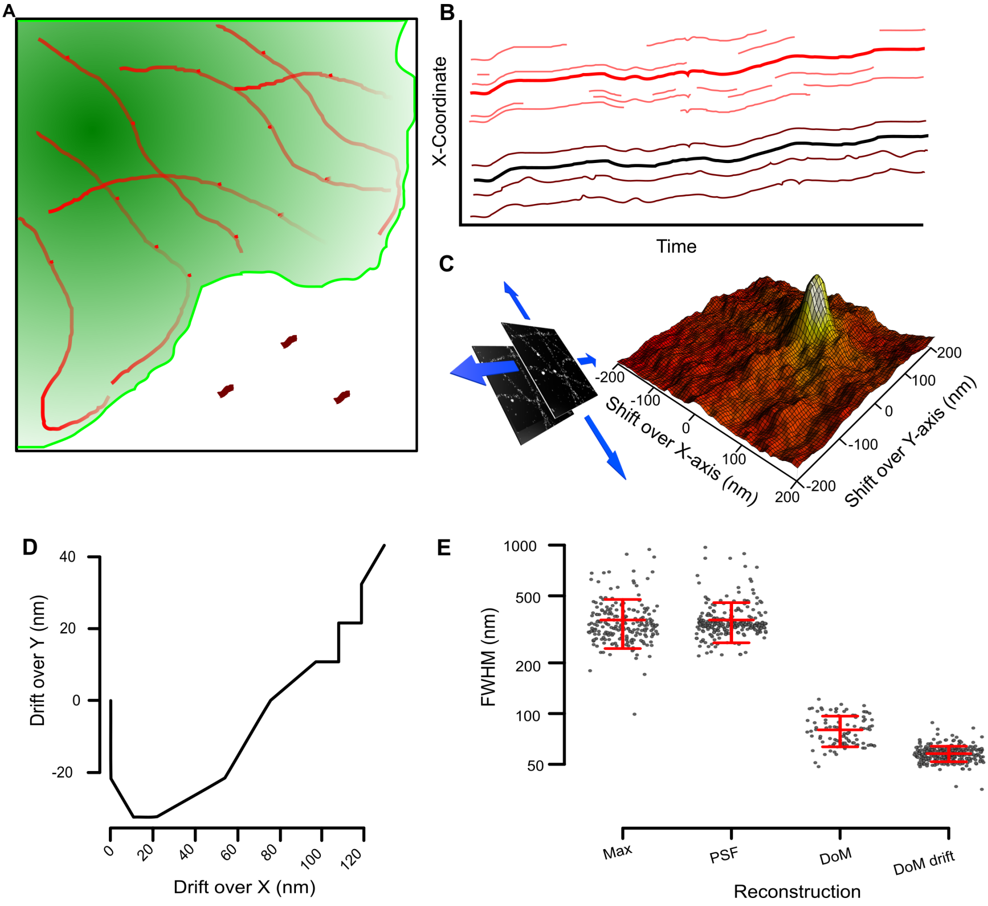
A
B
X-Coordinate
Time
C
-200
-100
0
100
200
Shift over X-axis (nm)
200
100
0
-100
-200
Shift over Y-axis (nm)
D
40
20
0
-20
Drift over Y (nm)
0
20
40
60
80
100
120
Drift over X (nm)
E
1000
500
200
100
50
FWHM (nm)
Max
PSF
DoM
DoM drift
Reconstruction

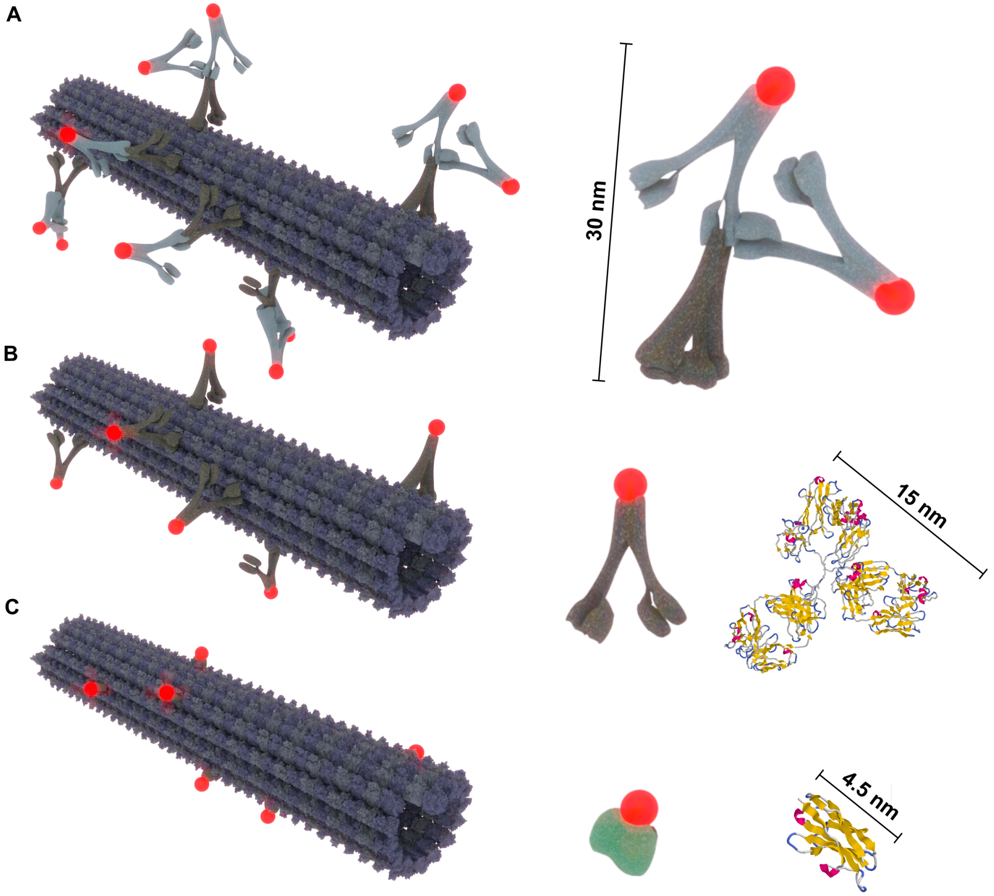

Figure 7.4: Comparison of microtubule labelling methods. **A** Model of a microtubule fragment labeled with the combination of an anti-tubulin primary antibody and a labeled secondary antibody targeting the primary antibody, a directly labeled anti-tubulin antibody **B** and a labeled $\mathrm{V_HH}$ fragment (C). On the right, the corresponding labelling units are shown, as well as the protein structure models for mouse $\mathrm{IgG_1}$ (MMDB ID 7492, Harris et al. (1998)) and llama $\mathrm{V_HH}$ (MMDB ID 113042, Schmitz et al. (2013)). Protein sizes where measured in RasMol. Note that the distance between fluorophore and microtubule can vary for the primary-secondary antibody combination, depending on the binding configuration of the secondary antibody. In the experiments described in chapter **8**, all antibodies used are IgG.

Resolution Estimate A final problem is how to assess the resolution of a superresolution image. Resolution, defined as the minimal distance at which two light sources can still be distinguished individually, can be described in conventional microscopy by Abbe's Law, as mentioned previously. In superresolution, resolution no longer solely depends on the wavelength used or on the numerical aperture of the objective, but also on factors such as localisation precision and labelling density (Ram et al., 2006; Fitzgerald et al., 2012). The precision with which the position of a fluorophore can be determined depends on the number of photons detected and the sampling resolution of its intensity profile. Microscopy using a digital recording device such as a CCD camera involves the conversion of a continuous visual signal into a discrete signal that can be processed by a computer, a process known as sampling. The Nyquist criterion states that the interval for sampling must be smaller than half the required resolution (Nyquist, 1928). Since the sampling resolution for a CCD camera is determined by its pixel size and the required resolution is equal to the point spread function of the fluorophore, most superresolution setups are tuned to result in an effective pixel size of approximately 100 nm. The number of photons detected depends on which fluorophore is used, exposure time, excitation laser power and quantum efficiency of the camera. Even with all these factors optimised, the 'true' resolution will still vary for each sample, depending on the extent to which the structure of interest is coated with fluorophores. If the labelling density is low, it is still possible to localise the individual fluorophores with high precision, but any information on the larger structure will be lost.

Although it is possible to determine the position of a single fluorophore with single nanometer resolution (Yildiz et al., 2003), during the development of superresolution techniques it was immediately appreciated that this does not reflect the actual resolution of the imaging technique (Bates et al., 2007). Localisation accuracy can be used to calculate the theoretical limit of resolution (Ram et al., 2006),but since it ignores the labelling density it will result in a far too optimistic estimate for the real resolving power. Methods that include labelling density in their resolution estimate have been proposed, but are difficult to validate when no ground truth is available.

As superresolution techniques became more widely available, this problem of ascertaining its true resolution -and thereby its practical applicability- has become more urgent. Although it is possible to describe resolution in terms of localisation precision (Thompson et al., 2002; Ober et al., 2004; Bates et al., 2008) or full width at half-maximum of the fluorophore or structure intensity profile (Patterson et al., 2010), several methods have been proposed that take into account both label density and localisation precision, for example the Information Transfer Function (ITF, (Mukamel and Schnitzer, 2012)), the Fundamental Resolution Measure (FREM) and its derivatives (Ram et al., 2006) and the Fourier Ring Correlation estimate (FRC, (Saxton and Baumeister, 1982; Nieuwenhuizen et al., 2013; Banterle et al., 2013)). However, although these techniques perform well on artificial datasets, it is hard to estimate their value on real-life sets. Our research indicates that, at least for FRC, specific imaging conditions can strongly influence the resulting resolution estimate. FRC splits the particle table with STORM localisations into two or more subsets,

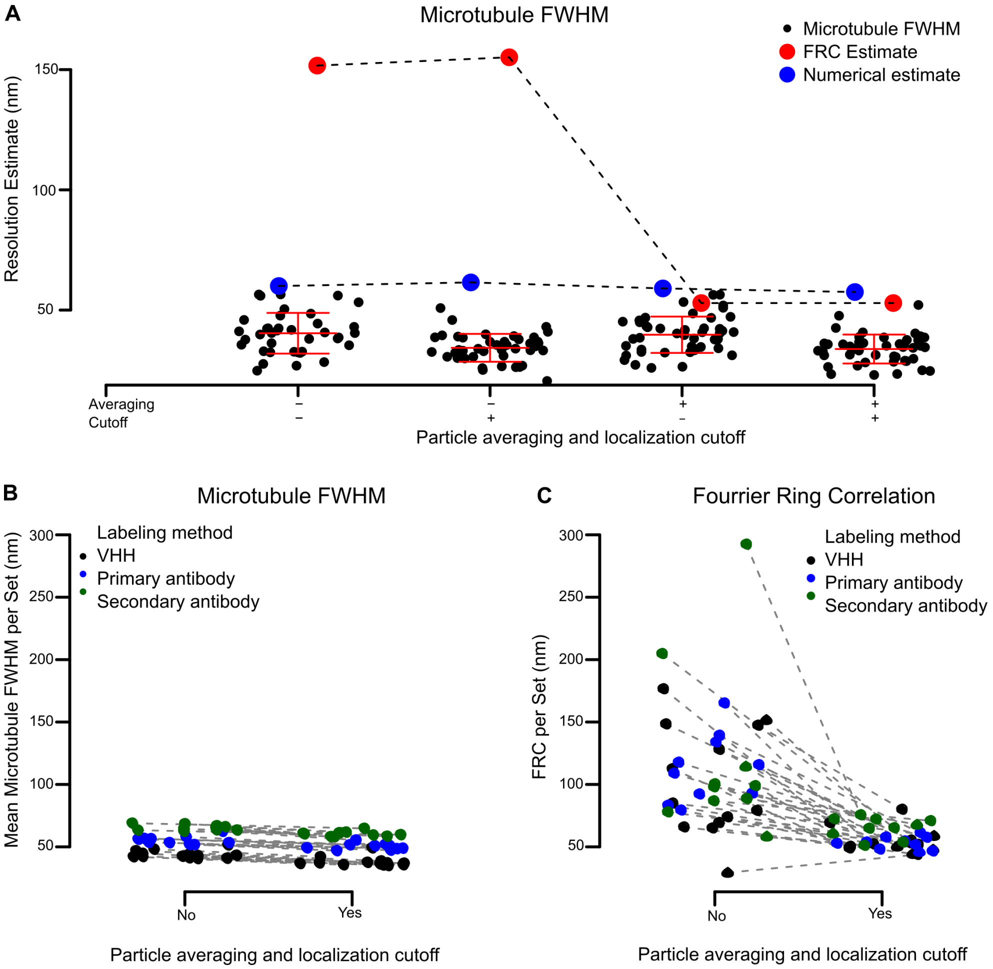

Figure 7.5: Effect of particle table post-processing on FRC resolution estimate. In a representative dataset of U2OS-cells labelled with anti-Tubulin nanobodies, the apparent width of 40 microtubules was measured by calculating the FWHM of a Gaussian curve fitted to the intensity profiles. In addition, the FRC resolution estimate was determined and a numerical estimate for the resolution was calculated as described in the text. Coordinates in the particle table corresponding to the same fluorophore where averaged (‘particle averaging’) and spots where filtered out if they showed a localisation error of more than 12.8 nm (0.2 pixel, ‘localisation cutoff’). The numerical estimate remains robust independent of the post-processing applied, but the FRC resolution estimate sharply drops when applying particle averaging. To see if this effect is unique to this dataset, we calculated the mean apparent microtubule width and FRC in 33 datasets, labelled with $\mathrm{V_HH}$, primary anti-tubulin antibody or the combination of primary anti-tubulin with labelled secondary antibody (N=11 for all three conditions). In all sets, the microtubule FWHM slightly decreases upon filtering, while the stratification of the labelling conditions remains intact (**B**). The FRC resolution estimate shows a sharp but variable decrease (actually increasing in one set) upon applying filtering. No separation of labelling methods is observed (**C**, identical to figure S8.5).

creates reconstructions of these subsets and determines the similarity in frequency space. We found that if the same fluorescent probe is localised in both subsets, this significantly reduces the resolution as determined by FRC. When multiple localisations of the same probe are averaged into one set of coordinates, the resolution estimate is reduced by a factor of three (figure 7.5**A**) and became more consistent over different experiments and with alternative estimates. Removing inaccurate localisations by applying a cutoff does not influence the FRC. The FWHM of microtubule profiles on the other hand is not affected by particle averaging and is only slightly reduced by applying a cutoff (figure 7.5**A-B**.

An intuitive and pragmatic approach to estimating resolution would be to calculate the probability of distinguishing two structures relative to the distance between their centres. A straightforward approach to achieve this estimate would be to look for pairs of microtubules and measure the minimal distance at which they can be distinguished. However, this estimate will be highly variable, since it depends on the accidental position of two microtubules and the shape of their density function. To circumvent this problem, we used a computational approach, in which we collected for each dataset a large number (>100) of intensity profiles perpendicular to the microtubule. These profiles were computationally combined in random pairs and the intensity was summated after shifting the centre of one of the distributions along the x-axis. This procedure was repeated 250 times at each point in the range from 0 to 100 nanometer with steps of 0.1 nm. The resulting probability distribution was fitted with a logistic function, with the distance at which the probability of distinguishing two structures exceeds 0.5 being considered the resolution estimate (figure 7.6**A**). Measuring the resolution of superresolution datasets using this simulation based approach excellently differentiates between the different labelling methods. There is a good correlation between resolution as measured using simulation and microtubule FWHM and FRC resolution estimates (figure 7.5**A**).

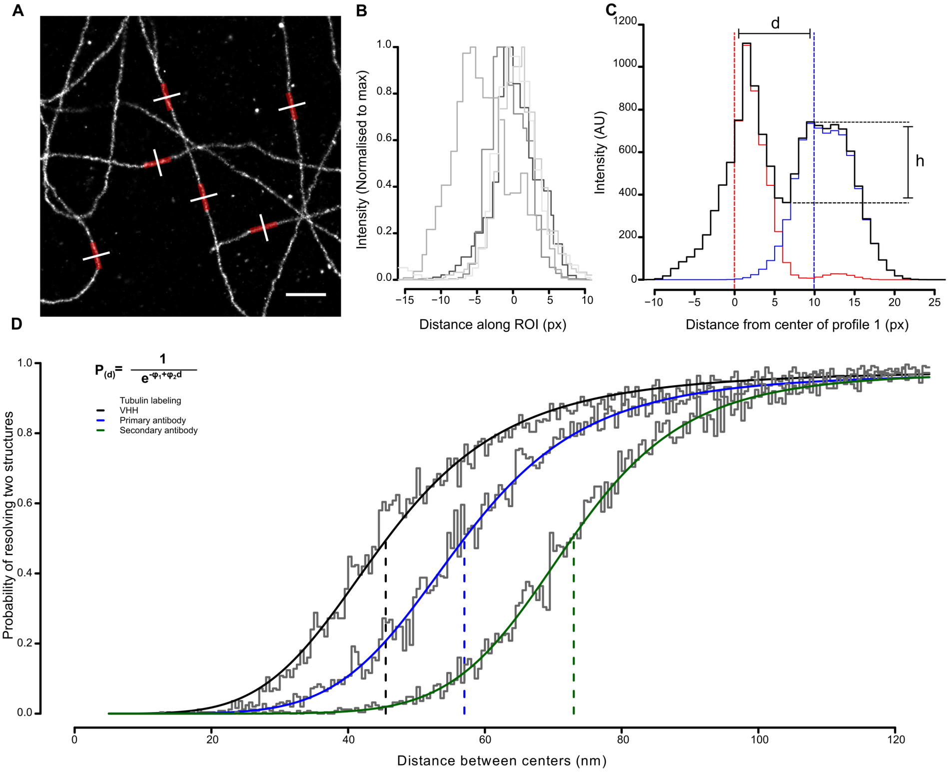

Figure 7.6: Numerical estimate of STORM resolution. A realistic estimate of STORM resolution should take into account both labelling density and localisation precision, as well as post-processing parameters such as reconstruction quality and drift correction. Since resolution is defined as the minimal distance between two objects at which they can be identified separately, we developed a method of resolution estimation that directly tests for resolving probability. (**A**) From a superresolution reconstruction of a microtubule network, a large number of cross-sections perpendicular to a microtubule where obtained. (**B**) The intensity profile of each of these cross-sections was stored in a dataset, from which n random combinations of two intensity profiles where taken. First, for each profile the location of the peak was determined by fitting with a Gaussian function. Then, one of the profiles is translated along the x-axis while the other profile remains stationary (**C**). For each distance d, a sum profile is calculated (black). A set of two profiles is considered resolved if, according to Rayleigh's criterion, the dip between the peaks (h) is at least 26.5% of the height of the lowest peak. As d increases, the resolving probability P_d will also increase in a logistic manner (**D**). The distance at which there is a 50% probability of resolving two objects can be considered a good practical estimate of a methods resolution. The method described in this figure has also been used to generate figure 8.2**C**, using profiles obtained from different datasets.

Discussion

In this chapter we have highlighted a number of practical issues encountered when performing superresolution microscopy and introduced approaches towards resolving these problems. We have also shown that the resolution that can be achieved is highly dependent on the labelling method used. The final image is only as good as the weakest link in the chain formed by localisation precision, drift correction, labelling method and sample quality. When all these components have been optimised, superresolution imaging can be an invaluable tool to visualise structure and function of individual molecules or cellular components far beyond the diffraction limit. The importance of this technique was recognised by the Royal Swedish Academy of Sciences, when they awarded the Nobel Prize in Chemistry 2014 to Eric Betzig, Stefan Hell and William Moerner for their contribution to the development of superresolution microscopy (Choquet, 2014).

The development of superresolution techniques has led to a revolution in fluorescence microscopy. An ever increasing number of papers have used these techniques to answer a specific scientific question, for example in neurobiology, where it enables analysis of receptor composition of the synapse (Dani et al., 2010; Willig and Barrantes, 2014; Ehmann et al., 2014), exploration of axonal architecture in neurons (Xu et al., 2013b) or provides new insights in the formation of aggregates associated with Alzheimer disease (Michel et al., 2014). Other research groups with an interest in virology have used STORM to image HIV envelope proteins in infected T-cells (Roy et al., 2013). A large number of studies have employed superresolution techniques to gain a better understanding of the cytoskeleton and the associated intracellular transport (Yau et al., 2014; Mikhaylova et al., 2015). From these publications, a more detailed and complex picture emerges of the organisation and function of the actin and microtubule network in cells in general and specifically in neurons (Zhong et al., 2014; Stewart and Shen, 2015). In the coming years, this collection of knowledge on the function of the cytoskeleton in healthy cells will be used to gain a better understanding of its dysfunction in disease. In this way, superresolution microscopy can be a powerful tool in the development and validation of new medical treatments which can be used in a large range of neurological disorders, including multiple sclerosis.

Resolving bundled microtubules using anti-tubulin nanobodies

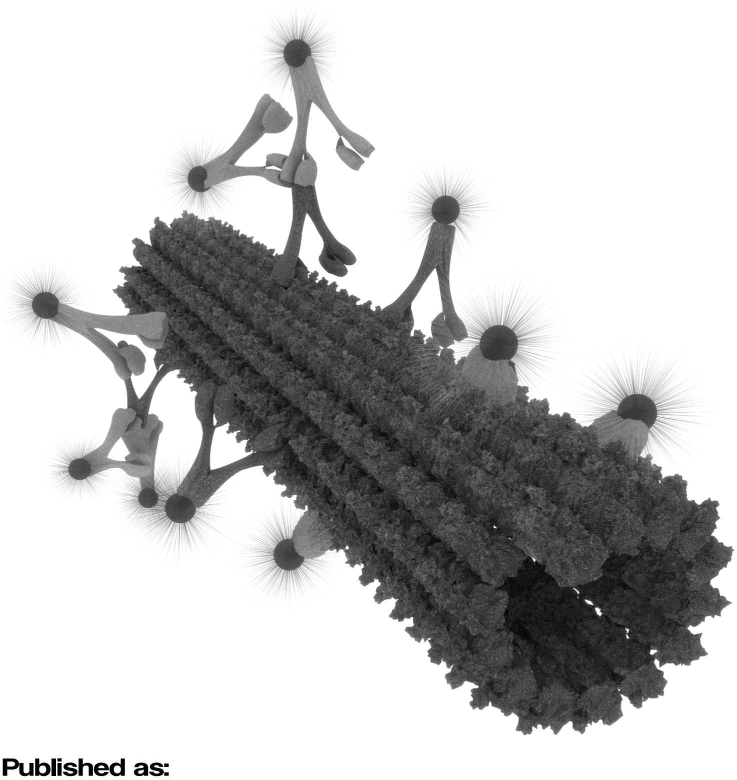

Published as:
Mikhaylova M, Cloin BM*, Finan K*, van den Berg R*, Teeuw J, Kijanka MM, Sokolowski M, Katrukha EA, Maidorn M, Opazo F, Moutel S, Vantard M, Perez F, van Bergen en Henegouwen PM, Hoogenraad CC, Ewers H, Kapitein LC; Resolving bundled microtubules using anti-tubulin nanobodies;
Nature Communications 2015. *Authors contributed equally.

8

RESOLVING BUNDLED MICROTUBULES USING ANTI-TUBULIN NANOBODIES

Abstract

Microtubules are hollow biopolymers of 25 nm diameter and are key constituents of the cytoskeleton. In neurons, microtubules are organized differently between axons and dendrites, but their precise organization in different compartments is not completely understood. Super-resolution microscopy techniques can detect specific structures at an increased resolution, but the narrow spacing between neuronal microtubules poses challenges because most existing labelling strategies increase the effective microtubule diameter by 20 nm to 40 nm and will thereby blend neighbouring microtubules into one structure. Here we develop single-chain antibody fragments (nanobodies) against tubulin to achieve super-resolution imaging of microtubules with a decreased apparent diameter. To test the resolving power of these novel probes, we generate microtubule bundles with a known spacing of 50 nm to 70 nm and successfully resolve individual microtubules. Individual bundled microtubules can also be resolved in different mammalian cells, including hippocampal neurons, allowing novel insights into fundamental mechanisms of microtubule organization in cell- and neurobiology.

Introduction

Microtubules are hollow biopolymers of 25 nm diameter and are key constituents of the cellular cytoskeleton, the mechanical framework of dynamic polymers and associated proteins that directs cell shape and facilitates intracellular transport (Kapitein and Hoogenraad, 2011). The exact spatial organization of microtubules and their bundling is of central importance to a number of fundamental cellular processes such as mitosis, cell polarization and the outgrowth of cellular processes, for example, in neurons (Kapitein and Hoogenraad, 2011). Conventional fluorescence microscopy allows selective labelling of microtubule modifications and associated proteins, but cannot resolve individual microtubules within tightly bundled microtubule arrays. Electron microscopy, in contrast, allows resolving individual microtubules, but is very labour intensive, while high-density labelling of specific proteins has remained challenging. Single-molecule localization microscopy (SMLM) provides selectivity at an increased resolution, but the extremely small spacing between neuronal microtubules (20 nm to 70 nm, Chen et al. (1992)) poses novel challenges, because existing labelling strategies typically increase the apparent microtubule diameter by 20 nm to 40 nm and will thereby blend neighbouring microtubules into one structure (Ries et al., 2012). It is therefore widely assumed that despite all progress in super-resolution microscopy, electron microscopy is still the only technique that allows insight into complex microtubule structures (Royle, 2015). Here, we use both computer simulations and experimental approaches to explore how labelling strategy affects SMLM imaging of microtubules. We develop single-chain antibody fragments (nanobodies) against tubulin and achieve super-resolution imaging of microtubules with a decreased apparent diameter, allowing us to optically resolve bundled microtubules.

Results

Simulations of microtubules with different labels

To explore the effect of label size and fluorescent probe positioning on resolving ability, we first performed numerical simulations to examine how labelling density, localization precision and fluorophore positioning affect the apparent microtubule width (determined as the full width at half maximum (FWHM) from Gaussian fits to intensity profiles integrated over 512 nm of microtubule length; Fig. 8.1a). Using a maximum localization uncertainty of 8 nm, we found that the apparent microtubule width was $\sim$31 nm for a fluorophore positioned directly at the microtubule surface (probe position of 0 nm, Fig. 8.1b). Placing the fluorophore further away increased the FWHM by double the displacement, that is, 41 nm for a fluorophore position of 5 nm. A more stringent precision cutoff resulted in decreased FWHM (Fig. 8.1c) and the FWHM decreased from 63 nm for a probe position of 15 nm and precision cutoff at 13 nm to 27 nm with fluorescent probes directly on the microtubule lattice and a precision cutoff of 3 nm.

To examine how label size affects the probability of resolving closely spaced microtubules, pairs of randomly picked profiles were superimposed with a set distance between the microtubule centres and the resulting profile was analysed. If the lowest intensity between the two microtubule centres was $>75\%$ of the intensity of the lowest peak, then the microtubules were considered to be resolved and the resolving probability was calculated as the fraction of resolvable cases out of 250. As expected, decreasing label size results in increasing the resolving probability (Fig. 8.1d). For example, given a labelling density of 7% and a precision cutoff of 13 nm, the probability of resolving microtubules with centres spaced 55 nm apart increased from 0.03 to 0.49

to 0.97 for probes positioned at 12.5 nm, 5 nm and 0 nm from the microtubule lattice, respectively (data taken from fit).

Generation and characterization of tubulin nanobodies

Conventional staining strategies often use a combination of primary antibodies binding a specific epitope, followed by a fluorescently tagged secondary antibody that recognizes the primary antibody, resulting in significant displacement of the fluorescent probe from the target (Fig. 8.1e). Typically, smaller labels have been obtained by directly conjugating a fluorophore to the primary antibody, or by using antibody fragments. Antibody fragments derived from heavy chain only camelid antibodies (nanobodies) are now emerging as promising alternatives, because of their small size (~15kDa, ~4 nm), as well as ease of selection and production. Previous work has demonstrated the usage of nanobodies to create smaller labels for SMLM. Overexpression of GFPtubulin and subsequent labelling with an anti-GFP nanobody conjugated to a fluorescent dye significantly decreased the effective diameter of individual microtubules (Ries et al., 2012). However, this strategy requires overexpression of GFPtubulin to very high levels, which will perturb cytoskeletal organization and is not possible in many biological systems.

To experimentally assess the effect of label size on resolving power, we created three novel labels for SMLM of endogenous tubulin, complementing the existing strategies using conventional antibodies. First, we developed two different nanobodies against

Figure 8.1 ***(on the next page)*****: Simulation of resolving power for different probe densities.**(**a**) Simulations of conventional (top) and single-molecule localization-based microtubule images for different probe densities, localization precision cutoffs and probe positions (distance between target molecule and fluorophore). Unless specified otherwise, probe position is 2.5 nm and precision cutoff is 8 nm. Probe density is 100% and 50% for the third and fourth row, respectively. A Gaussian localization accuracy distribution with mean±s.d. of 7.5±2.5 nm is used. (**b**) FWHM of Gaussian fits to microtubule cross sections integrated over 512 nm length as a function of probe density and for different probe positions. Error bars represent s.e.m. Each point is the average of 150 FWHMs measured on 512 nm long microtubule (MT; empty stretches along the MT were not included). (**c**) MT FWHM versus probe position for different cutoffs of the localization accuracy distribution. (**d**) Estimation of resolving power for staining of microtubules with probes at increasing distance from the microtubule. Probe density is 7%, localization precision cutoff threshold is 13 nm. Two-hundred and fifty profiles per distance. (**e**) Illustration of the different labelling strategies compared in this study. (**f**) Scheme of the in vitro microtubule bundling assay to test the resolving power of different microtubule labelling strategies. Rhodamine-labelled microtubules are assembled into planar bundles with defined spacing formed by the microtubule-bundler GFPAtMAP65-1. (**g**) Conventional (top) and SMLM (middle and bottom left) images and representative line scans (bottom right) of in vitro microtubule bundles stained with a fluorescently labelled primary anti-α-tubulin antibody (1ary-AF647) or two novel tubulin nanobodies (VHH#1 and VHH#2) conjugated to AF647. Scale bar, 1 µm. More examples are provided in Supplementary Fig. S8.3.

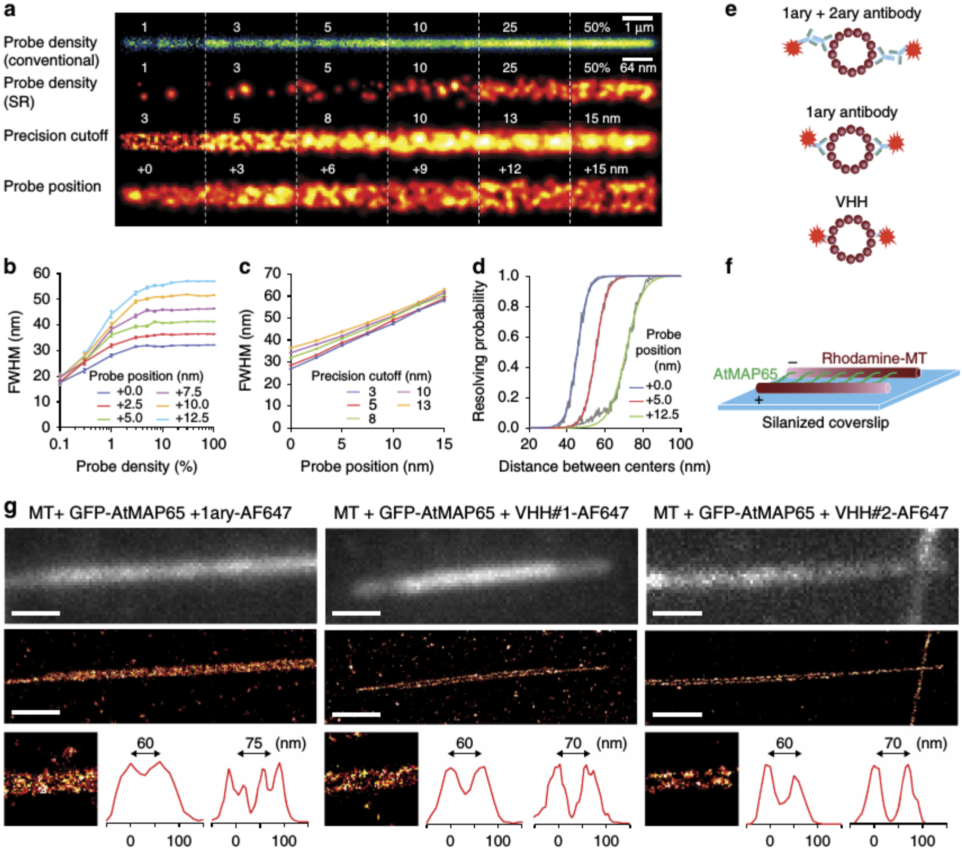
a
Probe density (conventional)
1
3
5
10
25
50%
1 µm
Probe density (SR)
1
3
5
10
25
50%
64 nm
Precision cutoff
3
5
8
10
13
15 nm
Probe position
+0
+3
+6
+9
+12
+15 nm
e
1ary + 2ary antibody
1ary antibody
VHH
b
FWHM (nm)
Probe density (%)
Probe position (nm)
+0.0
+2.5
+5.0
+7.5
+10.0
+12.5
c
FWHM (nm)
Probe position (nm)
Precision cutoff (nm)
3
5
8
10
13
d
Resolving probability
Distance between centers (nm)
Probe position (nm)
+0.0
+5.0
+12.5
f
AtMAP65
–
Rhodamine-MT
+
Silanized coverslip
g
MT+ GFP-AtMAP65 +1ary-AF647
MT + GFP-AtMAP65 + VHH#1-AF647
MT + GFP-AtMAP65 + VHH#2-AF647
60
75
(nm)
60
70
(nm)
60
70
(nm)
0
100

tubulin. One was derived from two rounds of phage display selection using a universal synthetic library of humanized nanobodies (VHH#1) and the other using an MRC7 cell library (VHH#2) (Supplementary Fig. S8.1a,b; see Methods section for details), similarly selected in two rounds of phage display. Immunoblotting with VHH#1 or VHH#2 on lysates of HEK293 cells overexpressing GFPα-tubulin or GFPβ-tubulin revealed that both nanobodies react with the endogenous tubulin as well as GFPβ-tubulin (Supplementary Fig. S8.2a,b). Conjugation of Alexa Fluor 647 (AF647) to the nanobodies did not interfere with their binding properties (Supplementary Fig. S8.2c; Supplementary Figs S8.3 and S8.4). As a second approach, recombinant human-derived single-chain variable fragments (scFvs) directed against α- and β-tubulin were purified and also coupled to AF647 (ref. (Nizak et al., 2003)). All bacterially expressed and purified labels were relatively pure and stable over long periods of time (Supplementary Fig. S8.2a).

Resolving microtubule bundles in vitro

To test the SMLM resolving power of the different microtubule labels, we established an in vitro bundling assay using polymerized microtubules in combination with the microtubule bundler AtMAP65-1, which promotes the formation of a planar network of antiparallel microtubules with a single-dimer spacing in between (Fig. 8.1f)(Gaillard et al., 2008). Silanized coverslips were used to stably attach the microtubule bundles to the coverslip surface to allow for subsequent staining procedures. As a control, we performed SMLM on non-stained samples to which fluorescently tagged tubulin (conjugated to HiLyte Fluor 647) was added in to the polymerization mix. In this condition, most bundles could be clearly resolved with an average spacing of 65 ± 2 nm (s.e.m., n=56, Supplementary Fig. S8.3a). Both VHH#1 and VHH#2 conjugated to AF647 efficiently decorated the bundles and in most cases the individual microtubules could be clearly distinguished when the microtubule centres were 60 nm to 70 nm apart (Fig. 8.1g, Supplementary Fig. S8.3b). In contrast, when a conventional primary anti-α-tubulin antibody directly coupled to AF647 was used, such bundled microtubules could often not be resolved.

Comparative analysis of microtubule labels in adherent cells

When we tested our nanobodies on microtubules in cells, we found that we could resolve microtubules that were spaced down to 40 nm (Fig. 8.2a). To quantitatively compare the nanobody approach with the other staining methods in cells, we labelled microtubules in fixed Ptk2 and COS-7 cells using different tubulin labels conjugated to AF647. We determined the FWHM from a Gaussian fit to intensity profiles perpendicular to the microtubule averaged over 512 nm length to rule out possible profile artifacts that could arise from low labelling density (Fig. 8.1b). We found that individual microtubules were densely labelled with the most common diameter (average mode±s.e.m.) varying from 39.3 ± 0.8 nm (VHH#2, N=10 data sets with in total n=1,365 profiles) to 54.0 ± 1.2 nm and 61.7 ± 0.8 nm (directly conjugated primary anti-tubulin antibody, N=10, n=2,462, and primary anti-tubulin+secondary-AF647, N=10, n=2460, respectively; Fig. 8.2b; Supplementary Fig. S8.4a,b; see Methods section for details and Supplementary Fig. S8.5a for statistical testing). Because in the rendering of the SMLM images we rejected all localizations with localization precision $\geq$13 nm, these values suggest that fluorophores coupled to primary antibodies are on average $\sim$12.5 nm displaced from the microtubule lattice (Fig. 8.1c). Strikingly, this distance is reduced to <2.5 nm for VHH#2.

To translate the observed microtubule FWHM into a resolution estimate, we again analysed composite profiles obtained by superimposing two randomly picked profiles with a set distance between the microtubule centres (Fig. 8.2c). On the basis of cumulative probability plots obtained for the VHH#1, VHH#2, primary and primarysecondary antibody labellings, $\sim$50% of all bundled microtubules with 25 nm lattice-to-lattice spacing (corresponding to 50 nm between peaks) will be resolved by the nanobody labels, whereas the directly conjugated primary antibodies or the sandwich labelling will only resolve $\sim$20% and $\sim$5% of all microtubule pairs, respectively. Consistent with the in vitro bundling results, VHHs are expected to resolve >90% of microtubule pairs with a lattice-to-lattice spacing of 60 nm, which is the typical spacing of tightly bundled microtubules in neuronal dendrites (Chen et al., 1992).

To further quantify the gain in resolution, we used the Fourier Ring Correlation resolution measure (FRCrm) as an independent, quantitative estimate of resolution

Figure 8.2 *(on the next page)*: (**a**) SMLM reconstruction of a Ptk2 cell stained with VHH#1 and intensity profile of closely spaced microtubules along the yellow line. Yellow arrows indicate microtubule ends. Scale bar, 1 µm. A larger field of view of the same cell can be found in Supplementary Fig. S8.4b. (**b**) Histograms of microtubule FWHM for different probes. scFvs: mixture of human single-chain antibody fragments (scFvs) recognising α- and β-tubulin. For representative images, see Supplementary Fig. S8.4a. From top to bottom: n=1,365, 547, 352, 2,462, 2,460 profiles from N=10, 5, 9, 10, 10 different acquisitions. Mean (blue) and mode (red) value are indicated ±s.e.m. (using N). (**c**) Estimation of resolving power for different labels obtained by combining arbitrarily selected line profiles at increasing distance between centres. (**d**) Scatter plot of FRC resolution estimate versus microtubule FWHM for images of microtubules in COS-7 cells stained with different labels. Error bars depict 95% confidence intervals. (**e**) Overview 3D-SMLM reconstruction of a U2OS cell stained with AF647-labelled VHH#1. The z-depth is colour-coded according to the scale on the left of the image. Scale bar, 5 µm. (**f**) Magnified image of the inset in (**e**). Colour code is the same as in (**e**). Scale bar, 500 nm. (**g**) Area containing parallel microtubules at different depth in the cell. Colour code is the same as in (**e**). Scale bar, 500 nm. (**h**) Collapsed cross section (z-x) of the volume depicted in (**g**). Scale bar, 100 nm. (**i-k**) SMLM reconstruction of microtubule bundles labelled with VHH#1 in the dendrites of a hippocampal primary neuron. Yellow arrows indicate microtubule ends and yellow lines were used for line scans across densely packed microtubule bundles (**j,k**). Inset shows the diffraction-limited fluorescence image. Scale bar, 2 µm. (**l**) 3D-SMLM reconstruction of a hippocampal primary neuron labelled with VHH#1. The Z-depth is colour-coded according to the scale on the left of the image. Yellow arrows indicate microtubule ends. Inset shows the diffraction-limited fluorescence image. Scale bar, 2 µm.

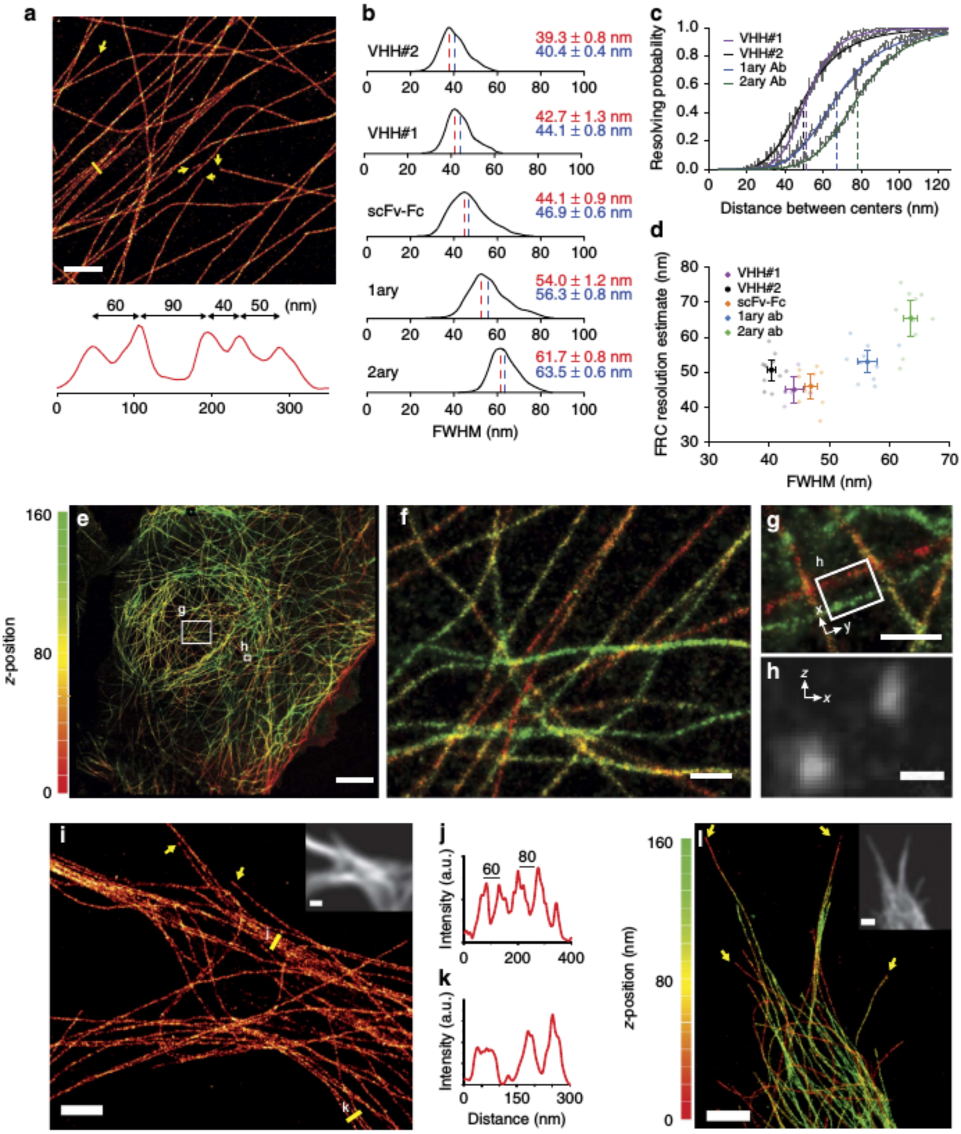
a
60
90
40
50
(nm)
0
100
200
300
b
VHH#2
39.3 ± 0.8 nm
40.4 ± 0.4 nm
VHH#1
42.7 ± 1.3 nm
44.1 ± 0.8 nm
scFv-Fc
44.1 ± 0.9 nm
46.9 ± 0.6 nm
1ary
54.0 ± 1.2 nm
56.3 ± 0.8 nm
2ary
61.7 ± 0.8 nm
63.5 ± 0.6 nm
0
20
40
60
80
100
FWHM (nm)
c
Resolving probability
1.0
0.8
0.6
0.4
0.2
0.0
VHH#1
VHH#2
1ary Ab
2ary Ab
0
20
40
60
80
100
120
Distance between centers (nm)
d
FRC resolution estimate (nm)
80
70
60
50
40
30
VHH#1
VHH#2
scFv-Fc
1ary ab
2ary ab
30
40
50
60
70
FWHM (nm)
160
80
0
z-position
e
g
h
f
g
h
x
y
h
z
x
i
j
k
j
Intensity (a.u.)
60
80
0
200
400
k
Intensity (a.u.)
0
150
300
Distance (nm)
160
80
0
z-position (nm)
l

that accounts for both localization precision and probe density (Nieuwenhuizen et al., 2013). Whereas direct application of the available FRC ImageJ-plugin to our data yielded highly variable results, this could be circumvented by data preprocessing to average different localizations emerging from the same fluorophore emitting over multiple frames (Supplementary Fig. S8.5b). As expected, smaller apparent diameters also resulted in better FRCrm resolution estimates, with the exception of VHH#2, whose lower labelling density resulted in a worse FRCrm compared to VHH#1, despites its smaller FWHM. For VHH#1, the average FRCrm was 454 nm (Fig. 8.2d). These results demonstrate that our novel anti-tubulin nanobodies provide improved resolution.

Tubulin nanobody for 3D-SMLM in U2OS cells and neurons

To test how anti-tubulin nanobodies performed in three dimentional (3D)-SMLM, we labelled microtubules in U2OS cells with VHH#1 and performed 3D-SMLM using the biplane approach (Lukinaviius et al., 2014). We found that microtubules could easily be resolved in z-direction (Fig. 8.2e-h) at distances of 100 nm. Finally, we used the VHH#1 nanobody to perform SMLM on microtubules in primary hippocampal neurons (Days in vitro, DIV1) and could successfully resolve individual microtubules in neurites (Fig. 8.2i-l). The cross-sections across densely packed microtubule bundles indicate a center-to-center spacing of 60 nm to 80 nm, consistent with earlier results using electron microscopy on cross sections (Chen et al., 1992). In several cases, ends of individual microtubules could be clearly identified (Figs 8.2i,l, arrows). Thus, tubulin nanobodies can be used to resolve neuronal microtubule bundles.

Discussion

We have introduced novel labels for microtubules that allow using SMLM to resolve previously inaccessible functional details of microtubule organization such as bundling, both in vitro and in fixed cells. These labels nicely complement the recently introduced live-cell marker for tubulin (Lukinaviius et al., 2014) that allows nanoscopy using STED (Stimulated Emission Depletion) microscopy and SIM (Structured Illumination Microscopy) in living cells, but does not remain bound to microtubules upon fixation (Supplementary Fig. S8.6). Microtubules are key components of many complex cytoskeletal assemblies and their organization, polymerization, motility and interactions with motor proteins are controlled by a plethora of posttranslational modifications and modulating proteins, such as microtubule polymerases, severing proteins and bundlers. Therefore, our ability to resolve individual microtubules in such cytoskeletal assemblies paves the way towards a deeper understanding of the mechanisms underlying microtubule organization and function, both in health and disease.

Methods

VHH#1 selection

VHH#1 was selected from a novel library of 3×10^9 humanized nanobodies. Briefly, commercial biotinylated tubulin (Cytoskeleton) was diluted to obtain a 10 nM to 20 nM solution (1 mL final) and efficient recovery of biotinylated tubulin was confirmed on 50 µL streptavidin-coated magnetic beads (Dynal). Fractions of bound and unbound samples were compared by western blot using streptavidin-HRP. Adequate amounts of beads and biotinylated antigen were incubated for 2 h with the phage library (1×10^{13} phages diluted in 1 mL of PBS containing 0.1% Tween-20 and 2% nonfat milk). Phages were previously adsorbed on empty streptavidin-coated magnetic beads to remove nonspecific binders. Phages bound to tubulin-coated beads were recovered on a magnet and washed 10 times (round 1) or 20 times (round 2) using PBS containing Tween-20 0.1%. Bound phages were eluted using 500 µL triethylamine (100 µM) for 10 min. Eluted phages were neutralized using 1 M Tris pH 7.4. Elution was repeated once more. *E. coli* (TG1) were infected with the eluted phages. Round 2 was carried out using 1×10^{12} phages as input. After round 2, 40 bacteria clones were picked at random and used to produce nanobodies in the culture medium. Nanobody specificity was analysed by immunofluorescence as described before (Nizak et al., 2003) and nanobodies staining microtubules were analysed further.

VHH#1 expression and purification

For production of VHH#1, WK6 *E. coli* containing the plasmid pHEN2-VHH#1-His$_6$-cMyc$_3$ were grown in 2 L of 'Terrific Broth' (17 mM KH$_2$PO$_4$, 72 mM K$_2$HPO$_4$, 12 g L^{-1} tryptone, 24 g L^{-1} yeast extract, 0.4% glycerol) containing 2 mM MgCl$_2$, 0.1% glucose, and 100 µg mL^{-1} ampicillin with shaking at 37 °C until the *E. coli* had an OD$_{600}$ of 0.6-0.9. Isopropyl β-D-1-thiogalactopyranoside (IPTG) was then added to a concentration of 0.5 mM, and the flasks were shaken at 28 °C overnight (~16 h). To extract the nanobody from the periplasmic space, cells were centrifuged (5,000g, 10 min), resuspended in 24 mL of TES buffer (0.2 M Tris pH 8.0, 0.5 mM EDTA, 0.5 M sucrose) and shaken for 1 h at 4 °C. The cell-TES mixture was then diluted by the addition of 36 mL of TES/4 buffer (50 mM Tris pH 8.0, 0.125 mM EDTA, 0.125 M sucrose), and shaken for 1 h at 4 °C. The cells were then pelleted (5,000g, 10 min), and the nanobody-containing supernatant removed. The His6-tagged VHH#1 was then purified using HisPur cobalt-agarose resin (Thermo Scientific) following manufacturers instructions. The eluted protein was concentrated ~10-fold using 'Vivaspin columns (3 kDa MWCO; General Electric). SDS-polyacrylamide gel electrophoresis (PAGE) and Coomassie-staining of the resulting gels revealed the nanobody to be >90% pure. VHH#1 was dialysed overnight against PBS at 4 °C to remove any residual imidazole. The 2 L of culture yielded ~50 µg of pure nanobody. The stability of VHH#1 was analysed by immunoblotting of a sample stored at 4 °C for >4 months. Two micrograms of VHH#1 were used for Coomassie staining and about 100 ng for immunoblotting using anti-VHH serum 976 (1:2,000 (ref. (Kijanka et al., 2013))) or mouse monoclonal anti-c-myc antibody (1:5,000, Abcam) recognising the carboxy-terminal myc-tag of VHH#1.

VHH#2 selection

The VHH phage display library was generated from llamas immunized with MCF7 cells (Kijanka et al., 2013). Two rounds of selection were performed as described (Kijanka et al., 2013). For selection of VHHs against tubulin, the bovine brain tubulin (Cytoskeleton) was directly coated onto 96-well NUNC Maxisorp plates (Thermo Scientific) in a series of dilutions 0 µg, 0.1 µg, 1 µg and 5 µg in PBS) by incubation for 30 min at room temperature and then overnight at 4 °C. Phages retrieved from the phage-glycerol stock were preincubated with 2% milk-PBS for 30 min at room temperature, and added to the tubulin-coated wells and kept at room temperature on a shaker for 2 h. Afterwards wells were washed extensively with 0.05% Tween-20 in PBS. Bound phages were eluted with 100 µL per well of 0.1 M triethylamine followed by recovery via infection of *E. coli* TG1. Phages from the first round were subjected to the second round of selection with 0 µg, 0.1 µg, 1 µg and 5 µg of coated tubulin. *E. coli* TG1 were infected with the phages from the second selection and plated on LB-agar plates supplemented with ampicillin. Ninety-six random colonies were picked for testing. Expression of VHHs targeted to the bacterial periplasm was induced by addition of 1 mM IPTG at 37 °C overnight. To obtain the periplasmic fraction, bacterial pellets were resuspended in 10 volumes of PBS (pH 7.4) containing protease inhibitor cocktail (Roche), subjected to two freeze/thaw cycles, and spun down for 15 min at 4,600 r.p.m. Periplasm was collected as supernatant fraction. Specificity of VHHs for tubulin was determined by enzyme-linked immunosorbent assay.

VHH#2 expression and purification

For efficient bacterial expression, four of the most successful and divergent VHH sequences were directly subcloned from pUR8100 into modified pET28a-EPEA vector using SfiI/NotI restriction sites. pET28a-EPEA was created inserting AAACAA-AGYQDYEPEA-STOP sequence (NotI/XhoI) in front of the C-terminal 6 × His-myc sequence which allows purification with Capture Select C-tag matrix (Life Technologies). Although all of the constructs were expressed and purified, from now on, we focused on one of the VHH sequences showing the best performance during protein production and labelling (Clone H, that is, VHH#2).

For protein production, an overnight culture of *E. coli* BL21(DE3) transformed with pET28a-VHH#2-EPEA was grown in LB supplemented with kanamycin till OD600∼0.8 and induced with 0.5 mM IPTG for 4 h at 2 °C or at 20 °C overnight. VHHs were purified from the periplasmic fraction in PBS (pH 7.4) containing 0.5% Triton-X100, protease inhibitor cocktail (Roche) and 0.5 mM TCEP and purified using Capture Select C-tag matrix according to the manufacturers instructions (Life Technologies). Bound VHH was eluted from the beads in buffer containing 2 M $MgCl_2$, 20 mM Tris-HCL (pH 7.0) and immediately dialyzed against PBS (pH 7.4). Impurities were removed by size exclusion chromatography performed on an ÄKTA FPLC system

(ÄKTA purifier, GE Healthcare, UK) using a Superdex 75 gel filtration column. Fractions containing VHH#2 were pooled and upconcentrated to 1 µg µL^{-1} to 1.5 µg µL^{-1}.

Cell culture and immunostaining

COS-7, MRC5 or Ptk2 cells were plated on 19 mm diameter glass coverslips or 8-well Labtek chambers (Thermo scientific), respectively and cultured in DMEM/Hams F10 (50/50%) medium supplemented with 10% FCS and 1% penicillin/streptomycin for 2-3 days. Culturing of primary neurons was described before(Kapitein et al., 2010b). Briefly, hippocampal primary neurons were prepared from embryonic day 18 rat brains. Cells were plated on coverslips coated with poly-L-lysine (30 µg mL^{-1}) and laminin (2 µg mL^{-1}) at a density of 40,000 per well. Hippocampal cultures were grown in Neurobasal medium (NB) supplemented with B27, 0.5 µM glutamine, 12.5 µMM glutamate and penicillin/streptomycin. For optimal microtubule imaging, cells were pre-extracted and fixed in extraction buffer containing 80 µM PIPES (pH 6.9), 7 mM MgCl$_2$, 1 mM EGTA, 0.3% Triton-X100 (Sigma-Aldrich), 150 mM NaCl, 5 mM glucose, 0.25% glutaraldehyde (Electron Microscopy Sciences) for 90 s at 37 °C and then in PBS with 4% PFA and 4% sucrose for 10 min at 37 °C. After fixation, cells were washed two times in PBS and cells were further permeabilized for 10 min in PBS with 0.25% Triton-X100. Cells were then washed three times in PBS, quenched for 10 min with 50 mM NH$_4$Cl in PBS, washed again and incubated with Image-IT (Molecular Probes) for 30 min at RT. After three washes with PBS, blocking buffer 1 (used for staining with antibody and VHH#2) containing 2% w/v 2% w/v BSA-c (Aurion)11, 0.2% w/v gelatin, 10 mM glycine, 50 mM NH$_4$Cl in PBS (pH 7.4) or blocking buffer 2 (used for VHH#1, also works for VHH#2) containing 10% FHS (Gibco, Life Technologies) and 0.1% Triton-X-100 in PBS (pH 7.4) was added for 30-45min. Primary antibodies or VHHs were diluted in corresponding blocking buffer and were incubated overnight at 4 °C (antibody) or 1-2 days at room temperature (VHHs). For the secondary antibody labelling, coverslips were washed from the primary antibody and anti-mouse antibody conjugated to AF647 were diluted in a same blocking buffer and added for 1 h to 1.5 h at room temperature. Antibodies were α-tubulin (Sigma-Aldrich, clone B-5-1-2, T5168) conjugated to AF647 (dilution 1:100), AF647 conjugated goat anti-mouse IgG (H+L) secondary antibody (Molecular Probes, Life Technologies, dilution 1:500). VHH#1 and VHH#2 were diluted to about 10 µg mL^{-1}. All coverslips were extensively washed with PBS shortly before imaging, post-fixed in PBS with 4% PFA and 0.25% GA for 10 min at room temperature and again extensively washed with PBS. For co-staining with F-actin marker, neurons already labelled with VHH#1-AF647 were washed in PBS and incubated with AF568 Phalloidin from Molecular probes (Life Technologies, 1:200 in PBS) for 20 min, extensively washed in PBS and mounted for imaging. For live staining with SiR-tubulin (Lukinaviius et al., 2014), 100 nm of the probe was added to the growth medium and incubated for 1 h at 37 °C, 5% CO2. MRC5 cells expressing plus-end microtubule marker EB3-GFP were used for the life imaging. COS7 cells were fixed with standard pre-extraction/fixation protocol (see above), mixture of 3% PFA and 1% glutaraldehyde for 10 min at 37 °C or 4% PFA for 10 min at 37 °C. Fixed cells were extensively washed in PBS and processed for imaging.

Ptk2 cells were fixed at 37 °C using prewarmed PEM buffer (15 mM PIPES pH 7, 1 mM $MgCl_2$, 10 mM EGTA) containing 0.1% Triton X-100 and 0.4% glutaraldehyde for 10 min. They were washed three times with PBS, incubated with PBS containing 50 mM NH_4Cl for 10 min, washed twice with PBS, incubated with freshly prepared PBS with 0.1 mg mL^{-1} sodium borohydride for 5 min, washed three times with PBS, incubated with Image-IT blocking solution (Life Technologies) for 30 min, washed three times with PBS, and then incubated with blocking buffer 2. Labelled VHH#1 nanobody was then added to a final concentration of 600 nM, and the cells incubated overnight at 25 °C (note that similar labelling was obtained with a 4 h incubation). The cells were then washed three times with PBS containing 0.1% Triton X-100, and twice with PBS and processed for imaging.

In vitro microtubule bundling assay

Rhodamine-labelled microtubuless were prepared from stabilized seeds as described earlier(Mohan et al., 2013), and stored at −80 °C. HiLyte Fluor 647-tubulin was purchased from Cytoskeleton and HiLyte Fluor 647-microtubules seeds were made in a same way like Rhodamine-microtubule seeds. The seeds were quickly transferred into a 37 °C water bath, incubated for 5 min and kept in the dark at room temperature for 24 h. Labelled microtubules were diluted 1:30 in PEM80 (80 mM PIPES, pH 6.9, 2 mM $MgCl_2$, 1 mM EGTA) containing 10 µM of Taxol (Sigma). Then 50 µL of this dilution was mixed with 0.2 ng of recombinant purified GFP-AtMAP65-1 (ref. (Gaillard et al., 2008)) and incubated for 20 min at room temperature to allow formation of bundles. Imaging flow chambers were assembled using microscope slides and coverslips connected with double-sided tape. Before each experiment coverslips were plasma cleaned for 10 min, coated for 1 min with 0.4% diethylenetriamine diluted in H_2O and baked for 1 h at 200 °C. Microtubules with and without GFP-AtMAP65-1 were washed into the flow channels and kept in the dark. After 20 min, unbound microtubules were washed out with PEM80 containing 1 µM Taxol. For the immunostainings, attached Rhodamine-microtubules were first fixed for 3 min with 4% PFA and 0.25% GA in PEM80, washed with PEM80 containing 1 µM Taxol, quenched for 10 min with 50 mM NH_4Cl in PBS, washed again and unspecific binding of proteins to the surface was blocked with blocking buffer 1 for 30 min at room temperature. Samples intended for staining with VHH#1 were in addition blocked with Image-IT for 30 min and then blocked with blocking buffer 2 (see above). Primary AF647-labelled anti-α-tubulin antibody (1:20), VHH#1 (10 ng µL^{-1}) or VHH#2 (10 ng µL^{-1}) were diluted in corresponding blocking buffer, added to the flow channels and incubated in room temperature for 2 h in the dark. Stained samples were postfixed for 3 min with 4% PFA and 0.25% glutaraldehyde in PEM80, washed with PEM80 and imaged immediately.

SMLM imaging

Imaging of fixed cells stained with microtubule probes conjugated to AF647 was performed using 10 mM to 100 mM mercaptoethylamine (MEA), 5% w/v glucose, 560 µg mL^{-1} glucose oxidase, 40 µg mL^{-1} catalase in PBS. Imaging mixture for in vitro microtubule samples contained 100 mM MEA, 5% w/v glucose, 560 µg mL^{-1} glucose oxidase, 40 g mL^{-1} catalase in PEM80 containing 1 µM Taxol.

SMLM microscopy (Betzig et al., 2006; Heilemann et al., 2008; Rust et al., 2006) was performed on a Nikon Ti microscope equipped with a 100 × Apo TIRF objective (NA. 1.49), a Perfect Focus System and an additional 2.5 × Optovar to achieve an effective pixel size of 64 nm. Evanescent or oblique laser illumination was achieved using a custom illumination pathway with a 15 MW 405 nm diode laser (Power Technology), a 50 MW 491 nm DPSS laser (Cobolt Calypso), and a 40 MW 640 nm diode laser (Power Technology). Fluorescence was detected using an Andor DU-897D EMCCD camera. All components were controlled by Micromanager software (Edelstein et al., 2010). For SMLM imaging of AF647, the sample was continuously illuminated with 640 nm wavelength light. In addition, the sample was illuminated with 405 nm light at increasing intensity to keep the number of fluorophores in the fluorescent state constant. Typically 5,000-15,000 frames were recorded per acquisition with exposure times of 30 ms to 40 ms.

SMLM imaging of Ptk2 cells was performed as described (Dempsey et al., 2011). Imaging chambers were filled with Buffer TN (50 mM Tris-HCl pH 8, 10 mM NaCl) containing 10% glucose, 10 mM MEA (pH adjusted to 8 with KOH; Sigma), 40 µg mL^{-1} catalase (Sigma, C40-100MG), and 0.5 mg mL^{-1} glucose oxidase (Sigma, G2133-50KU), and sealed with a coverslip. Imaging was performed using a standard Nikon NSTORM microscope, using a 647 nm laser adjusted to provide total internal reflection-based illumination. Videos were acquired using an iXon EMCCD (Andor) and a 100Hz frame rate, with a typical acquisition containing 50,000-100,000 frames. A 488 nm laser was sometimes used to increase the rate at which the AF 647 molecules exited the dark state; however, this was typically not necessary. Acquisitions were then processed to create super-resolution images using custom-written software (Ries et al., 2012) (Fig. 8.2, Supplementary Fig. S8.4b). For 3D-SMLM, we use the biplane method as described (Ries et al., 2012; Juette et al., 2008).

SMLM localization and rendering algorithms

For Fig. 8.1 and Supplementary Figs S8.3 and S8.4a, we used localization software written in Java as an ImageJ plugin, called Detection of Molecules. Each image in an acquired stack was convoluted with the two-dimensional (2D) Mexican hat kernel matching the microscopes point spread function (PSF) size. The intensity histogram of the convolved image was fitted to a Gaussian distribution and used to calculate the threshold intensity value (mean value of the fit plus three s.d.). The maximum intensity values within individual spots were chosen as initial positions for the peaks fitting performed on the original image. We used unweighted nonlinear least squares fitting with Levenberg-Marquardt algorithm to the assumed asymmetric 2D Gaussian PSF.

Only fits with a calculated width within ±30% of the measured PSFs standard deviation were accepted. Localizations within one pixel distance in a number of successive frames were considered to arise from the same molecule. In this case the weighted mean was calculated for each coordinate, where weights were equal to inverse squared localization precision. The resulting table with molecule coordinates and precision was used to render the final localization image with 5 nm pixel size for microtubule FWHM analysis, and 10- or 20 nm pixel size otherwise. Each molecule was plotted as a 2D Gaussian with integrated intensity equal to one and with s.d. equal to the localization precision. SMLM-localization and rendering of 3D data into images was done as described before (Ries et al., 2012).

Analysis of super-resolution images

To estimate the FWHM of the microtubules, line region of interests were drawn by hand on the microtubules in the reconstructed image. A custom-made ImageJ macro was then used to generate an intensity profile perpendicular to the region of interests, integrating the intensity values over a length of 500 nm. A Gaussian distribution was fitted to the intensity profile, from which the FWHM was derived as $FWHM = 2\sqrt{2log2} \times \sigma$.

In order to calculate the probability of separately resolving two microtubule profiles, all profiles used for FWHM calculation were normalized along the y axis to an area under the curve of 1 and centred on the x axis on the mean derived from the Gaussian distribution fit. To allow for subpixel shifts, bicubic interpolation was applied to the intensity profiles. Two profiles were randomly selected and positioned with their centres a distance between 5- and 125 nm apart from each other. The profiles were summed, and the dip in intensity between the two peaks was calculated. If this dip was >25% of the intensity of the lowest peak, the two profiles were considered to be resolved. After 250 iterations with different randomly selected profiles, the distance between the means was increased by 0.5 nm and the procedure was repeated. At each position, the ratio between resolved and non-resolved sets of intensity profiles was used to calculate the resolving probability. All analysis was performed in the open source software package R.

An independent estimate of image resolution was obtained using Fourier Ring Correlation (FRC), as described previously (Nieuwenhuizen et al., 2013). In short, particle tables generated by Detection of Molecules were converted to tables with only x- and y-coordinates for each localization remaining. The FRC plug-in for ImageJ created by the Delft University of Technology Quantitative Imaging Group was then used to obtain a resolution estimate. To obtain consistent results, it was essential to perform frame-to-frame fluorophore linking (see above, Supplementary Fig. S8.5).

Acknowledgements

We thank Amol Aher for preparing stabilized microtubule seeds, Jérémie Gaillard for AtMAP65 purification, Rachid El Khoulati for providing the pET28a-EPEA vector, Roderick Tas for technical support, and Elly van Donselaar for advice. This research is supported by the Dutch Technology Foundation STW, which is part of The Netherlands Organisation for Scientific Research (NWO). Additional support came from NWO (NWO-ALW-VICI to C.C.H and NWO-ALW-VIDI to L.C.K.) and the European Research Council (ERC Starting Grant to L.C.K.), CTMM (Mammoth project to MK and PvBeH). M.M. is recipient of a European Molecular Biology Organization (EMBO) Long-Term Fellowship (EMBO ALTF 884-2011) and Marie Curie IEF (FP7-PEOPLE-2011-IEF). The Swiss National Fund (H.E., K.F.). F.O. acknowledges the support from the Deutsche Forschungsgemeinschaft Center for Molecular Physiology of the Brain/Excellence Cluster 171, Göttingen, Germany. Support to MV came from CNRS (Centre National de la Recherche Scientifique).

Contributions

H.E. and L.C.K. conceived the project (independently). M.Mi. developed VHH#2, together with M.M.K., M.S. and P.M.P.v.B.e.H., who provided the MRC7 library. K.F., H.E., F.P. and S.M. developed VHH#1. M.Ma. and F.O. produced scFvs. M.Mi., B.C., R.v.d.B., and K.F. performed experiments and analysed the data. J.T. and E.K. developed simulations. M.V. contributed AtMAP65. C.H., H.E. and L.K. supervised the project.

Competing financial interests

The authors declare no competing financial interests.

Supplementary Information

Supplementary Figures

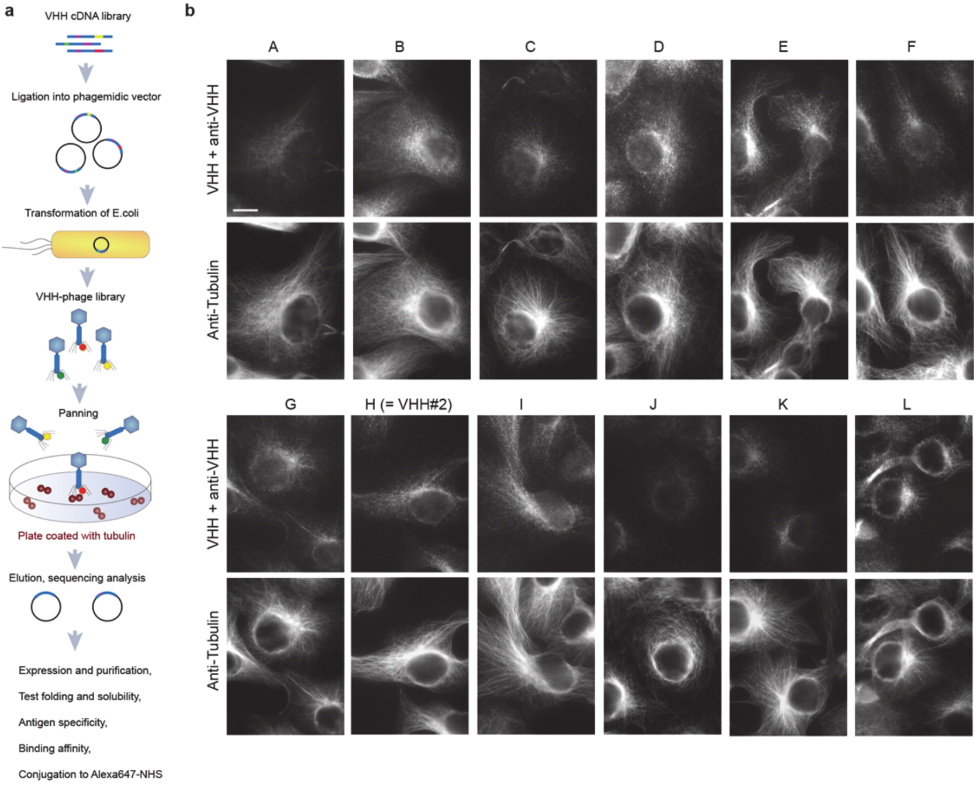

Figure S8.1: Nanobody selection. (**a**) Schematic workflow for production of tubulin nanobodies and steps required for selection and quality control of binders. For the details see Materials and methods. (**b**) Widefield images of COS-7 cells stained with the periplasm obtained from *E. coli* expressing different VHH sequences (named A-L). VHHs derived from two rounds of panning were tested by ELISA. Then the periplasmic fraction containing the strongest binders was applied on fixed COS-7 cells. Binding of VHHs was detected by immunostaining with polyclonal anti-VHH antibody and by co-localization with microtubules co-stained with mouse anti-α-tubulin antibody. VHH clone H is the same as VHH#2. Scale bars are 5 µm.

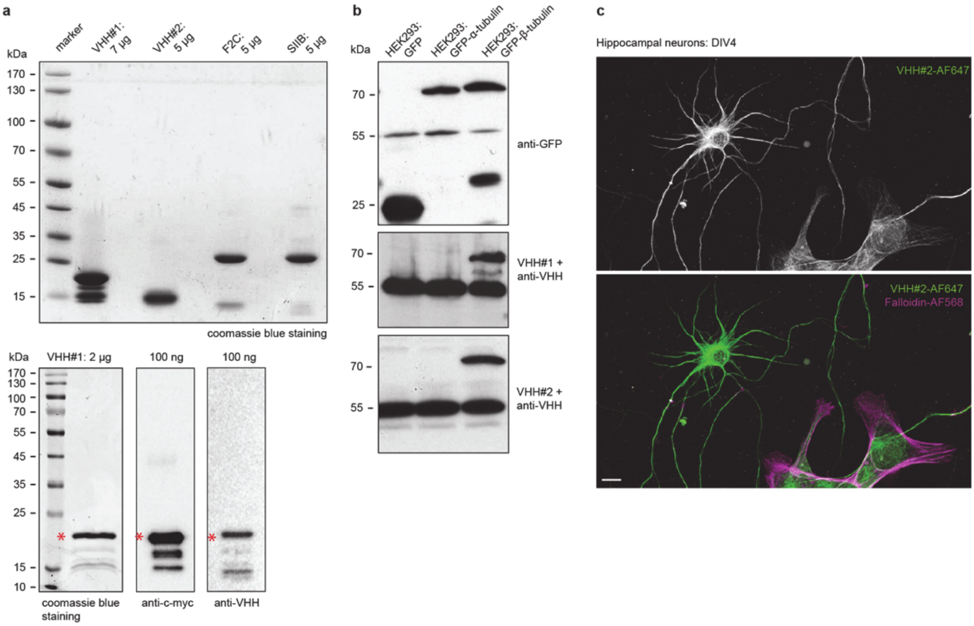

Figure S8.2: Biochemical properties of tubulin-binding probes. (**a**) Upper panel: Coomassie blue stained SDS-PAGE gel with purified VHH#1, VHH#2 and the antibody fragments F2C and SIIB. The smallest probe VHH#2 migrates at 15 kDa, followed by VHH#1 (20 kDa) and the antibody fragments (about 30 kDa). 5 µg to 7 µg of protein were loaded per lane. Lower panel: Coomassie blue stained SDS-PAGE gel with purified VHH#1 stored for more than four months at 4 °C and corresponding immunoblots with anti-VHH and anti-myc antibody. Red star indicates intact VHH#1-myc-6xhis band. (**b**) Immunoblot showing that both tubulin nanobodies are directed against β-tubulin. Lysates were prepared from HEK293 cells transfected with empty GFP plasmid, GFP-α-tubulin or GFP-β-tubulin, and stained with VHH#1, or VHH#2 followed by incubation with anti-VHH rabbit antibody. As a positive control for expression of GFP proteins, the same membranes were developed with anti-GFP rabbit antibody. VHH#1 and VHH#2 recognize the endogenous and overexpressed GFP-β-tubulin, but not GFP-α-tubulin. (**c**) Confocal image of DIV4 hippocampal neurons stained with VHH#2 directly labeled with AF647 and co-stained with F-actin marker Phalloidin-AF568. Note, that conjugation to AF647-NHS does not interfere with the epitope binding. Scale bar is 10 µm.

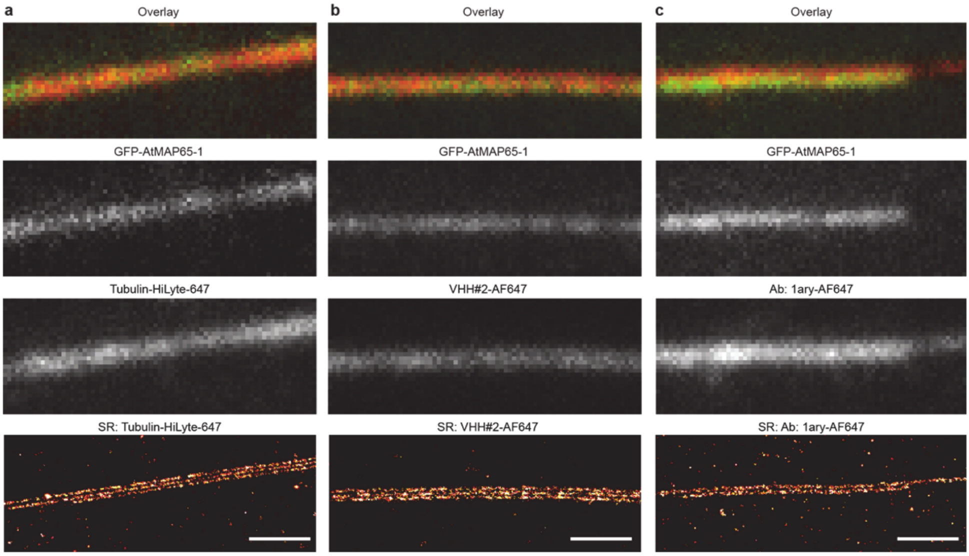

Figure S8.3: Examples of *in vitro* microtubule bundles resolved by dSTORM(**a-c**) GFP-AtMAP65-1 bundled microtubules copolymerized with tubulin-HiLyte647 (**a**), or copolymerized with Rhodamine-tubulin (channel is not shown) and labeled with VHH#2-AF647 (**b**) or a conventional primary antibody (1ary) labeled with Alexa647 (**c**). Bottom row shows SMLM reconstructions. Scale bar is 1 µm. Ab stands for antibody.

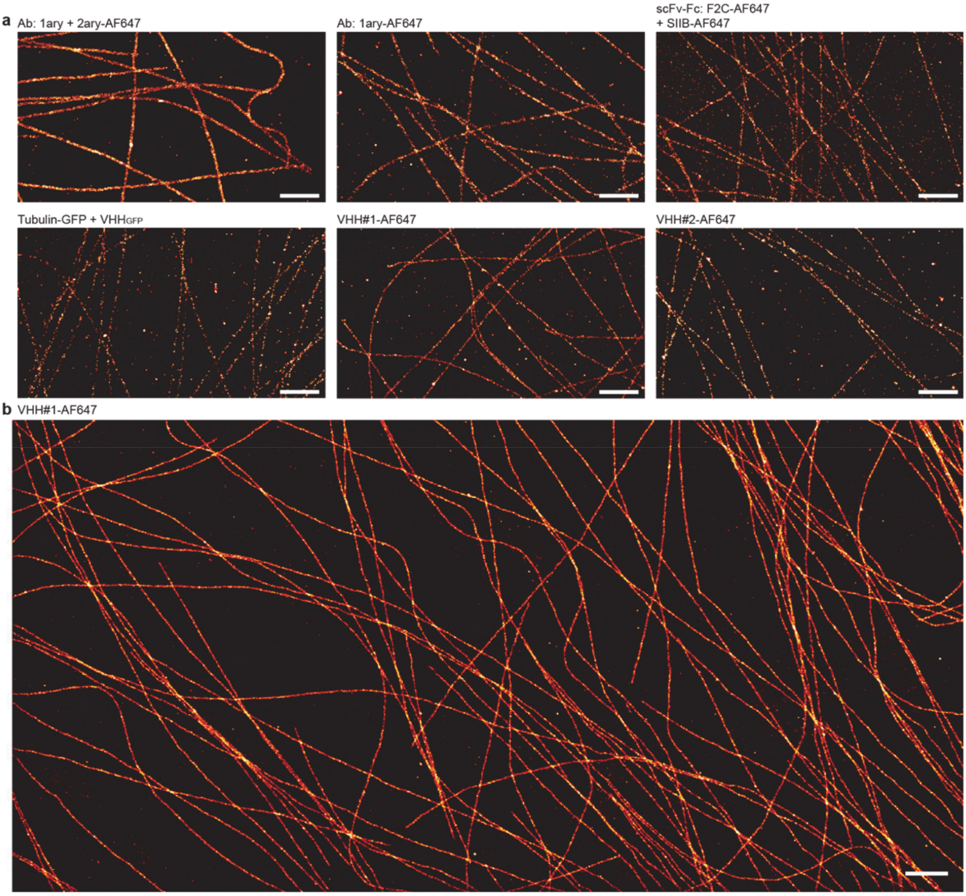

Figure S8.4: Examples of cellular stainings. (**a**) Representative images of COS7 cells stained with different labels and quantified in Fig 8.2e. Scale bars are 1 µm. Ab stands for antibody. (**b**) Large field of view SMLM reconstruction of microtubules in a Ptk2-cell (also shown in Fig 8.2d). Scale bar is 1 µm.

a

MEAN				
	VHH#1	**VHH#2**	**scFV-Fc**	**1ary Ab**
VHH#2	NS			
scFv-Fc	NS	<0.005		
1ary Ab	<0.005	<0.005	<0.005	
2ary Ab	<0.005	<0.005	<0.005	<0.005
MODE				
	VHH#1	**VHH#2**	**scFV-Fc**	**1ary Ab**
VHH#2	NS			
scFv-Fc	NS	<0.01		
1ary Ab	<0.005	<0.005	<0.005	
2ary Ab	<0.005	<0.005	<0.005	<0.005

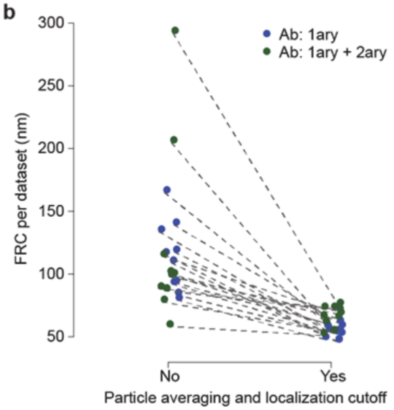

Figure S8.5: Significance and FRC correction effects. (**a**) p-values for comparing the mean values and mode values. This was tested using the Welch Two Sample t-test (two-sided), and using the Bonferroni correction for testing of multiple conditions. (**b**) Effect of frame-to-frame fluorophore linking on the FRC resolution estimate.

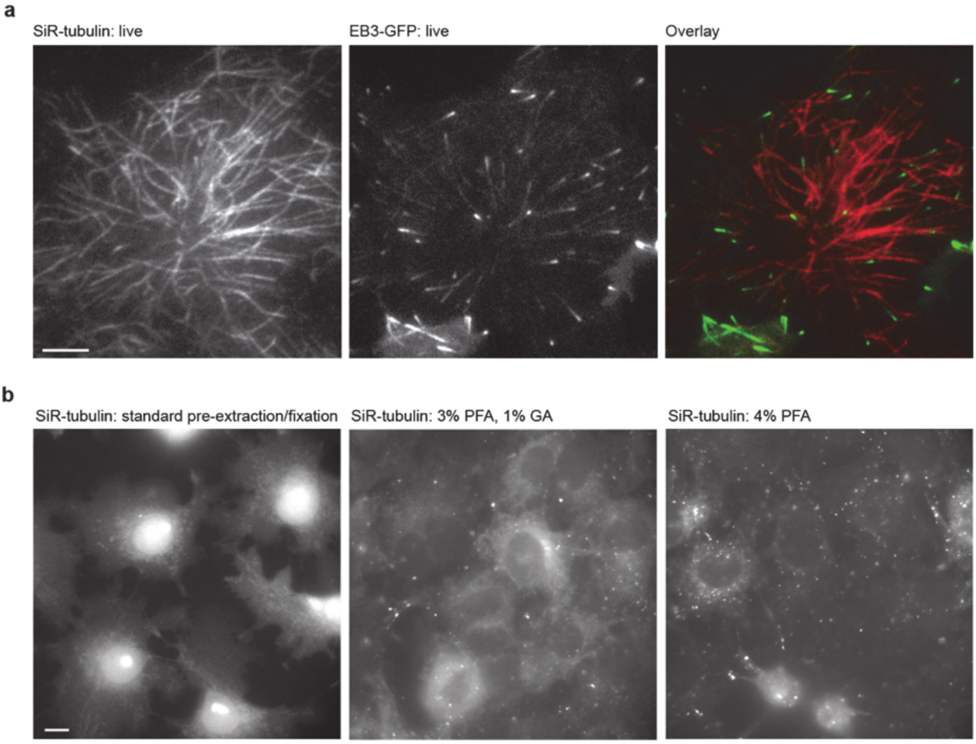

Figure S8.6: SiR Tubulin does not remain bound to microtubules upon fixation. (**a**) Still image from a live-cell recording of a MRC5 cells expressing EB3-GFP and incubated with SiR tubulin. (**b**) Example images of cells incubated with SiR tubulin before fixation using the indicated protocol. Scale bars are 5 µm. GA stands for glutaraldehyde.

Supplementary Methods

Purification and labelling of the antibody fragments F2C and SIIB

Human-derived single chain variable fragments (scFvs) were previously selected and characterized (Nizak et al., 2003). The antibody fragments were cloned in a custom designed plasmid (His$_{14\mathrm{x}}$-ZZ-SUMO-F2C or SIIB) and transformed into SHuffle *E. coli* strain for cytoplasmic expression. Bacteria were grown at 20 °C in Terrific Broth medium containing 4 mM $MgCl_2$, and 100 µg mL^{-1} kanamycin until OD$_{600}$ reached ~1.5. Expression was induced with 0.5 mM IPTG. Flasks were shaken at 160 rpm for ~16 h at 20 °C. EDTA was added to a final concentration of 0.5 mM and cultures were finally centrifuged at 6000 g for 10 min. Bacterial pellets were resuspended in binding buffer (50 mM HEPES, 500 mM NaCl, 5 mM $MgCl_2$, 20 mM imidazole, 10% glycerol) supplemented with 0.25 mM of PMSF before disruption by sonication on ice. Suspension was centrifuged for 60 min at 12.000 g and 4 °C. Supernatants were filtered (0.45 µm pore size) and incubated for one hour at room temperature with complete His-Tag purification resin (Roche) followed by several washes as recommended by the supplier. Elution was achieved using 500 mM imidazole in binding buffer. To remove the histidine-tag, His$_{14\mathrm{x}}$-ZZ-SUMO-scFvs proteins were incubated for 1 h at room temperature with yeast-derived His$_{6\mathrm{x}}$-SUMO protease (Ulp1). After specific cleavage of the SUMO-domain, antibody fragments were desalted and passed through a HisTrap 1 mL column using Äkta HPLC system to remove unwanted cleaved fragments and His$_{6\mathrm{x}}$-SUMO protease. The high purity (>90%) and the untagged nature of purified scFvs were analyzed via SDS-PAGE. Antibody fragments were conjugated to AF647 using succimidyl ester chemistry. The stock of fluorophore was dissolved in anhydrous DMSO at a final concentration of 10 µg µL^{-1}. The coupling reaction was performed in freshly prepared 100 mM $NaHCO_3$ buffer (pH 8.0). The reactive fluorophore was added in 6 fold molar excess to the scFvs containing solution while mixing for 1.5 hh at room temperature and protected from light. Unconjugated reactive fluorophores were quenched by adding an excess of hydroxylamine (~150 mM) with subsequent mixing for 15 min at room temperature. Antibody fragments were efficiently separated from uncoupled dye molecules using a 14 cm column (BioRad) packed with superfine G25 sephadex resin. Elution fractions were tested by immunostainings, the best fractions were pooled and stored at 4 °C adding to 0.05% sodium azide or in 50% glycerol at −20 °C.

ELISA assay for determining specificity of VHHs for tubulin

A flat-bottom 96-well plate (Maxisorp) was coated with 0.1 µg of bovine brain tubulin, washed with PBS and pre-blocked with 2% milk-PBS for 30 min at RT. 10 µL of periplasm fractions in 100 µL 2% milk-PBS was added to the wells and incubated for 90 min at RT. The plate was washed twice with PBS and the primary rabbit polyclonal anti-VHH antibody ((Kijanka et al., 2013), 1:2000) was added for 1 h at RT in 2% milk-PBS. Plate was again washed twice with PBS and incubated with secondary donkey anti-rabbit-PO antibody (Dako, 1:5000) for 1 hh at RT. After final washing steps, 100 µL perwell OPD+H_2O_2 was added and the plate was incubated for 30 min at RT. The reaction was stopped with 50 µL per well of H_2SO_4 and relative VHHs presence was analyzed by measuring optical density at λ= 490 nm with an Ultramark spectrophotometer (Biorad). Monoclonal anti-α-tubulin antibody (Sigma) was used as positive control. 14 colonies showing the strongest signal were selected for further study and VHH DNA was isolated and sequenced using an M13 reverse primer.

Determination of the tubulin subunit detected by VHH#1 and VHH#2.

HEK293 cells were plated on 10 cm^2 dishes and cultured in DMEM/Hams F10 (50/50%) medium supplemented with 10% FCS and 1% penicillin/streptomycin for 2 days. Cells were transfected using MaxPEI (PolyEthylenImine, Sigma) with 10 µg of pDNA encoding for empty EGFP, β-tubulin(2C)-EGFP or α-tubulin-EGFP in β-actin vectors and grown for 48 h at 37 °C and 5% CO_2 . Following transfection, dishes were washed with 1 mL of PBS and extracted with 500 µL extraction buffer (PBS pH 7.4, 1% TritonX-100, 2 mM Ca^{2+}, protease inhibitor cocktail). Cell suspensions were frozen at −80 °C, thawed, incubated on ice for 2 h, and finally spun down at 13.000 rpm for 15 min. Obtained supernatants samples were loaded on 12% SDS-PAGE gels, and transferred for 90 min at 15 V via semi-dry western blotting onto a PVDF membrane. The membrane was blocked with 5% milk-PBS for 1 h, and incubated with VHH#1 or VHH#2 (2 µg mL^{-1}) for 4 h at RT on a shaker. After PBS wash, membranes were incubated in either home-made primary rabbit anti-VHH serum 976 (1:2000 in milk-PBS; (Kijanka et al., 2013)) or rabbit anti-GFP antibody (1:5000 in PBS; Abcam) overnight at 4 °C. Next day, another cycle of PBS wash was performed, and HRP-conjugated secondary goat anti-rabbit antibodies (Dako) were added for 60 min at RT, blots were extensively washed and processed for developing.

Conjugation of fluophores to antibodies and VHHs

Conjugation of AF647 (Alexa Fluor®647 Carboxylic acid, Succiminidyl Ester, Molecular Probes, Life technologies) to monoclonal anti-α-tubulin antibody (Sigma) was performed according to the protocol described before (Cloin et al., 2015; Yau et al., 2014). Some modifications were introduced for labelling of VHH. Conjugation reaction was performed in freshly prepared 100 mM $NaHCO_3$ buffer (pH 8.0) where the ratio of VHH:fluorophore was 1:5 for VHH#1 and 1:3 for VHH#2. Samples were incubated for 1 h to 6 h at RT in the dark and labeled VHH was separated from non-conjugated dye by passing through a NAP25 column (GE Healthcare). Eluted VHH-AF647 was upconcentrated to 0.5 µg µL^{-1} to 0.7 µg µL^{-1}, labelling efficiency was measured as described before (Cloin et al., 2015). The absorption spectrum of the preparations revealed a labelling ratio of 1.5 fluorophores per VHH#1 and 0.3 fluorophores per VHH#2. Sodium azide was then added to the mixture to a final concentration of 0.05% and the proteins were stored at 4 °C.

Microtubule labelling simulations

Generative model Images of *in silico* microtubules were synthesized from a generative 3D model. First the main axis (backbone) of a straight microtubule with a specified length was marked. The backbone segment was populated with tubulin heterodimers forming a regular 25 nm diameter 3-start helix consisting of 13 straight protofilaments. The coordinates of tubulin subunits were spaced 8 nm apart from each other along the protofilament. Tubulin subunits were randomly labeled with fluorophores to achieve the desired probe density. If a tubulin molecule was marked as labeled, the fluorophore coordinates were generated and added to the model. The position of the fluorophore was determined by addition of the offset distance m extending outwards from the surface (i.e. in the radial direction) to the coordinates of the corresponding tubulin. A small rotation by angle ϕ (uniformly distributed on the interval from 10° till $-10°$) in the plane perpendicular to the microtubule axis was added to simulate flexibility in the binding of the antibody probe to the antigen. To simulate widefield images, the positions of fluorophores were projected onto a 2D plane and convoluted with a 2D isometric Gaussian kernel with a standard deviation equal to that of the point spread function of the microscope. This produced a continuous 2D distribution of intensity. Further the intensity was integrated over the area of each pixel of the future image. The final pixel intensity value was drawn from the Poisson distribution with the mean equal to the integrated intensity value from the previous step, to account for the shot noise of light registration.

Simulated super-resolution microscopy images of microtubules were generated using the same rendering algorithm as for the real SMLM dataset reconstruction (see above). To account for the uncertainty in the localization of fluorescent signal during ‘virtual’ SMLM acquisition, each fluorophore position was shifted by random displacement of magnitude d drawn from a Gaussian localization accuracy distribution with mean±SD of 7.5±2.5 nm. If the displacement magnitude d was above a specified precision cutoff threshold t, its random value is generated again until it is below the threshold, so the probe density remains constant. An angle of displacement direction θ was drawn from a uniform random distribution covering the full 360° for each of the fluorophores. The new position of the fluorophore was used to render its image.

Dataset The generative model was transcribed into a Matlab code and run in GNU Octave version 3.8.2 on Mac OS X 10.10.0, Intel Core i7 2.8 GHz, 16GB RAM. A dataset of images was generated where the model parameters (probe density, position of the probe and precision cutoff) varied in a wide range. The values for probe density were chosen at 0.1%, 0.3%, 1%, 5%, 7%, 10%, 15%, 30%, 50%, 75% and 100%. The values for mean probe position were chosen at 0.0 nm, 2.5 nm, 5.0 nm, 7.5 nm, 10.0 nm and 12.5 nm. The values for the precision cutoff threshold were chosen at 3 nm, 5 nm, 8 nm, 10 nm and 13 nm. For each combination of the three parameters a microtubule with a contour length of 80 µm was generated. The generated microtubule was centered within the field of view before being rendered into a widefield and super-resolution image. The widefield images were generated with a pixel size of

64 nm and the standard deviation of microscopes point spread function equal to 1.8 pixels (=115.2 nm). The super-resolution images were generated with a pixel size of 4 nm. All microscopy images were exported to local storage in 16-bit gray scale TIFF image format. Intensities were uniformly scaled prior to export to take advantage of the full dynamic range of the image format.

Analysis of simulated images The super-resolution images were sampled with a window 512 nm long (in axial direction) and 400 nm wide. The window was placed at non-overlapping intervals along the entire microtubule, resulting in 150 samples per microtubule. Empty regions (i.e. summed intensity of zero) were rejected from the analysis. This situation was particularly common for the low (<3%) probe density. An intensity line profile was derived from a sampled region by averaging the intensities along the axial direction. A 1D Gaussian function with four parameters (background level, peak amplitude, peak position, and peak width) was fitted to the intensity line profile using a Levenberg-Marquardt nonlinear regression algorithm. The regression algorithm was run for a maximum of 1000 iterations or until convergence was achieved with an accuracy of 1×10^{-3} . The mean and standard error of the FWHM were computed for each condition in the dataset. The FWHM was calculated from the fitted peak width as described. The analysis of the resolving probability of two microtubules was performed as described above.

Discussion

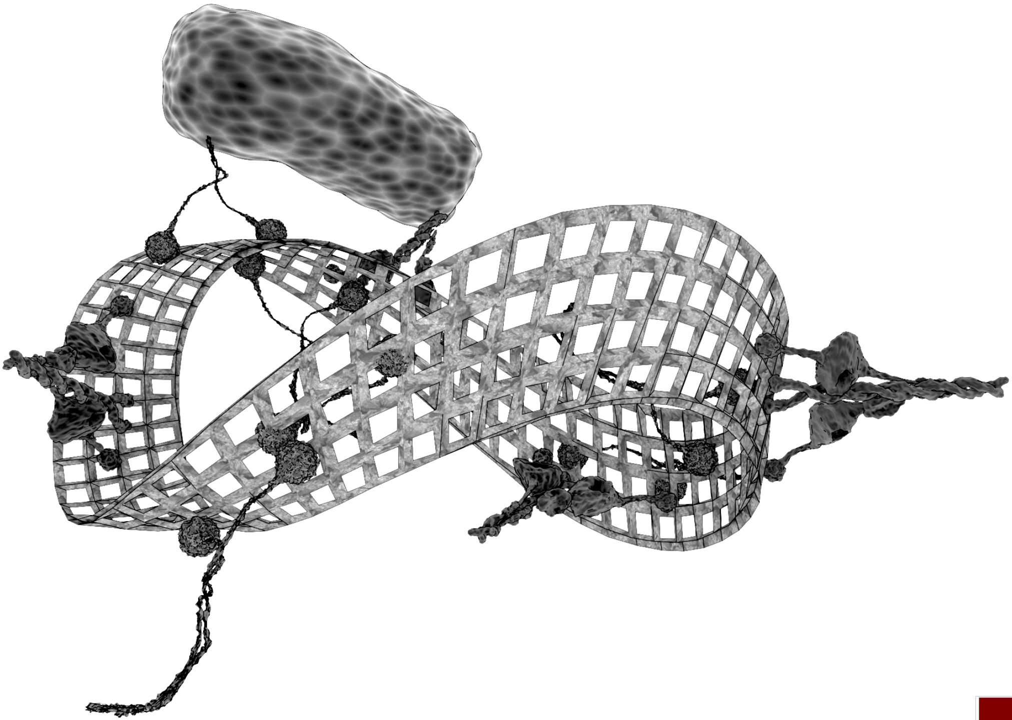

9

DISCUSSION

> Zonder transport staat alles stil.
> Without transport, nothing moves.
>
> Transport en Logistiek Nederland

Our society cannot exist without transport. We depend on a worldwide logistic network to move resources like oil from drills via refineries to its final destination. Food is transported from farms by trucks and ships to consumers, sometimes thousands of kilometers across several continents. If this transport comes to a halt, or even if the price of transport increases, all other civil processes are affected. In the microcosmos of the cell, a similar situation exists, with cells depending on transport along microtubules for their survival and proper functioning. As shown in this thesis, axonal transport is an essential mechanism in the development and maintenance of the central nervous system. Its components play a central role in synaptic plasticity and therefore in learning and memory. When transport fails, axons become increasingly vulnerable to degeneration, contributing to the development of a large variety of neurological disorders. Studying axonal transport, for example using advanced techniques like superresolution microscopy, is therefore an essential step towards understanding and curing these diseases.

The topics discussed in this thesis can be divided into three broad categories. Chapters 2 and 3 consider intracellular transport in the context of development, learning and memory. Chapters 4 through 6 on the other hand, investigate its role in disease, more specific its involvement in the processes leading to neurodegeneration. The final chapters, 7 and 8, discuss superresolution microscopy as a technique to visualize the microtubule network.

Transport and Development

Interest in the components of intracellular transport and their function spiked after 2013, when the Nobel Prize for Physiology and Medicine was awarded to James E. Rothman, Randy W. Schekman and Thomas C. Südhof(Pfeffer, 2013; Ray, 2014). Especially Thomas Südhof explored in his work the relation between transport and the maintenance and plasticity of synapses. Short-distance transport along actin filaments is essential for the fusion of synaptic vesicles with the plasma membrane and the subsequent release of neurotransmitters (Sudhof, 2014). Medium to long-range transport of for example CaMKII on the other hand enhances plasticity through an increase in synaptic AMPAr. Replacing the wildtype CaMKII with a mutant that is capable of autophosphorylation but cannot bind to microtubule-associated proteins blocks this potentiation (Lemieux et al., 2012). There is substantial evidence that while microtubule-based transport is essential for synaptic plasticity, it is also highly effected by the resulting increase in activity. Synaptic activity promotes the interaction between the actin and microtubule network, increasing the chance of a microtubule entering the spine (Merriam et al., 2013). This might result in a positive feedback loop, where increased synaptic activity leads to microtubules entering the spine, increasing the number of receptors available at the synapse, further enhancing plasticity.

It is fascinating to observe that influencing microtubule stability has a direct influence on learning capacities in cultured hippocampal neurons (Fanara et al., 2010), as well as in living mice (Uchida et al., 2014). Many of the molecular players involved in the crosstalk between synaptic plasticity and microtubule dynamics, such as stathmin and tau, are also implicated in neurodegenerative disorders like Alzheimer's disease, suggesting a common mechanism for both memory formation and memory loss (Uchida and Shumyatsky, 2015). The link between microtubule stability and the cognitive deficits was already proposed in the 1980's (Matsuyama and Jarvik, 1989) and a number of different models have been suggested to explain this link (Dubey et al., 2015). Effects of microtubule-stabilising drugs have been somewhat disappointing. It appears that unstable microtubules lead to increased neurodegeneration, but at the same time neurons need a pool of microtubules with a high turn-over. Stabilising the entire neuronal microtubule cytoskeleton using paclitaxel also increases the risk of axonal loss (Gornstein and Schwarz, 2014). This is a clinically relevant problem, since paclitaxel and other drugs with a similar effect are commonly used in the treatment of breast and ovarian cancer, amongst others. Peripheral neuropathy is often seen as a side-effect of treatment (Lee and Swain, 2006).

Despite these setbacks, therapeutical application of microtubule-stabilising drugs in neurodegenerative disorders is extensively studied. A promising approach could be influencing post-translational modifications (PMTs). As discussed in chapter 2, PMTs are chemical 'tags' attached to the tubulin subunits and regulating both protein binding and microtubule stability. In neurons, they are thought to be responsible for the unusually stable configuration of the microtubule cytoskeleton (Song et al., 2013). The balance between the different types of modifications is affected in a number of neurological disorders including Alzheimer's disease (Zhang et al., 2015). It is tempting to think that drugs effecting these modifications would provide a more subtle and selective way of influencing cytoskeleton stability. A candidate drug of specific interest is tubastatin A, a selective inhibitor of HDAC6. This histone deacetylase, unlike the name suggests, is an enzyme that specifically deacetylases microtubules. Its inhibition leads to an increased acetylation of tubulin and more stable microtubules. The therapeutic effects of tubastatin were first shown in a model for Charcot-Marie-Tooth (CMT), in which it completely reversed the axonal transport deficits and rescued the disease phenotype (d'Ydewalle et al., 2011). Since then, a similar effect has been shown for a mouse model for Alzheimer's disease (Govindarajan et al., 2013; Zhang et al., 2014) and Amyotrophic Lateral Sclerosis (ALS, (Taes et al., 2013)). It should be noted that in the case of Alzheimer's disease, there is also a direct effect of the drug on tau acetylation, but a drosophila study suggested the effect on microtubule acetylation is the primary cause of the rescue effect (Xiong et al., 2013), possibly by counteracting the effects of amyloid β on mitochondrial transport along microtubules (Kim et al., 2012). Although not yet tested in animal models, a similar beneficial effect of HDAC6 inhibition was found in neurons overexpressing huntingtin, the protein involved in Huntington's disease (Guedes-Dias et al., 2015). The early findings in CMT lead us to design a similar experiment for experimental autoimmune encephalitis (EAE), a mouse model of multiple sclerosis, to test if the microtubule-stabilising effect of tubastatin A could ameliorate neurodegeneration in this context as well. Unfortunately, this experiment failed due to technical issues with the chemicals required to induce EAE, resulting in none of the animals developing symptoms. There were no side-effects of the drug. Inhibitors of HDAC6 have shown great promise in animal experiments and might well enter clinical trials within the coming few years. They would represent the first generation of neuroprotective drugs utilising our new knowledge of the microtubule cytoskeleton.

Before we move from synapic plasticity towards neurodegeneration in more detail, we should consider that plasticity is only one aspect of development in which intracellular transport is involved. The central nervous system is more than just a collection of interconnected neurons. It is higly organized in different layers and regions, each with its own cellular composition and function. The cerebral cortex for example consists of six layers, which are easily differentiated under the microscope because of their unique cell composition and density. This organization arises relatively late in the development of the human fetus. Approximately six weeks after fertilisation, the raw shape of the central nervous system already exists, the so-called neural tube. In this hollow tube, the neuronal precursor cells are located around the lumen, in the ventricular zone (Carlson, 2004). In the cerebral cortex, these precursors divide, after which one of the daughter cells migrates upwards towards its final position in the cortex. The first wave of migration forms the bottom layer of the cortex, with each subsequent wave migrating past its predecessors to form a new layer. In human embryos, this process happens between week 15 and week 25 after fertilisation (Budday et al., 2015). The cerebellar cortex is formed through a slightly different process. In the first phase of development, cells migrate from the ventricular zone to the outer edge of the forming cerebellum. There they proliferate and then migrate inwards along radial glia cells. In humans, this migration starts in the third trimester of pregnancy and can proceed into the early postnatal period (Donkelaar et al., 2006).

It has been known for a long time that the microtubule cytoskeleton and motor proteins play a crucial role in neuronal migration. Microtubule associated proteins like LIS1, NudE and tubulin isoforms like TUBG1 are all implicated in forms of micro- and lissencephaly (Poirier et al., 2013; Moon and Wynshaw-Boris, 2013). It is thought that most of these proteins facilitate migration by enhancing the function of dynein heavy chain, the main force generator for both mitosis and migration (McKenney et al., 2010; Moon et al., 2014). The dynein motor protein is such an essential player in cell division, that it is technically difficult to create a knockout model in which migration can be studied. However, patients have been described with mutations in dynein heavy chain. As expected, even a minor reduction in dynein function leads to migration deficits and mental retardation as well as various other neurological problems (Willemsen et al., 2012). All these findings have created an image in which the migrating cells divide and move against a more or less static background of glia cells. Our findings on the *Bicd2* gene are indicative of a much more complex situation. Although *Bicd2* knockout animals show an almost complete block of migration, this is completely independent of expression in the migrating cells. Only loss of *Bicd2* in the radial glia cells is necessary and sufficient to cause the cortical migration phenotype. The exact mechanism behind this block of migration remains partially unknown. Although we have shown that the loss of *Bicd2* leads to a reduced expression of adhesion molecules on the plasma membrane of the Bergmann radial glia cells, we have not proven beyond doubt that this is the causal mechanism. It is still possible that the effect is mediated through the effects of *Bicd2* on dynein velocity (Schlager et al., 2014). Further resolving this issue has gained a certain urgency in the past few years, as it has become apparent that *Bicd2* is associated with dominant spinal muscular atrophy (Martinez-Carrera and Wirth, 2015) and might also contribute to the golgi fragmentation seen in other neurodegenerative disorders such as ALS (Haase and Rabouille, 2015; Jaarsma and Hoogenraad, 2015). As with synaptic plasticity, neurodevelopment and neurodegeneration are often closely linked. The same molecular players that help shape the nervous system, are also involved in its maintenance and response to ageing and disease. Careful examination of the developing brain can provide suprising clues towards understanding its diseases.

Transport and Disease

Disorders of the central nervous system are notoriously hard to study. The brain and spinal cord form an isolated biochemical compartment, separated from the rest of the body by the blood-brain barrier. Encased by the skull and the spinal column, advanced imaging techniques are required to map their structure and function in a living organism. Brain tissue quickly degrades and deforms after death, complicating the study of pathological hallmarks of disease. The function of the brain depends on the interaction between large networks of different types of neurons, making it hard to develop a proper experimental model. It is quite possible to prepare cultures of a single type of neuron (e.g. rodent hippocampal pyramidal neurons, (Banker and Cowan, 1977)) and studies in this model have provided us with a wealth of information on the development and function of individual neurons. It is however hard to translate these results to the function of the brain as a whole. A next step is to study the neurons in context, in a thin slice of brain tissue kept alive in culture (LaVail and Wolf, 1973). This model allows for observation of electrical activity in a functioning network formed by different types of neurons. Compared to the dispersed cell culture, it is more labor-intensive to culture and not as easy to manipulate or observe. Also, one should keep in mind that the readout is formed by increases or decreases in electrical or synaptic activity, not by behaviour. Often, the correlation between electrical patterns and observed behaviour is not entirely understand. To directly link behaviour to brain defects, an animal model is required. Animals with a predefined genetic modification can be treated with a drug and subjected to a test battery, after which the brain and spinal cord can be studied. The great advantage of this model is that clinically relevant behaviour, for example strength or intelligence, can be used as readout. Since the metabolism of many animals such as rodents closely mimics those of humans, it is not only possible to test the effects of a drug, but also get a first impression of toxicity, side-effects and optimal method of admission before testing it in a human population. However, animal studies have some major drawbacks. First of all, they come with major ethical issues. Great care is taken to minimize suffering and reduce the number of animals included in trials. From an economic viewpoint, generating a new genetically modified animal line requires a large amount of time and money. Housing and maintaining animals forms a major expense for research groups. From a scientific point of view, the main issue is to which extent the animal experiment actually models the human disease. The worst kind of model might be that, which closely mimicks the disease, but fails at just one vital characteristic. Such a model could be used for decades and define our understanding of a conditon, before it is realised that it is insufficient. When answering a research question, choosing the right model might just be the most important part of the approach.

This might never be more true than in the context of multiple sclerosis. As discussed in great length in chapters 4-6 of this thesis, finding an optimal model for MS would significantly increase our chances of understanding this complicated disease. Currently, even the category in which the disease should be classified remains a matter of heated debate. The main issue is whether MS is primary a neurodegenerative disease, with an autoimmune response as secondary effect, or primary an autoimmune disorder with neurodegeneration as result of prolonged exposure to an inflammatory environment (Mahad et al., 2015). Answering this question would be an important step towards developing more effective or even curative treatment. I would like to propose that both theories could be equally true, depending on the individual patient. There is a remarkable variation in both clinical presentation of MS patients, disease progression and even pathological features of plaques (Frischer et al., 2015). Instead of talking about MS as a single disease, further divided into disease pattern (relapsing-remitting, primary progressive, secondary progressive), it might be more adequate to think of MS as a spectrum, with neurodegeneration at end of the spectrum and autoimmunity on the other end. Following a Gaussian distribution, most patients will be somewhere in the middle, experiencing both the excacerbations caused by acute autoinflammation and the gradual decline resulting from neurodegeneration. In other individuals, neurodegeneration might be more pronounced, leading to relatively few relapses but a more pronounced continuous clinical deterioration. This hypothesis of an disease spectrum might also explain why such a large amount of genetic variation is found in the MS population (Jafari et al., 2011). Depending on the position of the individual patient along the spectrum, different alleles will determine his disease course. Some risk alleles, like variants in the HLA-region, will be found in a large proportions of patients, but other single-nucleotide polymorphisms might only be present in patients who are more on the neurodegenerative end of the spectrum. Genome-wide association studies that fail to take this diversity into account and consider all MS patients as a single cohort, will in general lack the power to detect polymorphisms only present in a subpopulation. It might also explain why a large number of patients does not respond to common immunemodulating therapies like interferon-β (Comabella et al., 2009; Bustamante et al., 2015).

To test this hypothesis and determine for individual patients the relative contribution of neurodegeneration and autoimmunity to their disease activity, it is essential to find reliable readouts for neurodegeneration in MS. Such a readout could be obtained using imaging techniques such as MRI (Filippi, 2015), cerebral spinal fluid biomarkers such as neurofilaments (Kuhle et al., 2011; Hoglund and Salter, 2013) or a combination of both (Gajofatto et al., 2013; Dickens et al., 2014). Molecules involved in axonal transport form an interesting candidate for such a biomarker. A reduced expression of various members of the kinesin superfamily has been observed in MS patients or MS models, such as KIF5A and KIF21B, but not KIF1B (Sombekke et al., 2011; Kreutzer et al., 2012; Hares et al., 2013). In contrast, others have reported an association between an increase in KIF21B and accelerated neurodegeneration in MS patients (Kreft et al., 2014). Part of this discrepancy might be explained by the fact that all these studies have looked at expression of individual motor proteins, which is not necessarily the same as transport activity and efficiency. It would be of great clinical and scientific interest of the efficiency of the axonal transport system could be measured in an individual patient, however, this would require direct observation of the central nervous system in a living individual. Fortunately, there is one area of the nervous system that can be directly observed from the outside: the retina. The retina contains several types of neurons which are involved in preprocessing of visual signals before conveying them to the visual areas of the cortex through the optical nerve. The axons of these neurons form the retinal nerve fibre layer (RNFL). Using optical coherence tomography (OCT), the thickness of this layer can be measured, which is becoming more and more common for diagnostics and measuring neurodegeneration in MS patients (Lidster and Baker, 2012; Bennett et al., 2015; Alvarez-Cermeno et al., 2016) In research settings, this technique has been modified to include a dynamic magnetic field gradient, through which magnetic particles can be imaged inside the retina (Wang et al., 2010). By linking magnetic particles to specific nanobodies targeting a molecule of interest, magnetomotive optical coherence tomography (MM-OCT) can be used to visualize the localisation and dynamics of a certain molecule in the intact retina of a living individual. A nanobody bound to a target such as mitochondria, could provide us with information on the distribution and transport dynamics of this organelle. Although such studies have yet to be performed, the required hardware, both in the form of imaging setups and molecular probes is readily available. It will be challenging to get probe inside retinal neurons, but not impossible. Even a very low efficiency of probe internalisation would lead to a wealth of information on the contribution of axonal transport to neurodegeneration in MS.

In order to test the effect of a reduced efficiency of axonal transport in a model for MS, we generated a knock-out mouse for the kinesin motor KIF1B. No animals were born with homozygous deletion of this motor protein, suggesting its complete loss is not compatible with life. Since embryos died in an early phase of development, the cause of death is not entirely clear. The microtubule cytoskeleton and its associated proteins play a crucial role in a multitude of embryological processes, as illustrated in chapter 3. As confirmed with western blot, the heterozygous animals only express half the amount of KIF1B protein, both the -α and -β isoforms, while the expression of other transport proteins is not affected. As described in chapter 5, there is no difference in disease course between heterozygous *Kif1b* knockout animals and their wildtype littermates, which could be due to redundancy in the neuronal transport system. It should be noted that this is only the most likely of a number of possible explanations. At the time these experiments were designed, the common idea was that disorders linked to genes associated with the transport system were solely caused by a reduced function or expression of the encoded gene. Since then, several studies have shown that a gain of function can be just as detrimental, for example in the case of *Kif21a*(Cheng et al., 2014). Also, mutations can influence the binding between motor protein and cargo. A reduced binding will lead to a decreased efficiency of transport but once again, an increased binding can also lead to defects, as shown with *Bicd2*-mutations in autosomal-dominant proximal spinal muscular atrophy (Peeters et al., 2013). A straight-forward link between reduced motor protein expression and susceptibility to EAE would have been an exciting finding, suggesting a relatively simple model for axonal degeneration and an avenue towards new therapeutic options. Unfortunately, biology is once again more complex than anticipated.

A final possibility that should be considered, as mentioned briefly in chapter 5, is that the *Kif1b* animals are in fact more vulnerable to neurodegeneration. The problem could be the experimental model and the timing of the experiments. In the paper describing the original *Kif1b* knockout, it was mentioned that the animals develop a neuropathy, but only after a year (Zhao et al., 2001). This fits with a model where the axonal transport system is slightly less efficient, with the animal gradually accumulating neuronal damage. In our experiments, the animals were only twelve weeks old. An optimal age to induce EAE, but perhaps not the best timing to study neurodegeneration. The same could be true for the type of EAE. A number of different variants of this procedure exist, each with its own advantages and drawbacks (Baker et al., 2011). In our experiment, we decided to use the most common approach by inducing EAE in twelve week old C57BL/6 mice by injecting them with $\text{MOG}_{35\text{-}55}$ peptide. Due to the background of the transgenic animals, using a different mouse strain was technically impossible. It would have been possible, although far more challenging, to induce a more chronic type of EAE. In such a model, the longer timeframe would expose a difference in accumulation of neuronal damage between

Kif1b knockouts and wildtype littermates, more accurately mimicking the expected mechanism in patients. Although unlikely to be performed due to technical -and financial- hurdles, it would provide valuable insights in the contribution of axonal transport to disease progression in multiple sclerosis.

Superresolution microscopy

Throughout the history of the neurosciences, progress in understanding the brain has mostly come from new methods of visualising the microanatomy of the nervous system, leading the neuroanatomist Floyd Bloom to remark that “the gain in brain lies mainly in the stain” (Appel, 1997; Micheva and Bruchez, 2012). The past century has seen a remarkable progress in histology, anatomy and neuroimaging. Just over a hundred years separate the Nobel prize for the first stainings of neurons (Golgi and Cajal, 1906) and that for superresolution microscopy (Betzig, Hell and Moerner, 2014 (Choquet, 2014)). In a single century we have gone from debating whether neurons are separate cells or a continuous network to imaging nanometer scale organization of the neuronal subcortical cytoskeleton (D’Este et al., 2016). We can now use superresolution microscopy to image single proteins in living cells with nanometer resolution, multicolor labelling and the ability to reconstruct structural organization in three dimensions(Leterrier et al., 2015).

However, it has proven difficult to translate these observations into new biological or medical insights. A vast majority of publications on superresolution either present a new method or refinement or describe cellular architecture with improved resolution. Few studies report new insights on protein function or disease mechanisms. Here, the technical complexity of superresolution microscopy could play a role. Research groups developing and deploying techniques like STORM mainly consist of physicists and chemists, with only a few collaborations existing between these groups and more biologically oriented or -even rarer- medical scientists. This leads to a situation where part of the scientific community has access to the most refined microscopy tools existing, but lacks a clear research goal, while another part has a variety of unanswered research questions, but is not aware of technical possibilities to answer them. Although improving superresolution microscopy towards subnanometer resolution is technically possible, bringing these two groups together might contribute far more to our understanding of the brain.

What are the questions to ask, to make superresolution microscopy contribute to our understanding of multiple sclerosis? As outlined in chapter 4, transport deficits could initiate a vicious cycle of impaired mitochondrial transport, reduced ATP availability and increased energy demand, further disintegrating axonal transport. Identifying the cellular components involved in this cycle would significantly improve our understanding of the neurodegenerative component of MS, and here superresolution microscopy would play a central role. It is the only technique with the proper resolution and labelling density to identify for example degradation of the subcortical actin cytoskeleton, loss of membrane organization, fragmentation of the axonal microtubule cytoskeleton or decay of mitochondria related to reduced cytoskeleton integrity in active MS lesions. MS is a difficult disease to mimick in an animal model(Baker and Amor, 2015), and confirming findings from animal studies in patients has proven hard. It would therefore be highly valuable to perform superresolution microscopy on human material, such as cell models derived from patients or post-mortem brain material.

The best results with STORM or any of the other techniques are obtained in a carefully controlled experimental setting. Preferably, a single layer of cells is cultured on top of a glass slide, mounted in an imaging ring in transparent medium and observed under the microscope. Cells that easily attach and detach from surfaces, such as most of the cell types of the immune system (Torreno-Pina et al., 2016) can be imaged in such a setup with relative ease. In contrast, neurons require a strong surface binding to mature properly. Although mouse neurons can be studied in this environment, culturing human neurons is far more challenging. Although not impossible, this either requires the ethically problematic use of human embryos (Napoli and Obeid:, 2016) or the experimental technique of converting human fibroblasts (Richner et al., 2015) or pluripotent stem cells (Vazin et al., 2014) into neurons. Fibroblasts can be harvested with little effort from patients, making it possible to relate the findings in cell-based assays directly to the clinical record of the individual patient. However, even though these converted cells express a variety of neuronal markers, it remains unclear to what extend findings in this system can be extrapolated to ‘true’ neurons. Still, a recent publication showed that these derived neurons can be used to study transport deficits found in spinal muscular atrophy (Xu et al., 2016). Findings in these culture systems still need to be confirmed in postmortem brain tissue from patients.

Fortunately, even on such technically challenging material superresolution imaging has been succesfully performed (Smith and Verkman, 2015). Using a combination of these approaches, we can test the efficiency and speed of for example mitochondrial transport in induced neurons from the fibroblasts of MS patients and compare these with healthy controls. It becomes possible to observe the integrity of the transport infrastructure in postmortem brain tissue and compare the distribution of motor proteins and cargoes in active demyelinating lesions with normal appearing white matter. And finally, we can observe the effect of drugs modifying the microtubule cytoskeleton -such as Tubastatin A- in human neurons, a critical step towards deploying such drugs in MS patients.

Future directions

Every study discussed in this thesis depended on the input of scientists in multiple disciplines, from clinical medicine to molecular biology, biophysics and chemistry. As such, it is part of an ongoing movement towards more interdisciplinary research (Van Noorden, 2015). Collaboration between scientists from entirely different backgrounds is not a bonus, but a necessity. If we want to develop a cure for multiple sclerosis, the best chance of succes is by coordinating a team consisting of both medical and basic scientists. Epidemiological research identifying risk factors should be combined with genetic assays mapping gene variants contributing to this risk. As cell biologists and neuroscientists study the mechanisms contributing to disease development and progression, their work depends on physicists, chemists and engineers developing new techniques, chemicals and equipment. Medical scientists are required to conduct clinical trials, supported by pharmacologists and statisticians. To make all these different backgrounds and ways of thinking work together, scientists are needed who have a thorough grasp of their own field, but also a genuine interest and basic knowledge of the tools available in other fields. This can only happen in a research environment where the training and funding of scientists supports such collaboration (Brown et al., 2015). Clinical medicine remains relatively isolated, with little collaboration outside of its own field (Van Noorden, 2015). Providing funding and institutional support to dedicated research masters for medical students would result in more medical doctors with an understanding of basic research. In the long run, such an investment would pay itself back, as these MD's can provide an essential bridge between clinical and basic research.

During the coming decades, the practice of neurology will see significant changes as the impressive advances in neuroscience are slowly translated into treatment. Two very distinct yet complementary approaches already become visible today. The neurobiological approach uses our improved understanding of the molecular processes controlling individual neurons. It aims at bringing neurodegenerative processes to a stop, or at the very least slowing them down. By developing drugs that regulate axonal transport, reduce the effects of glutamate exitotoxicity or in other ways preserve axonal integrity, such as through the stimulation of remyelination (Harlow et al., 2015), the ability of neurons to withstand stress and repair damage can be enhanced. A large variety of neurological disorders would be ameliorated when such therapies become available, with examples ranging from amyotrophic lateral sclerosis via multiple sclerosis to Alzheimer's dementia.

However, although this approach will be effective in reducing damage, it is highly unlikely that it will be able to repair what has already been lost. If an axon has been lost, the main function of the neuron will be gone, even if the cell body survives. Axons in the central nervous system do not regrow, and there might be a very good reason for this. Consider the analogy with a large processing center, where a thousand computers are working on a demanding simulation task. If ten computers break down, one percent of all calculation power will be lost. However, if these ten computers continue operating but send out incorrect results and interfere with the function of other units, the whole network might be compromised. Simply allowing a damaged neuron to regrow its axon or replacing it using stem cell therapy, might worsen the condition of a patient.

The second approach, neurocybernetics, starts where the neurobiology ended. It does not offer any therapy that slows down or cures neurological disease. Instead, it explores the possibility of restoring function and repairing the deficits caused by these disorders (Wander and Rao, 2014). Already, research in this field has resulted in protheses that can not only return limb function, but even sensibility (Donoghue, 2002;

Scherberger, 2009; Antfolk et al., 2013). It has led to the development of the cochlear implant (House and Urban, 1973) and the retinal chip (Zrenner et al., 2011), at least partially restoring the ability of the patient to hear and see. A next step might be to treat unilateral vocal cord paralysis caused by lesions to the recurrent nerve. Since the contraleral nerve is still intact and the vocal cords move symmetrical, the signal from the preserved nerve can be recorded and conveyed to the paralysed vocal cord. This effectively innervates both vocal cords using a single recurrent nerve. Not only does this treat the hoarseness and lack of voice volume patients experience, it also provides us with knowledge on how to use cybernetics to circumvent a nerve lesion. This same technique could be used with some modification on any peripheral nerve lesion, as long as a proper input signal is available that can be used to control the target muscle.

The main challenge would then be to move with this technique from the peripheral to the central nervous system. A logical starting point would be to apply the same logic to lesions in the spinal cord. If we can use electronics to bypass a lesion in a peripheral nerve, the same might hold true for ascending or descending tracts in the spinal cord. Brain activity measured in the motor cortex could be directly translated into an activation signal to the proper muscle. Sensory input could be detected by electrodes along the dorsal root ganglions and the spinal cord below the lesion and transmitted to the sensory cortex. In a final stage, perhaps even cortical functions themselves could be replaced, as is currently being investigated (Widge et al., 2014; Hao et al., 2015). Even when the neocortex is a bridge too far, it might prove possible to design a ‘cerebellum-on-a-chip’. This processing unit would receive its input from the neocortex, correct the signal based on sensory feedback and transmit it forward to the spinal cord and back to the cerebral cortex. Such a tool, as far-fetched as it would seem today, might one day significantly increase the quality of life in patients suffering from cerebellar degeneration.

As with most neurological disorders, a cure for multiple sclerosis is nowhere in sight. Considering the complexity of the disease and the variability of its presentation, it is doubtful if full recovery from the disorder will ever be possible. But a combination of the approaches mentioned in the previous paragraphs might well be able to slow down disease progression and reduce the effect of disability on the daily life of the people affected. Although the studies presented in this thesis only mention simulations, cells and rodents, the final goal was always to translate these findings to patients, and use the findings to bring a future without MS one tiny step closer.

Abstract

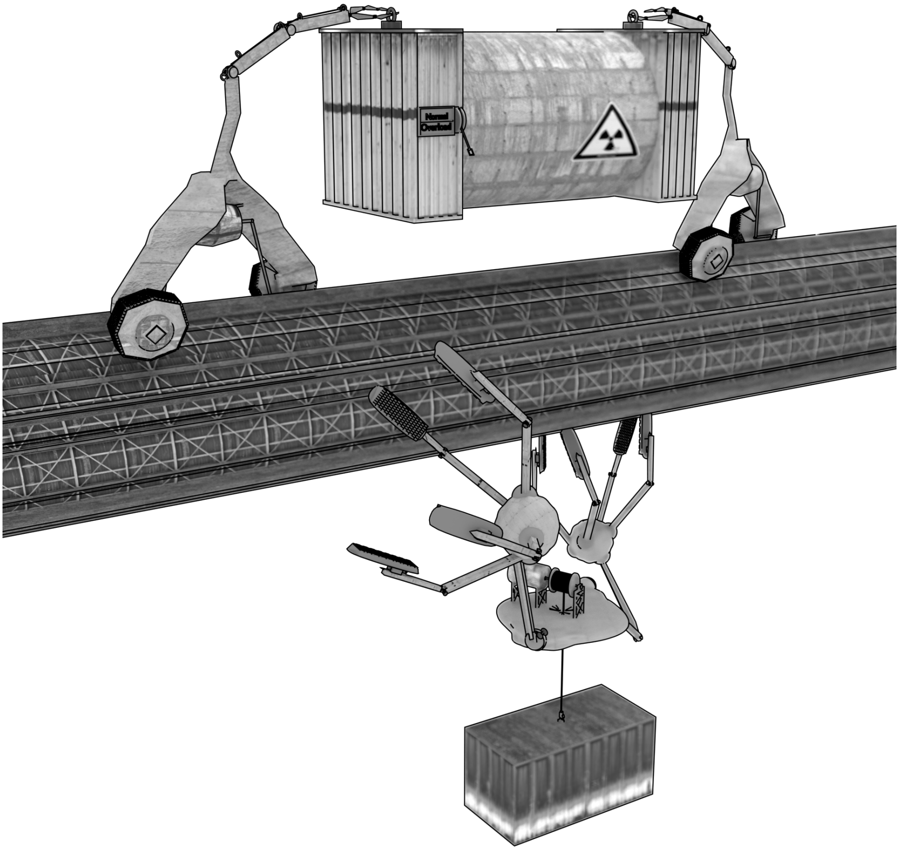

APPENDIX I

ABSTRACT

Brain cells are uniquely shaped among the many cell types of the body. While most cells are more or less rounded or square-shaped, neurons grow one or more long axons that can reach lengths of a meter or more. To keep these axons alive and functional, neurons are dependent on an intracellular transport system, along which cargoes are carried from the cellbody to the far edge of the cell and back again. This transport duty is performed by motor proteins which bind and through conformational changes can move along microtubules. The purpose of this thesis is to contribute to our knowledge of this transport system and its role in the development and function of the central nervous system, with a special focus on the role of this system in multiple sclerosis (MS.

This thesis can be divided in three separate parts. The first part focuses on the role of transport in development, first on the level of individual neurons and neuronal networks (**chapter 2**), then in the development of the cerebellar cortex (**chapter 3**). In the second part we examine the role of transport in MS (**chapters 4-6**). Finally, in the third part we demonstrate how the application of superresolution microscopy can contribute to a better understanding of the transport system (**chapters 7-8**).

In **chapter 2** we descibe the contribution of the neuronal transport system in the development and maintenance of synapses. These contact points between neurons can be reinforced or degraded, altering the communication within a neuronal network. Through this mechanism, the brain is able to store new information and learn new skills. Both the microtubuli cytoskeleton itself as well as the transport taking place along the cytoskeleton is essential for synapic plasticity and therefore for learning and memory. In **chapter 3** we examine the role of the adaptor protein BICD2 in the development of the cerebellum. This protein connects the motor protein dynein with the cargo vesicle. Removing this protein in mice leads to a completely disrupted cerebellar development, where the neurons do not migrate to their proper place in the cerebellar cortex. By removing the protein exclusively in one specific type of cells, we have shown that this developmental disorder only occurs when BICD2 is no longer present in Bergmann glia cells. In this celltype-specific knock-out, we found a reduction of adhesion molecules in the cellular membrane, possibly leading to a disrupted contact between these glia cells and the neurons migrating along them.

Chapter 4 provides an overview of literature on the role of intracellular transport in MS and presents a model to explain the contribution of transport to the development of this disease. In **chapter 5** we show the result of inducing experimental autoimmune encephalomyelitis (EAE) in a mouse in which one of the genes encoding the molecular motor KIF1B has been knocked out. Knocking down both copies of this gene is not compatible with life, but we found that removal of just one copy does not influence susceptibility to or severity of EAE. Since EAE was primarily designed as a model to study the immunological aspects of EAE, in **chapter 6** we present a number of analysis methods designed to increase the value of this model in studying MS.

Research on intracellular transport is highly dependent on advanced microscopy methods to visualise the movement of motor proteins and cargo. In **chapter 7** we explain how light microscopy is limited in resolution because of the physical properties of light and how this limit can be broken. The background of superresolution microscopy is explained, as well as methods to better calculate the achieved resolution and further improve the image quality through drift correction and labelling techniques. In **chapter 8** we apply these techniques by labelling the microtubule cytoskeleton with a $\mathrm{VH_H}$ antibody fragment targetting tubulin. Finally **chapter 9** summarizes the findings of this thesis and proposes a number of recommendations for future research.

Hersencellen onderscheiden zich onder meer van andere cellen in het lichaam door hun extreem lange uitlopers, axonen, die een meter of langer kunnen worden. Om deze axonen in leven te kunnen houden, zijn zij volledig afhankelijk van een intracellulair transportsysteem, waarmee ladingen vanaf het cellichaam naar de verste uitlopers worden vervoerd en weer terug. Dit transport wordt uitgevoerd door motoreiwitten die aan tubulinebuizen (microtubuli) kunnen binden en door hun vorm te veranderen zich daarlangs voortbewegen. Het doel van dit proefschrift is om bij te dragen aan onze kennis van dit transportsysteem en de rol daarvan in de ontwikkeling en werking van het centraal zenuwstelsel, met bijzondere aandacht voor de rol van dit systeem in multipele sclerosis (MS).

Dit proefschrift bestaat uit drie afzonderlijke onderdelen. Het eerste deel richt zich op de rol van transport in ontwikkeling, eerst op de schaal van individuele neuronen en neuronale netwerken (**hoofdstuk 2**), vervolgens in de ontwikkeling van de hersenschors (**hoofdstuk 3**). In het tweede deel onderzoeken we de rol van transport in MS (**hoofdstuk 4-6**). Tenslotte demonstreren we in het derde deel hoe het gebruik van superresolutiemicroscopietechnieken kan bijdragen aan een beter begrip van dit systeem (**hoofdstuk 7-8**).

In **hoofdstuk 2** beschrijven we de bijdrage van het neuronale transportsysteem bij de opbouw en het onderhoud van synapsen. Deze contactpunten tussen neuronen kunnen versterkt worden of juist afgebroken, waardoor de communicatie binnen een neuronaal netwerk veranderd. Via dit mechanisme kan het brein nieuwe informatie opslaan en nieuwe vaardigheden leren. Zowel de microtubuli zelf als het transport daarover is onmisbaar voor synaptische plasticiteit en daarmee voor leren en geheugen.

In **hoofdstuk 3** onderzoeken we de rol van het adaptoreiwit BICD2 in de ontwikkeling van de kleine hersenen. Dit eiwit verbindt het motoreiwit dynein met het blaasje dat de lading bevat. Het uitschakelen van dit eiwit in muizen leidt tot een volledig verstoorde ontwikkeling van de kleine hersenen, waarbij de hersencellen niet migreren naar de juiste laag van de hersenschors. Door het eiwit alleen te verwijderen in bepaalde celtypen, hebben we aan kunnen tonen dat de ontwikkelingsstoornis optreedt als BICD2 niet aanwezig is in Bergmann glia. Hierbij ontstaat een afname van adhesiemoleculen in de celmembraan, wat vermoedelijk leidt tot een verstoord contact tussen deze cellen en de neuronen die erlangs migreren.

Hoofdstuk 4 geeft een overzicht van de al gepubliceerde studies over de rol van intracellulair transport in MS en presenteert een model om de bijdrage van transport aan het ontwikkelen van deze ziekte te verklaren. In **hoofdstuk 5** tonen we de resultaten van het induceren van experimentele autoimmuun encefalomyelitis (EAE) in een muis waarin we een gen voor de moleculaire motor KIF1B hebben uitgeschakeld. Het uitschakelen van beide kopieën van dit gen is niet met het leven verenigbaar, maar het uitschakelen van een enkel gen leidt niet tot een grotere vatbaarheid voor EAE of een ernstiger beloop van dit model voor MS. Aangezien EAE in eerste instantie ontwikkeld is als een model om de immunologische aspecten van MS te onderzoeken, presenteren we in **hoofdstuk 6** een aantal analysemethoden waarmee de waarde van dit model voor het begrijpen van MS vergroot wordt.

Het onderzoek naar intracellulair transport is sterk afhankelijk van geavanceerde microscopietechnieken om de beweging van motoren en ladingen zichtbaar te maken. In **hoofdstuk 7** verklaren we hoe lichtmicroscopie in resolutie beperkt wordt door de golflengte van licht én hoe deze limiet doorbroken kan worden. De achtergrond van superresolutiemicroscopie wordt toegelicht, evenals methoden om de resolutie daarvan beter te berekenen en te optimaliseren door middel van correctie van drift en labelling van moleculen. De studie in **hoofdstuk 8** past deze methodes vervolgens toe om het microtubulecytoskelet met zeer hoge resolutie in beeld te brengen door dit aan te kleuren met $\mathrm{V_H H}$-moleculen gericht tegen tubuline. **Hoofdstuk 9** tenslotte bespreekt de bevindingen van alle onderzoeken in dit proefschrift en doet een aantal aanbevelingen voor toekomstig onderzoek.

B

Bibliography

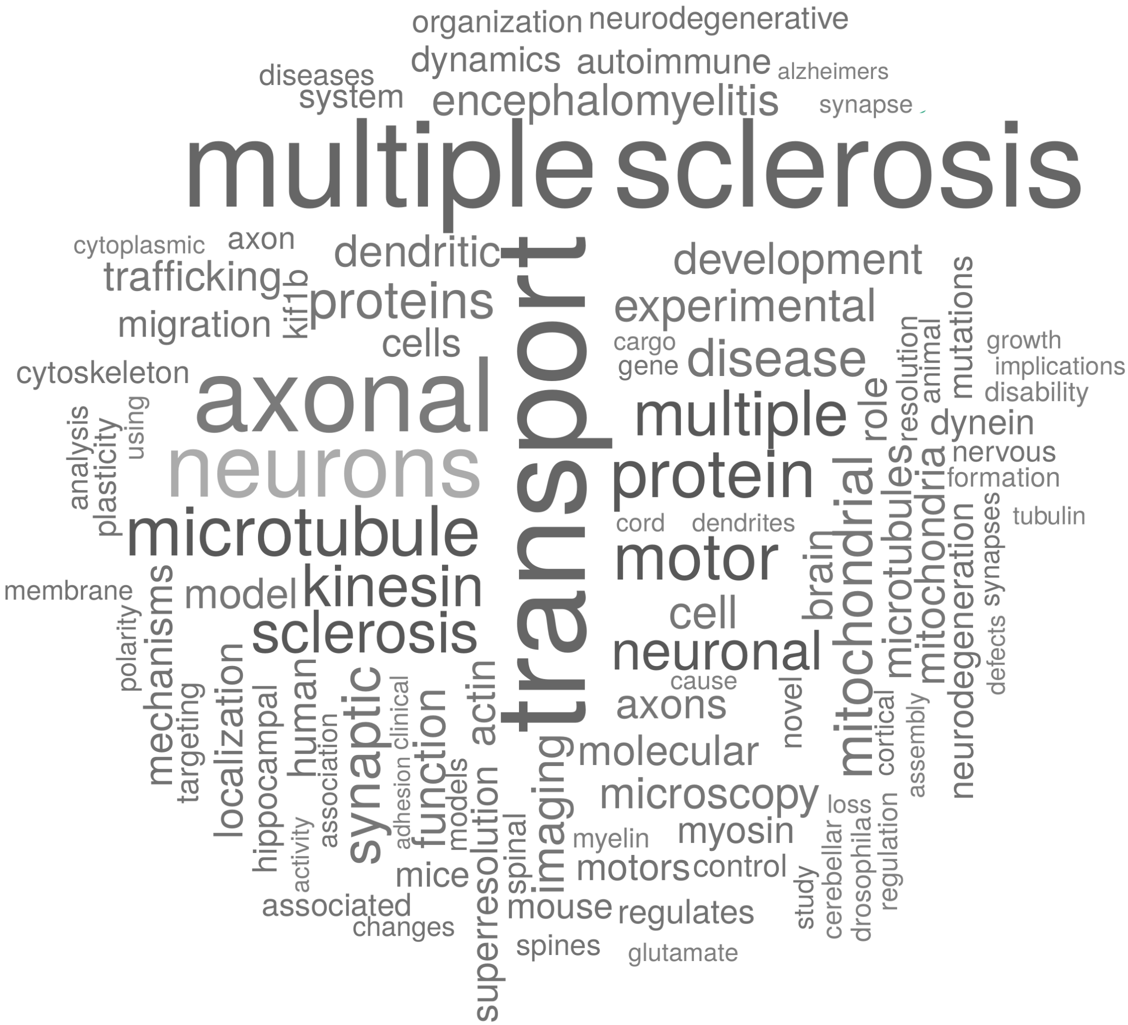

Wordcloud of nouns in the title of publications included in the references, with font size indicating relative frequency.

BIBLIOGRAPHY

Ackerley, S., Grierson, A. J., Brownlees, J., Thornhill, P., Anderton, B. H., Leigh, P. N., Shaw, C. E. and Miller, C. C. (2000). Glutamate slows axonal transport of neurofilaments in transfected neurons. *Journal of Cell Biology* **150**, 165–176.

Adams, N. C., Tomoda, T., Cooper, M., Dietz, G. and Hatten, M. E. (2002). Mice that lack astrotactin have slowed neuronal migration. *Development* **129**, 965–972.

Airy, G. (1835). On the diffraction of an object-glass with circular aperture. *Transactions of the Cambridge Philosophical Society* **5**, 283–291.

Akhmanova, A. and Hammer, J. A. (2010). Linking molecular motors to membrane cargo. *Current Opinion in Cell Biology* **22**, 479–487.

Akhmanova, A. and Steinmetz, M. O. (2008). Tracking the ends: a dynamic protein network controls the fate of microtubule tips. *Nature Reviews. Molecular Cell Biology* **9**, 309–22.

Al-Izki, S., Pryce, G., O'Neill, J. K., Butter, C., Giovannoni, G., Amor, S. and Baker, D. (2012). Practical guide to the induction of relapsing progressive experimental autoimmune encephalomyelitis in the biozzi abh mouse. *Mult Scler Relat Disord* **1**, 29–38.

Alastair, C. and Alasdair, C. (2008). Multiple sclerosis. *Lancet* **372**, 1502–17.

Alcina, A., Fedetz, M., Fernández, O., Saiz, A., Izquierdo, G., Lucas, M., Leyva, L., García-León, J., Abad-Grau, M., Alloza, I. et al. (2013). Identification of a functional variant in the kif5a-cyp27b1-mettl1-fam119b locus associated with multiple sclerosis. *Journal of Medical Genetics* **50**, 25–33.

Alcina, A., Vandenbroeck, K., Otaegui, D., Saiz, A., Gonzalez, J. R., Fernandez, O., Cavanillas, M. L., Cénit, M. C., Arroyo, R., Alloza, I. et al. (2010). The autoimmune disease-associated kif5a, cd226 and sh2b3 gene variants confer susceptibility for multiple sclerosis. *Genes and Immunity* **11**, 439–45.

Ali, M. Y., Lu, H., Bookwalter, C. S., Warshaw, D. M. and Trybus, K. M. (2008). Myosin v and kinesin act as tethers to enhance each others' processivity. *Proceedings of the National Academy of Sciences of the United States of America* **105**, 4691–6.

Alushin, G. M., Lander, G. C., Kellogg, E. H., Zhang, R., Baker, D. and Nogales, E. (2014). High-resolution microtubule structures reveal the structural transitions in -tubulin upon gtp hydrolysis. *Cell* **157**, 1117–29.

Alvarez-Cermeno, J. C., Muoz-Negrete, F. J., Costa-Frossard, L., de la Maza, S. S., Villar, L. M. and Rebolleda, G. (2016). Intrathecal lipid-specific oligoclonal igm synthesis associates with retinal axonal loss in multiple sclerosis. *J Neurol Sci* **360**, 41–4.

Ames, A., 3rd (2000). Cns energy metabolism as related to function. *Brain Res Brain Res Rev* **34**, 42–68.

Amiri, M. and Hollenbeck, P. J. (2008). Mitochondrial biogenesis in the axons of vertebrate peripheral neurons. *Dev Neurobiol* **68**, 1348–61.

Antfolk, C., D'Alonzo, M., Rosn, B., Lundborg, G., Sebelius, F. and Cipriani, C. (2013). Sensory feedback in upper limb prosthetics. *Expert Rev Med Devices* **10**, 45–54.

Appel, N. M. (1997). Classical and contemporary histochemical approaches for evaluating central nervous system microanatomy. *Ann N Y Acad Sci* **820**, 14–28.

Arbabi Ghahroudi, M., Desmyter, A., Wyns, L., Hamers, R. and Muyldermans, S. (1997). Selection and identification of single domain antibody fragments from camel heavy-chain antibodies. *FEBS Letters* **414**, 521–6.

Aulchenko, Y. S., Hoppenbrouwers, I. A., Ramagopalan, S. V., Broer, L., Jafari, N., Hillert, J., Link, J., Lundström, W., Greiner, E., Sadovnick, A. D. et al. (2008). Genetic variation in the kif1b locus influences susceptibility to multiple sclerosis. *Nature Genetics* **40**, 1402–3.

Baas, P. W., Black, M. M. and Banker, G. A. (1989). Changes in microtubule polarity orientation during the development of hippocampal neurons in culture. *Journal of Cell Biology* **109**, 3085–94.

Baas, P. W., Deitch, J. S., Black, M. M. and Banker, G. A. (1988). Polarity orientation of microtubules in hippocampal neurons: uniformity in the axon and nonuniformity in the dendrite. *Proceedings of the National Academy of Sciences of the United States of America* **85**, 8335–9.

Bai, J., Ramos, R. L., Ackman, J. B., Thomas, A. M., Lee, R. V. and LoTurco, J. J. (2003). Rnai reveals doublecortin is required for radial migration in rat neocortex. *Nature Neuroscience* **6**, 1277–1283.

Baker, D. and Amor, S. (2015). Mouse models of multiple sclerosis: lost in translation? *Curr Pharm Des* **21**, 2440–52.

Baker, D., Gerritsen, W., Rundle, J. and Amor, S. (2011). Critical appraisal of animal models of multiple sclerosis. *Multiple Sclerosis* **17**, 647–657.

Baker, D., Lidster, K., Sottomayor, A. and Amor, S. (2014). Two years later: journals are not yet enforcing the arrive guidelines on reporting standards for pre-clinical animal studies. *PLoS Biology* **12**, e1001756.

Banker, G. A. and Cowan, W. M. (1977). Rat hippocampal neurons in dispersed cell culture. *Brain Res* **126**, 397–42.

Banterle, N., Bui, K. H., Lemke, E. A. and Beck, M. (2013). Fourier ring correlation as a resolution criterion for super-resolution microscopy. *Journal of Structural Biology* **183**, 363–7.

Baran, R., Castelblanco, L., Tang, G., Shapiro, I., Goncharov, A. and Jin, Y. (2010). Motor neuron synapse and axon defects in a c. elegans alpha-tubulin mutant. *PLoS One* **5**, e9655.

Barkus, R. V., Klyachko, O., Horiuchi, D., Dickson, B. J. and Saxton, W. M. (2008). Identification of an axonal kinesin-3 motor for fast anterograde vesicle transport that facilitates retrograde transport of neuropeptides. *Molecular Biology of the Cell* **19**, 274–83.

Baron, W. and Hoekstra, D. (2010). On the biogenesis of myelin membranes: sorting, trafficking and cell polarity. *FEBS Lett* **584**, 1760–70.

Bartsch, S., Bartsch, U., Dörries, U., Faissner, A., Weller, A., Ekblom, P. and Schachner, M. (1992). Expression of tenascin in the developing and adult cerebellar cortex. *Journal of Neuroscience* **12**, 736–749.

Bates, M., Huang, B., Dempsey, G. T. and Zhuang, X. (2007). Multicolor super-resolution imaging with photo-switchable fluorescent probes. *Science* **317**, 1749–53.

Bates, M., Huang, B. and Zhuang, X. (2008). Super-resolution microscopy by nanoscale localization of photo-switchable fluorescent probes. *Current Opinion in Chemical Biology* **12**, 505–14.

Baxter, A. G. (2007). The origin and application of experimental autoimmune encephalomyelitis. *Nat Rev Immunol* **7**, 904–12.

Bearer, E. L. and Reese, T. S. (1999). Association of actin filaments with axonal microtubule tracts. *Journal of Neurocytology* **28**, 85–98.

Bel, C., Oguievetskaia, K., Pitaval, C., Goutebroze, L. and Faivre-Sarrailh, C. (2009). Axonal targeting of caspr2 in hippocampal neurons via selective somatodendritic endocytosis. *Journal of Cell Science* **122**, 3403–3413.

Belbasis, L., Bellou, V., Evangelou, E., Ioannidis, J. P. and Tzoulaki, I. (2015). Environmental risk factors and multiple sclerosis: an umbrella review of systematic reviews and meta-analyses. *Lancet Neurol* **14**, 263–73.

Belvindrah, R., Nalbant, P., Ding, S., Wu, C., Bokoch, G. M. and Müller, U. (2006). Integrin-linked kinase regulates bergmann glial differentiation during cerebellar development. *Molecular and Cellular Neurosciences* **33**, 109–125.

Bennett, J. L., de Seze, J., Lana-Peixoto, M., Palace, J., Waldman, A., Schippling, S., Tenembaum, S., Banwell, B., Greenberg, B., Levy, M. et al. (2015). Neuromyelitis optica and multiple sclerosis: Seeing differences through optical coherence tomography. *Mult Scler* **21**, 678–88.

Betzig, E., Harootunian, A., Lewis, A. and Isaacson, M. (1986). Near-field diffraction by a slit: implications for superresolution microscopy. *Applied Optics* **25**, 1890.

Betzig, E., Patterson, G. H., Sougrat, R., Lindwasser, O. W., Olenych, S., Bonifacino, J. S., Davidson, M. W., Lippincott-Schwartz, J. and Hess, H. F. (2006). Imaging intracellular fluorescent proteins at nanometer resolution. *Science* **313**, 1642–5.

Bilsland, L. G., Sahai, E., Kelly, G., Golding, M., Greensmith, L. and Schiavo, G. (2010). Deficits in axonal transport precede als symptoms in vivo. *Proc Natl Acad Sci U S A* **107**, 20523–8.

Bissar-Tadmouri, N., Nelis, E., Zuchner, S., Parman, Y., Deymeer, F., Serdaroglu, P., De Jonghe, P., Van Gerwen, V., Timmerman, V., Schroder, J. M. et al. (2004). Absence of kif1b mutation in a large turkish cmt2a family suggests involvement of a second gene. *Neurology* **62**, 1522–1525.

Bitsch, A., Schuchardt, J., Bunkowski, S., Kuhlmann, T. and Brück, W. (2000). Acute axonal injury in multiple sclerosis. correlation with demyelination and inflammation. *Brain* **123 (Pt 6)**, 1174–83.

Blanpied, T. A. and Ehlers, M. D. (2004). Microanatomy of dendritic spines: emerging principles of synaptic pathology in psychiatric and neurological disease. *Biological Psychiatry* **55**, 1121–7.

Blender Online Community (2015). *Blender - a 3D modelling and rendering package*. Blender Foundation, Blender Institute, Amsterdam.

Boldogh, I. R. and Pon, L. A. (2007). Mitochondria on the move. *Trends in Cell Biology* **17**, 502–10.

Bollen, K. and Barb, K. (1981). Pearson's r and coarsely categorized measures. *American Sociological Review* **46**, 232–239.

Bonnon, C., Bel, C., Goutebroze, L., Maigret, B., Girault, J. A. and Faivre-Sarrailh, C. (2007). Pgy repeats and n-glycans govern the trafficking of paranodin and its selective association with contactin and neurofascin-155. *Mol Biol Cell* **18**, 229–41.

Bonnon, C., Goutebroze, L., Denisenko-Nehrbass, N., Girault, J. A. and Faivre-Sarrailh, C. (2003). The paranodal complex of f3/contactin and caspr/paranodin traffics to the cell surface via a non-conventional pathway. *J Biol Chem* **278**, 48339–47.

Bove, R. and Chitnis, T. (2013). Sexual disparities in the incidence and course of ms. *Clinical Immunology* **149**, 201–10.

Bove, R. and Chitnis, T. (2014). The role of gender and sex hormones in determining the onset and outcome of multiple sclerosis. *Multiple Sclerosis* **20**, 520–6.

Brown, R. R., Deletic, A. and Wong, T. H. (2015). Interdisciplinarity: How to catalyse collaboration. *Nature* **525**, 315–7.

Budday, S., Steinmann, P. and Kuhl, E. (2015). Physical biology of human brain development. *Front Cell Neurosci* **9**, 257.

Budde, M. D., Xie, M., Cross, A. H. and Song, S. K. (2009). Axial diffusivity is the primary correlate of axonal injury in the experimental autoimmune encephalomyelitis spinal cord: a quantitative pixelwise analysis. *Journal of Neuroscience* **29**, 2805–13.

Buddeberg, B. S., Kerschensteiner, M., Merkler, D., Stadelmann, C. and Schwab, M. E. (2004). Behavioral testing strategies in a localized animal model of multiple sclerosis. *Journal of Neuroimmunology* **153**, 158–70.

Buffo, A. and Rossi, F. (2013). Origin, lineage and function of cerebellar glia. *Progress in Neurobiology* **109**, 42–63.

Bullock, S. L. and Ish-Horowicz, D. (2001). Conserved signals and machinery for rna transport in drosophila oogenesis and embryogenesis. *Nature* **414**, 611–616.

Burton, P. R. (1988). Dendrites of mitral cell neurons contain microtubules of opposite polarity. *Brain Research* **473**, 107–15.

Bustamante, M. F., Morcillo-Surez, C., Malhotra, S., Rio, J., Leyva, L., Fernndez, O., Zettl, U. K., Killestein, J., Brassat, D., Garca-Merino, J. A. et al. (2015). Pharmacogenomic study in patients with multiple sclerosis: Responders and nonresponders to ifn-. *Neurol Neuroimmunol Neuroinflamm* **2**, e154.

Cai, Q., Pan, P.-Y. and Sheng, Z.-H. (2007). Syntabulin-kinesin-1 family member 5b-mediated axonal transport contributes to activity-dependent presynaptic assembly. *Journal of Neuroscience* **27**, 7284–96.

Cai, Q. and Sheng, Z. H. (2009a). Mitochondrial transport and docking in axons. *Exp Neurol* **218**, 257–67.

Cai, Q. and Sheng, Z.-H. (2009b). Moving or stopping mitochondria: Miro as a traffic cop by sensing calcium. *Neuron* **61**, 493–6.

Campbell, G. R. and Mahad, D. J. (2012). Mitochondrial changes associated with demyelination: consequences for axonal integrity. *Mitochondrion* **12**, 173–9.

Campbell, G. R., Worrall, J. T. and Mahad, D. J. (2014a). The central role of mitochondria in axonal degeneration in multiple sclerosis. *Mult Scler* **20**, 1806–13.

Campbell, P. D., Shen, K., Sapio, M. R., Glenn, T. D., Talbot, W. S. and Marlow, F. L. (2014b). Unique function of kinesin kif5a in localization of mitochondria in axons. *J Neurosci* **34**, 14717–32.

Carlson, B. M. (2004). *Human Embryology and Developmental Biology*. Elsevier Mosby.

Carrington, W. A., Lynch, R. M., Moore, E. D., Isenberg, G., Fogarty, K. E. and Fay, F. S. (1995). Superresolution three-dimensional images of fluorescence in cells with minimal light exposure. *Science* **268**, 1483–7.

Carson, J. H., Worboys, K., Ainger, K. and Barbarese, E. (1997). Translocation of myelin basic protein mrna in oligodendrocytes requires microtubules and kinesin. *Cell Motil Cytoskeleton* **38**, 318–28.

Carter, A. P., Garbarino, J. E., Wilson-Kubalek, E. M., Shipley, W. E., Cho, C., Milligan, R. A., Vale, R. D. and Gibbons, I. R. (2008). Structure and functional role of dynein's microtubule-binding domain. *Science* **322**, 1691–5.

Chabot, S., Williams, G. and Yong, V. W. (1997). Microglial production of tnf-alpha is induced by activated t lymphocytes. involvement of vla-4 and inhibition by interferonbeta-1b. *J Clin Invest* **100**, 604–12.

Charcot, M. (1868). Histologie de la sclerose en plaques. *Gaz Hosp* **141**, 554–557.

Chatterjee, T., Chatterjee, B. K., Majumdar, D. and Chakrabarti, P. (2015). Antibacterial effect of silver nanoparticles and the modeling of bacterial growth kinetics using a modified gompertz model. *Biochimica et Biophysica Acta* **1850**, 299–306.

Chédotal, A. (2010). Should i stay or should i go? becoming a granule cell. *Trends in Neurosciences* **33**, 163–172.

Cheever, T. R. and Ervasti, J. M. (2013). Actin isoforms in neuronal development and function. *Int Rev Cell Mol Biol* **301**, 157–213.

Chen, J., Kanai, Y., Cowan, N. J. and Hirokawa, N. (1992). Projection domains of map2 and tau determine spacings between microtubules in dendrites and axons. *Nature* **360**, 674–7.

Cheng, L., Desai, J., Miranda, C. J., Duncan, J. S., Qiu, W., Nugent, A. A., Kolpak, A. L., Wu, C. C., Drokhlyansky, E., Delisle, M. M. et al. (2014). Human cfeom1 mutations attenuate kif21a autoinhibition and cause oculomotor axon stalling. *Neuron* **82**, 334–49.

Chereau, R., Tnnesen, J. and Ngerl, U. V. (2015). Sted microscopy for nanoscale imaging in living brain slices. *Methods* **88**, 57–66.

Chevalier-Larsen, E. and Holzbaur, E. L. (2006). Axonal transport and neurodegenerative disease. *Biochimica et Biophysica Acta* **1762**, 1094–1108.

Chiquet-Ehrismann, R. and Tucker, R. P. (2011). Tenascins and the importance of adhesion modulation. *Cold Spring Harbor Perspectives in Biology* **3**.

Chizhikov, V. and Millen, K. J. (2003). Development and malformations of the cerebellum in mice. *Molecular Genetics and Metabolism* **80**, 54–65.

Choquet, D. (2014). The 2014 nobel prize in chemistry: a large-scale prize for achievements on the nanoscale. *Neuron* **84**, 1116–9.

Chung, R. S., McCormack, G. H., King, A. E., West, A. K. and Vickers, J. C. (2005). Glutamate induces rapid loss of axonal neurofilament proteins from cortical neurons in vitro. *Exp Neurol* **193**, 481–8.

Chuong, C. M., Crossin, K. L. and Edelman, G. M. (1987). Sequential expression and differential function of multiple adhesion molecules during the formation of cerebellar cortical layers. *Journal of Cell Biology* **104**, 331–342.

Cingolani, L. and Goda, Y. (2008). Actin in action: the interplay between the actin cytoskeleton and synaptic efficacy. *Nature Reviews. Neuroscience* **9**, 344–56.

Claussen, M. and Suter, B. (2005). Bicd-dependent localization processes: from drosophilia development to human cell biology. *Annals of Anatomy* **187**, 539–553.

Cloin, B. M., Hoogenraad, C. C., Mikhaylova, M. and Kapitein, L. C. (2015). *Immunocytochemistry and Related Techniques*, volume 101. Springer, 389-408 pp.

Cohen-Adad, J. and Wheeler-Kingshott, C. (2014). *Quantitative MRI of the Spinal Cord.* Elsevier Science.

Colin, E., Zala, D., Liot, G., Rangone, H., Borrell-Pagès, M., Li, X.-J., Saudou, F. and Humbert, S. (2008). Huntingtin phosphorylation acts as a molecular switch for anterograde/retrograde transport in neurons. *EMBO Journal* **27**, 2124–34.

Comabella, M., Craig, D. W., Morcillo-Surez, C., Ro, J., Navarro, A., Fernndez, M., Martin, R. and Montalban, X. (2009). Genome-wide scan of 500,000 single-nucleotide polymorphisms among responders and nonresponders to interferon beta therapy in multiple sclerosis. *Arch Neurol* **66**, 972–8.

Conde, C. and Caceres, A. (2009). Microtubule assembly, organization and dynamics in axons and dendrites. *Nature Reviews. Neuroscience* **180**, 619–632.

Conti, M. A. and Adelstein, R. S. (2008). Nonmuscle myosin ii moves in new directions. *Journal of Cell Science* **121**, 11–8.

Coutelis, J. B. and Ephrussi, A. (2007). Rab6 mediates membrane organization and determinant localization during drosophila oogenesis. *Development* **134**, 1419–1430.

Craig, A. M., Blackstone, C. D., Huganir, R. L. and Banker, G. (1993). The distribution of glutamate receptors in cultured rat hippocampal neurons: postsynaptic clustering of ampa-selective subunits. *Neuron* **10**, 1055–1068.

Craner, M. J., Newcombe, J., Black, J. A., Hartle, C., Cuzner, M. L. and Waxman, S. G. (2004). Molecular changes in neurons in multiple sclerosis: altered axonal expression of nav1.2 and nav1.6 sodium channels and na+/ca2+ exchanger. *Proc Natl Acad Sci U S A* **101**, 8168–73.

Dani, A., Huang, B., Bergan, J., Dulac, C. and Zhuang, X. (2010). Superresolution imaging of chemical synapses in the brain. *Neuron* **68**, 843–56.

Dasgupta, S., Jana, M., Liu, X. and Pahan, K. (2002). Myelin basic protein-primed t cells induce nitric oxide synthase in microglial cells. implications for multiple sclerosis. *J Biol Chem* **277**, 39327–33.

De Vos, K., Severin, F., Van Herreweghe, F., Vancompernolle, K., Goossens, V., Hyman, A. and Grooten, J. (2000). Tumor necrosis factor induces hyperphosphorylation of kinesin light chain and inhibits kinesin-mediated transport of mitochondria. *Journal of Cell Biology* **149**, 1207–1214.

De Vos, K. J., Grierson, A. J., Ackerley, S. and Miller, C. C. J. (2008). Role of axonal transport in neurodegenerative diseases. *Annual Review of Neuroscience* **31**, 151–73.

De Wit, J., Toonen, R. F., Verhaagen, J. and Verhage, M. (2006). Vesicular trafficking of semaphorin 3a is activity-dependent and differs between axons and dendrites. *Traffic* **7**, 1060–77.

Dehmelt, L. and Halpain, S. (2005). The map2/tau family of microtubule-associated proteins. *Genome Biology* **6**, 204–204.

Dempsey, G. T., Vaughan, J. C., Chen, K. H., Bates, M. and Zhuang, X. (2011). Evaluation of fluorophores for optimal performance in localization-based super-resolution imaging. *Nature Methods* **8**, 1027–36.

Dendrou, C. A. and Fugger, L. (2014). Please mind the gap: axonal transport deficits in multiple sclerosis neurodegeneration. *Neuron* **84**, 1105–7.

Dent, E. W. and Gertler, F. B. (2003). Cytoskeletal dynamics and transport in growth cone motility and axon guidance. *Neuron* **40**, 209–227.

Desnos, C., Huet, S. and Darchen, F. (2007). 'should i stay or should i go?': myosin v function in organelle trafficking. *Biology of the Cell* **99**, 411–23.

D'Este, E., Kamin, D., Velte, C., Gttfert, F., Simons, M. and Hell, S. W. (2016). Subcortical cytoskeleton periodicity throughout the nervous system. *Sci Rep* **6**, 22741.

Dickens, A. M., Larkin, J. R., Griffin, J. L., Cavey, A., Matthews, L., Turner, M. R., Wilcock, G. K., Davis, B. G., Claridge, T. D., Palace, J. et al. (2014). A type 2 biomarker separates relapsing-remitting from secondary progressive multiple sclerosis. *Neurology* **83**, 1492–9.

Dityatev, A., Seidenbecher, C. I. and Schachner, M. (2010). Compartmentalization from the outside: the extracellular matrix and functional microdomains in the brain. *Trends in Neurosciences* **33**, 503–512.

Dixit, R., Ross, J. L., Goldman, Y. E. and Holzbaur, E. L. F. (2008). Differential regulation of dynein and kinesin motor proteins by tau. *Science* **319**, 1086–9.

Donkelaar, H., Lammens, M. and Hori, A. (2006). *Clinical Neuroembryology: Development and Developmental Disorders of the Human Central Nervous System*. Medicine (Springer-11650; ZDB-2-SME). Springer Berlin Heidelberg.

Donoghue, J. P. (2002). Connecting cortex to machines: recent advances in brain interfaces. *Nat Neurosci* **5 Suppl**, 1085–8.

Du, S., Itoh, N., Askarinam, S., Hill, H., Arnold, A. P. and Voskuhl, R. R. (2014). Xy sex chromosome complement, compared with xx, in the cns confers greater neurodegeneration during experimental autoimmune encephalomyelitis. *Proceedings of the National Academy of Sciences of the United States of America* **111**, 2806–2811.

Dubey, J., Ratnakaran, N. and Koushika, S. P. (2015). Neurodegeneration and microtubule dynamics: death by a thousand cuts. *Front Cell Neurosci* **9**, 343.

Dubois, N. C., Hofmann, D., Kaloulis, K., Bishop, J. M. and Trumpp, A. (2006). Nestin-cre transgenic mouse line nes-cre1 mediates highly efficient cre/loxp mediated recombination in the nervous system, kidney, and somite-derived tissues. *Genesis* **44**, 355–360.

Dunn, S. E. and Steinman, L. (2013). The gender gap in multiple sclerosis: intersection of science and society. *JAMA Neurology* **70**, 634–5.

Duraku, L. S., Niehof, S. P., Misirli, Y., Everaers, M., Hoendervangers, S., Holstege, J., Boele, H. J., Koekkoek, S. K., Smits, E. S., Selles, R. W. et al. (2014). Rotterdam advanced multiple plate: a novel method to measure cold hyperalgesia and allodynia in freely behaving rodents. *Journal of Neuroscience Methods* **224**, 1–12.

Dutta, R., McDonough, J., Yin, X., Peterson, J., Chang, A., Torres, T., Gudz, T., Macklin, W. B., Lewis, D. A., Fox, R. J. et al. (2006). Mitochondrial dysfunction as a cause of axonal degeneration in multiple sclerosis patients. *Ann Neurol* **59**, 478–89.

Dutta, R. and Trapp, B. D. (2007). Pathogenesis of axonal and neuronal damage in multiple sclerosis. *Neurology* **68**, S22–31; discussion S43–54.

d'Ydewalle, C., Krishnan, J., Chiheb, D. M., Van Damme, P., Irobi, J., Kozikowski, A. P., Vanden Berghe, P., Timmerman, V., Robberecht, W. and Van Den Bosch, L. (2011). Hdac6 inhibitors reverse axonal loss in a mouse model of mutant hspb1-induced charcot-marie-tooth disease. *Nat Med* **17**, 968–74.

Ebbing, B., Mann, K., Starosta, A., Jaud, J., Schöls, L., Schüle, R. and Woehlke, G. (2008). Effect of spastic paraplegia mutations in kif5a kinesin on transport activity. *Human Molecular Genetics* **17**, 1245–52.

Ebers, G. C. (2001). Natural history of multiple sclerosis. *Journal of Neurology, Neurosurgery and Psychiatry* **71 Suppl 2**, ii16–9.

Edelstein, A., Amodaj, N., Hoover, K., Vale, R. and Stuurman, N. (2010). Computer control of microscopes using manager. *Current Protocols in Molecular Biology* **Chapter 14**, Unit14.20.

Edgar, J. M., McLaughlin, M., Yool, D., Zhang, S. C., Fowler, J. H., Montague, P., Barrie, J. A., McCulloch, M. C., Duncan, I. D., Garbern, J. et al. (2004). Oligodendroglial modulation of fast axonal transport in a mouse model of hereditary spastic paraplegia. *J Cell Biol* **166**, 121–31.

Ehmann, N., van de Linde, S., Alon, A., Ljaschenko, D., Keung, X. Z., Holm, T., Rings, A., DiAntonio, A., Hallermann, S., Ashery, U. et al. (2014). Quantitative super-resolution imaging of bruchpilot distinguishes active zone states. *Nature Communications* **5**, 4650.

Einheber, S., Meng, X., Rubin, M., Lam, I., Mohandas, N., An, X., Shrager, P., Kissil, J., Maurel, P. and Salzer, J. L. (2013). The 4.1b cytoskeletal protein regulates the domain organization and sheath thickness of myelinated axons. *Glia* **61**, 240–53.

Einheber, S., Zanazzi, G., Ching, W., Scherer, S., Milner, T. A., Peles, E. and Salzer, J. L. (1997). The axonal membrane protein caspr, a homologue of neurexin iv, is a component of the septate-like paranodal junctions that assemble during myelination. *J Cell Biol* **139**, 1495–506.

Erck, C., Peris, L., Andrieux, A., Meissirel, C., Gruber, A. D., Vernet, M., Schweitzer, A., Saoudi, Y., Pointu, H., Bosc, C. et al. (2005). A vital role of tubulin-tyrosine-ligase for neuronal organization. *Proceedings of the National Academy of Sciences of the United States of America* **102**, 7853–8.

Errede, M., Girolamo, F., Ferrara, G., Strippoli, M., Morando, S., Boldrin, V., Rizzi, M., Uccelli, A., Perris, R., Bendotti, C. et al. (2012). Blood-brain barrier alterations in the cerebral cortex in experimental autoimmune encephalomyelitis. *Journal of Neuropathology and Experimental Neurology* **71**, 840–54.

Fanara, P., Husted, K. H., Selle, K., Wong, P. Y., Banerjee, J., Brandt, R. and Hellerstein, M. K. (2010). Changes in microtubule turnover accompany synaptic plasticity and memory formation in response to contextual fear conditioning in mice. *Neuroscience* **168**, 167–78.

Fang, C., Bourdette, D. and Banker, G. (2012). Oxidative stress inhibits axonal transport: implications for neurodegenerative diseases. *Mol Neurodegener* **7**, 29.

Federico, A., Cardaioli, E., Da Pozzo, P., Formichi, P., Gallus, G. N. and Radi, E. (2012). Mitochondria, oxidative stress and neurodegeneration. *J Neurol Sci* **322**, 254–62.

Fejtova, A., Davydova, D., Bischof, F., Lazarevic, V., Altrock, W. D., Romorini, S., Schöne, C., Zuschratter, W., Kreutz, M. R., Garner, C. C. et al. (2009). Dynein light chain regulates axonal trafficking and synaptic levels of bassoon. *Journal of Cell Biology* **185**, 341–55.

Ferguson, B., Matyszak, M. K., Esiri, M. M. and Perry, V. H. (1997). Axonal damage in acute multiple sclerosis lesions. *Brain* **120 (Pt 3)**, 393–9.

Filippi, M. (2015). Mri measures of neurodegeneration in multiple sclerosis: implications for disability, disease monitoring, and treatment. *J Neurol* **262**, 1–6.

Fitzgerald, J. E., Lu, J. and Schnitzer, M. J. (2012). Estimation theoretic measure of resolution for stochastic localization microscopy. *Physical Review Letters* **109**, 048102.

Flegel, M., Knox, K. and Nickel, D. (2012). Step-length variability in minimally disabled women with multiple sclerosis or clinically isolated syndrome. *International journal of MS care* **14**, 26–30.

Fleming, K. K., Bovaird, J. A., Mosier, M. C., Emerson, M. R., LeVine, S. M. and Marquis, J. G. (2005). Statistical analysis of data from studies on experimental autoimmune encephalomyelitis. *J Neuroimmunol* **170**, 71–84.

Franklin, R. J. and Ffrench-Constant, C. (2008). Remyelination in the cns: from biology to therapy. *Nat Rev Neurosci* **9**, 839–55.

Friese, M. A. and Fugger, L. (2009). Pathogenic cd8(+) t cells in multiple sclerosis. *Ann Neurol* **66**, 132–41.

Frischer, J. M., Bramow, S., Dal-Bianco, A., Lucchinetti, C. F., Rauschka, H., Schmidbauer, M., Laursen, H., Sorensen, P. S. and Lassmann, H. (2009). The relation between inflammation and neurodegeneration in multiple sclerosis brains. *Brain* **132**, 1175–89.

Frischer, J. M., Weigand, S. D., Guo, Y., Kale, N., Parisi, J. E., Pirko, I., Mandrekar, J., Bramow, S., Metz, I., Brck, W. et al. (2015). Clinical and pathological insights into the dynamic nature of the white matter multiple sclerosis plaque. *Ann Neurol* **78**, 710–21.

Frost, N. A., Kerr, J. M., Lu, H. E. and Blanpied, T. A. (2010a). A network of networks: cytoskeletal control of compartmentalized function within dendritic spines. *Current Opinion in Neurobiology* **20**, 578–587.

Frost, N. A., Shroff, H., Kong, H., Betzig, E. and Blanpied, T. A. (2010b). Single-molecule discrimination of discrete perisynaptic and distributed sites of actin filament assembly within dendritic spines. *Neuron* **67**, 86–99.

Gaillard, J., Neumann, E., Van Damme, D., Stoppin-Mellet, V., Ebel, C., Barbier, E., Geelen, D. and Vantard, M. (2008). Two microtubule-associated proteins of arabidopsis map65s promote antiparallel microtubule bundling. *Mol Biol Cell* **19**, 4534–44.

Gajofatto, A., Calabrese, M., Benedetti, M. D. and Monaco, S. (2013). Clinical, mri, and csf markers of disability progression in multiple sclerosis. *Dis Markers* **35**, 687–99.

Garrido, J. J., Fernandes, F., Giraud, P., Mouret, I., Pasqualini, E., Fache, M. P., Jullien, F. and Dargent, B. (2001). Identification of an axonal determinant in the c-terminus of the sodium channel na(v)1.2. *EMBO Journal* **20**, 5950–5961.

Gentil, B. J. and Cooper, L. (2012). Molecular basis of axonal dysfunction and traffic impairments in cmt. *Brain Research Bulletin* **88**, 444–53.

Geurts, J. J. and Barkhof, F. (2008). Grey matter pathology in multiple sclerosis. *Lancet Neurol* **7**, 841–51.

Gindhart, J. G. (2006). Towards an understanding of kinesin-1 dependent transport pathways through the study of protein-protein interactions. *Briefings in Functional Genomics and Proteomics* **5**, 74–86.

Glater, E. E., Megeath, L. J., Stowers, R. S. and Schwarz, T. L. (2006). Axonal transport of mitochondria requires milton to recruit kinesin heavy chain and is light chain independent. *Journal of Cell Biology* **173**, 545–57.

Goldstein, L. S. (2001). Kinesin molecular motors: transport pathways, receptors, and human disease. *Proceedings of the National Academy of Sciences of the United States of America* **98**, 6999–7003.

Goldstein, L. S. and Yang, Z. (2000). Microtubule-based transport systems in neurons: the roles of kinesins and dyneins. *Annual Review of Neuroscience* **23**, 39–71.

Gompertz, B. (1825). On the nature of the function expressive of the law of human mortality, and on a new mode of determining the value of life contingencies. *Philosophical Transactions of the Royal Society of London* **115**, 513–585.

Gong, T. W., Winnicki, R. S., Kohrman, D. C. and Lomax, M. I. (1999). A novel mouse kinesin of the unc-104/kif1 subfamily encoded by the kif1b gene. *Gene* **239**, 117–27.

Goodin, D. S. (2014). The epidemiology of multiple sclerosis: insights to disease pathogenesis. *Handbook of Clinical Neurology* **122**, 231–66.

Goris, A., Boonen, S., D'hooghe, M. and Dubois, B. (2010). Replication of kif21b as a susceptibility locus for multiple sclerosis. *Journal of Medical Genetics* **47**, 775–6.

Gornstein, E. and Schwarz, T. L. (2014). The paradox of paclitaxel neurotoxicity: Mechanisms and unanswered questions. *Neuropharmacology* **76 Pt A**, 175–83.

Gorski, J. A., Talley, T., Qiu, M., Puelles, L., Rubenstein, J. L. and Jones, K. R. (2002). Cortical excitatory neurons and glia, but not gabaergic neurons, are produced in the emx1-expressing lineage. *Journal of Neuroscience* **22**, 6309–6314.

Gouveia, S. M. and Akhmanova, A. (2010). Cell and molecular biology of microtubule plus end tracking proteins: end binding proteins and their partners. *International Review of Cell and Molecular Biology* **285**, 1–74.

Govek, E. E., Hatten, M. E. and Van Aelst, L. (2011). The role of rho gtpase proteins in cns neuronal migration. *Developmental Neurobiology* **71**, 528–553.

Govek, E.-E., Newey, S. E., Akerman, C. J., Cross, J. R., Van der Veken, L. and Van Aelst, L. (2004). The x-linked mental retardation protein oligophrenin-1 is required for dendritic spine morphogenesis. *Nature Neuroscience* **7**, 364–72.

Govindarajan, N., Rao, P., Burkhardt, S., Sananbenesi, F., Schlter, O. M., Bradke, F., Lu, J. and Fischer, A. (2013). Reducing hdac6 ameliorates cognitive deficits in a mouse model for alzheimer's disease. *EMBO Mol Med* **5**, 52–63.

Grigoriev, I., Splinter, D., Keijzer, N., Wulf, P. S., Demmers, J., Ohtsuka, T., Modesti, M., Maly, I. V., Grosveld, F., Hoogenraad, C. C. et al. (2007). Rab6 regulates transport and targeting of exocytotic carriers. *Developmental Cell* **13**, 305–14.

Gross, S. P., Vershinin, M. and Shubeita, G. T. (2007). Cargo transport: two motors are sometimes better than one. *Current Biology* **17**, R478–86.

Grothendieck, G. (2013). *nls2: Non-linear regression with brute force.* R package version 0.2.

Grumet, M., Hoffman, S., Crossin, K. L. and Edelman, G. M. (1985). Cytotactin, an extracellular matrix protein of neural and non-neural tissues that mediates glia-neuron interaction. *Proceedings of the National Academy of Sciences of the United States of America* **82**, 8075–8079.

Guedes-Dias, P., de Proena, J., Soares, T. R., Leito-Rocha, A., Pinho, B. R., Duchen, M. R. and Oliveira, J. M. (2015). Hdac6 inhibition induces mitochondrial fusion, autophagic flux and reduces diffuse mutant huntingtin in striatal neurons. *Biochim Biophys Acta* **1852**, 2484–93.

Guillaud, L., Wong, R. and Hirokawa, N. (2008). Disruption of kif17-mint1 interaction by camkii-dependent phosphorylation: a molecular model of kinesin-cargo release. *Nature Cell Biology* **10**, 19–29.

Gunawardena, S. and Goldstein, L. S. (2004). Cargo-carrying motor vehicles on the neuronal highway: transport pathways and neurodegenerative disease. *Journal of Neurobiology* **58**, 258–271.

Gustafsson, M. G. (2000). Surpassing the lateral resolution limit by a factor of two using structured illumination microscopy. *J Microsc* **198**, 82–7.

Guy, J., Ellis, E. A., Tark, E. F., 3rd, Hope, G. M. and Rao, N. A. (1989). Axonal transport reductions in acute experimental allergic encephalomyelitis: qualitative analysis of the optic nerve. *Curr Eye Res* **8**, 261–9.

Ha, J., Lo, K., Myers, K. R., Carr, T. M., Humsi, M. K., Rasoul, B. A., Segal, R. A. and Pfister, K. K. (2008). A neuron-specific cytoplasmic dynein isoform preferentially transports trkb signaling endosomes. *Journal of Cell Biology* **181**, 1027–39.

Haase, G. and Rabouille, C. (2015). Golgi fragmentation in als motor neurons. new mechanisms targeting microtubules, tethers, and transport vesicles. *Front Neurosci* **9**, 448.

Hafezparast, M., Klocke, R., Ruhrberg, C., Marquardt, A., Ahmad-Annuar, A., Bowen, S., Lalli, G., Witherden, A. S., Hummerich, H., Nicholson, S. et al. (2003). Mutations in dynein link motor neuron degeneration to defects in retrograde transport. *Science* **300**, 808–12.

Hafler, D. A., Compston, A., Sawcer, S., Lander, E. S., Daly, M. J., De Jager, P. L., De Bakker, P., Gabriel, S. B., Mirel, D. B., Ivinson, A. J. et al. (2007). Risk alleles for multiple sclerosis identified by a genomewide study. *New England Journal of Medicine* **357**, 851–62.

Hamilton, F., Rochester, L., Paul, L., Rafferty, D., O'Leary, C. P. and Evans, J. J. (2009). Walking and talking: an investigation of cognitive-motor dual tasking in multiple sclerosis. *Multiple Sclerosis* **15**, 1215–27.

Hammond, J. W., Cai, D. and Verhey, K. J. (2008). Tubulin modifications and their cellular functions. *Current Opinion in Cell Biology* **20**, 71–6.

Hammond, J. W., fang Huang, C., Kaech, S., Jacobson, C., Banker, G. and Verhey, K. J. (2010). Posttranslational modifications of tubulin and the polarized transport of kinesin-1 in neurons. *Molecular Biology of the Cell* **21**, 572–583.

Hao, S., Tang, B., Wu, Z., Ure, K., Sun, Y., Tao, H., Gao, Y., Patel, A. J., Curry, D. J., Samaco, R. C. et al. (2015). Forniceal deep brain stimulation rescues hippocampal memory in rett syndrome mice. *Nature* **526**, 430–4.

Hares, K., Kemp, K., Rice, C., Gray, E., Scolding, N. and Wilkins, A. (2013). Reduced axonal motor protein expression in non-lesional grey matter in multiple sclerosis. *Mult Scler* .

Hares, K., Redondo, J., Kemp, K., Rice, C., Scolding, N. and Wilkins, A. (2016). Axonal motor protein kif5a and associated cargo deficits in multiple sclerosis lesional and normal-appearing white matter. *Neuropathol Appl Neurobiol* .

Harlow, D. E., Honce, J. M. and Miravalle, A. A. (2015). Remyelination therapy in multiple sclerosis. *Front Neurol* **6**, 257.

Harris, L. J., Skaletsky, E. and McPherson, A. (1998). Crystallographic structure of an intact igg1 monoclonal antibody. *J Mol Biol* **275**, 861–72.

Hatten, M. E. (1999). Central nervous system neuronal migration. *Annual Review of Neuroscience* **22**, 511–539.

Hawker, K. (2011). Progressive multiple sclerosis: characteristics and management. *Neurol Clin* **29**, 423–34.

Hecht, E. (2002). *Optics.* Pearson Education, 4 edition.

Heilemann, M., van de Linde, S., Schttpelz, M., Kasper, R., Seefeldt, B., Mukherjee, A., Tinnefeld, P. and Sauer, M. (2008). Subdiffraction-resolution fluorescence imaging with conventional fluorescent probes. *Angew Chem Int Ed Engl* **47**, 6172–6.

Hempen, B. and Brion, J. P. (1996). Reduction of acetylated alpha-tubulin immunoreactivity in neurofibrillary tangle-bearing neurons in alzheimer's disease. *J Neuropathol Exp Neurol* **55**, 964–72.

Hintzen, R., Aulchenko, Y., Ebers, G. and Van Duijn, C. (2010). Reply to "lack of support for association between the kif1b rs10492972[c] variant and multiple sclerosis". *Nature Genetics* **42**, 470–471.

Hippenmeyer, S., Youn, Y. H., Moon, H. M., Miyamichi, K., Zong, H., Wynshaw-Boris, A. and Luo, L. (2010). Genetic mosaic dissection of lis1 and ndel1 in neuronal migration. *Neuron* **68**, 695–709.

Hirokawa, N., Niwa, S. and Tanaka, Y. (2010). Molecular motors in neurons: transport mechanisms and roles in brain function, development, and disease. *Neuron* **68**, 610–38.

Hirokawa, N. and Noda, Y. (2008). Intracellular transport and kinesin superfamily proteins , kifs : Structure , function , and dynamics. *Physiological Reviews* **88**, 1089 –1118.

Hirokawa, N., Noda, Y., Tanaka, Y. and Niwa, S. (2009). Kinesin superfamily motor proteins and intracellular transport. *Nature Reviews. Molecular Cell Biology* **10**, 682–96.

Hirokawa, N. and Takemura, R. (2005). Molecular motors and mechanisms of directional transport in neurons. *Nature Reviews. Neuroscience* **6**, 201–214.

Hiruma, H., Katakura, T., Takahashi, S., Ichikawa, T. and Kawakami, T. (2003). Glutamate and amyloid beta-protein rapidly inhibit fast axonal transport in cultured rat hippocampal neurons by different mechanisms. *J Neurosci* **23**, 8967–77.

Hoglund, K. and Salter, H. (2013). Molecular biomarkers of neurodegeneration. *Expert Rev Mol Diagn* **13**, 845–61.

Hollenbeck, P. J. and Saxton, W. M. (2005). The axonal transport of mitochondria. *Journal of Cell Science* **118**, 5411–9.

Honkura, N., Matsuzaki, M., Noguchi, J., Ellis-Davies, G. C. R. and Kasai, H. (2008). The subspine organization of actin fibers regulates the structure and plasticity of dendritic spines. *Neuron* **57**, 719–29.

Hoogenraad, C. C., Akhmanova, A., Howell, S. A., Dortland, B. R., De Zeeuw, C. I., Willemsen, R., Visser, P., Grosveld, F. and Galjart, N. (2001). Mammalian golgi-associated bicaudal-d2 functions in the dynein-dynactin pathway by interacting with these complexes. *EMBO Journal* **20**, 4041–4054.

Hoogenraad, C. C. and Bradke, F. (2009). Control of neuronal polarity and plasticity–a renaissance for microtubules? *Trends in Cell Biology* **19**, 669–76.

Hoogenraad, C. C., Koekkoek, B., Akhmanova, A., Krugers, H., Dortland, B., Miedema, M., Van Alphen, A., Kistler, W. M., Jaegle, M., Koutsourakis, M. et al. (2002). Targeted mutation of cyln2 in the williams syndrome critical region links clip-115 haploinsufficiency to neurodevelopmental abnormalities in mice. *Nature Genetics* **32**, 116–127.

Hoogenraad, C. C., Milstein, A. D., Ethell, I. M., Henkemeyer, M. and Sheng, M. (2005). Grip1 controls dendrite morphogenesis by regulating ephb receptor trafficking. *Nature Neuroscience* **8**, 906–15.

Hoogenraad, C. C., Wulf, P., Schiefermeier, N., Stepanova, T., Galjart, N., Small, J. V., Grosveld, F., De Zeeuw, C. and Akhmanova, A. (2003). Bicaudal d induces selective dynein-mediated microtubule minus end-directed transport. *EMBO Journal* **22**, 6004–6015.

Horresh, I., Bar, V., Kissil, J. L. and Peles, E. (2010). Organization of myelinated axons by caspr and caspr2 requires the cytoskeletal adapter protein 4.1b. *J Neurosci* **30**, 2480–9.

Hotulainen, P. and Hoogenraad, C. C. (2010). Actin in dendritic spines: connecting dynamics to function. *Journal of Cell Biology* **189**, 619–629.

Hotulainen, P., Llano, O., Smirnov, S., Tanhuanpää, K., Faix, J., Rivera, C. and Lappalainen, P. (2009). Defining mechanisms of actin polymerization and depolymerization during dendritic spine morphogenesis. *Journal of Cell Biology* **185**, 323–39.

Houdusse, A. and Carter, A. P. (2009). Dynein swings into action. *Cell* **136**, 395–6.

House, W. F. and Urban, J. (1973). Long term results of electrode implantation and electronic stimulation of the cochlea in man. *Ann Otol Rhinol Laryngol* **82**, 504–17.

Howard, J. and Hyman, A. A. (2009). Growth, fluctuation and switching at microtubule plus ends. *Nature Reviews. Molecular Cell Biology* **10**, 569–574.

Howarth, C., Gleeson, P. and Attwell, D. (2012). Updated energy budgets for neural computation in the neocortex and cerebellum. *J Cereb Blood Flow Metab* **32**, 1222–32.

Hu, D. J., Baffet, A. D., Nayak, T., Akhmanova, A., Doye, V. and Vallee, R. B. (2013). Dynein recruitment to nuclear pores activates apical nuclear migration and mitotic entry in brain progenitor cells. *Cell* **154**, 1300–1313.

Hu, Q. D., Ang, B. T., Karsak, M., Hu, W. P., Cui, X. Y., Duka, T., Takeda, Y., Chia, W., Sankar, N., Ng, Y. K. et al. (2003). F3/contactin acts as a functional ligand for notch during oligodendrocyte maturation. *Cell* **115**, 163–75.

Huang, B., Wang, W., Bates, M. and Zhuang, X. (2008). Three-dimensional super-resolution imaging by stochastic optical reconstruction microscopy. *Science* **319**, 810–3.

Huang, J. D., Brady, S. T., Richards, B. W., Stenolen, D., Resau, J. H., Copeland, N. G. and Jenkins, N. A. (1999). Direct interaction of microtubule- and actin-based transport motors. *Nature* **397**, 267–70.

Huizinga, R., Kreft, K. L., Onderwater, S., Boonstra, J. G., Brands, R., Hintzen, R. Q. and Laman, J. D. (2012). Endotoxin- and atp-neutralizing activity of alkaline phosphatase as a strategy to limit neuroinflammation. *Journal of Neuroinflammation* **9**.

Husmann, K., Faissner, A. and Schachner, M. (1992). Tenascin promotes cerebellar granule cell migration and neurite outgrowth by different domains in the fibronectin type iii repeats. *Journal of Cell Biology* **116**, 1475–1486.

Huynh, M. A., Ikeuchi, Y., Netherton, S., De la Torre-Ubieta, L., Kanadia, R., Stegmüller, J., Cepko, C., Bonni, S. and Bonni, A. (2011). An isoform-specific snon1-foxo1 repressor complex controls neuronal morphogenesis and positioning in the mammalian brain. *Neuron* **69**, 930–944.

Iijima, M., Somiya, M., Yoshimoto, N., Niimi, T. and Kuroda, S. (2012). Nano-visualization of oriented-immobilized iggs on immunosensors by high-speed atomic force microscopy. *Scientific Reports* **2**, 790.

Ikegami, K., Heier, R. L., Taruishi, M., Takagi, H., Mukai, M., Shimma, S., Taira, S., Hatanaka, K., Morone, N., Yao, I. et al. (2007). Loss of alpha-tubulin polyglutamylation in rosa22 mice is associated with abnormal targeting of kif1a and modulated synaptic function. *Proc Natl Acad Sci U S A* **104**, 3213–8.

Ikegami, K. and Setou, M. (2010). Unique post-translational modifications in specialized microtubule architecture. *Cell Structure and Function* **35**, 15–22.

International Multiple Sclerosis Genetics Consortium (IMSGC) (2010). Comprehensive follow-up of the first genome-wide association study of multiple sclerosis identifies kif21b and tmem39a as susceptibility loci. *Human Molecular Genetics* **19**, 953–62.

International Multiple Sclerosis Genetics Consortium (IMSGC) (2013). Network-based multiple sclerosis pathway analysis with gwas data from 15,000 cases and 30,000 controls. *American Journal of Human Genetics* **92**, 854–865.

Jaarsma, D. and Hoogenraad, C. C. (2015). Cytoplasmic dynein and its regulatory proteins in golgi pathology in nervous system disorders. *Front Neurosci* **9**, 397.

Jafari, N., Broer, L., van Duijn, C. M., Janssens, A. C. and Hintzen, R. Q. (2011). Perspectives on the use of multiple sclerosis risk genes for prediction. *PLoS One* **6**, e26493.

Janke, C. and Bulinski, J. C. (2011). Post-translational regulation of the microtubule cytoskeleton: mechanisms and functions. *Nat Rev Mol Cell Biol* **12**, 773–86.

Janke, C. and Kneussel, M. (2010). Tubulin post-translational modifications: encoding functions on the neuronal microtubule cytoskeleton. *Trends in Neurosciences* **1**, 1–11.

Januschke, J., Nicolas, E., Compagnon, J., Formstecher, E., Goud, B. and Guichet, A. (2007). Rab6 and the secretory pathway affect oocyte polarity in drosophila. *Development* **134**, 3419–3425.

Jaworski, J., Hoogenraad, C. C. and Akhmanova, A. (2008). Microtubule plus-end tracking proteins in differentiated mammalian cells. *International Journal of Biochemistry and Cell Biology* **40**, 619–637.

Jaworski, J., Kapitein, L. C., Gouveia, S. M., Dortland, B. R., Wulf, P. S., Grigoriev, I., Camera, P., Spangler, S. A., Di Stefano, P., Demmers, J. et al. (2009). Dynamic microtubules regulate dendritic spine morphology and synaptic plasticity. *Neuron* **61**, 85–100.

Jersild, C., Fog, T., Hansen, G. S., Thomsen, M., Svejgaard, A. and Dupont, B. (1973). Histocompatibility determinants in multiple sclerosis, with special reference to clinical course. *Lancet* **2**, 1221–5.

Jin, Y. and Garner, C. C. (2008). Molecular mechanisms of presynaptic differentiation. *Annual Review of Cell and Developmental Biology* **24**, 237–262.

Jones, B. J. and Roberts, D. J. (1968). The quantitative measurement of motor inco-ordination in naive mice using an acelerating rotarod. *Journal of Pharmacy and Pharmacology* **20**, 302–304.

Jones, M. V., Nguyen, T. T., Deboy, C. A., Griffin, J. W., Whartenby, K. A., Kerr, D. A. and Calabresi, P. A. (2008). Behavioral and pathological outcomes in mog 35-55 experimental autoimmune encephalomyelitis. *Journal of Neuroimmunology* **199**, 83–93.

Jones, P. L. and Jones, F. S. (2000). Tenascin-c in development and disease: gene regulation and cell function. *Matrix Biology* **19**, 581–596.

Jones, S. A., Shim, S. H., He, J. and Zhuang, X. (2011). Fast, three-dimensional super-resolution imaging of live cells. *Nature Methods* **8**, 499–508.

Joshi, D. C., Zhang, C. L., Lin, T. M., Gusain, A., Harris, M. G., Tree, E., Yin, Y., Wu, C., Sheng, Z. H., Dempsey, R. J. et al. (2015). Deletion of mitochondrial anchoring protects dysmyelinating shiverer: implications for progressive ms. *J Neurosci* **35**, 5293–306.

Juette, M. F., Gould, T. J., Lessard, M. D., Mlodzianoski, M. J., Nagpure, B. S., Bennett, B. T., Hess, S. T. and Bewersdorf, J. (2008). Three-dimensional sub-100 nm resolution fluorescence microscopy of thick samples. *Nat Methods* **5**, 527–9.

Jurgens, T., Jafari, M., Kreutzfeldt, M., Bahn, E., Brck, W., Kerschensteiner, M. and Merkler, D. (2016). Reconstruction of single cortical projection neurons reveals primary spine loss in multiple sclerosis. *Brain* **139**, 39–46.

Kaether, C., Skehel, P. and Dotti, C. G. (2000). Axonal membrane proteins are transported in distinct carriers: a two-color video microscopy study in cultured hippocampal neurons. *Molecular Biology of the Cell* **11**, 1213–1224.

Kalia, L. V., Kalia, S. K. and Salter, M. W. (2008). Nmda receptors in clinical neurology: excitatory times ahead. *Lancet Neurol* **7**, 742–55.

Källen, B. and Nilsson, O. (1986). Dissociation between histological and clinical signs of experimental auto-immune encephalomyelitis. *Acta Pathologica et Microbiologica Scandinavica. Section A, Pathology* **94**, 159–64.

Kang, J.-S., Tian, J.-H., Pan, P.-Y., Zald, P., Li, C., Deng, C. and Sheng, Z.-H. (2008). Docking of axonal mitochondria by syntaphilin controls their mobility and affects short-term facilitation. *Cell* **132**, 137–48.

Kapitein, L. C. and Hoogenraad, C. C. (2011). Which way to go? cytoskeletal organization and polarized transport in neurons. *Molecular and Cellular Neurosciences* **46**, 9–20.

Kapitein, L. C., Schlager, M. A., Kuijpers, M., Wulf, P. S., van Spronsen, M., MacKintosh, F. C. and Hoogenraad, C. C. (2010a). Mixed microtubules steer dynein-driven cargo transport into dendrites. *Current Biology* **20**, 290–9.

Kapitein, L. C., Yau, K. W. and Hoogenraad, C. C. (2010b). Microtubule dynamics in dendritic spines. *Methods Cell Biol* **97**, 111–32.

Karbowski, M. and Neutzner, A. (2012). Neurodegeneration as a consequence of failed mitochondrial maintenance. *Acta Neuropathol* **123**, 157–71.

Kardon, J. R. and Vale, R. D. (2009). Regulators of the cytoplasmic dynein motor. *Nature Reviews. Molecular Cell Biology* **10**, 854–65.

Kasai, H., Fukuda, M., Watanabe, S., Hayashi-Takagi, A. and Noguchi, J. (2010). Structural dynamics of dendritic spines in memory and cognition. *Trends in Neurosciences* **33**, 121–129.

Kasprowicz, A., Szuba, A., Volkmann, D., Baluska, F. and Wojtaszek, P. (2009). Nitric oxide modulates dynamic actin cytoskeleton and vesicle trafficking in a cell type-specific manner in root apices. *J Exp Bot* **60**, 1605–17.

Kassiotis, G., Pasparakis, M., Kollias, G. and Probert, L. (1999). Tnf accelerates the onset but does not alter the incidence and severity of myelin basic protein-induced experimental autoimmune encephalomyelitis. *European Journal of Immunology* **29**, 774–80.

Kaul, N., Soppina, V. and Verhey, K. J. (2014). Effects of -tubulin k40 acetylation and detyrosination on kinesin-1 motility in a purified system. *Biophys J* **106**, 2636–43.

Keays, D. A., Tian, G., Poirier, K., Huang, G. J., Siebold, C., Cleak, J., Oliver, P. L., Fray, M., Harvey, R. J., Molnár, Z. et al. (2007). Mutations in alpha-tubulin cause abnormal neuronal migration in mice and lissencephaly in humans. *Cell* **128**, 45–57.

Kevenaar, J. T. and Hoogenraad, C. C. (2015). The axonal cytoskeleton: from organization to function. *Front Mol Neurosci* **8**, 44.

Kijanka, M., Warnders, F. J., El Khattabi, M., Lub-de Hooge, M., van Dam, G. M., Ntziachristos, V., de Vries, L., Oliveira, S. and van Bergen En Henegouwen, P. M. (2013). Rapid optical imaging of human breast tumour xenografts using anti-her2 vhhs site-directly conjugated to irdye 800cw for image-guided surgery. *Eur J Nucl Med Mol Imaging* **40**, 1718–29.

Kijima, K., Numakura, C., Izumino, H., Umetsu, K., Nezu, A., Shiiki, T., Ogawa, M., Ishizaki, Y., Kitamura, T., Shozawa, Y. et al. (2005). Mitochondrial gtpase mitofusin 2 mutation in charcot-marie-tooth neuropathy type 2a. *Human Genetics* **116**, 23–27.

Kim, C., Choi, H., Jung, E. S., Lee, W., Oh, S., Jeon, N. L. and Mook-Jung, I. (2012). Hdac6 inhibitor blocks amyloid beta-induced impairment of mitochondrial transport in hippocampal neurons. *PLoS One* **7**, e42983.

Kim, E. and Sheng, M. (2004). Pdz domain proteins of synapses. *Nature Reviews. Neuroscience* **5**, 771–781.

Kim, J. H., Budde, M. D., Liang, H. F., Klein, R. S., Russell, J. H., Cross, A. H. and Song, S. K. (2006). Detecting axon damage in spinal cord from a mouse model of multiple sclerosis. *Neurobiol Dis* **21**, 626–32.

Kiryu-Seo, S., Ohno, N., Kidd, G. J., Komuro, H. and Trapp, B. D. (2010). Demyelination increases axonal stationary mitochondrial size and the speed of axonal mitochondrial transport. *Journal of Neuroscience* **30**, 6658–66.

Klar, T. A., Jakobs, S., Dyba, M., Egner, A. and Hell, S. W. (2000). Fluorescence microscopy with diffraction resolution barrier broken by stimulated emission. *Proceedings of the National Academy of Sciences of the United States of America* **97**, 8206–10.

Klüver, H. and Barrera, E. (1953). A method for the combined staining of cells and fibers in the nervous system. *J Neuropathol Exp Neurol* **12**, 400403.

Komuro, H. and Rakic, P. (1995). Dynamics of granule cell migration: a confocal microscopic study in acute cerebellar slice preparations. *Journal of Neuroscience* **15**, 1110–1120.

Konishi, Y. and Setou, M. (2009). Tubulin tyrosination navigates the kinesin-1 motor domain to axons. *Nature Neuroscience* **12**, 559–67.

Koritschoner, R. and Schweinburg, F. (1925). Induktion von paralyse und rckenmarksentzndung durch immunisierung von kaninchen mit menschlichem rckenmarksgewebe. *Zeitschrift fr Immunittsforschung und Experimentelle Therapie* **42**, 217–83.

Kornek, B., Storch, M. K., Bauer, J., Djamshidian, A., Weissert, R., Wallstroem, E., Stefferl, A., Zimprich, F., Olsson, T., Linington, C. et al. (2001). Distribution of a calcium channel subunit in dystrophic axons in multiple sclerosis and experimental autoimmune encephalomyelitis. *Brain* **124**, 1114–24.

Korobova, F. and Svitkina, T. (2010). Molecular architecture of synaptic actin cytoskeleton in hippocampal neurons reveals a mechanism of dendritic spine morphogenesis. *Molecular Biology of the Cell* **21**, 165–176.

Kostic, M., Zivkovic, N. and Stojanovic, I. (2013). Multiple sclerosis and glutamate excitotoxicity. *Rev Neurosci* **24**, 71–88.

Koutsis, G., Karadima, G., Floroskufi, P., Sfagos, C., Vassilopoulos, D. and Panas, M. (2011). The rs10492972 kif1b polymorphism and disease progression in greek patients with multiple sclerosis. *Journal of Neurology* **258**, 1726–1728.

Kramann, N., Neid, K., Menken, L., Schlumbohm, C., Stadelmann, C., Fuchs, E., Brck, W. and Wegner, C. (2014). Increased meningeal t and plasma cell infiltration is associated with early subpial cortical demyelination in common marmosets with experimental autoimmune encephalomyelitis. *Brain Pathology* .

Kreft, K. L., van Meurs, M., Wierenga-Wolf, A. F., Melief, M. J., van Strien, M. E., Hol, E. M., Oostra, B. A., Laman, J. D. and Hintzen, R. Q. (2014). Abundant kif21b is associated with accelerated progression in neurodegenerative diseases. *Acta Neuropathol Commun* **2**, 144.

Kreutzer, M., Seehusen, F., Kreutzer, R., Pringproa, K., Kummerfeld, M., Claus, P., Deschl, U., Kalkul, A., Beineke, A., Baumgrtner, W. et al. (2012). Axonopathy is associated with complex axonal transport defects in a model of multiple sclerosis. *Brain Pathol* **22**, 454–71.

Kriegstein, A. and Alvarez-Buylla, A. (2009). The glial nature of embryonic and adult neural stem cells. *Annual Review of Neuroscience* **32**, 149–184.

Krucker, T., Siggins, G. R. and Halpain, S. (2000). Dynamic actin filaments are required for stable long-term potentiation (ltp) in area ca1 of the hippocampus. *Proceedings of the National Academy of Sciences of the United States of America* **97**, 6856–61.

Kruse, J., Keilhauer, G., Faissner, A., Timpl, R. and Schachner, M. (1985). The j1 glycoprotein–a novel nervous system cell adhesion molecule of the l2/hnk-1 family. *Nature* **316**, 146–148.

Kudryavtseva, E. A., Rozhdestvenskii, A. S., Kakulya, A. V., Khanokh, E. V., Delov, R. A., Malkova, N. A., Korobko, D. S., Platonov, F. A., Aref, E. G., Zagorskaya, N. N. et al. (2011). Polymorphic locus rs10492972 of the kif1b gene association with multiple sclerosis in russia: case control study. *Molecular Genetics and Metabolism* **104**, 390–394.

Kueh, H. Y. and Mitchison, T. J. (2009). Structural plasticity in actin and tubulin polymer dynamics. *Science* **325**, 960–963.

Kuhle, J., Leppert, D., Petzold, A., Regeniter, A., Schindler, C., Mehling, M., Anthony, D. C., Kappos, L. and Lindberg, R. L. (2011). Neurofilament heavy chain in csf correlates with relapses and disability in multiple sclerosis. *Neurology* **76**, 1206–13.

Kuhlmann, T., Lingfeld, G., Bitsch, A., Schuchardt, J. and Brück, W. (2002). Acute axonal damage in multiple sclerosis is most extensive in early disease stages and decreases over time. *Brain* **125**, 2202–12.

Kühn, T., Ihalainen, T. O., Hyväluoma, J., Dross, N., Willman, S. F., Langowski, J., Vihinen-Ranta, M. and Timonen, J. (2011). Protein diffusion in mammalian cell cytoplasm. *PLoS One* **6**, e22962.

Kurtzke, J. F. (1983). Rating neurologic impairment in multiple sclerosis: an expanded disability status scale (edss). *Neurology* **33**, 1444–52.

L, C., A, B. E., A, T., C, B. M., F, L. M., H, P. V. and P, C. M. (1999). The major brain isoform of kif1b lacks the putative mitochondria-binding domain. *Mammalian Genome* **10**, 617–22.

Labonte, D., Thies, E., Pechmann, Y., Groffen, A. J., Verhage, M., Smit, A. B., van Kesteren, R. E. and Kneussel, M. (2013). Trim3 regulates the motility of the kinesin motor protein kif21b. *PLoS One* **8**, e75603.

LaMonte, B. H., Wallace, K. E., Holloway, B. A., Shelly, S. S., no, J. A., Tokito, M., Winkle, T. V., Howland, D. S. and Holzbaur, E. L. F. (2002). Disruption of dynein/dynactin inhibits axonal transport in motor neurons causing late-onset progressive degeneration. *Neuron* **34**, 715–27.

Landis, D. M., Hall, A. K., Weinstein, L. A. and Reese, T. S. (1988). The organization of cytoplasm at the presynaptic active zone of a central nervous system synapse. *Neuron* **1**, 201–9.

Landis, D. M. and Reese, T. S. (1983). Cytoplasmic organization in cerebellar dendritic spines. *Journal of Cell Biology* **97**, 1169–78.

Lappe-Siefke, C., Goebbels, S., Gravel, M., Nicksch, E., Lee, J., Braun, P. E., Griffiths, I. R. and Nave, K. A. (2003). Disruption of cnp1 uncouples oligodendroglial functions in axonal support and myelination. *Nat Genet* **33**, 366–74.

Lasiecka, Z. M. and Winckler, B. (2011). Mechanisms of polarized membrane trafficking in neurons – focusing in on endosomes. *Mol Cell Neurosci* **48**, 278–87.

Lassmann, H. (2005). Heterogeneity of multiple sclerosis: implications for therapy targeting regeneration. *Ernst Schering Research Foundation Workshop* **53**, 11–22.

Lau, C. G. and Zukin, R. S. (2007). Nmda receptor trafficking in synaptic plasticity and neuropsychiatric disorders. *Nature Reviews. Neuroscience* **8**, 413–26.

LaVail, J. H. and Wolf, M. K. (1973). Postnatal development of the mouse dentate gyrus in organotypic cultures of the hippocampal formation. *Am J Anat* **137**, 47–65.

Lawrence, C. J., Dawe, R. K., Christie, K. R., Cleveland, D. W., Dawson, S. C., Endow, S. A., Goldstein, L. S. B., Goodson, H. V., Hirokawa, N., Howard, J. et al. (2004). A standardized kinesin nomenclature. *Journal of Cell Biology* **167**, 19–22.

Lee, J. J. and Swain, S. M. (2006). Peripheral neuropathy induced by microtubule-stabilizing agents. *J Clin Oncol* **24**, 1633–42.

Lee, Y., Morrison, B. M., Li, Y., Lengacher, S., Farah, M. H., Hoffman, P. N., Liu, Y., Tsingalia, A., Jin, L., Zhang, P. W. et al. (2012). Oligodendroglia metabolically support axons and contribute to neurodegeneration. *Nature* **487**, 443–8.

Lein, E. S., Hawrylycz, M. J., Ao, N., Ayres, M., Bensinger, A., Bernard, A., Boe, A. F., Boguski, M. S., Brockway, K. S., Byrnes, E. J. et al. (2007). Genome-wide atlas of gene expression in the adult mouse brain. *Nature* **445**, 168–176.

Lemieux, M., Labrecque, S., Tardif, C., Labrie-Dion, ., Lebel, . and De Koninck, P. (2012). Translocation of camkii to dendritic microtubules supports the plasticity of local synapses. *J Cell Biol* **198**, 1055–73.

Leterrier, C., Lainé, J., Darmon, M., Boudin, H., Rossier, J. and Lenkei, Z. (2006). Constitutive activation drives compartment-selective endocytosis and axonal targeting of type 1 cannabinoid receptors. *Journal of Neuroscience* **26**, 3141–3153.

Leterrier, C., Potier, J., Caillol, G., Debarnot, C., Rueda Boroni, F. and Dargent, B. (2015). Nanoscale architecture of the axon initial segment reveals an organized and robust scaffold. *Cell Rep* **13**, 2781–93.

Lewis, T. L., Mao, T., Svoboda, K. and Arnold, D. B. (2009). Myosin-dependent targeting of transmembrane proteins to neuronal dendrites. *Nature Neuroscience* **12**, 568–76.

Li, H., DeRosier, D. J., Nicholson, W. V., Nogales, E. and Downing, K. H. (2002). Microtubule structure at 8 a resolution. *Structure* **10**, 1317–28.

Li, J. Y. and Conforti, L. (2013). Axonopathy in huntington's disease. *Exp Neurol* **246**, 62–71.

Liao, G. and Gundersen, G. G. (1998). Kinesin is a candidate for cross-bridging microtubules and intermediate filaments. selective binding of kinesin to detyrosinated tubulin and vimentin. *Journal of Biological Chemistry* **273**, 9797–803.

Lidster, K. and Baker, D. (2012). Optical coherence tomography detection of neurodegeneration in multiple sclerosis. *CNS Neurol Disord Drug Targets* **11**, 518–27.

Lill, C. M., Luessi, F., Alcina, A., Sokolova, E. A., Ugidos, N., de la Hera, B., Guillot-Nol, L., Malhotra, S., Reinthaler, E., Schjeide, B. M. et al. (2015). Genome-wide significant association with seven novel multiple sclerosis risk loci. *J Med Genet* **52**, 848–55.

Lin, M. T. and Beal, M. F. (2006). Mitochondrial dysfunction and oxidative stress in neurodegenerative diseases. *Nature* **443**, 787–95.

Lin, T. H., Kim, J. H., Perez-Torres, C., Chiang, C. W., Trinkaus, K., Cross, A. H. and Song, S. K. (2014). Axonal transport rate decreased at the onset of optic neuritis in eae mice. *Neuroimage* **100**, 244–53.

Lin, Y., Chen, L., Lin, C., Luo, Y., Tsai, R. Y. and Wang, F. (2009). Neuron-derived fgf9 is essential for scaffold formation of bergmann radial fibers and migration of granule neurons in the cerebellum. *Developments in Biologicals* **329**, 44–54.

Lincoln, M. R., Montpetit, A., Cader, M. Z., Saarela, J., Dyment, D. A., Tiislar, M., Ferretti, V., Tienari, P. J., Sadovnick, A. D., Peltonen, L. et al. (2005). A predominant role for the hla class ii region in the association of the mhc region with multiple sclerosis. *Nature Genetics* **37**, 1108–12.

Lipka, E. and Mller, S. (2014). Nitrosative stress triggers microtubule reorganization in arabidopsis thaliana. *J Exp Bot* **65**, 4177–89.

Lippincott-Schwartz, J. and Manley, S. (2009). Putting super-resolution fluorescence microscopy to work. *Nature Methods* **6**, 21–3.

Lisman, J. E., Raghavachari, S. and Tsien, R. W. (2007). The sequence of events that underlie quantal transmission at central glutamatergic synapses. *Nature Reviews. Neuroscience* **8**, 597–609.

Liu, Y. T., Laurá, M., Hersheson, J., Horga, A., Jaunmuktane, Z., Brandner, S., Pittman, A., Hughes, D., Polke, J. M., Sweeney, M. G. et al. (2014). Extended phenotypic spectrum of kif5a mutations: From spastic paraplegia to axonal neuropathy. *Neurology* **83**, 612–9.

Lu, F., Selak, M., O'Connor, J., Croul, S., Lorenzana, C., Butunoi, C. and Kalman, B. (2000). Oxidative damage to mitochondrial dna and activity of mitochondrial enzymes in chronic active lesions of multiple sclerosis. *J Neurol Sci* **177**, 95–103.

Lukinaviius, G., Reymond, L., D'Este, E., Masharina, A., Göttfert, F., Ta, H., Güther, A., Fournier, M., Rizzo, S., Waldmann, H. et al. (2014). Fluorogenic probes for live-cell imaging of the cytoskeleton. *Nat Methods* **11**, 731–3.

Lyons, D. A., Naylor, S. G., Scholze, A. and Talbot, W. S. (2009). Kif1b is essential for mrna localization in oligodendrocytes and development of myelinated axons. *Nature Genetics* **41**, 854–8.

Ma, S., Kwon, H. J. and Huang, Z. (2012). Ric-8a, a guanine nucleotide exchange factor for heterotrimeric g proteins, regulates bergmann glia-basement membrane adhesion during cerebellar foliation. *Journal of Neuroscience* **32**, 14979–14993.

Maas, C., Belgardt, D., Lee, H. K., Heisler, F. F., Lappe-Siefke, C., Magiera, M. M., Van Dijk, J., Hausrat, T. J., Janke, C. and Kneussel, M. (2009). Synaptic activation modifies microtubules underlying transport of postsynaptic cargo. *Proceedings of the National Academy of Sciences of the United States of America* **106**, 8731–6.

Maas, C., Tagnaouti, N., Loebrich, S., Behrend, B., Lappe-Siefke, C. and Kneussel, M. (2006). Neuronal cotransport of glycine receptor and the scaffold protein gephyrin. *Journal of Cell Biology* **172**, 441–51.

Macaskill, A. F., Rinholm, J. E., Twelvetrees, A. E., Arancibia-Carcamo, I. L., Muir, J., Fransson, A., Aspenstrom, P., Attwell, D. and Kittler, J. T. (2009). Miro1 is a calcium sensor for glutamate receptor-dependent localization of mitochondria at synapses. *Neuron* **61**, 541–55.

Machold, R. and Fishell, G. (2005). Math1 is expressed in temporally discrete pools of cerebellar rhombic-lip neural progenitors. *Neuron* **48**, 17–24.

Maday, S., Twelvetrees, A. E., Moughamian, A. J. and Holzbaur, E. L. (2014). Axonal transport: cargo-specific mechanisms of motility and regulation. *Neuron* **84**, 292–309.

Mahad, D., Lassmann, H. and Turnbull, D. (2008). Review: Mitochondria and disease progression in multiple sclerosis. *Neuropathol Appl Neurobiol* **34**, 577–89.

Mahad, D. H., Trapp, B. D. and Lassmann, H. (2015). Pathological mechanisms in progressive multiple sclerosis. *Lancet Neurol* **14**, 183–93.

Mahad, D. J., Ziabreva, I., Campbell, G., Lax, N., White, K., Hanson, P. S., Lassmann, H. and Turnbull, D. M. (2009). Mitochondrial changes within axons in multiple sclerosis. *Brain* **132**, 1161–1174.

Mandelkow, E. and Mandelkow, E.-M. (2002). Kinesin motors and disease. *Trends in Cell Biology* **12**, 585–91.

Manley, S., Gillette, J. M. and Lippincott-Schwartz, J. (2010). Single-particle tracking photoactivated localization microscopy for mapping single-molecule dynamics. *Methods in Enzymology* **475**, 109–20.

Margeta, M. A., Shen, K. and Grill, B. (2008). Building a synapse: lessons on synaptic specificity and presynaptic assembly from the nematode c. elegans. *Current Opinion in Neurobiology* **18**, 69–76.

Martinelli-Boneschi, F., Esposito, F., Scalabrini, D., Fenoglio, C., Rodegher, M. E., Brambilla, P., Colombo, B., Ghezzi, A., Capra, R., Collimedaglia, L. et al. (2010). Lack of replication of kif1b gene in an italian primary progressive multiple sclerosis cohort. *European Journal of Neurology* **17**, 740–745.

Martinez-Carrera, L. A. and Wirth, B. (2015). Dominant spinal muscular atrophy is caused by mutations in bicd2, an important golgin protein. *Front Neurosci* **9**, 401.

Masafumi, M., Ruri, Y., Keiji, M. and Hiroshi, K. (2009). Altered motor activity of alternative splice variants of the mammalian kinesin-3 protein kif1b. *Traffic* **10**, 1647–54.

Massella, A., D'Intino, G., Fernndez, M., Sivilia, S., Lorenzini, L., Giatti, S., Melcangi, R. C., Calz, L. and Giardino, L. (2012). Gender effect on neurodegeneration and myelin markers in an animal model for multiple sclerosis. *BMC Neuroscience* **13**, 12.

Matanis, T., Akhmanova, A., Wulf, P., Del Nery, E., Weide, T., Stepanova, T., Galjart, N., Grosveld, F., Goud, B., De Zeeuw, C. I. et al. (2002). Bicaudal-d regulates copi-independent golgi-er transport by recruiting the dynein-dynactin motor complex. *Nature Cell Biology* **4**, 986–92.

Matsuyama, S. S. and Jarvik, L. F. (1989). Hypothesis: microtubules, a key to alzheimer disease. *Proc Natl Acad Sci U S A* **86**, 8152–6.

Mattson, M. P., Engle, M. G. and Rychlik, B. (1991). Effects of elevated intracellular calcium levels on the cytoskeleton and tau in cultured human cortical neurons. *Mol Chem Neuropathol* **15**, 117–42.

McCutchen, C. W. (1967). Superresolution in microscopy and the abbe resolution limit. *Journal of the Optical Society of America* **57**, 1190–2.

McGavern, D. B., Murray, P. D., Rivera-Quiñones, C., Schmelzer, J. D., Low, P. A. and Rodriguez, M. (2000). Axonal loss results in spinal cord atrophy, electrophysiological abnormalities and neurological deficits following demyelination in a chronic inflammatory model of multiple sclerosis. *Brain* **123 Pt 3**, 519–531.

McKenney, R. J., Vershinin, M., Kunwar, A., Vallee, R. B. and Gross, S. P. (2010). Lis1 and nude induce a persistent dynein force-producing state. *Cell* **141**, 304–14.

Merriam, E. B., Millette, M., Lumbard, D. C., Saengsawang, W., Fothergill, T., Hu, X., Ferhat, L. and Dent, E. W. (2013). Synaptic regulation of microtubule dynamics in dendritic spines by calcium, f-actin, and drebrin. *J Neurosci* **33**, 16471–82.

Michel, C. H., Kumar, S., Pinotsi, D., Tunnacliffe, A., St George-Hyslop, P., Mandelkow, E., Mandelkow, E. M., Kaminski, C. F. and Kaminski Schierle, G. S. (2014). Extracellular monomeric tau protein is sufficient to initiate the spread of tau protein pathology. *J Biol Chem* **289**, 956–67.

Micheva, K. D. and Bruchez, M. P. (2012). The gain in brain: novel imaging techniques and multiplexed proteomic imaging of brain tissue ultrastructure. *Curr Opin Neurobiol* **22**, 94–100.

Mikhaylova, M., Cloin, B. M., Finan, K., van den Berg, R., Teeuw, J., Kijanka, M. M., Sokolowski, M., Katrukha, E. A., Maidorn, M., Opazo, F. et al. (2015). Resolving bundled microtubules using anti-tubulin nanobodies. *Nat Commun* **6**, 7933.

Millecamps, J.-P., S Julien (2013). Axonal transport deficits and neurodegenerative diseases. *Nature Reviews. Neuroscience* **14**, 161–76.

Miller, K. E., DeProto, J., Kaufmann, N., Patel, B. N., Duckworth, A. and Van Vactor, D. (2005). Direct observation demonstrates that liprin-alpha is required for trafficking of synaptic vesicles. *Current Biology* **15**, 684–9.

Mitchison, T. and Kirschner, M. (1984). Dynamic instability of microtubule growth. *Nature* **312**, 237–242.

Mix, E., Meyer-Rienecker, H., Hartung, H. P. and Zettl, U. K. (2010). Animal models of multiple sclerosis–potentials and limitations. *Prog Neurobiol* **92**, 386–404.

Mlodzianoski, M. J., Schreiner, J. M., Callahan, S. P., Smolkov, K., Dlaskov, A., Santorov, J., Jezek, P. and Bewersdorf, J. (2011). Sample drift correction in 3d fluorescence photoactivation localization microscopy. *Optics Express* **19**, 15009–19.

Mohan, R., Katrukha, E. A., Doodhi, H., Smal, I., Meijering, E., Kapitein, L. C., Steinmetz, M. O. and Akhmanova, A. (2013). End-binding proteins sensitize microtubules to the action of microtubule-targeting agents. *Proc Natl Acad Sci U S A* **110**, 8900–5.

Mok, H., Shin, H., Kim, S., Lee, J. R., Yoon, J. and Kim, E. (2002). Association of the kinesin superfamily motor protein kif1balpha with postsynaptic density-95 (psd-95), synapse-associated protein-97, and synaptic scaffolding molecule psd-95/discs large/zona occludens-1 proteins. *Journal of Neuroscience* **22**, 5253–5258.

Monsma, P. C., Li, Y., Fenn, J. D., Jung, P. and Brown, A. (2014). Local regulation of neurofilament transport by myelinating cells. *J Neurosci* **34**, 2979–88.

Moon, H. M. and Wynshaw-Boris, A. (2013). Cytoskeleton in action: lissencephaly, a neuronal migration disorder. *Wiley Interdiscip Rev Dev Biol* **2**, 229–45.

Moon, H. M., Youn, Y. H., Pemble, H., Yingling, J., Wittmann, T. and Wynshaw-Boris, A. (2014). Lis1 controls mitosis and mitotic spindle organization via the lis1-ndel1-dynein complex. *Hum Mol Genet* **23**, 449–66.

Moore, S. M., Khalaj, A. J., Kumar, S., Winchester, Z., Yoon, J., Yoo, T., Martinez-Torres, L., Yasui, N., Katzenellenbogen, J. A. and Tiwari-Woodruff, S. K. (2014). Multiple functional therapeutic effects of the estrogen receptor agonist indazole-cl in a mouse model of multiple sclerosis. *Proc Natl Acad Sci U S A* **111**, 18061–6.

Morfini, G., Burns, M., Binder, L. I., Kanaan, N. M., LaPointe, N., Bosco, D. A., Brown, R. H., Brown, H., Tiwari, A., Hayward, L. et al. (2009). Axonal transport defects in neurodegenerative diseases. *Journal of Neuroscience* **29**, 12776–86.

Morrison, E. E., Moncur, P. M. and Askham, J. M. (2002). Eb1 identifies sites of microtubule polymerisation during neurite development. *Brain Research. Molecular Brain Research* **98**, 145–52.

Moutsianas, L., Jostins, L., Beecham, A. H., Dilthey, A. T., Xifara, D. K., Ban, M., Shah, T. S., Patsopoulos, N. A., Alfredsson, L., Anderson, C. A. et al. (2015). Class ii hla interactions modulate genetic risk for multiple sclerosis. *Nat Genet* **47**, 1107–13.

Mukamel, E. A. and Schnitzer, M. J. (2012). Unified resolution bounds for conventional and stochastic localization fluorescence microscopy. *Physical Review Letters* **109**, 168102.

Munirajan, A. K., Ando, K., Mukai, A., Takahashi, M., Suenaga, Y., Ohira, M., Koda, T., Hirota, T., Ozaki, T. and Nakagawara, A. (2008). Kif1bbeta functions as a haploinsufficient tumor suppressor gene mapped to chromosome 1p36.2 by inducing apoptotic cell death. *Journal of Biological Chemistry* **283**, 24426–24434.

Muthusamy, N., Chen, Y. J., Yin, D. M., Mei, L. and Bergson, C. (2015). Complementary roles of the neuron-enriched endosomal proteins neep21 and calcyon in neuronal vesicle trafficking. *J Neurochem* **132**, 20–31.

Nacka-Aleksić, M., Djikić, J., Pilipović, I., Stojić-Vukanić, Z., Kosec, D., Bufan, B., Arsenović-Ranin, N., Dimitrijević, M. and Leposavić, G. (2015). Male rats develop more severe experimental autoimmune encephalomyelitis than female rats: Sexual dimorphism and diergism at the spinal cord level. *Brain Behav Immun* .

Nagai, M., Ichimiya, S., Ozaki, T., Seki, N., Mihara, M., Furuta, S., Ohira, M., Tomioka, N., Nomura, N., Sakiyama, S. et al. (2000). Identification of the full-length kiaa0591 gene encoding a novel kinesin-related protein which is mapped to the neuroblastoma suppressor gene locus at 1p36.2. *International Journal of Oncology* **16**, 907–916.

Nakada, C., Ritchie, K., Oba, Y., Nakamura, M., Hotta, Y., Iino, R., Kasai, R. S., Yamaguchi, K., Fujiwara, T. and Kusumi, A. (2003). Accumulation of anchored proteins forms membrane diffusion barriers during neuronal polarization. *Nature Cell Biology* **5**, 626–32.

Nakahara, J., Kanekura, K., Nawa, M., Aiso, S. and Suzuki, N. (2009). Abnormal expression of tip30 and arrested nucleocytoplasmic transport within oligodendrocyte precursor cells in multiple sclerosis. *J Clin Invest* **119**, 169–81.

Nangaku, M., Sato-Yoshitake, R., Okada, Y., Noda, Y., Takemura, R., Yamazaki, H. and Hirokawa, N. (1994). Kif1b, a novel microtubule plus end-directed monomeric motor protein for transport of mitochondria. *Cell* **79**, 1209–20.

Napoli, A. and Obeid:, I. (2016). Comparative analysis of human and rodent brain primary neuronal culture spontaneous activity using micro-electrode array technology. *J Cell Biochem* **117**, 559–65.

Nash, J. E., Appleby, V. J., Corrêa, S. A. L., Wu, H., Fitzjohn, S. M., Garner, C. C., Collingridge, G. L. and Molnár, E. (2010). Disruption of the interaction between myosin vi and sap97 is associated with a reduction in the number of ampars at hippocampal synapses. *Journal of Neurochemistry* **112**, 677–90.

Neefjes, J. and Van der Kant, R. (2014). Stuck in traffic: an emerging theme in diseases of the nervous system. *Trends in Neurosciences* **37**, 66–76.

Neveling, K., Martinez-Carrera, L. A., Hölker, I., Heister, A., Verrips, A., Hosseini-Barkooie, S. M., Gilissen, C., Vermeer, S., Pennings, M., Meijer, R. et al. (2013). Mutations in bicd2, which encodes a golgin and important motor adaptor, cause congenital autosomal-dominant spinal muscular atrophy. *American Journal of Human Genetics* **92**, 946–954.

Nguyen, T. T., Oh, S. S., Weaver, D., Lewandowska, A., Maxfield, D., Schuler, M. H., Smith, N. K., Macfarlane, J., Saunders, G., Palmer, C. A. et al. (2014). Loss of miro1-directed mitochondrial movement results in a novel murine model for neuron disease. *Proc Natl Acad Sci U S A* **111**, E3631–40.

Nieuwenhuizen, R. P., Lidke, K. A., Bates, M., Puig, D. L., Grnwald, D., Stallinga, S. and Rieger, B. (2013). Measuring image resolution in optical nanoscopy. *Nature Methods* **10**, 557–62.

Niwa, S., Tanaka, Y. and Hirokawa, N. (2008). Kif1bbeta- and kif1a-mediated axonal transport of presynaptic regulator rab3 occurs in a gtp-dependent manner through denn/madd. *Nature Cell Biology* **10**, 1269–79.

Nizak, C., Martin-Lluesma, S., Moutel, S., Roux, A., Kreis, T. E., Goud, B. and Perez, F. (2003). Recombinant antibodies against subcellular fractions used to track endogenous golgi protein dynamics in vivo. *Traffic* **4**, 739–53.

Nolte, C., Matyash, M., Pivneva, T., Schipke, C. G., Ohlemeyer, C., Hanisch, U. K., Kirchhoff, F. and Kettenmann, H. (2001). Gfap promoter-controlled egfp-expressing transgenic mice: a tool to visualize astrocytes and astrogliosis in living brain tissue. *Glia* **33**, 72–86.

Norihiro, N., Yoshihide, M., Masafumi, M., Shingo, T., Hiroki, I. and Hiroshi, K. (2002). Kif1bbeta2, capable of interacting with chp, is localized to synaptic vesicles. *Journal of Cell Science* **132**, 483–91.

Nyquist, H. (1928). Certain topics in telegraph transmission theory. *Transactions of the American Institute of Electrical Engineers* **2**, 617–644.

Oates, E. C., Rossor, A. M., Hafezparast, M., Gonzalez, M., Speziani, F., MacArthur, D. G., Lek, M., Cottenie, E., Scoto, M., Foley, A. R. et al. (2013). Mutations in bicd2 cause dominant congenital spinal muscular atrophy and hereditary spastic paraplegia. *American Journal of Human Genetics* **92**, 965–973.

Ober, R. J., Ram, S. and Ward, E. S. (2004). Localization accuracy in single-molecule microscopy. *Biophysical Journal* **86**, 1185–200.

Ohira, M., Kageyama, H., Mihara, M., Furuta, S., Machida, T., Shishikura, T., Takayasu, H., Islam, A., Nakamura, Y., Takahashi, M. et al. (2000). Identification and characterization of a 500-kb homozygously deleted region at 1p36.2-p36.3 in a neuroblastoma cell line. *Oncogene* **19**, 4302–4307.

Ohno, N., Chiang, H., Mahad, D. J., Kidd, G. J., Liu, L., Ransohoff, R. M., Sheng, Z. H., Komuro, H. and Trapp, B. D. (2014). Mitochondrial immobilization mediated by syntaphilin facilitates survival of demyelinated axons. *Proc Natl Acad Sci U S A* **111**, 9953–8.

Ohno, N., Kidd, G. J., Mahad, D., Kiryu-Seo, S., Avishai, A., Komuro, H. and Trapp, B. D. (2011). Myelination and axonal electrical activity modulate the distribution and motility of mitochondria at cns nodes of ranvier. *J Neurosci* **31**, 7249–58.

Ohshima, T., Gilmore, E. C., Longenecker, G., Jacobowitz, D. M., Brady, R. O., Herrup, K. and Kulkarni, A. B. (1999). Migration defects of cdk5(-/-) neurons in the developing cerebellum is cell autonomous. *Journal of Neuroscience* **19**, 6017–6026.

Okamoto, K.-I., Nagai, T., Miyawaki, A. and Hayashi, Y. (2004). Rapid and persistent modulation of actin dynamics regulates postsynaptic reorganization underlying bidirectional plasticity. *Nature Neuroscience* **7**, 1104–12.

Olmos, G. and Llad, J. (2014). Tumor necrosis factor alpha: a link between neuroinflammation and excitotoxicity. *Mediators Inflamm* **2014**, 861231.

Ori-McKenney, K. M., Xu, J., Gross, S. P. and Vallee, R. B. (2010). A cytoplasmic dynein tail mutation impairs motor processivity. *Nature Cell Biology* **12**, 1228–34.

Osterweil, E., Wells, D. G. and Mooseker, M. S. (2005). A role for myosin vi in postsynaptic structure and glutamate receptor endocytosis. *Journal of Cell Biology* **168**, 329–38.

Ou, C.-Y., Poon, V. Y., Maeder, C. I., Watanabe, S., Lehrman, E. K., Fu, A. K. Y., Park, M., Fu, W.-Y., Jorgensen, E. M., Ip, N. Y. et al. (2010). Two cyclin-dependent kinase pathways are essential for polarized trafficking of presynaptic components. *Cell* **141**, 846–58.

Pachner, A. R. (2011). Experimental models of multiple sclerosis. *Current Opinion in Neurology* **24**, 291–9.

Pandey, K. and Sharma, S. K. (2011). Activity-dependent acetylation of alpha tubulin in the hippocampus. *J Mol Neurosci* **45**, 1–4.

Pathak, D., Sepp, K. J. and Hollenbeck, P. J. (2010). Evidence that myosin activity opposes microtubule-based axonal transport of mitochondria. *Journal of Neuroscience* **30**, 8984–92.

Patterson, G., Davidson, M., Manley, S. and Lippincott-Schwartz, J. (2010). Superresolution imaging using single-molecule localization. *Annual Review of Physical Chemistry* **61**, 345–67.

Paz Soldán, M. M., Raman, M. R., Gamez, J. D., Lohrey, A. K., Chen, Y., Pirko, I. and Johnson, A. J. (2015). Correlation of brain atrophy, disability, and spinal cord atrophy in a murine model of multiple sclerosis. *J Neuroimaging* .

Peeters, K., Litvinenko, I., Asselbergh, B., Almeida-Souza, L., Chamova, T., Geuens, T., Ydens, E., Zimoń, M., Irobi, J., De Vriendt, E. et al. (2013). Molecular defects in the motor adaptor bicd2 cause proximal spinal muscular atrophy with autosomal-dominant inheritance. *American Journal of Human Genetics* **92**, 955–964.

Pennuto, M., Bonanomi, D., Benfenati, F. and Valtorta, F. (2003). Synaptophysin i controls the targeting of vamp2/synaptobrevin ii to synaptic vesicles. *Molecular Biology of the Cell* **14**, 4909–4919.

Petrache, I., Birukova, A., Ramirez, S. I., Garcia, J. G. and Verin, A. D. (2003). The role of the microtubules in tumor necrosis factor-alpha-induced endothelial cell permeability. *Am J Respir Cell Mol Biol* **28**, 574–81.

Pfeffer, S. R. (2013). A prize for membrane magic. *Cell* **155**, 1203–6.

Pierre-Antoine, G. (2011). When is the absence of evidence, evidence of absence? use of equivalence-based analyses in genetic epidemiology and a conclusion for the kif1b rs10492972*c allelic association in multiple sclerosis. *Genetic Epidemiology* **35**, 568–71.

Pitt, D., Werner, P. and Raine, C. S. (2000). Glutamate excitotoxicity in a model of multiple sclerosis. *Nat Med* **6**, 67–70.

Podbielska, M., Banik, N. L., Kurowska, E. and Hogan, E. L. (2013). Myelin recovery in multiple sclerosis: the challenge of remyelination. *Brain Sci* **3**, 1282–324.

Poirier, K., Lebrun, N., Broix, L., Tian, G., Saillour, Y., Boscheron, C., Parrini, E., Valence, S., Pierre, B. S., Oger, M. et al. (2013). Mutations in tubg1, dync1h1, kif5c and kif2a cause malformations of cortical development and microcephaly. *Nat Genet* **45**, 639–47.

Polfliet, M. M., Van de Veerdonk, F., Dpp, E. A., Van Kesteren-Hendrikx, E. M., Van Rooijen, N., Dijkstra, C. D. and Van den Berg, T. K. (2002). The role of perivascular and meningeal macrophages in experimental allergic encephalomyelitis. *Journal of Neuroimmunology* **122**, 1–8.

Pollard, T. D. and Cooper, J. A. (2009). Actin, a central player in cell shape and movement. *Science* **326**, 1208–1212.

Priller, C., Bauer, T., Mitteregger, G., Krebs, B., Kretzschmar, H. A. and Herms, J. (2006). Synapse formation and function is modulated by the amyloid precursor protein. *J Neurosci* **26**, 7212–21.

Puls, I., Jonnakuty, C., LaMonte, B. H., Holzbaur, E. L. F., Tokito, M., Mann, E., Floeter, M. K., Bidus, K., Drayna, D., Oh, S. J. et al. (2003). Mutant dynactin in motor neuron disease. *Nature Genetics* **33**, 455–6.

R, B. D., N, H. R., J, S. G., Mathew, C., J, S. R., Jeannette, L.-S., An, G., Rita, D., Bénédicte, D., Janna, S. et al. (2010). Lack of support for association between the kif1b rs10492972[c] variant and multiple sclerosis. *Nature Genetics* **42**.

R Core Team (2014). *R: A Language and Environment for Statistical Computing*. R Foundation for Statistical Computing, Vienna, Austria.

Rahn, E. J., Iannitti, T., Donahue, R. R. and Taylor, B. K. (2014). Sex differences in a mouse model of multiple sclerosis: neuropathic pain behavior in females but not males and protection from neurological deficits during proestrus. *Biology of Sex Differences* **5**, 4.

Ralf, G., Christopher, L. and Hans, L. (2006). Understanding pathogenesis and therapy of multiple sclerosis via animal models: 70 years of merits and culprits in experimental autoimmune encephalomyelitis research. *Brain* **129**, 1953–71.

Ram, S., Ward, E. S. and Ober, R. J. (2006). Beyond rayleigh's criterion: a resolution measure with application to single-molecule microscopy. *Proceedings of the National Academy of Sciences of the United States of America* **103**, 4457–62.

Ransohoff, R. M. (2012). Animal models of multiple sclerosis: the good, the bad and the bottom line. *Nature Neuroscience* **15**, 1074–7.

Ransohoff, R. M., Hafler, D. A. and Lucchinetti, C. F. (2015). Multiple sclerosis-a quiet revolution. *Nat Rev Neurol* .

Rasband, M. N. (2010). The axon initial segment and the maintenance of neuronal polarity. *Nature Reviews. Neuroscience* **11**.

Rasola, A. and Bernardi, P. (2011). Mitochondrial permeability transition in ca(2+)-dependent apoptosis and necrosis. *Cell Calcium* **50**, 222–33.

Ray, K. (2014). From fission to fusion: a perspective on the research that won the nobel prize in physiology or medicine, 2013. *J Biosci* **39**, 3–12.

Reed, N. A., Cai, D., Blasius, T. L., Jih, G. T., Meyhofer, E., Gaertig, J. and Verhey, K. J. (2006). Microtubule acetylation promotes kinesin-1 binding and transport. *Curr Biol* **16**, 2166–72.

Renaud, J., Kerjan, G., Sumita, I., Zagar, Y., Georget, V., Kim, D., Fouquet, C., Suda, K., Sanbo, M., Suto, F. et al. (2008). Plexin-a2 and its ligand, sema6a, control nucleus-centrosome coupling in migrating granule cells. *Nature Neuroscience* **11**, 440–449.

Rex, C. S., Gavin, C. F., Rubio, M. D., Kramar, E. A., Chen, L. Y., Jia, Y., Huganir, R. L., Muzyczka, N., Gall, C. M. and Miller, C. A. (2010). Myosin iib regulates actin dynamics during synaptic plasticity and memory formation. *Neuron* **67**, 603–617.

Richner, M., Victor, M. B., Liu, Y., Abernathy, D. and Yoo, A. S. (2015). Microrna-based conversion of human fibroblasts into striatal medium spiny neurons. *Nat Protoc* **10**, 1543–55.

Riemer, J. and Kins, S. (2013). Axonal transport and mitochondrial dysfunction in alzheimer's disease. *Neurodegener Dis* **12**, 111–24.

Ries, J., Kaplan, C., Platonova, E., Eghlidi, H. and Ewers, H. (2012). A simple, versatile method for gfp-based super-resolution microscopy via nanobodies. *Nature Methods* **9**, 582–4.

Rio, C., Rieff, H. I., Qi, P., Khurana, T. S. and Corfas, G. (1997). Neuregulin and erbb receptors play a critical role in neuronal migration. *Neuron* **19**, 39–50.

Rocca, M. A., Messina, R. and Filippi, M. (2013). Multiple sclerosis imaging: recent advances. *J Neurol* **260**, 929–35.

Rodriguez, M. and Scheithauer, B. (1994). Ultrastructure of multiple sclerosis. *Ultrastruct Pathol* **18**, 3–13.

Rogowski, K., Van Dijk, J., Magiera, M. M., Bosc, C., Deloulme, J.-C., Bosson, A., Peris, L., Gold, N. D., Lacroix, B., Grau, M. B. et al. (2010). A family of protein-deglutamylating enzymes associated with neurodegeneration. *Cell* **143**, 564–78.

Rolls, M. M., Satoh, D., Clyne, P. J., Henner, A. L., Uemura, T. and Doe, C. Q. (2007). Polarity and intracellular compartmentalization of drosophila neurons. *Neural Development* **2**, 7.

Rothbauer, U., Zolghadr, K., Tillib, S., Nowak, D., Schermelleh, L., Gahl, A., Backmann, N., Conrath, K., Muyldermans, S., Cardoso, M. C. et al. (2006). Targeting and tracing antigens in live cells with fluorescent nanobodies. *Nature Methods* **3**, 887–9.

Roy, N. H., Chan, J., Lambel, M. and Thali, M. (2013). Clustering and mobility of hiv-1 env at viral assembly sites predict its propensity to induce cell-cell fusion. *Journal of Virology* **87**, 7516–25.

Royle, S. J. (2015). Super-duper resolution imaging of mitotic microtubules. *Nat Rev Mol Cell Biol* **16**, 67.

Ruberti, F. and Dotti, C. G. (2000). Involvement of the proximal c terminus of the ampa receptor subunit glur1 in dendritic sorting. *Journal of Neuroscience* **20**.

Rudolf, R., Bittins, C. M. and Gerdes, H.-H. (2011). The role of myosin v in exocytosis and synaptic plasticity. *Journal of Neurochemistry* **116**, 177–91.

Rust, M. J., Bates, M. and Zhuang, X. (2006). Sub-diffraction-limit imaging by stochastic optical reconstruction microscopy (storm). *Nature Methods* **3**, 793–5.

Ryu, J., Liu, L., Wong, T. P., Wu, D. C., Burette, A., Weinberg, R., Wang, Y. T. and Sheng, M. (2006). A critical role for myosin iib in dendritic spine morphology and synaptic function. *Neuron* **49**, 175–82.

Saab, A. S., Tzvetanova, I. D. and Nave, K. A. (2013). The role of myelin and oligodendrocytes in axonal energy metabolism. *Curr Opin Neurobiol* **23**, 1065–72.

Sampo, B., Kaech, S., Kunz, S. and Banker, G. (2003). Two distinct mechanisms target membrane proteins to the axonal surface. *Neuron* **37**, 611–624.

Satoh, D., Sato, D., Tsuyama, T., Saito, M., Ohkura, H., Rolls, M. M., Ishikawa, F. and Uemura, T. (2008). Spatial control of branching within dendritic arbors by dynein-dependent transport of rab5-endosomes. *Nature Cell Biology* **10**, 1164–71.

Sawcer, S., Franklin, R. J. and Ban, M. (2014). Multiple sclerosis genetics. *Lancet Neurol* **13**, 700–9.

Saxton, W. O. and Baumeister, W. (1982). The correlation averaging of a regularly arranged bacterial cell envelope protein. *Journal of Microscopy* **127**, 127–38.

Scherberger, H. (2009). Neural control of motor prostheses. *Curr Opin Neurobiol* **19**, 629–33.

Schindelin, J., Arganda-Carreras, I., Frise, E., Kaynig, V., Longair, M., Pietzsch, T., Preibisch, S., Rueden, C., Saalfeld, S., Schmid, B. et al. (2012). Fiji: an open-source platform for biological-image analysis. *Nat. Methods* **9**, 676–82.

Schlager, M. and Hoogenraad, C. C. (2009). Basic mechanisms for recognition and transport of synaptic cargos. *Molecular Brain* **2**, 25.

Schlager, M., Kapitein, L. C., Grigoriev, I., Burzynski, G. M., Wulf, P. S., Keijzer, N., De Graaff, E., Fukuda, M., Shepherd, I. T., Akhmanova, A. et al. (2010). Pericentrosomal targeting of rab6 secretory vesicles by bicaudal-d-related protein 1 (bicdr-1) regulates neuritogenesis. *EMBO Journal* **29**, 1637–51.

Schlager, M. A., Serra-Marques, A., Grigoriev, I., Gumy, L. F., Esteves da Silva, M., Wulf, P. S., Akhmanova, A. and Hoogenraad, C. C. (2014). Bicaudal d family adaptor proteins control the velocity of dynein-based movements. *Cell Rep* **8**, 1248–56.

Schlisio, S., Kenchappa, R. S., Vredeveld, L. C., George, R. E., Stewart, R., Greulich, H., Shahriari, K., Nguyen, N. V., Pigny, P., Dahia, P. L. et al. (2008). The kinesin kif1bbeta acts downstream from egln3 to induce apoptosis and is a potential 1p36 tumor suppressor. *Genes and Development* **22**, 884–893.

Schliwa, M. and Woehlke, G. (2003). Molecular motors. *Nature* **422**, 759–765.

Schmitz, K. R., Bagchi, A., Roovers, R. C., van Bergen en Henegouwen, P. M. and Ferguson, K. M. (2013). Structural evaluation of egfr inhibition mechanisms for nanobodies/vhh domains. *Structure* **21**, 1214–24.

Schnitzer, M. J. and Block, S. M. (1997). Kinesin hydrolyses one atp per 8-nm step. *Nature* **388**, 386–90.

Schroer, T. A. (2004). Dynactin. *Annual Review of Cell and Developmental Biology* **20**, 759–79.

Schwarz, T. L. (2013). Mitochondrial trafficking in neurons. *Cold Spring Harb Perspect Biol* **5**.

Schwendimann, R. N. and Alekseeva, N. (2007). Gender issues in multiple sclerosis. *International Review of Neurobiology* **79**, 377–92.

Setou, M., Nakagawa, T., Seog, D.-H. and Hirokawa, N. (2000). Kinesin superfamily motor protein kif17 and mlin-10 in nmda receptor-containing vesicle transport. *Science* **288**, 1796–1802.

Setou, M., Seog, D.-H., Tanaka, Y., Kanai, Y., Takei, Y., Kawagishi, M. and Hirokawa, N. (2002). Glutamate-receptor-interacting protein grip1 directly steers kinesin to dendrites. *Nature* **417**, 83–7.

Sheng, M. and Hoogenraad, C. C. (2007). The postsynaptic architecture of excitatory synapses: a more quantitative view. *Annual Review of Biochemistry* **76**, 823–847.

Sheng, Z. H. (2014). Mitochondrial trafficking and anchoring in neurons: New insight and implications. *J Cell Biol* **204**, 1087–98.

Shepherd, J. D. and Huganir, R. L. (2007). The cell biology of synaptic plasticity: Ampa receptor trafficking. *Annual Review of Cell and Developmental Biology* **23**, 613–643.

Sherman, D. L. and Brophy, P. J. (2005). Mechanisms of axon ensheathment and myelin growth. *Nat Rev Neurosci* **6**, 683–90.

Shi, F. M., Yao, L. L., Pei, B. L., Zhou, Q., Li, X. L., Li, Y. and Li, Y. Z. (2009). Cortical microtubule as a sensor and target of nitric oxide signal during the defence responses to verticillium dahliae toxins in arabidopsis. *Plant Cell Environ* **32**, 428–38.

Shivanna, M. and Srinivas, S. P. (2009). Microtubule stabilization opposes the (tnf-alpha)-induced loss in the barrier integrity of corneal endothelium. *Exp Eye Res* **89**, 950–9.

Shroff, H., Galbraith, C. G., Galbraith, J. A., White, H., Gillette, J., Olenych, S., Davidson, M. W. and Betzig, E. (2007). Dual-color superresolution imaging of genetically expressed probes within individual adhesion complexes. *Proceedings of the National Academy of Sciences of the United States of America* **104**, 20308–13.

Shroff, H., White, H. and Betzig, E. (2008). Photoactivated localization microscopy (palm) of adhesion complexes. *Current Protocols in Cell Biology* **Chapter 4**, Unit 4.21.

Simons, M. and Trajkovic, K. (2006). Neuron-glia communication in the control of oligodendrocyte function and myelin biogenesis. *J Cell Sci* **119**, 4381–9.

Singh, V., van Pelt, E. D., Stoop, M. P., Stingl, C., Ketelslegers, I. A., Neuteboom, R. F., Catsman-Berrevoets, C. E., Luider, T. M. and Hintzen, R. Q. (2015). Gray matter-related proteins are associated with childhood-onset multiple sclerosis. *Neurol Neuroimmunol Neuroinflamm* **2**, e155.

Sirajuddin, M., Rice, L. M. and Vale, R. D. (2014). Regulation of microtubule motors by tubulin isotypes and post-translational modifications. *Nat Cell Biol* **16**, 335–44.

Smith, A. J., Liu, Y., Peng, H., Beers, R., Racke, M. K. and Lovett-Racke, A. E. (2011). Comparison of a classical th1 bacteria versus a th17 bacteria as adjuvant in the induction of experimental autoimmune encephalomyelitis. *Journal of Neuroimmunology* **237**, 33–38.

Smith, A. J. and Verkman, A. S. (2015). Superresolution imaging of aquaporin-4 cluster size in antibody-stained paraffin brain sections. *Biophys J* **109**, 2511–22.

Socie, M. J., Motl, R. W., Pula, J. H., Sandroff, B. M. and Sosnoff, J. J. (2013). Gait variability and disability in multiple sclerosis. *Gait and Posture* **38**, 51–5.

Solecki, D. J. (2012). Sticky situations: recent advances in control of cell adhesion during neuronal migration. *Current Opinion in Neurobiology* **22**, 791–798.

Sombekke, M. H., Jafari, N., Bendfeldt, K., Mueller-Lenke, N., Radue, E. W., Naegelin, Y., Kappos, L., Matthews, P. M., Polman, C. H., Barkhof, F. et al. (2011). No influence of kif1b on neurodegenerative markers in multiple sclerosis. *Neurology* **76**, 1843–5.

Song, A.-H., Wang, D., Chen, G., Li, Y., Luo, J., Duan, S. and ming Poo, M. (2009). A selective filter for cytoplasmic transport at the axon initial segment. *Cell* **136**, 1148–1160.

Song, Y., Kirkpatrick, L. L., Schilling, A. B., Helseth, D. L., Chabot, N., Keillor, J. W., Johnson, G. V. and Brady, S. T. (2013). Transglutaminase and polyamination of tubulin: posttranslational modification for stabilizing axonal microtubules. *Neuron* **78**, 109–23.

Sorbara, C. D., Wagner, N. E., Ladwig, A., Nikić, I., Merkler, D., Kleele, T., Marinković, P., Naumann, R., Godinho, L., Bareyre, F. M. et al. (2014). Pervasive axonal transport deficits in multiple sclerosis models. *Neuron* **84**, 1183–90.

Splinter, D., Razafsky, D. S., Schlager, M. A., Serra-Marques, A., Grigoriev, I., Demmers, J., Keijzer, N., Jiang, K., Poser, I., Hyman, A. A. et al. (2012). Bicd2, dynactin, and lis1 cooperate in regulating dynein recruitment to cellular structures. *Molecular Biology of the Cell* **23**, 4226–4241.

Splinter, D., Tanenbaum, M. E., Lindqvist, A., Jaarsma, D., Flotho, A., Yu, K. L., Grigoriev, I., Engelsma, D., Haasdijk, E. D., Keijzer, N. et al. (2010). Bicaudal d2, dynein, and kinesin-1 associate with nuclear pore complexes and regulate centrosome and nuclear positioning during mitotic entry. *PLoS Biology* **8**.

Sriram, S. and Steiner, I. (2005). Experimental allergic encephalomyelitis: a misleading model of multiple sclerosis. *Ann Neurol* **58**, 939–45.

Steinman, L. and Zamvil, S. S. (2005). Virtues and pitfalls of eae for the development of therapies for multiple sclerosis. *Trends in Immunology* **26**, 565–571.

Steinman, L. and Zamvil, S. S. (2006). How to successfully apply animal studies in experimental allergic encephalomyelitis to research on multiple sclerosis. *Annals of Neurology* **60**, 12–21.

Stepanova, T., Slemmer, J., Hoogenraad, C. C., Lansbergen, G., Dortland, B., De Zeeuw, C. I., Grosveld, F., Van Cappellen, G., Akhmanova, A. and Galjart, N. (2003). Visualization of microtubule growth in cultured neurons via the use of eb3-gfp (end-binding protein 3-green fluorescent protein). *Journal of Neuroscience* **23**, 2655–64.

Stewart, E. and Shen, K. (2015). Storming towards a clear picture of the cytoskeleton in neurons. *Elife* **4**.

Stiess, M., Maghelli, N., Kapitein, L. C., Gomis-Rüth, S., Wilsch-Bräuninger, M., Hoogenraad, C. C., Tolić-Nørrelykke, I. M. and Bradke, F. (2010). Axon extension occurs independently of centrosomal microtubule nucleation. *Science* **327**, 704–707.

Stirling, D. P. and Stys, P. K. (2010). Mechanisms of axonal injury: internodal nanocomplexes and calcium deregulation. *Trends Mol Med* **16**, 160–70.

Stone, M. C., Roegiers, F. and Rolls, M. M. (2008). Microtubules have opposite orientation in axons and dendrites of drosophila neurons. *Molecular Biology of the Cell* **19**, 4122–9.

Stowell, J. N. and Craig, A. M. (1999). Axon/dendrite targeting of metabotropic glutamate receptors by their cytoplasmic carboxy-terminal domains. *Neuron* **22**, 525–536.

Stroissnigg, H., Tranckov, A., Descovich, L., Fuhrmann, J., Kutschera, W., Kostan, J., Meixner, A., Nothias, F. and Propst, F. (2007). S-nitrosylation of microtubule-associated protein 1b mediates nitric-oxide-induced axon retraction. *Nat Cell Biol* **9**, 1035–45.

Stromnes, I. M. and Goverman, J. M. (2006). Active induction of experimental allergic encephalomyelitis. *Nat Protoc* **1**, 1810–9.

Stys, P. K., Zamponi, G. W., Van Minnen, J. and Geurts, J. J. (2012). Will the real multiple sclerosis please stand up? *Nat Rev Neurosci* **13**, 507–14.

Sudhof, T. C. (2004). The synaptic vesicle cycle. *Annual Review of Neuroscience* **27**, 509–547.

Sudhof, T. C. (2014). The molecular machinery of neurotransmitter release (nobel lecture). *Angew Chem Int Ed Engl* **53**, 12696–717.

Sun, X. Y., Takagishi, Y., Okabe, E., Chishima, Y., Kanou, Y., Murase, S., Mizumura, K., Inaba, M., Komatsu, Y., Hayashi, Y. et al. (2009). A novel caspr mutation causes the shambling mouse phenotype by disrupting axoglial interactions of myelinated nerves. *J Neuropathol Exp Neurol* **68**, 1207–18.

Sweeney, H. L. and Houdusse, A. (2010). Myosin vi rewrites the rules for myosin motors. *Cell* **141**, 573–82.

't Hart, B. A., Gran, B. and Weissert, R. (2011). Eae: imperfect but useful models of multiple sclerosis. *Trends in Molecular Medicine* **17**, 119–25.

't Hart, B. A., Hintzen, R. Q. and Laman, J. D. (2009). Multiple sclerosis - a response-to-damage model. *Trends Mol Med* **15**, 235–44.

Taes, I., Timmers, M., Hersmus, N., Bento-Abreu, A., Van Den Bosch, L., Van Damme, P., Auwerx, J. and Robberecht, W. (2013). Hdac6 deletion delays disease progression in the sod1g93a mouse model of als. *Hum Mol Genet* **22**, 1783–90.

Tanaka, T., Serneo, F. F., Higgins, C., Gambello, M. J., Wynshaw-Boris, A. and Gleeson, J. G. (2004). Lis1 and doublecortin function with dynein to mediate coupling of the nucleus to the centrosome in neuronal migration. *Journal of Cell Biology* **165**, 709–721.

Tanaka, Y., Kanai, Y., Okada, Y., Nonaka, S., Takeda, S., Harada, A. and Hirokawa, N. (1998). Targeted disruption of mouse conventional kinesin heavy chain, kif5b, results in abnormal perinuclear clustering of mitochondria. *Cell* **93**, 1147–1158.

Tarabeux, J., Champagne, N., Brustein, E., Hamdan, F. F., Gauthier, J., Lapointe, M., Maios, C., Piton, A., Spiegelman, D., Henrion, E. et al. (2010). De novo truncating mutation in kinesin 17 associated with schizophrenia. *Biological Psychiatry* **68**, 649–56.

Taveggia, C., Feltri, M. L. and Wrabetz, L. (2010). Signals to promote myelin formation and repair. *Nat Rev Neurol* **6**, 276–87.

Teuling, E., Van Dis, V., Wulf, P. S., Haasdijk, E. D., Akhmanova, A., Hoogenraad, C. C. and Jaarsma, D. (2008). A novel mouse model with impaired dynein/dynactin function develops amyotrophic lateral sclerosis (als)-like features in motor neurons and improves lifespan in sod1-als mice. *Human Molecular Genetics* **17**, 2849–62.

Thibault, K., Calvino, B. and Pezet, S. (2011). Characterisation of sensory abnormalities observed in an animal model of multiple sclerosis: a behavioural and pharmacological study. *European Journal of Pain* **15**, 231.e1–16.

Thompson, R. E., Larson, D. R. and Webb, W. W. (2002). Precise nanometer localization analysis for individual fluorescent probes. *Biophysical Journal* **82**, 2775–83.

Tian, D. H., Perera, C. J. and Moalem-Taylor, G. (2013). Neuropathic pain in animal models of nervous system autoimmune diseases. *Mediators of Inflammation* **2013**, 298326.

Tischfield, M. A., Baris, H. N., Wu, C., Rudolph, G., Van Maldergem, L., He, W., Chan, W.-M., Andrews, C., Demer, J. L., Robertson, R. L. et al. (2010). Human tubb3 mutations perturb microtubule dynamics, kinesin interactions, and axon guidance. *Cell* **140**, 74–87.

Torreno-Pina, J. A., Manzo, C., Salio, M., Aichinger, M. C., Oddone, A., Lakadamyali, M., Shepherd, D., Besra, G. S., Cerundolo, V. and Garcia-Parajo, M. F. (2016). The actin cytoskeleton modulates the activation of inkt cells by segregating cd1d nanoclusters on antigen-presenting cells. *Proc Natl Acad Sci U S A* **113**, E772–81.

Trapp, B. D. and Nave, K. A. (2008). Multiple sclerosis: an immune or neurodegenerative disorder? *Annu Rev Neurosci* **31**, 247–69.

Trapp, B. D. and Stys, P. K. (2009). Virtual hypoxia and chronic necrosis of demyelinated axons in multiple sclerosis. *Lancet Neurology* **8**, 280–291.

Tremlett, H., Yinshan, Z. and Devonshire, V. (2008). Natural history of secondary-progressive multiple sclerosis. *Multiple Sclerosis* **14**, 314–24.

Trushina, E. and McMurray, C. T. (2007). Oxidative stress and mitochondrial dysfunction in neurodegenerative diseases. *Neuroscience* **145**, 1233–48.

Tsilidis, K. K., Panagiotou, O. A., Sena, E. S., Aretouli, E., Evangelou, E., Howells, D. W., Al-Shahi Salman, R., Macleod, M. R. and Ioannidis, J. P. (2013). Evaluation of excess significance bias in animal studies of neurological diseases. *PLoS Biology* **11**, e1001609.

Twelvetrees, A. E., Yuen, E. Y., Arancibia-Carcamo, I. L., MacAskill, A. F., Rostaing, P., Lumb, M. J., Humbert, S., Triller, A., Saudou, F., Yan, Z. et al. (2010). Delivery of gabaars to synapses is mediated by hap1-kif5 and disrupted by mutant huntingtin. *Neuron* **65**, 53–65.

Uchida, S., Martel, G., Pavlowsky, A., Takizawa, S., Hevi, C., Watanabe, Y., Kandel, E. R., Alarcon, J. M. and Shumyatsky, G. P. (2014). Learning-induced and stathmin-dependent changes in microtubule stability are critical for memory and disrupted in ageing. *Nat Commun* **5**, 4389.

Uchida, S. and Shumyatsky, G. P. (2015). Deceivingly dynamic: Learning-dependent changes in stathmin and microtubules. *Neurobiol Learn Mem* **124**, 52–61.

Vale, R. D. (2003). The molecular motor toolbox for intracellular transport. *Cell* **112**, 467–480.

Vale, R. D., Schnapp, B. J., Reese, T. S. and Sheetz, M. P. (1985). Movement of organelles along filaments dissociated from the axoplasm of the squid giant axon. *Cell* **40**, 449–54.

Van den Berg, R. and Hoogenraad, C. C. (2012). Molecular motors in cargo trafficking and synapse assembly. *Advances in Experimental Medicine and Biology* **970**, 173–96.

Van der Vaart, B., Van Riel, W. E., Doodhi, H., Kevenaar, J. T., Katrukha, E. A., Gumy, L., Bouchet, B. P., Grigoriev, I., Spangler, S. A., Yu, K. L. et al. (2013). Cfeom1-associated kinesin kif21a is a cortical microtubule growth inhibitor. *Dev Cell* **27**, 145–60.

Van Noorden, R. (2015). Interdisciplinary research by the numbers. *Nature* **525**, 306–7.

Van Spronsen, M. and Hoogenraad, C. C. (2010). Synapse pathology in psychiatric and neurologic disease. *Current Neurology and Neuroscience Reports* **10**, 207–14.

Van Spronsen, M., Mikhaylova, M., Lipka, J., Schlager, M. A., Van den Heuvel, D. J., Kuijpers, M., Wulf, P. S., Keijzer, N., Demmers, J., Kapitein, L. C. et al. (2013). Trak/milton motor-adaptor proteins steer mitochondrial trafficking to axons and dendrites. *Neuron* **77**, 485–502.

Vazin, T., Ball, K. A., Lu, H., Park, H., Ataeijannati, Y., Head-Gordon, T., Poo, M. M. and Schaffer, D. V. (2014). Efficient derivation of cortical glutamatergic neurons from human pluripotent stem cells: a model system to study neurotoxicity in alzheimer's disease. *Neurobiol Dis* **62**, 62–72.

Verhey, K. J. and Hammond, J. W. (2009). Traffic control: regulation of kinesin motors. *Nature Reviews. Molecular Cell Biology* **10**, 765–77.

Villacé, P., Marión, R. M. and Ortín, J. (2004). The composition of staufen-containing rna granules from human cells indicates their role in the regulated transport and translation of messenger rnas. *Nucleic Acids Research* **32**, 2411–20.

Vives-Bauza, C., Zhou, C., Huang, Y., Cui, M., de Vries, R. L., Kim, J., May, J., Tocilescu, M. A., Liu, W., Ko, H. S. et al. (2010). Pink1-dependent recruitment of parkin to mitochondria in mitophagy. *Proc Natl Acad Sci U S A* **107**, 378–83.

Wade, R. H. (2007). Microtubules: an overview. *Methods Mol Med* **137**, 1–16.

Wagner, O. I., Esposito, A., Köhler, B., Chen, C.-W., Shen, C.-P., Wu, G.-H., Butkevich, E., Mandalapu, S., Wenzel, D., Wouters, F. S. et al. (2009). Synaptic scaffolding protein syd-2 clusters and activates kinesin-3 unc-104 in c. elegans. *Proceedings of the National Academy of Sciences of the United States of America* **106**, 19605–10.

Walker-Caulfield, M. E., Hatfield, J. K. and Brown, M. A. (2015). Dynamic changes in meningeal inflammation correspond to clinical exacerbations in a murine model of relapsing-remitting multiple sclerosis. *Journal of Neuroimmunology* **278**, 112–22.

Wander, J. D. and Rao, R. P. (2014). Brain-computer interfaces: a powerful tool for scientific inquiry. *Curr Opin Neurobiol* **25**, 70–5.

Wang, J., Wang, M. R., Jiang, H., Shen, M., Cui, L. and Bhattacharya, S. K. (2010). Detection of magnetic particles in live dba/2j mouse eyes using magnetomotive optical coherence tomography. *Eye Contact Lens* **36**, 346–51.

Wang, X., Imura, T., Sofroniew, M. V. and Fushiki, S. (2011). Loss of adenomatous polyposis coli in bergmann glia disrupts their unique architecture and leads to cell nonautonomous neurodegeneration of cerebellar purkinje neurons. *Glia* **59**, 857–868.

Wang, X. and Schwarz, T. L. (2009). The mechanism of ca2+ -dependent regulation of kinesin-mediated mitochondrial motility. *Cell* **136**, 163–174.

Wang, Y., Schnitzbauer, J., Hu, Z., Li, X., Cheng, Y., Huang, Z.-L. and Huang, B. (2014). Localization events-based sample drift correction for localization microscopy with redundant cross-correlation algorithm. *Optics Express* **22**, 15982–91.

Wang, Z., Edwards, J. G., Riley, N., Provance, D. W., Karcher, R., Li, X. D., Davison, I. G., Ikebe, M., Mercer, J. A., Kauer, J. A. et al. (2008). Myosin vb mobilizes recycling endosomes and ampa receptors for postsynaptic plasticity. *Cell* **135**, 535–548.

Watson, C., Paxinos, G. and Kayalioglu, G., eds. (2009). *The Spinal Cord.* San Diego: Academic Press.

Wekerle, H., Flügel, A., Fugger, L., Schett, G. and Serreze, D. (2012). Autoimmunity's next top models. *Nature Medicine* **18**, 66–70.

Wharton, R. P. and Struhl, G. (1989). Structure of the drosophila bicaudald protein and its role in localizing the the posterior determinant nanos. *Cell* **59**, 881–92.

Widge, A. S., Dougherty, D. D. and Moritz, C. T. (2014). Affective brain-computer interfaces as enabling technology for responsive psychiatric stimulation. *Brain Comput Interfaces (Abingdon)* **1**, 126–136.

Willemsen, M. H., Vissers, L. E., Willemsen, M. A., van Bon, B. W., Kroes, T., de Ligt, J., de Vries, B. B., Schoots, J., Lugtenberg, D., Hamel, B. C. et al. (2012). Mutations in dync1h1 cause severe intellectual disability with neuronal migration defects. *J Med Genet* **49**, 179–83.

Willig, K. I. and Barrantes, F. J. (2014). Recent applications of superresolution microscopy in neurobiology. *Current Opinion in Chemical Biology* **20**, 16–21.

Winckler, B., Forscher, P. and Mellman, I. (1999). A diffusion barrier maintains distribution of membrane proteins in polarized neurons. *Nature* **397**, 698–701.

Winckler, B. and Mellman, I. (2010). Trafficking guidance receptors. *Cold Spring Harbor Perspectives in Biology* **2**.

Winsor, C. P. (1932). The gompertz curve as a growth curve. *Proceedings of the National Academy of Sciences of the United States of America* **18**, 1–8.

Wisco, D., Anderson, E. D., Chang, M. C., Norden, C., Boiko, T., Fölsch, H. and Winckler, B. (2003). Uncovering multiple axonal targeting pathways in hippocampal neurons. *Journal of Cell Biology* **162**, 1317–1328.

Witte, H., Neukirchen, D. and Bradke, F. (2008). Microtubule stabilization specifies initial neuronal polarization. *Journal of Cell Biology* **180**, 619–32.

Witte, M. E., Geurts, J. J., De Vries, H. E., Van der Valk, P. and Van Horssen, J. (2010). Mitochondrial dysfunction: a potential link between neuroinflammation and neurodegeneration? *Mitochondrion* **10**, 411–8.

Witte, M. E., Mahad, D. J., Lassmann, H. and van Horssen, J. (2014). Mitochondrial dysfunction contributes to neurodegeneration in multiple sclerosis. *Trends Mol Med* **20**, 179–87.

Wolswijk, G. and Balesar, R. (2003). Changes in the expression and localization of the paranodal protein caspr on axons in chronic multiple sclerosis. *Brain* **126**, 1638–49.

Wong, R. W., Setou, M., Teng, J., Takei, Y. and Hirokawa, N. (2002). Overexpression of motor protein kif17 enhances spatial and working memory in transgenic mice. *Proceedings of the National Academy of Sciences of the United States of America* **99**, 14500–14505.

Woolner, S. and Bement, W. M. (2009). Unconventional myosins acting unconventionally. *Trends in Cell Biology* **19**, 245–52.

Xia, C. H., Roberts, E. A., Her, L. S., Liu, X., Williams, D. S., Cleveland, D. W. and Goldstein, L. S. (2003). Abnormal neurofilament transport caused by targeted disruption of neuronal kinesin heavy chain kif5a. *J Cell Biol* **161**, 55–66.

Xiong, Y., Zhao, K., Wu, J., Xu, Z., Jin, S. and Zhang, Y. Q. (2013). Hdac6 mutations rescue human tau-induced microtubule defects in drosophila. *Proc Natl Acad Sci U S A* **110**, 4604–9.

Xu, C. C., Denton, K. R., Wang, Z. B., Zhang, X. and Li, X. J. (2016). Abnormal mitochondrial transport and morphology as early pathological changes in human models of spinal muscular atrophy. *Dis Model Mech* **9**, 39–49.

Xu, H., Yang, Y., Tang, X., Zhao, M., Liang, F., Xu, P., Hou, B., Xing, Y., Bao, X. and Fan, X. (2013a). Bergmann glia function in granule cell migration during cerebellum development. *Molecular Neurobiology* **47**, 833–844.

Xu, K., Babcock, H. P. and Zhuang, X. (2012). Dual-objective storm reveals three-dimensional filament organization in the actin cytoskeleton. *Nature Methods* **9**, 185–8.

Xu, K., Zhong, G. and Zhuang, X. (2013b). Actin, spectrin, and associated proteins form a periodic cytoskeletal structure in axons. *Science* **339**, 452–6.

Yamada, K., Andrews, C., Chan, W. M., McKeown, C. A., Magli, A., De Berardinis, T., Loewenstein, A., Lazar, M., O'Keefe, M., Letson, R. et al. (2003). Heterozygous mutations of the kinesin kif21a in congenital fibrosis of the extraocular muscles type 1 (cfeom1). *Nat Genet* **35**, 318–21.

Yamasaki, T., Kawaji, K., Ono, K., Bito, H., Hirano, T., Osumi, N. and Kengaku, M. (2001). Pax6 regulates granule cell polarization during parallel fiber formation in the developing cerebellum. *Development* **128**, 3133–3144.

Yau, K. W., Van Beuningen, S. F., Cunha-Ferreira, I., Cloin, B. M., Van Battum, E. Y., Will, L., Schtzle, P., Tas, R. P., Van Krugten, J., Katrukha, E. A. et al. (2014). Microtubule minus-end binding protein camsap2 controls axon specification and dendrite development. *Neuron* **82**, 1058–73.

Yeh, I. T., Lenci, R. E., Qin, Y., Buddavarapu, K., Ligon, A. H., Leteurtre, E., Do Cao, C., Cardot-Bauters, C., Pigny, P. and Dahia, P. L. (2008). A germline mutation of the kif1b beta gene on 1p36 in a family with neural and nonneural tumors. *Human Genetics* **124**, 279–285.

Yildiz, A., Forkey, J. N., McKinney, S. A., Ha, T., Goldman, Y. E. and Selvin, P. R. (2003). Myosin v walks hand-over-hand: single fluorophore imaging with 1.5-nm localization. *Science* **300**, 2061–5.

Yildiz, A., Tomishige, M., Vale, R. D. and Selvin, P. R. (2004). Kinesin walks hand-over-hand. *Science* **303**, 676–678.

Yue, Q., Groszer, M., Gil, J. S., Berk, A. J., Messing, A., Wu, H. and Liu, X. (2005). Pten deletion in bergmann glia leads to premature differentiation and affects laminar organization. *Development* **132**, 3281–3291.

Yuste, R. and Bonhoeffer, T. (2001). Morphological changes in dendritic spines associated with long-term synaptic plasticity. *Annual Review of Neuroscience* **24**, 1071–1089.

Zambonin, J. L., Zhao, C., Ohno, N., Campbell, G. R., Engeham, S., Ziabreva, I., Schwarz, N., Lee, S. E., Frischer, J. M., Turnbull, D. M. et al. (2011). Increased mitochondrial content in remyelinated axons: implications for multiple sclerosis. *Brain* **134**, 1901–13.

Zhang, F., Su, B., Wang, C., Siedlak, S. L., Mondragon-Rodriguez, S., Lee, H. G., Wang, X., Perry, G. and Zhu, X. (2015). Posttranslational modifications of -tubulin in alzheimer disease. *Transl Neurodegener* **4**, 9.

Zhang, L., Liu, C., Wu, J., Tao, J. J., Sui, X. L., Yao, Z. G., Xu, Y. F., Huang, L., Zhu, H., Sheng, S. L. et al. (2014). Tubastatin a/acy-1215 improves cognition in alzheimer's disease transgenic mice. *J Alzheimers Dis* **41**, 1193–205.

Zhao, C., Takita, J., Tanaka, Y., Setou, M., Nakagawa, T., Takeda, S., Yang, H. W., Terada, S., Nakata, T., Takei, Y. et al. (2001). Charcot-marie-tooth disease type 2a caused by mutation in a microtubule motor kif1bbeta. *Cell* **105**, 587–97.

Zhao, J. J., Gao, S., Jing, J. Z., Zhu, M. Y., Zhou, C. and Chai, Z. (2014). Increased na+/ca2+ exchanger activity promotes resistance to excitotoxicity in cortical neurons of the ground squirrel (a hibernator). *PLoS One* **9**, e113594.

Zheng, Y., Wildonger, J., Ye, B., Zhang, Y., Kita, A., Younger, S. H., Zimmerman, S., Jan, L. Y. and Jan, Y. N. (2008). Dynein is required for polarized dendritic transport and uniform microtubule orientation in axons. *Nature Cell Biology* **10**, 1172–1180.

Zhong, G., He, J., Zhou, R., Lorenzo, D., Babcock, H. P., Bennett, V. and Zhuang, X. (2014). Developmental mechanism of the periodic membrane skeleton in axons. *Elife* **3**.

Zhuo, L., Theis, M., Alvarez-Maya, I., Brenner, M., Willecke, K. and Messing, A. (2001). hgfap-cre transgenic mice for manipulation of glial and neuronal function in vivo. *Genesis* **31**, 85–94.

Zrenner, E., Bartz-Schmidt, K. U., Benav, H., Besch, D., Bruckmann, A., Gabel, V. P., Gekeler, F., Greppmaier, U., Harscher, A., Kibbel, S. et al. (2011). Subretinal electronic chips allow blind patients to read letters and combine them to words. *Proc Biol Sci* **278**, 1489–97.

Zuchner, S., Mersiyanova, I. V., Muglia, M., Bissar-Tadmouri, N., Rochelle, J., Dadali, E. L., Zappia, M., Nelis, E., Patitucci, A., Senderek, J. et al. (2004). Mutations in the mitochondrial gtpase mitofusin 2 cause charcot-marie-tooth neuropathy type 2a. *Nature Genetics* **36**, 449–451.

About the Author

■ **Computer Skills**

■ **Research Interests**

■ **Hobbies**

BCI: brain-computer interface

C

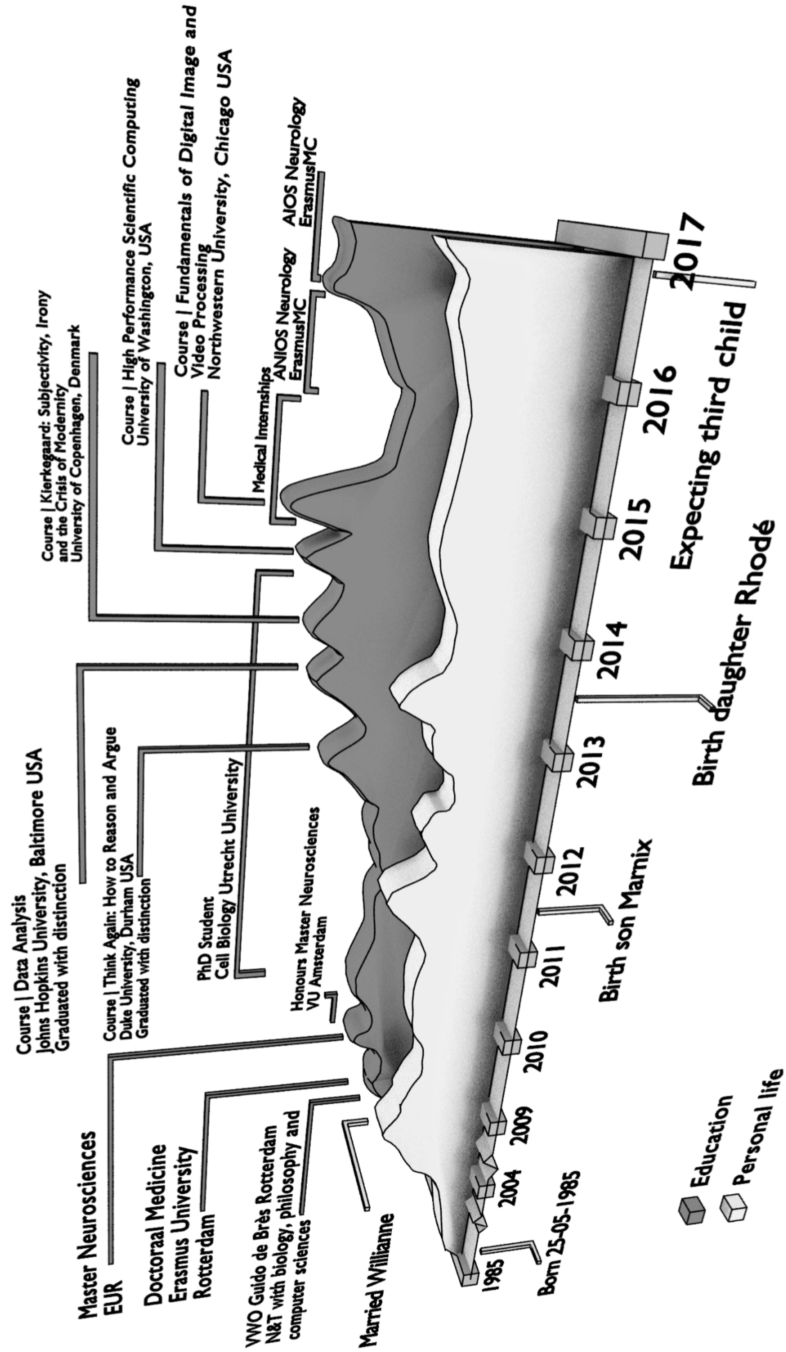
Master Neurosciences
EUR
Doctoraal Medicine
Erasmus University
Rotterdam
VWO Guido de Brès Rotterdam
N&T with biology, philosophy and
computer sciences
Married Willianne
Course | Data Analysis
Johns Hopkins University, Baltimore USA
Graduated with distinction
Course | Think Again: How to Reason and Argue
Duke University, Durham USA
Graduated with distinction
Honours Master Neurosciences
VU Amsterdam
PhD Student
Cell Biology Utrecht University
Course | Kierkegaard: Subjectivity, Irony
and the Crisis of Modernity
University of Copenhagen, Denmark
Course | High Performance Scientific Computing
University of Washington, USA
Course | Fundamentals of Digital Image and
Video Processing
Northwestern University, Chicago USA
Medical Internships
ANIOS Neurology
ErasmusMC
AIOS Neurology
ErasmusMC
1985
2004
2009
2010
2011
2012
2013
2014
2015
2016
2017
Born 25-05-1985
Birth son Marnix
Birth daughter Rhodé
Expecting third child
Education
Personal life

Portfolio

Name:	Robert van den Berg
PhD period:	2009-2016
Departments:	ErasmusMC dept. of Neurology, UU Cell Biology
Promotors:	Prof. dr. R.Q. Hintzen Prof. dr. C.C. Hoogenraad
Research School:	Graduate school neurosciences Amsterdam Rotterdam (ONWAR)

PhD Training		
Courses	*Year*	*Workload (ECTS)*
Art. 9 course for animal research	2009	1.5
Think Again: How to Reason and Argue *Duke University, Durham, USA* *With Distinction*	2012	1.5
Data Analysis *Johns Hopkins University, Baltimore, USA* *With Distinction*	2013	2
Kierkegaard: Subjectivity, Irony and the Crisis of Modernity *University of Copenhagen, Denmark*	2013	1.5
High Performance Scientific Computing *University of Washington, USA*	2014	1.5
Fundamentals of Digital Image and Video Processing *Northwestern University, Chicago, USA*	2014	1.5
Conferences		
MGC Student Meeting *Bruges, Belgium*	2009	0.5
FENS Neuroscience Meeting *Amsterdam, The Netherlands*	2010	1
Science Online Meeting *London, UK*	2010	1
Annual Dutch Meeting on Molecular and Cellular Biophysics *Veldhoven, The Netherlands* *Poster presentations*	2010 2011 2012	2
Mechanisms of Cytoskeleton Dynamics and Intracellular Trafficking *Warsaw, Poland* *Poster presentation*	2010	1
Annual Multiple Sclerosis Meeting	2011	0.5

Publications

De Graaff E, Maat P, Hulsenboom E, **Van den Berg R**, Van den Bent M, Demmers J, Lugtenburg PJ, Hoogenraad CC, Sillevis Smitt P (2012). Identification of delta/notch-like epidermal growth factor-related receptor as the Tr antigen in paraneoplastic cerebellar degeneration. Annals of Neurology *71(6)*: 815-24.

Van den Berg R, Hoogenraad CC (2012). Molecular motors in cargo trafficking and synapse assembly. Advances in Experimental Medicine and Biology *970*:173-96.

Jaarsma D* , **Van den Berg R*** , Wulf P.S.* , Van Erp S , Keijzer N , Schlager M, De Graaff E, De Zeeuw CI, Pasterkamp J, Akhmanova A, Hoogenraad CC (2014). A role for Bicaudal-D2 in radial cerebellar granule cell migration. Nature Communications *5*: 3411.

Mikhaylova M, Cloin BM*, Finan K*, **Van den Berg R***, Teeuw J, Kijanka MM, Sokolowski M, Katrukha EA, Maidorn M, Opazo F, Moutel S, Vantard M, Perez F, Van Bergen en Henegouwen PM, Hoogenraad CC, Ewers H, Kapitein LC (2015). Resolving bundled microtubules using anti-tubulin nanobodies. Nature Communications *6*: 7933.

Van den Berg R, Van Meurs M, Laman JD, Hintzen RQ, Hoogenraad CC. Heterozygous Kif1b deletion does not affect clinical disease or neuropathology in a demyelinating EAE model of multiple sclerosis. *To be submitted.*

Van den Berg R, Laman JD, Van Meurs, M, Hintzen RQ, Hoogenraad CC (2016). Rotarod motor performance and advanced spinal cord lesion image analysis refine assessment of neurodegeneration in experimental autoimmune encephalomyelitis. J. Neuroscience Methods *262*:66-76.

Van den Berg R, Hoogenraad CC, Hintzen RQ. Axonal Transport Deficits in Multiple Sclerosis; Spiralling into the Abyss. *To be submitted.*

* Authors contributed equally to this manuscript.

Acknowledgements

D

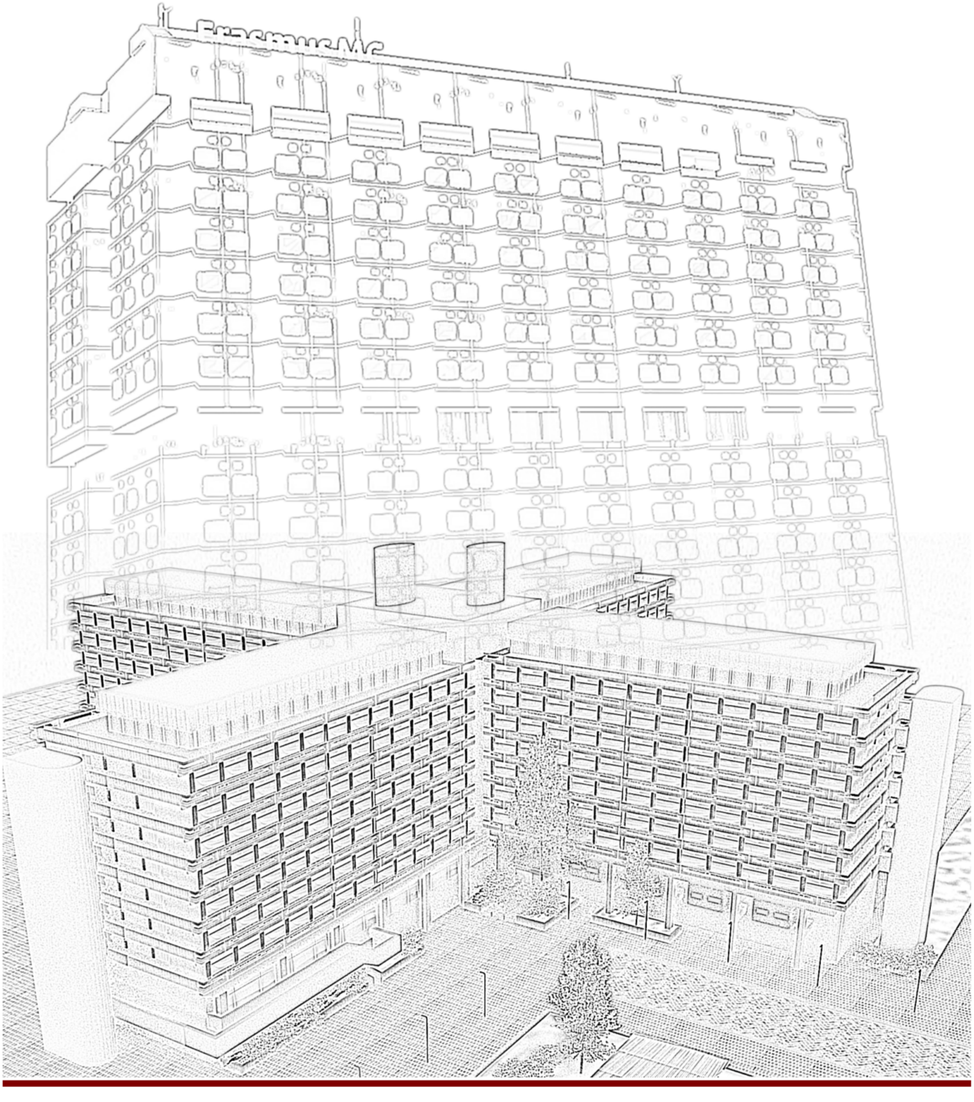

APPENDIX IV

ACKNOWLEDGEMENTS/DANKWOORD

> I may not have gone where I intended to go, but I think I have ended up where I needed to be.
>
> Douglas Adams

Het proefschrift dat nu voor u ligt is het resultaat van een langdurig groeiproces. Het is geschreven in de loop van zes jaar, in allerlei verschillende locaties en omstandigheden. Zes jaar is lang genoeg om van student-in-antikraakpand naar getrouwde vader te gaan, met kinderen die oud genoeg zijn om de verdediging bij te wonen. Dit boekje is geschreven in laboratoria, tijdens nachtdiensten in het ziekenhuis en aan het ziekenhuisbed van mijn kind. Als je start met een promotie begin je tijdens de meest vormende periode van je leven aan een traject waarvan je het beloop niet kunt overzien. De plannen die je vooraf had gemaakt, blijken in de praktijk te lijden onder logistiek, financiën en de wetten van de natuur. Het doel van een promotietraject is te leren zelfstandig onderzoek uit te kunnen voeren, het is een voorbereiding op een verdere carrière als onderzoeker. Dat doel is bereikt. Dit boekje is af, nu wordt het tijd om de geleerde technieken te gebruiken en nieuw onderzoek in gang te zetten.

Het groeiproces van dit proefschrift is begeleid door een groot aantal personen. In de eerste plaats mijn beide promotoren. Professor Hoogenraad, beste Casper, je kwam er bij terugkeer van vakantie achter dat er een nieuwe masterstudent in je lab was begonnen, nu ruim acht jaar geleden. Je hebt me zowel bij mijn masteronderzoek als tijdens mijn promotie uitgebreid de ruimte gegeven om mijn eigen onderzoekslijnen op te zetten en mijn interesses achterna te gaan. Als geneeskundestudent, niet gehinderd door enige kennis van basaal onderzoek, kreeg ik de mogelijkheid om mij naar eigen interesse te verdiepen in verschillende subdomeinen van de biologie en biofysica. Die mogelijkheid heeft mij een enthousiasme voor onderzoek en een repertoire aan onderzoekstechnieken opgeleverd die ik, ook na het afronden van dit promotietraject, nog vaak hoop in te zetten. Wat betreft je eigenschappen als begeleider zegt het genoeg dat al je studenten er unaniem voor kozen om met je mee te gaan naar Utrecht en daar een nieuwe onderzoeksgroep op te zetten. Professor Hintzen, Rogier, we hebben elkaar tijdens dit promotietraject minder gezien dan oorspronkelijk de bedoeling was, door de onverwachte verhuizing naar Utrecht. Je enthousiasme voor nieuwe inzichten en onderzoeksmogelijkheden werkte aanstekelijk, ook als de van tevoren geplande projecten niet altijd de gewenste resultaten opleverden. De afgelopen jaren hebben we heel wat meer contact gekregen in de kliniek, ik kijk er naar uit om daar nog veel van je te gaan leren.

Mijn dank gaat ook uit naar mijn commissie. Professor Sillevis Smitt, beste Peter, bedankt voor je werk als secretaris van de kleine commissie. Professor De Zeeuw, beste Chris, ik bewaar goede herinningen aan mijn tijd op de afdeling Neurowetenschappen, fijn dat je de moeite wilde nemen om in de commissie plaats te nemen. Professor Van Horssen, dank voor uw deelname aan de kleine commissie. Professor Wyman, ik waardeer het dat u een bijdrage wilt leveren aan mijn promotie. Lukas, je hebt in de afgelopen jaren zoveel begeleiding gegeven aan mijn onderzoek dat je een soort officieuze co-promotor bent geworden. Professor Laman, beste Jon, de afgelopen jaren heb ik je scherpe blik, heldere feedback en betrokkenheid bij het onderzoek zeer gewaardeerd.

Een promotieplechtigheid is niet compleet zonder de bijdrage van de paranymfen. Mariëlla, we hebben lange tijd samen op het lab gewerkt, zowel in Rotterdam als in Utrecht. Ik heb onze gesprekken en je persoonlijke betrokkenheid en interesse in anderen altijd erg op prijs gesteld, fijn dat je als mijn paranymf op wilt treden. Ad, toen we op de middelbare school naast elkaar in de bank zaten zijn we begonnen aan een discussie over het leven, het heelal en de rest, en daar eigenlijk nooit meer mee opgehouden. Optreden als paranymf is een mooie aansluiting op alle -pseudo-wetenschappelijke gesprekken die we al gehad hebben.

De tijd van de eenzame wetenschapper die op een zolderkamer-annex-laboratorium briljant onderzoek uitvoerde, is al lange tijd voorbij. Wetenschap is teamwork. Ik heb ontzettend geluk gehad met de teams waarin ik de afgelopen jaren heb gewerkt. In de eerste plaats groep Hoogenraad, eerst in Rotterdam en vervolgens in Utrecht. Phebe, behalve jou zijn er weinig mensen meer over uit die eerste periode. Je bent de constante drijfkracht achter het lab, altijd klaar om mensen te begeleiden, ondersteunen en waar nodig een feestje te organiseren. My office mates in Utrecht, Marta, Petra, Elena and Joanna, thanks for the ‘gezelligheid’, all the coffee and conversations. A special thanks also to the people in the Kapitein group for introducing me into the wonderful world of biophysics and superresolution microscopy. Eugene, your enthousiasm on science and software was always inspiring.

Ieder onderzoek is afhankelijk van het gebruikte gereedschap, wat in dit digitale tijdperk vaak neerkomt op software. Dit boekje en al het hierin beschreven onderzoek is tot stand gekomen zonder gebruik van commerciële software. Van beeldbewerking en statistiek tot grafische vormgeving, alle toegepaste programma’s zijn open source, vrij om te gebruiken en vrij om aan te passen. Deze programma's worden bijgehouden door een grote internationale gemeenschap van vrijwilligers, meestal naast een voltijdsbaan. Een overzicht van de software waarmee dit boekje tot stand is gekomen, kan gevonden worden in tabel A.1.

Eigenlijk is dit boekje een duo-productie en hoort er nog een extra naam op de voorkant te staan. Willianne, van acht jaar huwelijk ben ik zes jaar bezig geweest met promotie-onderzoek en het afronden van dit boekje. Vakanties, avonden en weekenden zijn bijna standaard opgeofferd aan werk en studie, zeker toen er naast een promotietraject ook een voltijdbaan als arts bijkwam. Bedankt voor je nooit aflatende steun, ook in de zorg voor onze kinderen met alle kleine en soms heel grote zorgen die daarbij horen. Marnix, Rhodé, jullie hele leven is papa al bezig om 'een boekje te schrijven'. Dankzij jullie werd ik er regelmatig aan herinnerd dat een lego-toren bouwen soms veel belangrijker is dan een proefschrift.

Open source software		*Commerciëel alternatief*
	Algemene software	
Besturingssysteem		
Linux Arch	`www.archlinux.org`	Windows, Apple OS
Linux Ubuntu	`www.ubuntu.com`	
Kantoorsoftware		
LibreOffice	`www.libreoffice.org`	Microsoft Office
Emacs	`www.gnu.org/software/emacs`	
Publiceren		
LaTeX	`www.latex-project.org`	InDesign, RefWorks, Endnote
	Beeldbewerking	
Vector graphics		
Inkscape	`www.inkscape.org`	Adobe Illustrator
Raster graphics		
GIMP	`www.gimp.org`	Adobe Photoshop
Wetenschappelijke beeldbewerking		
FIJI/ImageJ	`fiji.sc`	Huygens Suite
3D illustraties		
Blender	`www.blender.org`	Maya
	Programmeren	
Data analyse		
R	`cran.r-project.org`	SPSS
Rstudio	`www.rstudio.com`	
Beeldanalyse		
Python	`www.python.org`	LabView
Octave	`www.gnu.org/software/octave`	Matlab
Integrated Development Environment (IDE)		
Emacs, Rstudio		LabVIEW
Eclipse	`www.eclipse.org`	Microsoft Visual Studio

Table A.1: Veel gebruikte commerciële softwarepakketten en open source alternatieven. Een overzicht open source programma's die een gelijkwaardige vervanging vormen voor de meest voorkomende commerciële software binnen de wetenschap. Al de hier beschreven open source programma's zijn gebruikt voor de vervaardiging van dit proefschrift.